UNIVERSITAT POLITÈCNICA DE CATALUNYA BARCELONATECH

Modelling and control strategies for Hybrid AC/DC Grids

Adedotun Jeremiah Agbemuko

Universitat Politècnica de Catalunya
Electrical Engineering Department

PhD Thesis

Modelling and Control Strategies for Hybrid AC/DC Grids

Author: **Adedotun Jeremiah Agbemuko**

Advisors: **Dr. José Luis Domínguez-García**
Prof. Oriol Gomis-Bellmunt

Examiners: **Prof. Carlos E. Ugalde-Loo**
Dr. Agustí Egea Àlvarez
Prof. Luis Sainz Sapera

Barcelona, November 2019

Catalonia Institute for Energy Research (IREC)
Electrical Engineering Research Area
Jardins de les Dones de Negre 1 2nd floor,
08930 Sant Adrià de Besòs, Barcelona, Spain

Printed in Barcelona by TPI Copisteria
First Print, October 2019

To María with $d \to \infty + 1 \quad \forall \mathbb{R}$

Acknowledgements

This thesis would not have been made possible without the financial support of the European Union H2020 research and innovation programme under Marie-Skłodowska-Curie action— INCITE and executed at Catalonia Institute for Energy Research (IREC).

First and foremost, I am sincerely indebted to my supervisor, Dr. José Luis Domínguez-García at IREC for his supervision, constant reassurance, and the considerable freedom he gave on the scope of this work. I am equally grateful to my academic supervisor, Prof. Oriol Gomis-Bellmunt at the department of electrical engineering, Polytechnic University of Catalonia (UPC) who provided guidance on directions and continued support. My sincere appreciation also goes to Dr. Eduardo Prieto-Araujo who stepped in numerous times to assist in the supervision, providing constructive criticism that improved many parts of this thesis. I would also like to appreciate Prof. Nicolas Retiere at G2ELab Grenoble, France who hosted me during my secondment and constantly kept in touch even over an extended period after I left. Appreciation also goes to Prof. Lennart Harnefors at ABB Corporate Research Centre in Vasterås, Sweden who hosted my final secondment and an important part of this thesis.

Not to forget the ever-present INCITE project manager, Dr. Marta Fonrodona for standing in the middle of often exhausting bureaucracies and making everything much easier to deal with. A special mention to my colleagues at IREC, Sara, Thibault, other colleagues in the INCITE project, colleagues at IREC and CITCEA-UPC for all the assistance.

Finally, no one has been more important to me in the pursuit of this work than my Fiancée María, who stood gracefully and bore the brunt especially in the last few months of this process. Appreciation goes to my family and siblings who gave me the platform to get to this point, and the Zamorano-Hernanz family for the constant love and support. I truly appreciate you all.

Abstract

The proposals for large-scale deployment of renewable energy sources are leading to the need for more cross-border interconnections creating a pan-European power system, at the EU level. Such interconnections may take advantage of existing AC systems, but also of the DC links or DC grids under development; hence, evolving to hybrid AC/DC grids. Although hybrid AC/DC transmission grids are far from being truly large-scale, they are beginning to evolve as key components of future transmission infrastructures. By hybrid AC/DC grids, power electronic interfaces are invariably implied. As a consequence, several challenges are beginning to emerge at the network level due to the increasing adoption of these devices.

The dynamics and interactions that may appear in such integrated systems are relatively unknown since they will interconnect at least two subnetworks of AC and DC characteristics. Understanding how several classes of interaction could occur is key to the proper design of controllers to mitigate them. Further, changes to how subnetworks should be securely operated in unison are required. Therefore, a rethought is necessary in the presence of these devices. Nevertheless, the answer to the question of how to detect detrimental behaviours? Is central to any proposed solution.

Currently, traditional methods for modelling and analysis are showing inadequacies. Lack of consistent methods to model and analyse the phenomena often result in complicated solutions as existing literature suggests. Even more important are models that are tractable, flexible, and technology-agnostic to allow abstraction of the underlying challenges. Hence, methods to better understand and assess the mechanism of interactions at system-level, that may impact secure operation are required. Also, methods that are intuitive and efficient to detect sources of interactions, and isolate them as rapidly as possible are preferred. This goes to the heart of flexibility and tractability. Therefore, this thesis presents

methodologies and strategies for modelling and control of large-scale hybrid AC/DC transmission grids from a systematic perspective, with the consideration of the controllable devices.

This thesis employs several high-level methodologies that possess physical connotation, are technology agnostic, and provide tractability for control. Subsequently, recommended control strategies are easy to adopt as their physical significance can be established. The principal findings of this thesis are that system interactions between subnetworks are dependent on the broad characteristics of each subnetwork. Thus, manipulating any of these characteristics subject to considerations improves the overall behaviour. Within each subnetwork, interactions depend mainly on the dynamics of existing controllers, and the interconnection between several devices. Then, questions on how to detect and mitigate interactions as efficiently as possible, while incorporating the most relevant behaviour are answered. Furthermore, the conflict of control requirements of each subnetwork of the hybrid AC/DC network is highlighted. Thus, information about these requirements is leveraged to achieve overall compromises without jeopardizing minimum performance. To conclude, following the assessment of detrimental interactions and their corresponding mechanism, control strategies that consider these are proposed and demonstrated.

Resum

Per complir amb l'objectiu del gran desplegament de les energies renovables cal ampliar les interconnexions entre diferents països creant una xarxa elèctrica de transmissió a nivell europeu. Aquestes interconexions poden aprofitar els sistemes en corrent altern (CA) ja existents però també de nodes en corrent continu (CC) or xarxes en CC. Tot i que les xarxes de transmissió híbrides CA i CC són encara lluny de ser una realitat, s'estan començant a posicionar com un component principal de les infrastructures de transmissió del futur. A les xarxes CA i CC, l'electrònica de potencia n'és part fortament implicada. Com a conseqüéncia de l'ús d'aquests elements, diversos reptes comencen a emergir degut a la seva complexitat inherent i la seva gran utilització.

Les dinàmiques i les interaccions que poden aparèixer en aquest sistema integrat són desconegudes doncs aquest interconnectarà com a mínim dues subxarxes amb diferents característiques com són la CA i la CC. Entendre com diferents interaccions poden succeir és clau per a poder dissenyar de manera adequada els controlladors i mitigar-les. A més a més, calen canvis en l'operació coordinada de les subxarxes. Aleshores, repensar com resoldre el problema és necessari quan ens trobem en presència d'aquestes components. Però, la responsta a la pregunta; Com detectem comportaments negatius? és rellevant per a qualsevol solució que es vulgui proposar.

Els mètodes tradicionals de modelització i anàlisi mostren insuficiències. La manca de mètodes coherents per modelar i analitzar els fenòmens sovint es tradueix en solucions complicades com suggereix la literatura existent. Encara són més importants els models tractables, flexibles i agnòstics que permetin l'abstracció dels reptes subjacents. Per tant, es requereixen mètodes per comprendre i valorar millor el mecanisme d'interaccions a

nivell del sistema que puguin afectar un funcionament segur. A més, es prefereixen mètodes intutius i eficients per detectar fonts d'interaccions i aïllar-les el més ràpidament possible. Això arriba al cor de la flexibilitat i la traçabilitat. Per tant, aquesta tesi discuteix les estratègies de modelatge i control de les xarxes de transmissió híbrides CA / CC a gran escala des d'una perspectiva sistemàtica, tenint en compte els dispositius controlables.

Aquesta tesi utilitza una potent metodologia d'alt nivell que té una connotació física, és tecnologia agnòstica i tractable. Posteriorment, les estratègies de control recomanades són fácils d'adoptar ja que es pot establir la seva significació física. Els principals resultats d'aquesta tesi són que les interaccions del sistema entre subxarxes depenen de les àmplies característiques de cada subxarxa. Per tant, la manipulació d'aquestes característiques subjectes a consideracions millora el comportament general. Dins de cada subxarxa, les interaccions depenen principalment de la dinàmica dels controladors existents en dispositius controlables i de la interconnexió entre diversos dispositius. A continuació, es responen preguntes sobre com detectar i mitigar les interaccions de la manera més eficaç possible, alhora que incorporant el comportament més rellevant. A més, es posa de manifest el conflicte de requisits de control de cada subxarxa de la xarxa híbrida CA / CC. Així, es pot aprofitar la informació sobre aquests requisits per aconseguir compromisos generals sense posar en perill el rendiment mínim. Validar i demostrar aquests models i estratègies de control ha estat una contribució clau en aquesta tesi.

Contents

List of Tables

List of Figures

Glossary, Notations, Nomenclature

1 Acronyms

AC	Alternating Current
AVC	Alternating-Voltage Control
AVR	Automatic Voltage Regulator
DC	Direct Current
DVC	Direct-Voltage Control
EU	European Union
HVDC	High Voltage Direct Current
IGBT	Insulated Gate Bipolar Transistor
LTI	Linear Time Invariant
MIMO	Multi-Input Multi-Output
MMC	Multi-level Modular Converter
MTDC	Multi Terminal Direct Current
NPC	Neutral Clamped Converter
ODE	Ordinary differential equation
OHL	Over head line
PCC	Point of Common Coupling
PLL	Phase-Locked Loop
POC	Point of Common-coupling
PSS	Power System Stabilizers
PWM	Pulse Width Modulation
RES (RESs)	Renewable Energy Source(s)
SISO	Single-Input Single-Output
SCR	Short Circuit Ratio

SRF	Synchronous Reference Frame
SVD	Singular Value Decomposition
VSC (VSCs)	Voltage Source Converter(s)

2 Notation and Nomenclature

$\mathbb{R}$	Real space
$\mathbb{R}^n$	Linear space of real vectors of dimension n
$\mathbb{R}^{n\times m}$	Matrices with n rows and m columns and elements in $\mathbb{R}$
$\mathbb{R}^{n\times m\times l}$	Three dimensional matrices with n rows, m columns, and l arrays
n	Number of terminals or nodes
N	Number of random samples in a statistical system
$u_{cd,q}$	Converter voltages in the dq domain
$u_{fd,q}$	Filter voltages in the dq domain
$i_{cd,q}$	Converter currents in the dq domain
$i_{gd,q}$	Grid currents in the dq domain
U_f	Filter voltage magnitude
P_{dc}	Active power on DC side
P_{ac}	Active power on AC side
P	Power on DC side
Q	Reactive power on DC side
V_{dc}	Direct-voltage
I_n	DC network current
I_{dc}	Converter DC injection
θ_p	PLL output angle
$\Delta\theta_p$	PLL output angle
h_{cl}^i	Closed loop transfer function of inner current loop
H_{ol}^v	Open loop transfer function of the DVC
H_{cl}^v	Closed loop transfer function of the DVC
x^0	Operating point of an arbitrary variable x
K_x	Controller of an arbitrary external variable x
$\mathbf{W}$	Weighting matrix
$\mathbf{Z}$	Matrix Z
diag(.)	Diagonal operator
A_{ij}	ij^{th} element of a matrix A
$\|\|.\|\|_2$	2-norm
$\|\|.\|\|_\infty$	∞-norm

1 Introduction

1.1 Context and Motivation

Following a significant debate at the end of the 20th century on the consequences of climate change to the environment, a "clarion call" was initiated to reduce CO_2 emissions partly responsible for climate changes [2]. Ever since, governing bodies and stakeholders have been taking bold steps in addressing this salient issue. One such step proposed by the European Union (EU) is to reduce the emission levels of CO_2 to 80%-95% of levels detected in 1990 by year 2050 [3–7].

The electrical power system was identified as a vital sector in achieving this target. Thus, it was proposed that by 2050, the power system should be emissions-free [8]. This is an audacious target and deliberate actions such as gradual decommissioning and reduction in operating hours of fossil-fuel power plants, and restrictions on the manufacture of carbon-emitting power plants are currently being implemented [9].

Based on the proposed framework by the EU for bulk resource transmission, it will be required to connect distinct RESs (Renewable energy sources) across the entire continent and potentially beyond. This is to maintain the security of supply, improve the flexibility of energy markets, and mitigate the effects of seasonal intermittency and geographic sparsity of resources. As a consequence of these, connections will have to go beyond borders, span dozens of energy markets, and regions. One of such ambitious large-scale interconnection of distinct resources is proposed by the Global Energy Interconnection Development and Cooperation Organization (GEIDCO) shown in Fig. 1.1 [10]. In a future system such as this, there is no option short of very long-distance transmission of bulk power. Currently, traditional AC systems are already at their technical limits, lack inherent operational flexibility and required controllability in

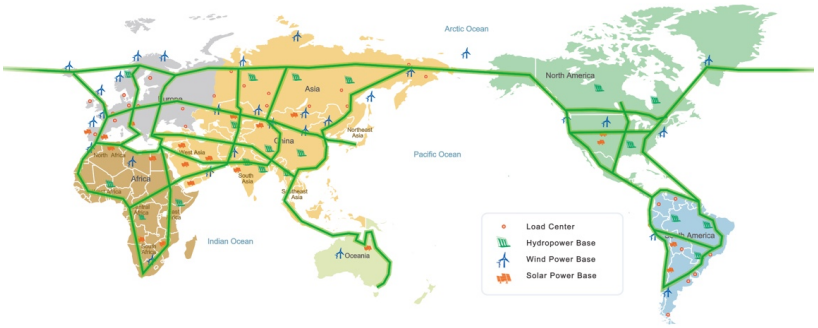

Figure 1.1: Conceptual interconnection of diverse resources across continents [Source: GEIDCO]

the face of intermittent RESs, and costly for very long-distance projects. In other cases such as long-distance offshore resource interconnection to the mainland grid, AC transmission is simply not an option in numerous cases [11–13].

The high voltage DC (HVDC) transmission technology offers a higher degree of controllability, flexibility, less costly in the long term, environmentally friendly, with potential to interconnect diverse resources, and particularly suited to long-distance interconnections amongst other benefits [14–16]. However, HVDC systems are expected to connect to existing and potentially new AC systems. Hence, even though the pervasiveness of HVDC is envisaged, they will not be operated in isolation for the foreseeable future. Rather, the operation will be in connection with the AC system. Therefore, future power systems would be a hybrid combination of AC/DC systems; at least at the MW power range and transmission level [17–19]. This would be an ideal scenario for power transmission to leverage on both AC/DC technologies which are both complementary.

The fundamental differences between AC and DC in broad would almost invariably imply power electronic devices will be employed as an interface in a hybrid AC/DC grids [20–22]. Power electronic devices commonly offer significant controllability, flexibility, relative ease of integration, and better overall efficiency of the entire system. However, pervasive power electronic deployment comes with several drawbacks that must be dealt with given the promises of these devices [23, 24].

It is well established that converter based generation and transmission gradually leads to loss of global system inertia [25]. Other challenges include detrimental interactions in the form of resonances, harmonics, and stability issues considering two distinct grid behaviours, among other challenges that are not yet completely understood [26–28]. Hybrid AC/DC

grids with pervasive power electronic devices are an "unknown territory" with potentially undiscovered phenomena that may threaten the secure operation of future transmission systems.

Therefore, modelling methodologies that are fundamental in nature, reliant on physical considerations, and most importantly technology and structure agnostic are prerequisites for detecting, analysing, and mitigating unwanted phenomena and interactions. Importantly, given the extreme controllability of power electronic devices, ideal mitigation methods can rely on exploiting the controllability of these devices to obtain an overall desired behaviour of both AC/DC grids. In summary, the entirety of this thesis is devoted to fundamental modelling and detection of detrimental interactions. Subsequently, analysis and mitigation of these interactions in a potential hybrid AC/DC grid set up, through the exploitation of controllability of devices are carried out. In all, a system-level approach is adopted with a consideration of the capabilities of the devices themselves.

1.2 HVDC Transmission Systems

The current HVAC transmission system in numerous regions are already being operated near capacity [29]. Given the constraints of long-distance AC transmission, stakeholders are averse to investing in costly projects except feasibility studies show otherwise [30–32]. Fig. 1.2 shows a predicted levelized cost comparison between HVAC and HVDC transmission over a distance for overhead line (OHL) systems [1]. It shows that HVDC will be preferred for long-distance transmission [14,33]. As previously mentioned, for cases such as far offshore integration of wind energy to mainland grid through the use of cables, HVAC transmission based on existing tech-

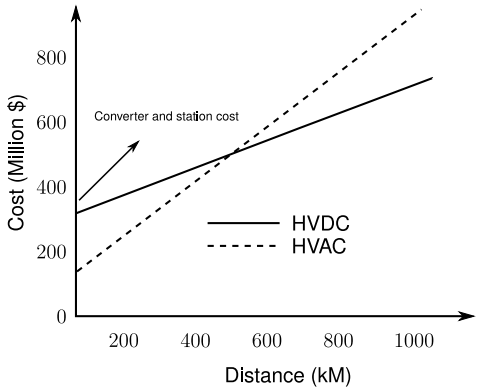

Figure 1.2: Basic levelized cost of HVAC transmission over HVDC [1]

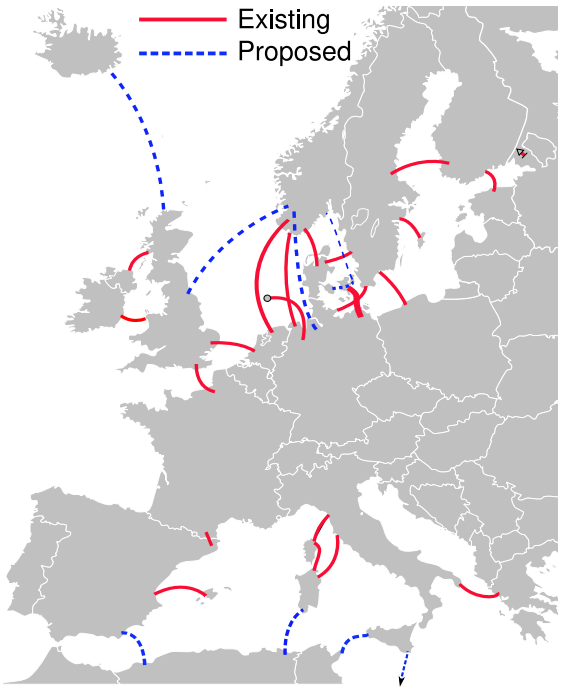

Figure 1.3: Existing and proposed HVDC links in Europe (Source: Wikimedia commons)

nologies may not be an option beyond a certain distance. HVDC provides huge benefits in costs, technical advantages, and easily meets requirements for extremely long (inter-)intra-continental connections [34–38]. The first commercial HVDC link was put into operation in 1954 connecting mainland Sweden to Gotland. Since then, many HVDC links have been put into operation. Several countries are already cooperating through cross-border HVDC interconnections as listed in Table 1.1 and many others are in the advanced stages [39]. To show the expected HVDC interconnections within the existing HVAC transmission grid, Fig. 1.3 depicts the current and planned HVDC interconnections in Europe. The first phase of interconnections is expected to be hybrid AC/DC grids with HVDC links, with a progression towards large-scale meshed hybrid AC/DC grids often referred to as super-grids by interconnecting several HVDC links [32].

There are currently two main technologies for the implementation of HVDC grids, namely; line commutated converter (LCC) technology, often referred to as HVDC classic, and the newer voltage source converter (VSC) technology, often referred to as HVDC light [40]. LCCs, though only semi-controllable, have been the backbone of HVDC transmission

Table 1.1: Existing HVDC links between countries within Europe

Project	Distance	Scheme	Voltage	Capacity
BritNed (GB-NL)	260km	Bipolar	± 450kV	1000MW
NorNed (NO-NL)	580km	Bipolar	± 450kV	700MW
Kontek (DK-NL)	170km	monopolar	-	350MW
Skagerrak (DK-NO)	250km	Bipolar	multiple	1700MW
BalticCable (DE-SE)	250km	Monopolar	450kV	600MW
Italy-Greece (IT-GR)	313km	Monopolar	400kV	500MW
SwePol (SE-PL)	254km	Monopolar	450kV	600MW
EstLink (EE-AL)	105km	Bipolar	± 150kV	350MW
NemoLink (GB-BE)	140km	Monopolar	400kV	1000MW
East West (IE-GB)	261km	Bipolar	± 200kV	500MW
INELFE (ES-FR)	65km	Bipolar	± 320kV	2000MW
LitPol (LT-PL)	341km	Bipolar	± 70kV	500MW
NordBalt (EE-AL)	450km	Bipolar	± 300kV	700MW

systems since the 1970s and are expected to still dominate the ultra-high power markets for a few years to come [41, 42]. LCC is a mature technology and is currently the preferred technology for long-distance ($>$ 1000 km), high power ($>$ 5000 MW) transmission as currently implemented in China [42, 43]. Notwithstanding the superiority of the LCC technology in terms of power and voltage handling capabilities, implementations of this technology are starting to wane in favour of the VSC as the power and voltage handling capabilities of the latter improves. At the current technological pace, VSC technology is expected to become the default choice in the coming decades and they have been heralded as the backbone of future transmission systems. They offer full controllability, flexibility, and

capability to interconnect any physical grid and its corresponding architecture while solving nearly all challenges of the LCC technology [44–49]. Without reservations, the rest of this thesis is devoted to VSC-HVDC and associated technologies.

1.2.1 VSC-HVDC Technology

Advances in power electronics and associated controls have significantly fast-tracked the development of the VSC as a promising technology for high voltage transmission [16, 50–56]. The advantages of VSC are numerous to mention and applications of VSC technologies to transmission projects are on the increase. One of the major challenges of VSCs today from a research perspective is the often complicated control strategies and monitoring required [57]. On a positive note, the controllability of the VSC is one of its greatest strengths when properly exploited. Several topologies are currently available for implementing the voltage source concept. However, three broad topologies have stood out for high power applications, namely; two-level, three-level, and multi-level topologies.

Topologies of the VSC for HVDC Transmission

The two-level topology is the simplest topology that can be applied to a VSC and is the basic building block of any arbitrary level. Fig. 1.4 depicts the circuit configuration of a two-level converter with the capability to conduct current in both directions and block voltage in one direction. The switches are designed with anti-parallel diodes to provide a path for residual currents amongst other significant functions. Each AC phase consists of phase reactors made up of mainly inductances to smooth the alternating current. The DC side consists of DC capacitors that maintain the DC voltage for a period depending on the size of the capacitance. The DC network is connected to the DC positive and negative rails [58]. The most common method for switching is the pulse width modulation (PWM) that compares a reference sinusoidal signal at the desired fundamental frequency with a repetitive switching triangular waveform to generate the switching pulses [59]. The triangular waveform dictates the switching frequency of the VSC. The two-level converter is termed so, as it generates two voltage levels viz. $+V_d/2$ and $-V_d/2$.

For a three-level VSC, Fig. 1.5 shows the circuit diagram of the three-level diode clamped VSC. The major difference in waveforms between the two and three-levels VSC is the addition of a third voltage level viz. 0.

The state-of-art of VSC technologies is the modular multilevel converter (MMC). This concept has attracted significant interest in HVDC applications and is the main topology for VSC-HVDC transmission projects [60–67]. Theoretically, as the name suggests, infinite voltage levels can be

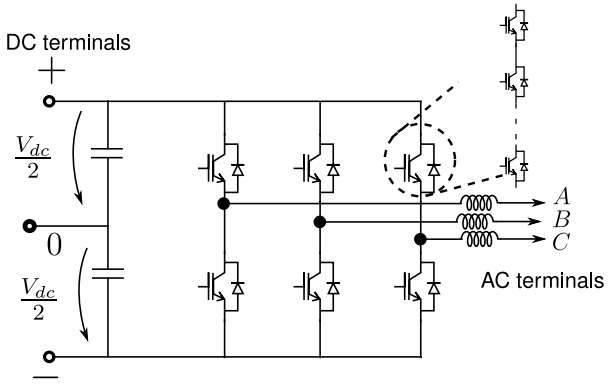

Figure 1.4: Circuit diagram of a three phase two-level VSC

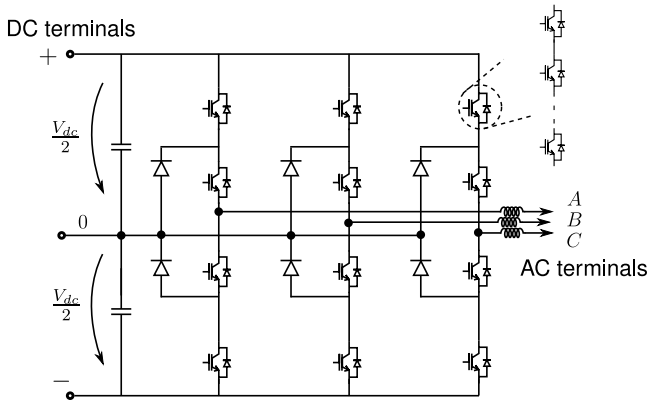

Figure 1.5: Circuit diagram of a three phase three-level diode clamped VSC

obtained, thus allowing a significantly better reconstruction of the sinusoidal AC signal. Advantages of MMC over the two and three-level VSC include very low harmonic contents due to a far superior reconstruction of voltages and currents, modularity, higher efficiency, scalability to arbitrary voltage levels, inherent redundancy of components, with no requirement for a common DC side capacitor. Fig. 1.6 shows the circuit configuration of the MMC showing the basic structure and components consisting of the submodules and arm reactors. Despite the superior performance obtainable from the MMC topology, the complex internal dynamics requires complicated control structures. Moreover, the required number of switching devices is arbitrarily high, in addition to other circuit-level complexities. Internal dynamics that must be controlled include circulating

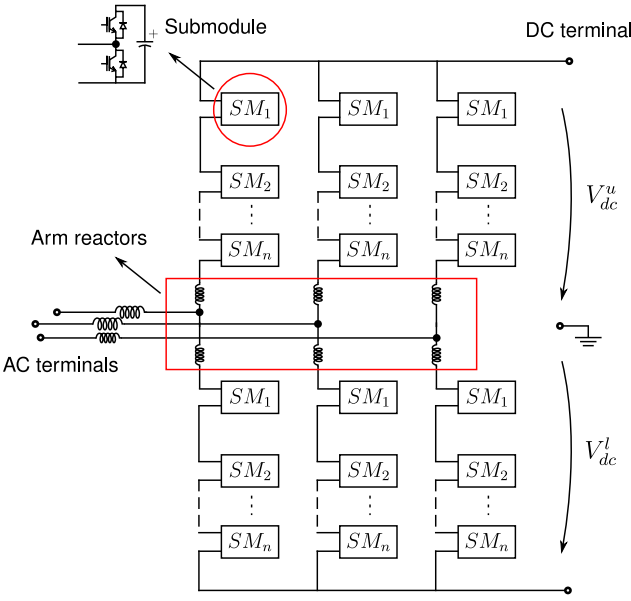

Figure 1.6: Circuit diagram of a multi-level VSC

currents, submodule capacitor balancing, for which extreme care must be applied.

Irrespective of the topology adopted, the VSC can be represented as an ideal voltage and/or current source for which the control system can freely determine the magnitude and phase subject to external limits and requirements. Similarly, for network-level analysis and control design, the equivalent bus dynamics of an MMC and two-level VSCs are similar [58]. For instance, the equivalent bus dynamics of a three-phase MMC (Fig. 1.6) can be expressed as

$$6\frac{C_{sm}}{N_{sm}}\frac{dV_{dc}}{dt} = I_{dc} - I_n \tag{1.1}$$

where C_{sm} is the submodule capacitance, N_{sm} is the number of submodules per arm. The above is similar to that of a two-level VSC. However, this disregards the internal dynamics. This is possible if all internal dynamics are properly controlled in closed-loop. Then, the terminal-level input-output responses for both topologies and external dynamics relative to network variables are largely similar [68,69]. Therefore, for system-level generalizations and extensibility, the basic topology of the VSC is adopted in this thesis; with an assumption that internal dynamics of more complex topologies are properly controlled and parameters are comparable.

1.2.2 Physical Architecture of Hybrid AC/DC Grids

Rapid advances in the field of power electronics have opened up potentials for vast hybrid AC/DC grids based on VSC technology. Fig. 1.7 shows the basic architecture of a VSC-HVDC grid in several basic network configurations consisting of two VSC stations connected by a cable or overhead line as the case may be. The asymmetric monopolar configuration is the most basic consisting of one conductor and ground, or two conductors. The monopolar consists of two conductors with opposite voltage polarities. Whereas, the bipolar configuration may be an extension of the asymmetric monopolar configuration or built completely as bipolar and in both cases, there are two converters per station. The interconnected AC grid on either side of the DC network may be synchronous or asynchronous grids, or two points within the same control area often referred to as embedded HVDC or back-to-back implementations where both converters are located within the same vicinity. In the same manner, either one of the AC grids may be an energy resource such as wind and solar power plants, or an offshore load centre.

One of the major advantages and focal points of the rapid adoption of VSC-HVDC transmission is the capability to interconnect several VSCs on the DC side in a meshed configuration similar to HVAC transmission systems. Going into the future, this capability is expected to be widely exploited allowing the interconnection of VSC-HVDC links to share resources, increase reliability, and reduce costs of operation. For instance, in the North Sea region of Europe where significant energy resources are currently being tapped, plans are being proposed to form offshore meshed VSC-HVDC grids and elsewhere in the continent. The embedded HVDC grid can as well be adopted to segment the different AC grids of each country and/or region while allowing to interconnect as many divers resources as possible. Additionally, each country may also adopt meshed HVDC grids to segment control areas, decongest the AC grid, and overall strengthening of the system as shown in Fig. 1.8 taking Spain as an example.

1.3 Scope and Methodology of Research

This thesis focuses on analytical modelling from physical considerations of a VSC interfaced AC/DC grid for broad system-level analysis and control. Studies focus on broad stability — local and global, interaction phenomena, and mechanism of interactions between AC-AC, AC-DC, DC-DC interfaces of the VSC. More importantly, the impact of control algorithms of the VSC on these interaction phenomena and dynamic behaviour as seen from each subnetwork is investigated. Furthermore, better control algo-

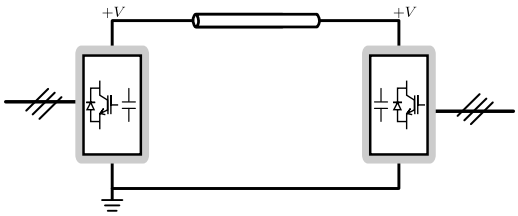

(a) Asymmetrical monopolar configuration

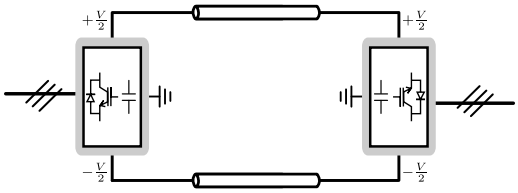

(b) Symmetrical monopolar configuration

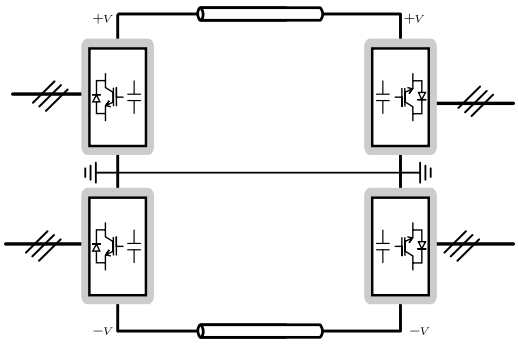

(c) Bipolar configuration

Figure 1.7: Basic network configurations of converters in an arbitrary HVDC grid

rithms and strategies that consider detrimental interactions are proposed both at the subnetwork level and the entire network at large. Therefore, the small-signal dynamic modelling and analysis framework is extensively employed. At this juncture, it is important to make clear the usage of the term "subnetwork". In the entirety of this thesis, a subnetwork is a collective term used to describe all nodes in each AC or DC grids of a hybrid AC/DC network. Whereas, the hybrid grid itself is the network that connects these subnetworks.

To conclude, a significant portion of the analytical and control design parts of this thesis are heavily dependent on frequency domain derivations and analysis, and in other cases, statistical based methods are applied.

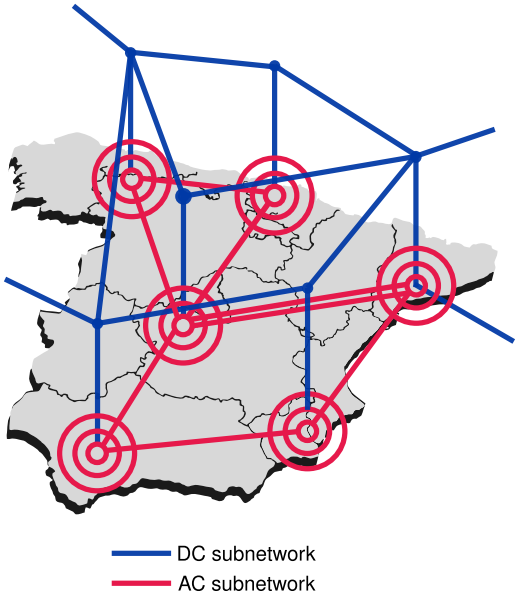

Figure 1.8: Adoption of the HVDC grid to segment AC control areas

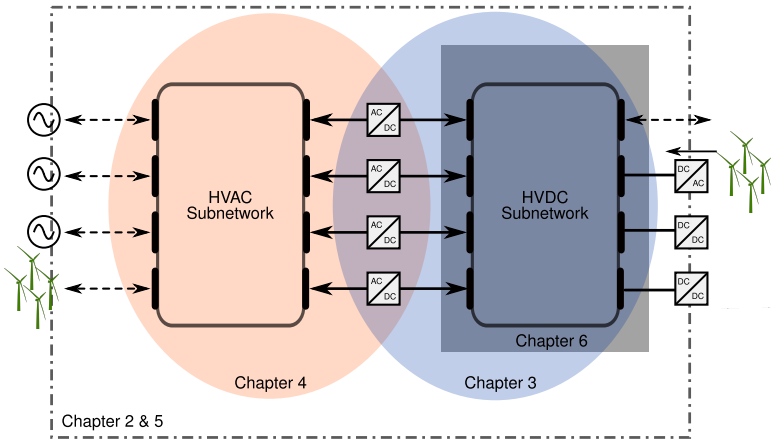

Figure 1.9: Illustrative overview of thesis as structured and related chapters

Detailed nonlinear simulations in the time domain are employed to assess the detected phenomena and validate the control strategies. Fig. 1.9 depicts an illustrative overview of this thesis in relation to hybrid AC/DC grids with related chapters.

The main objectives of this thesis are summarized as follows:

1. Develop suitable analytical tools and models that sufficiently captures the system-level dynamics of both the AC and DC sides of a VSC concurrently. Models are expected to be technology or structure agnostic and mathematically tractable for system-level analysis and control design or modification.
2. Identify the impacts and relationships between the controlled variables at the converter level and system-level dynamic behaviour in hybrid AC/DC grids.
3. Propose easy to adopt control algorithms, strategies, and guidelines to guarantee (to some extent) acceptable system-level dynamic behaviour and stability. Importantly, and where possible, such strategies and algorithms should not require explicit knowledge of the internal structure of the converter.
4. Provide recommendations to avoid detrimental interactions and improve overall behaviour.
5. Assess the potential for interoperability and related issues with multi-vendor converter technologies in hybrid AC/DC grids.
6. Explore novel methods to analyse the collective system-level dynamics of large-scale HVDC grids.

1.4 Scientific Contributions of Thesis

The main contributions of this thesis are summarized below based on the overall structure of the thesis.

Contributions related to Hybrid AC/DC grids

- Modular development and comparison of methods for concurrent modelling of the AC/DC sides of a VSC for input-output representation. Subsequently, the extension of terminal-level equivalents to network-level while keeping modularity and tractability for control.
- Detailed insights into required trade-offs of control from a physical perspective (considering the distinct nature of each AC and DC grid) for a stable hybrid AC/DC grid. Then, guidelines and recommendations to meet these trade-offs especially under special conditions such as weak grids are presented.
- Development and verification of control strategies for hybrid AC/DC grids that meet trade-off requirements for stable operation of hybrid AC/DC grids.
- Demonstration of modularity, scalability, and flexibility of the modelling approach employed and control strategies developed.

Contributions related to the AC grid

- Compact and modular method to represent the VSC in AC grid studies and analysis.
- A comprehensive characterization of the VSC input-output behaviour as modelled from physical considerations and under several varying conditions is presented. This knowledge is leveraged in designing effective controls (both adaptive and otherwise) to better cover the expected operating range of the converter in an arbitrary network.
- A robust and quite simple control design is proposed to significantly improve the active power capabilities of VSCs connected to very weak AC grids. This design stems from a better approach to the analysis of the interactions between the VSC and the connected AC grid.
- Analysis of potential interactions between the controllers of synchronous generators and VSCs leading to the poor dynamic performance of such hybrid AC/DC grids. Then, simple methods to alleviate these interactions are presented.

Contributions related to the DC grid

- An integrated framework is proposed to model and analyse the input-output behaviour of VSC-HVDC grids as single entities. This includes methods for assessing converter-converter interactions and how to mitigate them.
- An advanced robust control approach is proposed to decouple interacting VSCs in multi-vendor VSC-HVDC grids. Besides, flexibility and modularity of the approach are demonstrated.
- A methodology is proposed to design droop-based local control strategies as a first step in mitigating potential global interaction.
- An advanced yet basic theoretical modelling framework is proposed to model and analyse the aggregate behaviour of large-scale HVDC grids with concepts borrowed from molecular physics and complex networks.

1.5 Thesis Outline

Fig. 1.10 depicts the overall methodology employed in this thesis and organized as follows.

- **Chapter 2** presents the impedance-based modelling framework as a tractable and physically insightful framework for the representation of the input-output behaviour of a VSC on either side of the converter. This modelling methodology supports an extensive part

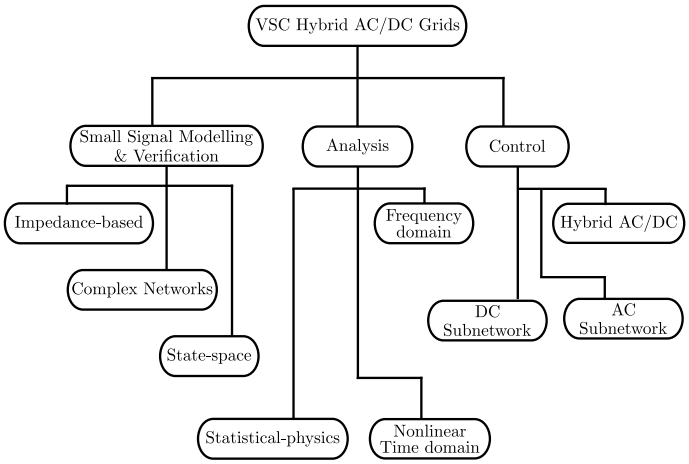

Figure 1.10: Overview scope and methodology adopted in this thesis and related chapters

of the analysis and control strategies explored in this thesis. The impedance models of the VSC based on several control strategies and all other identified subsystems are obtained as "stand-alone" subsystems. Subsequently, the subsystems are interconnected in the physical structure of the grid and aggregated into subnetwork equivalents in matrix form.

- **Chapter 3** presents the interaction analysis and control of VSC-HVDC grids of arbitrary structures in a hybrid AC/DC grid. The major aim is to understand the mechanism of interactions within the DC grid, control requirements, and potential conflicts of control requirement with the AC grid. A methodology for interaction analysis and network control design is then proposed.
- **Chapter 4** presents the interaction analysis and control of VSC-interfaced AC grids similar to the previous chapter. The major aim of this chapter is to highlight the behaviour of the AC grid distinct from the DC grid, including the influence of AC network characteristics, control mode, power direction, operating points, etc. Also, this chapter presents the control requirement of the AC side of a VSC that may potentially conflict with the requirements for the DC side in the previous chapter. The analysis presented allows obtaining insights on how to design or re-design effective controllers.
- **Chapter 5** presents the interaction analysis and control of an interconnected meshed hybrid AC/DC grid. The major contribution of this chapter is to recommend guidelines and control design trade-offs for guaranteed robust performance and stability of each connected

AC and DC grids and the entire network under practical considerations. Also, information from the the previous two chapters is integrated into the control of the hybrid AC/DC grid at large.

- **Chapter 6** presents a novel modelling and analysis approach to model the coherency of large-scale HVDC grids from a theoretical perspective such as complex networks theory. The analysis presented allow to compare the influence of control strategies and topological structure on the dynamic and the steady-state evolution of direct-voltages as a measure of system coherency. Also, operational recommendations and guidelines are presented for improving the overall behaviour of large-scale VSC-HVDC grids.
- **Chapter 7** concludes the thesis and discusses recommendations, guidelines, and future research.

2

Impedance-Based Modelling of Hybrid AC/DC Grids

This chapter presents the modelling methodology that underpins the analyses, developments, and strategies explored in this thesis. The entire system is decomposed from network-level to subnetworks and further to components that make up each subnetwork. Then, appropriate models are developed for each identified component at the subsystem-level and extended through to the network-level. Given the system-level models, key indices and tools for analysis of network phenomena and control are formulated with a view towards modularity and extensibility to any system of arbitrary structure and components. Importantly, derivations are carried out in a concise and modular manner that facilitates easy automation of derivations.

2.1 State-of-art of Impedance-based Modelling

The last decade has witnessed an exponential increase in the adoption of power electronics as interfaces in the power system [20]. The increasing adoption of these devices in the integration of renewable energy sources (RESs) has meant both AC and DC grids will have equal importance. However, such hybrid grids will combine the dynamics of AC and DC systems, as well as introduce new interactions. Therefore, proper modelling is required to identify and mitigate these interactions in a systematic manner. Intuitive methods that allow modelling the system without detailed information are lacking as issues related to transmission VSC AC/DC grids are only starting to emerge. However, the impedance framework is an intuitive and well-established tool in solving many challenges.

Impedance modelling involving power electronic converters first started

as a generalized method to model device level behaviour more than three decades ago [70]. The impedance-based framework has been re-emerging over the last decade as a powerful tool to model grids interfaced by VSCs [71–73]. After all, on a fundamental level, the power system no matter how large is made up of impedances. Hence, impedance is a basic physical property of the system. This is the core of the impedance framework, and every component in the system can be represented to some detail in the form of the impedance they impose.

In the same vein, the control system of these devices can be treated as dynamic impedances. This is true for VSCs where controllers often control voltages using currents, and vice-versa. For cases where voltages and currents are not directly controlled, controlled variables can be transformed into equivalent voltages and currents, through a linearization procedure. The relationship between voltages and currents are impedances. Therefore, the entire physical system and collection of controls can be easily integrated into the impedance framework [74]. This allows to adopt existing, well-established, and quite extensive power system and control theory tools to analyse, design, or re-design if necessary any subsystem or the system in general [75–78]. Therefore, analysis and solutions stem from physical considerations with added intuitiveness. To further support the applicability of impedance-based modelling, conclusions on stability can be derived similarly as traditional stability approaches such as state-space [79, 80].

Broadly speaking, the impedance framework has been extensively adopted to model and analyse stability and interaction behaviour of grid connected converters from the AC side through varying perspectives such as resonance analysis and mitigation [77, 78, 81–87], generalized system-level stability and impedance shaping through control design [71, 88–91], analysis [74, 75, 92–98], and to a lesser extent on DC side [79, 80, 99–105].

Several different domains for obtaining impedances have been routinely applied in research efforts. The most common of these are the *dq*, sequence, and phase domain impedances. Each offers several advantages and disadvantages compared to others. However, there is often no clear-cut benefit of impedances obtained or derived in one domain over another that facilitates an easy choice. For instance, *pn* sequence domain derivations offer a direct method to inherently deal with phase imbalances [106, 107]. However, if balanced phases may be assumed, then similar conclusions may be derived from both *pn* and *dq* derivations. On the alternative, *dq* derivations inherently assume a linear time-invariant (LTI) system (similar to linear controller designs) and controllers are often implemented in *dq* frame. Then *dq* derivations offers an advantage on ease of integration of controllers with the physical system. Increasingly however, extra functionalities are being demanded of VSC controllers such as additional control of

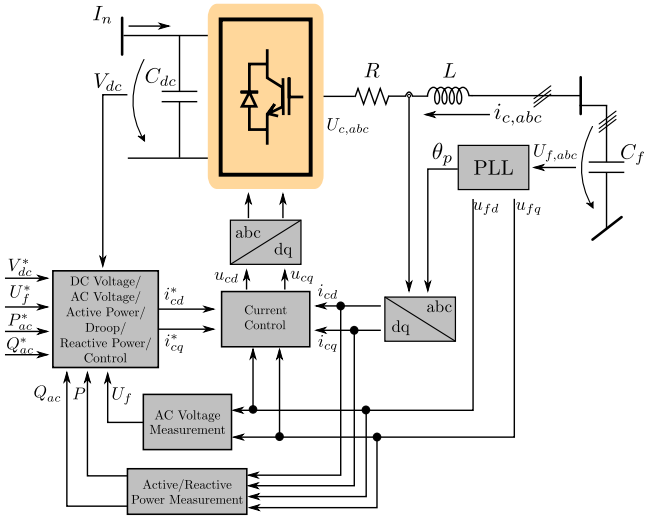

Figure 2.1: Single line circuit diagram and control layout of a VSC station

sequence components under potential unbalances. Then, the *pn* sequence derivation again offers clear benefit on ease of analysis [108]. Therefore, the control structure may dictate the actual choice of the domain to represent impedances over another. Nevertheless, several works have established the equivalence between these domains and unified them in a manner that allows easy transformation between them if required [106, 108, 109]. In this work, the *dq* domain derivation is adopted since controllers typical of high voltage and power are directly implemented in this domain.

In summary, in many of the works in literature, the focus has been disproportionately the AC side of a single VSC, thus effectively ignoring the entirety of the DC side much less an interconnected one. Secondly, how models are derived are specific and obscures the inherent simplicity of the impedance framework and the corresponding insights it provides. In this regard, existing impedance-based modelling of VSCs as applied in literature are not sufficiently generic nor modular to allow ease of applicability to multi-converter system-level studies, especially on the DC side. In this chapter, the AC and DC impedances of the VSC as a subsystem in *dq* domain are concurrently derived. Furthermore, all interaction transfer functions between variables of both AC and DC through the VSC are isolated in a modular and compact manner.

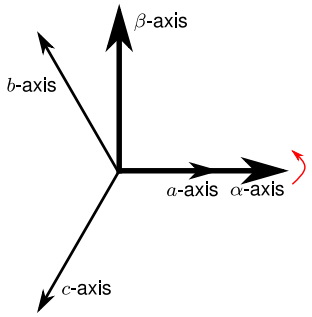

Figure 2.2: Relationship between space-vectors and *abc* domain quantities

2.2 Impedance Models of the VSC in dq Frame

In a hybrid AC/DC grid setup, the most important component is the converter, specifically the VSC as adopted in this thesis. The VSC is responsible for interfacing the AC and DC subnetworks. Therefore, while each subnetwork maintains its individual dynamics, the VSC is responsible for the ensuing shared dynamics between both. This section presents a sequentially derived analytical impedance of the VSC on either side as a stand-alone subsystem, in a manner that decouples both sides while isolating all interaction functions between both.

The single-line terminal circuit and control block diagram of the VSC substation as employed in this thesis is shown in Fig. 2.1. The innermost loop consists of the current control which is the heart of the vector current control for VSC-HVDC applications [110]. Whereas the outer-loops consist of a combination direct-voltage, alternating-voltage, active power, and/or reactive power controls, that provide the references to the inner current loop.

2.2.1 Current Controlled VSC

For any set of balanced three-phase quantities in the *abc* domain, an equivalent stationary complex vector $\mathbf{v}$ can be defined as

$$\mathbf{v} = \frac{2}{3}(v_a + v_b e^{j\frac{2\pi}{3}} + v_c e^{j\frac{4\pi}{3}}) \tag{2.1}$$

where v_a, v_b, and v_c are the three phase quantities. Therefore, at any arbitrary time instant, $\mathbf{v}$ is described with two stationary quantities such that,

$$\mathbf{v} = v_\alpha + jv_\beta \tag{2.2}$$

where v_α aligns with the phase a quantity, and v_β lags v_α by 90° as shown in Fig. 2.2. This vector can be transformed into the rotating *dq* frame

with a speed equal to the fundamental angular frequency ω_1 such that the equivalent vector in dq domain is given as

$$\mathbf{v}_{dq} = \mathbf{v}e^{-j\omega_1 t} \tag{2.3}$$

where $\mathbf{v}_{dq}$ is the dq domain vector. From the physical side of Fig. 2.1 the physical equation of the AC side of the VSC can be expressed in $\alpha\beta$ space-vectors as

$$L\frac{d\mathbf{i}}{dt} = \mathbf{u}_f - \mathbf{u}_c - R\mathbf{i} \tag{2.4}$$

where $\mathbf{u}_f$ are the PCC voltages in $\alpha\beta$ domain following the transformation from (2.1). These can be transformed into the dq domain following (2.3) to obtain the dynamic open-loop equation of the physical AC side as

$$\begin{aligned} L\frac{di_{cd}}{dt} &= u_{fd} - u_{cd} - Ri_{cd} - j\omega_1 Li_{cq} \\ L\frac{di_{cq}}{dt} &= u_{fq} - u_{cq} - Ri_{cq} + j\omega_1 Li_{cd} \end{aligned} \tag{2.5}$$

where i_{cd}, i_{cq} are the converter AC currents flowing from the filter bus or PCC to the converter; u_{fd}, u_{fq}, and u_{cd}, u_{cq} are the voltages (to neutral) at the PCC and converter terminals respectively, all in grid reference frame; R, L are the AC filter resistance and inductance respectively, and ω_1 is the grid angular frequency. In Laplace domain, the physical system can be re-written as

$$\begin{aligned} i_{cd} &= y_{ac}(s)\left(u_{fd} - u_{cd}\right) - y_{ac}(s)\omega_1 Li_{cq} \\ i_{cq} &= y_{ac}(s)\left(u_{fq} - u_{cq}\right) + y_{ac}(s)\omega_1 Li_{cd} \end{aligned} \tag{2.6}$$

with

$$y_{ac}(s) = \frac{1}{sL + R}$$

where $y_{ac}(s)$ is the physical admittance of the system otherwise known as the primitive admittance, and $s = d/dt$. The current controller interacts directly with the physical system through the converter alternating-voltages.

Since the converter's output voltages are related to the converter's own frame, the voltages can be obtained from the current control in dq frame from Fig. 2.3 as

$$\begin{aligned} u^c_{cd} &= -K_c(s)(i^*_{cd} - i^c_{cd}) - j\omega_1 Li^c_{cq} + F_d(s)u^c_{fd} \\ u^c_{cq} &= -K_c(s)(i^*_{cq} - i^c_{cq}) + j\omega_1 Li^c_{cd} + F_q(s)u^c_{fq} \end{aligned} \tag{2.7}$$

where variables with superscript 'c' are converter frame variables of the corresponding grid reference variables; '*' variables are reference values;

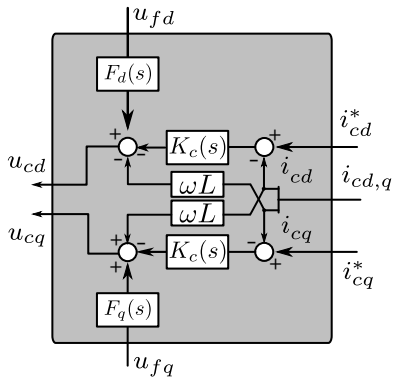

Figure 2.3: Block diagram of current control loop

$K_c(s)$ is the current *proportional-integral* (PI) compensator, $F_d(s)$ and $F_q(s)$ are the filters of the PCC voltage feedforward, of arbitrary structures on each of d and q-axes, with

$$K_c(s) = k_{pi} + \frac{k_{ii}}{s},$$
$$F_d(s) = F_q(s) = \frac{\beta_n s^n + \cdots + \beta_{n1} s + \beta_{n0}}{\alpha_d s^d + \alpha_{d-1} s^{d-1} + \cdots + \alpha_{d1} s + \alpha_{d0}},$$

where k_{pi} and k_{ii} are the PI gains of the current compensators, β, α are the corresponding numerator and denominator coefficients of the feedforward filters.

The impact of the current control on the physical system can be obtained by eliminating the control dependent converter voltages from the physical equations. However, both equations are on different reference frames *viz.* grid and converter reference frames. Therefore, a transformation is required from one frame to another. The PLL device through Park's transformation is responsible for this transformation. Hence, the PLL as a closed-loop controlled device also imposes its dynamics on the converter. The form of Park adopted in this thesis is given as

$$\mathbf{T}(\theta_p) = k \begin{pmatrix} \cos(\theta_p) & \cos(\theta_p - \frac{2\pi}{3}) & \cos(\theta_p + \frac{2\pi}{3}) \\ \sin(\theta_p) & \sin(\theta_p - \frac{2\pi}{3}) & \sin(\theta_p + \frac{2\pi}{3}) \\ \frac{1}{2} & \frac{1}{2} & \frac{1}{2} \end{pmatrix} \tag{2.8}$$

where $k = 2/3$, and θ_p is the output of the PLL. The transformations between grid and converter frame for variables, given the output PLL angle are clearly detailed in Appendix B.

The PLL output angle can be obtained from the PLL block diagram

shown in Fig. 2.4 as

$$\theta_p = \frac{1}{s}\left(2\pi f_1 - K_{pll}(s)u^c_{fq}\right), \tag{2.9}$$

$$K_{pll}(s) = k_{ppll} + \frac{k_{ipll}}{s},$$

where k_{ppll} and k_{ipll} are the PI gains of the PLL compensator, and f_1 is the system base frequency. The PLL takes one of the output of Park's transformation u^c_{fq} as an input in order to compute the synchronization angle; u^c_{fq} can be obtained from the converter to grid transformation (see Appendix B) as

$$(u_{fd} + ju_{fq})e^{-j\theta_p} = \underbrace{(u_{fd}\cos\theta_p + u_{fq}\sin\theta_p)}_{u^c_{fd}} + j\underbrace{(u_{fq}\cos\theta_p - u_{fd}\sin\theta_p)}_{u^c_{fq}} \tag{2.10}$$

and u^c_{fq} can be eliminated from (2.9). However, the introduction of θ_p introduces nonlinearity to the system for which up till equation (2.7) is inherently linear by physical principles. Therefore, the inclusion of nonlinear PLL angle θ_p requires linearization around an initial operating point. The transformation expressions can then be linearized as

$$\begin{aligned}
\Delta i^c_{cd,q} &= \mathbf{T}^i(\Delta i_{cd}, \Delta i_{cq}, \Delta\theta_p)^T, \\
\Delta u^c_{fd,q} &= \mathbf{T}^v(\Delta u_{fd}, \Delta u_{fq}, \Delta\theta_p)^T, \\
\Delta u_{cd,q} &= \mathbf{T}(\Delta u^c_{cd}, \Delta u^c_{cq}, \Delta\theta_p)^T,
\end{aligned} \tag{2.11}$$

where $\mathbf{T}$ is the linearized transformation matrix between converter and grid frame variables, $\mathbf{T}^i$, $\mathbf{T}^v$ are the corresponding linearized inverse transformation matrices between grid and converter frame variables (detailed in Appendix B). To include the impact of PLL control dynamics on the

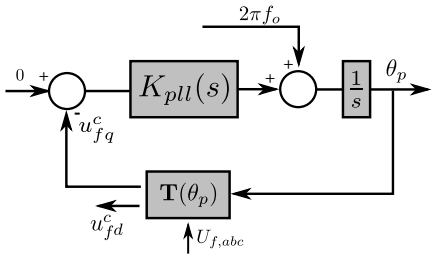

Figure 2.4: Basic structure of a conventional PLL

transformation variables, $\Delta\theta_p$ can be obtained by linearizing (2.9) as

$$\begin{aligned}\Delta\theta_p &= -\frac{K_{pll}(s)}{s}\Delta u_{fq}^c \\ &= -\frac{K_{pll}(s)}{s}\left(-\sin\theta_p^0\Delta u_{fd} + \cos\theta_p^0\Delta u_{fq} - (u_{fd}^0\cos\theta_p^0 + u_{fq}^0\sin\theta_p^0)\Delta\theta_p\right) \\ &= H_{d\theta}(s)\Delta u_{fd} - H_{q\theta}(s)\Delta u_{fq}\end{aligned} \tag{2.12}$$

where $H_{d\theta}(s)$ and $H_{q\theta}(s)$ are transfer functions that predict the complete impact of the PLL on each of d and q-axes of a vector controlled VSC (see Appendix B). Subsequently, $\Delta\theta_p$ can be eliminated from (2.11) by back-substitution of (2.12) into the corresponding variables to obtain augmented transformation and inverse transformation matrices given as

$$\begin{pmatrix}\Delta u_{fd}^c \\ \Delta u_{fq}^c\end{pmatrix} = \begin{pmatrix}T_{11}^v + T_{13}^v H_{d\theta}(s) & T_{12}^v + T_{13}^v H_{q\theta}(s) \\ T_{21}^v + T_{23}^v H_{d\theta}(s) & T_{22}^v + T_{23}^v H_{q\theta}(s)\end{pmatrix}\begin{pmatrix}\Delta u_{fd} \\ \Delta u_{fq}\end{pmatrix} \tag{2.13a}$$

$$\begin{pmatrix}\Delta i_{cd}^c \\ \Delta i_{cq}^c\end{pmatrix} = \begin{pmatrix}T_{11}^i & T_{12}^i \\ T_{21}^i & T_{22}^i\end{pmatrix}\begin{pmatrix}\Delta i_{cd} \\ \Delta i_{cq}\end{pmatrix} + \underbrace{\begin{pmatrix}T_{13}^i H_{d\theta}(s) & T_{13}^i H_{q\theta}(s) \\ T_{23}^i H_{d\theta}(s) & T_{23}^i H_{q\theta}(s)\end{pmatrix}}_{\mathbf{Y}_{pll}(s)}\begin{pmatrix}\Delta u_{fd} \\ \Delta u_{fq}\end{pmatrix} \tag{2.13b}$$

$$\begin{pmatrix}\Delta u_{cd} \\ \Delta u_{cq}\end{pmatrix} = \begin{pmatrix}T_{11} & T_{12} \\ T_{21} & T_{22}\end{pmatrix}\begin{pmatrix}\Delta u_{cd}^c \\ \Delta u_{cq}^c\end{pmatrix} + \begin{pmatrix}T_{13} H_{d\theta}(s) & T_{13} H_{q\theta}(s) \\ T_{23} H_{d\theta}(s) & T_{23} H_{q\theta}(s)\end{pmatrix}\begin{pmatrix}\Delta u_{fd} \\ \Delta u_{fq}\end{pmatrix} \tag{2.13c}$$

where $\mathbf{Y}_{pll}(s)$ is the corresponding admittance imposed by the PLL as seen by the current control loop. The augmented inverse transformation matrices of (2.13a) and (2.13b) are applied to the corresponding linearized version of (2.7) to obtain

$$\begin{aligned}\begin{pmatrix}\Delta u_{cd}^c \\ \Delta u_{cq}^c\end{pmatrix} = -K_c(s)\begin{pmatrix}\Delta i_{cd}^* \\ \Delta i_{cq}^*\end{pmatrix} + K_c(s)\begin{pmatrix}T_{11}^i & T_{12}^i \\ T_{21}^i & T_{22}^i\end{pmatrix}\begin{pmatrix}\Delta i_{cd} \\ \Delta i_{cq}\end{pmatrix} + \\ \underbrace{\begin{pmatrix}V_{11}(s) & V_{12}(s) \\ V_{21}(s) & V_{22}(s)\end{pmatrix}}_{\mathbf{V}(s)}\begin{pmatrix}\Delta u_{fd} \\ \Delta u_{fq}\end{pmatrix}\end{aligned} \tag{2.14}$$

where $\mathbf{V}(s)$ is an augmented matrix detailed in Appendix B.2. To include the impact of inner-current controller and PLL dynamics on the physical system, (2.14) is eliminated from the transformation in (2.13c), and the resulting $\Delta u_{cd,q}$ eliminated from the linearized version of the physical

system in (2.6) and $\Delta i_{cd,q}$ solved to obtain

$$\begin{pmatrix}\Delta i_{cd}\\ \Delta i_{cq}\end{pmatrix} = \underbrace{\begin{pmatrix} h^i_{cl}(s) & -h^i_{cl,dq}(s)\\ h^i_{cl,qd}(s) & h^i_{cl}(s)\end{pmatrix}}_{\mathbf{H}^i_{cl}(s)}\begin{pmatrix}\Delta i^*_{cd}\\ \Delta i^*_{cq}\end{pmatrix} + \underbrace{\begin{pmatrix} y_{dd}(s) & y_{dq}(s)\\ y_{qd}(s) & y_{qq}(s)\end{pmatrix}}_{\mathbf{Y}_{ac}(s)}\begin{pmatrix}\Delta u_{fd}\\ \Delta u_{fq}\end{pmatrix} \tag{2.15}$$

$$h^i_{cl}(s) = \frac{h^i_{ol}(s)\cos\theta^0_p}{1+h^i_{ol}(s)} = \frac{K_c(s)y_{ac}(s)\cos\theta^0_p}{1+K_c(s)y_{ac}(s)},$$

$$h^i_{cl,dq}(s) = h^i_{cl,qd}(s) = \frac{h^i_{ol}(s)\sin\theta^0_p}{1+h^i_{ol}(s)} = \frac{K_c(s)y_{ac}(s)\sin\theta^0_p}{1+K_c(s)y_{ac}(s)},$$

where $\mathbf{H}^i_{cl}(s)$ is the closed-loop reference to output transfer matrix of the inner-current controller, and $\mathbf{Y}_{ac}(s)$ is the output admittance of a current controlled converter. The components of the impedance model of the inner-current loop and PLL are detailed in Appendix B.3.

The expression in (2.15) fully describes the input-output behaviour of a current-controlled VSC with a PLL device. Observe from (2.15) that the closed-loop reference to output transfer matrix $\mathbf{H}^i_{cl}(s)$ is cross-coupled, counter to expectations. This shows that the PLL and its deviation angle introduces a cross-coupling between the axes of the inner-loop that were designed to be decoupled. For a properly designed and tuned PLL, and fairly strong AC grid with short circuit ratio (SCR $>$ 3), $\theta^0_p \approx 0$ and this cross-coupling disappears. However, for a poorly tuned PLL and/or very weak grids where $\theta^0_p \not\approx 0$, the PLL interacts significantly with the inner-loop resulting in instability and reduced capabilities.

Fig. 2.5 shows the closed-loop reference to output transfer functions of the current controlled VSC with an all-pass feedforward filter $F(s) = 1$, at an operating point of -200MW (inversion), and a PLL closed-loop bandwidth of 20Hz. As can be observed, for the given PLL at this operating point, the closed-loop reference to output transfer function is 1 which indicates the efficacy of current control up to the designed bandwidth. Whereas, the off-diagonal coupling $h^i_{cl,dq}(s) = h^i_{cl,qd}(s)$ introduced by the PLL is approximately 0. Hence, its impact may be neglected if uncertain conditions hold. Fig. 2.6 shows the frequency response of the impedance model of the current-controlled converter with the impacts of PLL included.

2.2.2 Alternating/Direct-Voltage Controlled VSC

In VSC-HVDC applications, it is rare for the converter to be operated in current control mode only. In most cases, the alternating-voltage magnitude at the PCC and direct-voltage on the DC side are often controlled (directly or indirectly) to a constant set-point through a hierarchical control

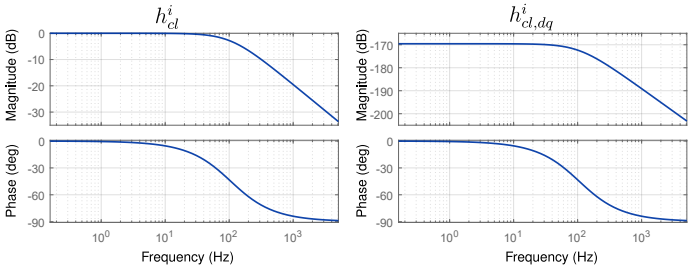

Figure 2.5: Closed-loop reference to output transfer functios of the current controlled VSC.

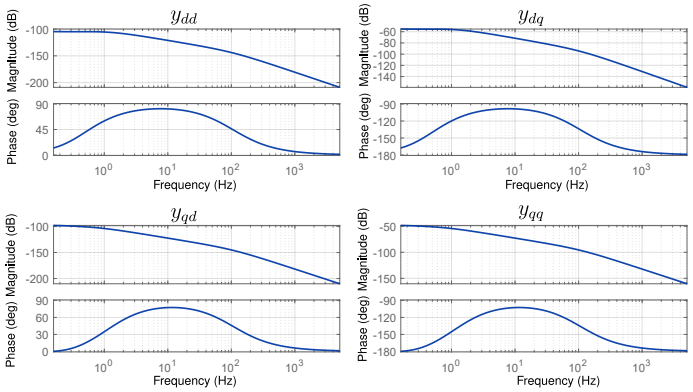

Figure 2.6: Output impedance models of the current controlled VSC with PLL impacts

scheme [49] as shown in Fig. 2.1. Each of alternating and direct-voltages are then controlled using either axis of the current loop respectively. In this thesis, the direct-voltage is controlled with a PI compensator on the d-axis through the converter active current i_{cd}, whereas, the alternating-voltage is controlled with a PI compensator through the converter reactive current i_{cq} as shown in Fig. 2.7. In other cases, the alternating-voltage is indirectly controlled through control of the reactive power.

For a combination of alternating and direct-voltage controlled VSC, each added controller impacts on the overall dynamics by reshaping the admittance of the inner-current loop described by $\mathbf{Y}_{ac}(s)$ in equation (2.15). The introduction of DC side dynamics also introduces an equivalent impedance imposed on the converter on the DC side in addition to the reshaped admittance on the AC side.

In a similar manner as previously, consideration is first given to the physical system, while subsequently "walking backwards" to include the

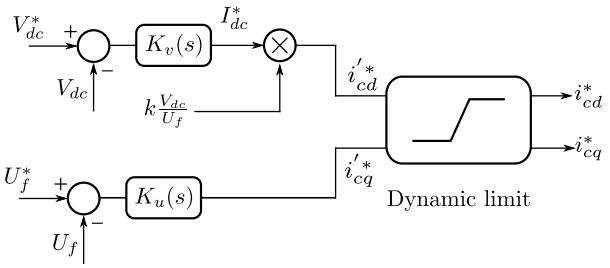

Figure 2.7: Alternating/direct-voltage control block diagram

impact of the controllers on physical dynamics. Starting with the DC side of the VSC, the dynamic open-loop equation of the physical system from Fig. 2.1 can be expressed as

$$C_{dc}\frac{dV_{dc}}{dt} = I_{dc} + I_n \tag{2.16}$$

where C_{dc} is the equivalent capacitance of the DC side, V_{dc} is the terminal direct-voltage, I_{dc} is the direct current injection from power balance with AC side, and I_n is the current flowing into the VSC from the DC network or source. In Laplace domain, the physical system can be re-written as

$$V_{dc} = z_{dc}(s)\,(I_{dc} + I_n) \tag{2.17}$$

with

$$z_{dc}(s) = \frac{1}{sC_{dc}}$$

where $z_{dc}(s)$ is the primitive impedance of the physical DC side. The direct-voltage is controlled by sending a corresponding active current reference command i_{cd}^* to the inner-current loop calculated from the required balancing current from the DC side. The output of the direct-voltage controller (DVC) is expressed as

$$I_{dc}^* = K_v(s)(V_{dc}^* - V_{dc}) + I_n \tag{2.18}$$

with

$$K_v(s) = k_{pv} + \frac{k_{iv}}{s}$$

where $K_v(s)$ is the PI compensator, k_{pv} and k_{iv} are the PI gains, V_{dc}^* is the reference direct-voltage command, and I_{dc}^* is reference injection current. The reference active current command can be calculated as

$$i_{cd}^* = k\frac{P_{dc}^*}{u_{fd}}; \quad P_{dc}^* = I_{dc}^* V_{dc}^* \tag{2.19}$$

where P^*_{dc} is the reference DC side power, $k = 2/3$ is the power variant constant. Due to the inclusion of the nonlinear power variable, linearization of corresponding expressions must be made around an operating point. Assuming a constant direct-voltage reference command, (2.19) can be linearized as

$$\Delta i^*_{cd} = k\frac{u^0_{fd}\Delta P^*_{dc} - P^0_{dc}\Delta u_{fd}}{(u^0_{fd})^2} \tag{2.20}$$

where $P^0_{dc} = P^*_{dc}$ is the operating point as calculated from power flow. Around an operating point, the active power P^*_{dc} reference can be linearized as

$$\begin{aligned}\Delta P^*_{dc} &= I^*_{dc}\Delta V^*_{dc} + V^0_{dc}\Delta I^*_{dc}\\ &= V^0_{dc}\Delta I^*_{dc}\end{aligned} \tag{2.21}$$

where the reference direct-voltage command is assumed constant. Thus,

$$\Delta i^*_{cd} = k\frac{u^0_{fd}V^0_{dc}\Delta I^*_{dc} - P^0_{dc}\Delta u_{fd}}{(u^0_{fd})^2}. \tag{2.22}$$

Subsequently, (2.18) can be linearized around the established operating point as

$$\Delta I^*_{dc} = -K_v(s)\Delta V_{dc} \tag{2.23}$$

thus, ΔI^*_{dc} can be eliminated from (2.22) by substituting (2.23) to obtain

$$\Delta i^*_{cd} = -k\left(\frac{V^0_{dc}K_v(s)}{u^0_{fd}}\Delta V_{dc} + \frac{P^0_{dc}}{(u^0_{fd})^2}\Delta u_{fd}\right). \tag{2.24}$$

The above predicts the impacts of open-loop direct-voltage control dynamics and disturbances to d-axis voltage on the active current reference command.

For the alternating-voltage controller (AVC), the reference reactive current command can be obtained as

$$i^*_{cq} = K_u(s)(U^*_f - U_f) + i_{cq}; \quad U_f = \sqrt{(u_{fd})^2 + (u_{fq})^2} \tag{2.25}$$

with

$$K_u(s) = k_{pu} + \frac{k_{iu}}{s}$$

where $K_u(s)$ is the PI compensator, k_{pu} and k_{iu} are the PI gains, U^*_f and U_f are the PCC voltage magnitude reference command and measurement respectively. Due to the nonlinearity of U_f, it can be linearized as

$$\Delta U_f = \frac{u^0_{fd}}{U^0_f}\Delta u_{fd} + \frac{u^0_{fq}}{U^0_f}\Delta u_{fq} \tag{2.26}$$

and substituted into the linearized version of (2.25) with reference command assumed constant, to obtain

$$\Delta i_{cq}^{*} = -K_u(s)\left(\frac{u_{fd}^0}{U_f^0}\Delta u_{fd} + \frac{u_{fq}^0}{U_f^0}\Delta u_{fq}\right). \tag{2.27}$$

Next, to close the inner-loop with the outer direct and alternating-voltage loops, Δi_{cd}^{*} and Δi_{cq}^{*} can be eliminated from the d and q-axes expressions of (2.15) by substituting (2.24) and (2.27) to obtain

$$\Delta i_{cd} = y_d^d(s)\Delta u_{fd} + y_q^d(s)\Delta u_{fq} - y_{dc}^d(s)\Delta V_{dc} \tag{2.28a}$$

$$\Delta i_{cq} = y_d^q(s)\Delta u_{fd} + y_q^q(s)\Delta u_{fq} - y_{dc}^q(s)\Delta V_{dc} \tag{2.28b}$$

where $y_d^d(s)$, $y_q^d(s)$, $y_{dc}^d(s)$, $y_d^q(s)$, $y_q^q(s)$, $y_{dc}^q(s)$ are *auxiliary admittances* that describe the impact of alternating-voltage disturbances, and open-loop direct-voltage control on the converter currents on both axes. They are termed auxiliary variables as they are not directly measurable at the output of the converter.

For a stable PLL at any operating point, $h_{cl,dq}^i(s) = 0$ from (2.15), since $\sin\theta_p^0 \approx 0$. Thus, its corresponding impact vanishes from (2.15) and (2.28), simplifying the auxiliary admittances to

$$y_d^d(s) = y_{dd}(s) - \frac{kh_{cl}^i(s)P_{dc}^0}{(u_{fd}^0)^2}, \quad y_q^d(s) = y_{dq}(s), \quad y_{dc}^d(s) = \frac{kK_v(s)V_{dc}^0 h_{cl}^i(s)}{u_{fd}^0},$$

$$y_d^q(s) = y_{qd}(s) - \frac{K_u(s)h_{cl}^i(s)u_{fd}^0}{U_f^0}, \quad y_q^q(s) = y_{qq}(s) - \frac{K_u(s)h_{cl}^i(s)u_{fq}^0}{U_f^0},$$

$$y_{dc}^q(s) = 0.$$

Therefore, Δi_c^q simplifies as

$$\Delta i_c^q = \underbrace{y_d^q(s)}_{Y_{qd}(s)}\Delta u_{fd} + \underbrace{y_q^q(s)}_{Y_{qq}(s)}\Delta u_{fq} \tag{2.29}$$

where $Y_{qd}(s)$ and $Y_{qq}(s)$ are the measurable output cross-admittance and admittance respectively on the q-axis. Fig. 2.8 shows the frequency response of the auxiliary admittance transfer functions y_d, and of the alternating/direct-voltage controlled converter. Most importantly from these frequency responses, there are no build up of resonances in the open-loop direct-voltage control.

For the d-axis equivalent, the direct-voltage loop must be closed with the physical dynamics of the DC side by eliminating ΔV_{dc} from (2.28a). To do this, ΔI_{dc} can be eliminated from the physical system in (2.17) by

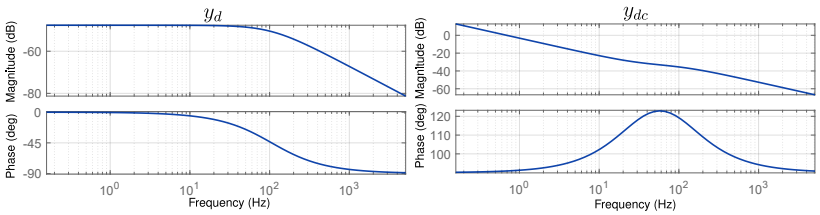

Figure 2.8: Inner auxiliary admittances of the alternating/direct-voltage controlled VSC

equating the linearized power balance between the AC and DC sides such that

$$\Delta I_{dc} = \frac{u_{fd}^0 \Delta i_{cd} + i_{cd}^0 \Delta u_{fd} + u_{fq}^0 \Delta i_{cq} + i_{cq}^0 \Delta u_{fq} - k I_{dc}^0 \Delta V_{dc}}{k V_{dc}^0}. \tag{2.30}$$

Subsequently, Δi_{cd} and Δi_{cq} from (2.28a) and (2.29) respectively are substituted into ΔI_{dc} and the result substituted into the linearized version of (2.17) to obtain

$$\Delta V_{dc} = H_{dd}(s)\Delta u_{fd} + H_{qq}(s)\Delta u_{fq} + Z_{oc}(s)\Delta I_n \tag{2.31}$$

with

$$H_{dd}(s) = \frac{z_{dc}(s)\left(u_{fd}^0 y_d^d(s) + u_{fq}^0 Y_{qd}(s) + i_{cd}^0\right)}{k V_{dc}^0 + z_{dc}(s)\left(u_{fd}^0 y_{dc}^d(s) + k I_{dc}^0\right)},$$

$$H_{qq}(s) = \frac{z_{dc}(s)\left(u_{fd}^0 y_{dq}(s) + u_{fq}^0 Y_{qq}(s) + i_{cq}^0\right)}{k V_{dc}^0 + z_{dc}(s)\left(u_{fd}^0 y_{dc}^d(s) + k I_{dc}^0\right)},$$

$$Z_{oc}(s) = \frac{z_{dc}(s) k V_{dc}^0}{k V_{dc}^0 + z_{dc}(s)\left(u_{fd}^0 y_{dc}^d(s) + k I_{dc}^0\right)},$$

where $Z_{oc}(s)$ is the measurable feedback impedance imposed on the DC side of the VSC. $Z_{oc}(s)$ describes the behaviour of local direct-voltage to bus disturbances without an adjoining network or any other active device. $H_{dd}(s)$ and $H_{qq}(s)$ are transfer gains that predict the impacts of alternating-voltage disturbances on the direct-voltage and vice-versa. They predict the interaction between the AC and DC sides with respect to voltage dynamics. For a strong AC grid, Δu_{fd} and Δu_{fq} terms easily cancel out and $Z_{oc}(s)$ becomes the most important function for DC side studies. However, for weak grids that need support, $H_{dd}(s)$ and $H_{qq}(s)$ describe analytically the response of direct-voltage to AC grid disturbances.

Therefore to prevent coupled behaviour it is important that both transfer functions are ≈ 0 around frequencies of interest. In addition, these transfer functions can be utilized to allow the DC grid support the AC grid depending on the global control strategy adopted.

Finally, to include the impact of closed-loop direct-voltage control and DC side dynamics on the AC side, (2.31) is substituted into the d-axis equivalent of (2.28a) to obtain

$$\Delta i_{cd} = Y_{dd}(s)\Delta u_{fd} + Y_{dq}(s)\Delta u_{fq} - H_{dc}(s)\Delta I_n \tag{2.32}$$

$$\begin{aligned} Y_{dd}(s) &= y_d^d(s) - y_{dc}^d(s)H_{dd}(s), \\ Y_{dq}(s) &= y_{dq}(s) - y_{dc}^d(s)H_{qq}(s), \\ H_{dc}(s) &= y_{dc}^d(s)Z_{oc}(s), \end{aligned}$$

where $Y_{dq}(s)$ and $Y_{qq}(s)$ are the measurable output cross-admittance and admittance respectively on the d-axis, and $H_{dc}(s)$ is a transfer gain that predicts the interaction between the active current on AC side and current from the DC side.

Equations (2.32), (2.29), and (2.31) fully describe the impedance models of an AC/direct-voltage controlled converter on both sides, combined compactly into a matrix form as

$$\begin{pmatrix} \Delta i_{cd} \\ \Delta i_{cq} \\ \Delta V_{dc} \end{pmatrix} = \left(\begin{array}{cc|c} Y_{dd}(s) & Y_{dq}(s) & -H_{dc}^d(s) \\ Y_{qd}(s) & Y_{qq}(s) & 0 \\ \hline H_{dd}(s) & H_{qq}(s) & Z_{oc}(s) \end{array}\right) \begin{pmatrix} \Delta u_{fd} \\ \Delta u_{fq} \\ \Delta I_n \end{pmatrix} \tag{2.33}$$

where the diagonal sub-matrices are the impedance models on either side of the VSC, and the off-diagonal sub-matrices are the interaction transfer functions between the AC and DC sides of the VSC.

Fig. 2.9 shows the frequency response of the impedance models of the alternating and direct-voltage controlled VSC as derived in Equation (2.33) and its numerical verification. In general, the derived models and numerical verification agree. Differences and deviations are a result of the accuracy of estimation algorithms, high-frequency sampling induced delays, and uneven sampling which the analytical derivation does not consider. In general, the output admittances on the AC side (top left) have well-damped resonances. However, the interaction functions between the AC and DC sides show interaction resonances around 22Hz. This indicates a potential interaction between the AC and DC sides due to DC side dynamics and control dominated by the DVC.

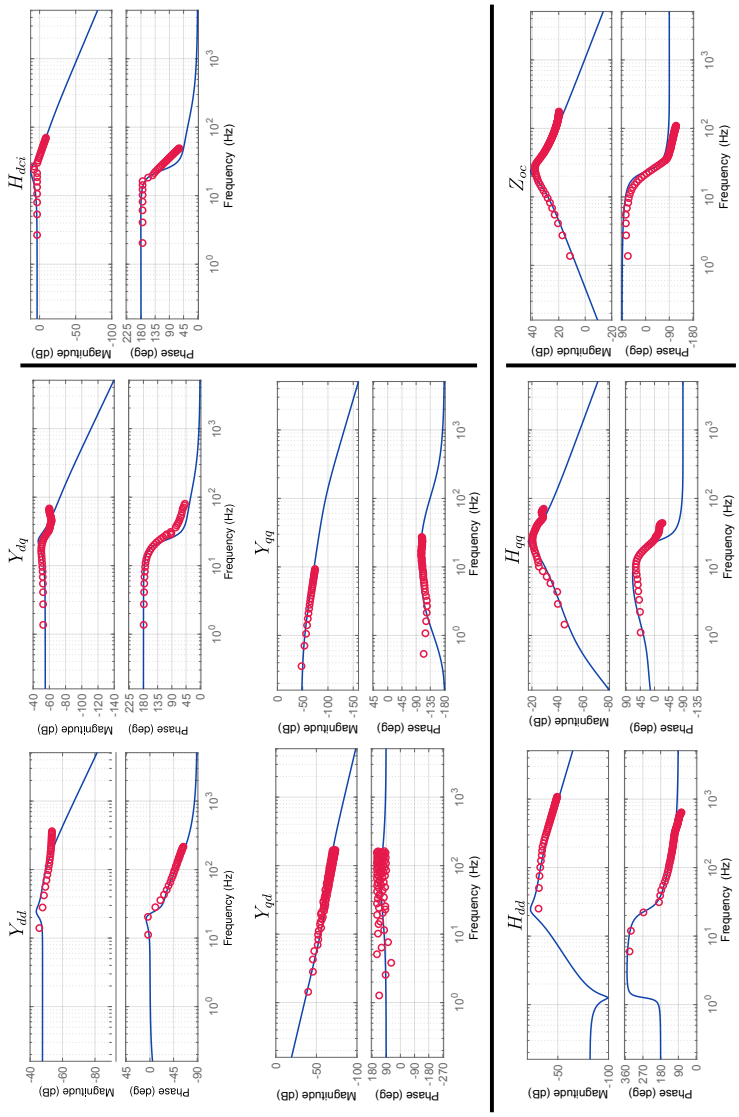

Figure 2.9: Output impedance models and verification response of the alternating and direct-voltage controlled VSC (Blue: Sequential derivation, Red: Numerical verification).

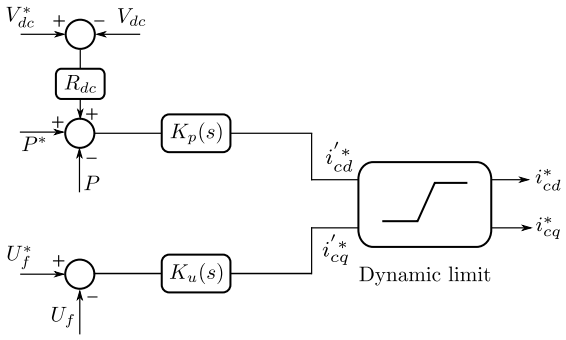

Figure 2.10: Alternating-voltage and droop/active power control block diagram

2.2.3 Alternating-Voltage/Droop/Active Power Controlled VSC

In typical VSC-HVDC applications, at least one VSC controls the active power, with the potential to also control the direct-voltage in droop mode as suggested in literature. To demonstrate flexibility, both the droop and active power controlled VSC can be modelled together such that a switch from one control mode to the other is facilitated by a change in the droop gain R_{dc}. In active power mode, the droop gain is simply set to 0. Thus, the active power/droop controller provides the reference active current command to the current loop on the d-axis, with a similar AVC as previously, shown in Fig. 2.10.

For any converter in alternating-voltage/droop or active power control modes as shown, the total reference power command P_t^* can be expressed as

$$P_t^* = P^* + \Delta P^* \tag{2.34}$$

where P^* is the scheduled power reference from power flow, and ΔP^* is the balancing reference from droop action given as

$$\Delta P^* = R_{dc}(V_{dc}^* - V_{dc}) \tag{2.35}$$

where R_{dc} is the droop gain, V_{dc}^* and V_{dc} are the reference and measured voltages respectively. Thus,

$$P_t^* = P^* + R_{dc}(V_{dc}^* - V_{dc}) \tag{2.36}$$

For active power measurements from the AC side, the reference active current command of the inner-current loop can be obtained as

$$i_{cd}^* = K_p(s)(P_t^* - P) \tag{2.37}$$

with

$$K_p(s) = k_{pp} + \frac{k_{ip}}{s}$$

where P is the measured active power, $K_p(s)$ is the active power PI compensator, and k_{pp}, k_{ip} are the PI gains. In a similar manner, (2.37) can be linearized as

$$\begin{aligned}\Delta i_{cd}^{*} &= K_p(s)\Delta P_t^{*} - \Delta P \\ &= K_p(s)\left(R_{dc}(\Delta V_{dc}^{*} - \Delta V_{dc}) - \Delta P\right) \\ &= -K_p(s)\left(R_{dc}\Delta V_{dc} + \Delta P\right)\end{aligned} \tag{2.38}$$

where

$$\Delta P = \Delta P_{ac} = \frac{1}{k}(u_{fd}^0\Delta i_{cd} + i_{cd}^0\Delta u_{fd} + u_{fq}^0\Delta i_{cq} + i_{cq}^0\Delta u_{fq}) \tag{2.39}$$

thus,

$$\Delta i_{cd}^{*} = -K_p(s)\left(R_{dc}\Delta V_{dc} + \frac{u_{fd}^0\Delta i_{cd} + i_{cd}^0\Delta u_{fd} + u_{fq}^0\Delta i_{cq} + i_{cq}^0\Delta u_{fq}}{k}\right). \tag{2.40}$$

Similarly, since the AVC structure remains the same, the reactive current reference command is equivalent to that of (2.27). Thus, Δi_{cd}^{*} can be eliminated from the d-axis equivalent of (2.15) (noting that, $h_{cl,dq}^{i}(s) = 0$) to obtain

$$\Delta i_{cd} = y_d^p(s)\Delta u_{fd} + y_q^p(s)\Delta u_{fq} - H_q(s)\Delta i_{cq} - y_{dc}^p\Delta V_{dc} \tag{2.41}$$

$$\begin{aligned}y_d^p(s) &= \frac{k y_{dd}(s) - K_p(s)h_{cl}^i(s)i_{cd}^0}{k + K_p(s)h_{cl}^i(s)u_{fd}^0}, \\ y_q^p(s) &= \frac{k y_{dq}(s) - K_p(s)h_{cl}^i(s)i_{cq}^0}{k + K_p(s)h_{cl}^i(s)u_{fd}^0}, \\ H_q(s) &= \frac{K_p(s)h_{cl}^i(s)u_{fq}^0}{k + K_p(s)h_{cl}^i(s)u_{fd}^0}, \\ y_{dc}^p(s) &= \frac{kK_p(s)h_{cl}^i(s)R_{dc}}{k + K_p(s)h_{cl}^i(s)u_{fd}^0},\end{aligned}$$

whereas, Δi_{cq} remains as (2.29) and must be eliminated from (2.41) such that

$$\Delta i_{cd} = y_d^{dp}(s)\Delta u_{fd} + y_q^{dp}(s)\Delta u_{fq} - y_{dc}^{dp}(s)\Delta V_{dc} \tag{2.42}$$

$$\begin{aligned}y_d^{dp}(s) &= y_d^p(s) - H_q(s)Y_{qd}(s), \\ y_q^{dp}(s) &= y_q^p(s) - H_q(s)Y_{qq}(s), \\ y_{dc}^{dp} &= y_{dc}^p(s),\end{aligned}$$

where $y_d^{dp}(s)$, $y_q^{dp}(s)$, and y_{dc}^{dp} are the auxiliary admittances for the droop controlled converter. It is clear that in this case of the droop/active power controlled VSC, the d-axis equivalents consist of the entirety of q-axis equivalents. This shows the increased coupling between both d and q-axes, and AC/DC sides of a droop/active power controlled VSC.

Subsequently, the impact of the physical dynamics of the direct-voltage can be included in a similar manner as previously by back-substituting (2.29) and (2.42) into ΔI_{dc} in (2.30) and the results into the linearized physical dynamics of DC side in (2.17) to obtain

$$\Delta V_{dc} = H_{dd}^{dp}(s)\Delta u_{fd} + H_{qq}^{dp}(s)\Delta u_{fq} + Z_{oc}^{dp}(s)\Delta I_n \tag{2.43}$$

$$\begin{aligned}
H_{dd}^{dp}(s) &= \frac{z_{dc}(s)\left(u_{fd}^0 y_d^{dp}(s) + u_{fq}^0 Y_{qd}(s) + i_{cd}^0\right)}{kV_{dc}^0 + z_{dc}(s)\left(u_{fd}^0 y_{dc}^{dp}(s) + kI_{dc}^0\right)},\\
H_{qq}^{dp}(s) &= \frac{z_{dc}(s)\left(u_{fd}^0 y_q^{dp}(s) + u_{fq}^0 Y_{qq}(s) + i_{cq}^0\right)}{kV_{dc}^0 + z_{dc}(s)\left(u_{fd}^0 y_{dc}^{dp}(s) + kI_{dc}^0\right)},\\
Z_{oc}^{dp}(s) &= \frac{z_{dc}(s)kV_{dc}^0}{kV_{dc}^0 + z_{dc}(s)\left(u_{fd}^0 y_{dc}^{dp}(s) + kI_{dc}^0\right)},
\end{aligned}$$

where $Z_{oc}^{dp}(s)$ is the measurable DC impedance imposed by droop/active power control, $H_{dd}^{dp}(s)$ and $H_{qq}^{dp}(s)$ are the transfer gains of interaction between the AC and DC sides. Variables with the superscript '$^{\mathrm{dp}}$' are the equivalent droop/active power variables when compared to the direct-voltage counterparts. To close the outer-loops and impact of DC side dynamics on the AC side, ΔV_{dc} is eliminated from (2.42) by back-substituting (2.43) to obtain

$$\Delta i^{cd} = Y_{dd}^{dp}(s)\Delta u_{fd} + Y_{dq}^{dp}(s)\Delta u_{fq} - H_{dc}^{dp}(s)\Delta I_n \tag{2.44}$$

$$\begin{aligned}
Y_{dd}^{dp}(s) &= y_d^{dp}(s) - y_{dc}^{dp}(s)H_{dd}^{dp}(s),\\
Y_{dq}^{dp}(s) &= y_q^{dp}(s) - y_{dc}^{dp}(s)H_{qq}^{dp}(s),\\
H_{dc}^{dp}(s) &= y_{dc}^{dp}(s)Z_{oc}^{dp}(s),
\end{aligned}$$

where $Y_{dd}^{dp}(s)$, $Y_{dq}^{dp}(s)$, and $H_{dc}^{dp}(s)$ are the corresponding admittance, cross-admittance, and current interaction gain respectively of the droop/active power controlled VSC. In a similar manner, the corresponding equations for droop/active power controlled VSC can be sorted in a compact matrix

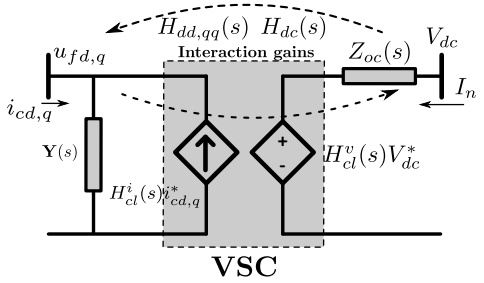

Figure 2.11: Equivalent terminal circuit of the VSC as modelled showing the measurable impedances on AC and DC sides.

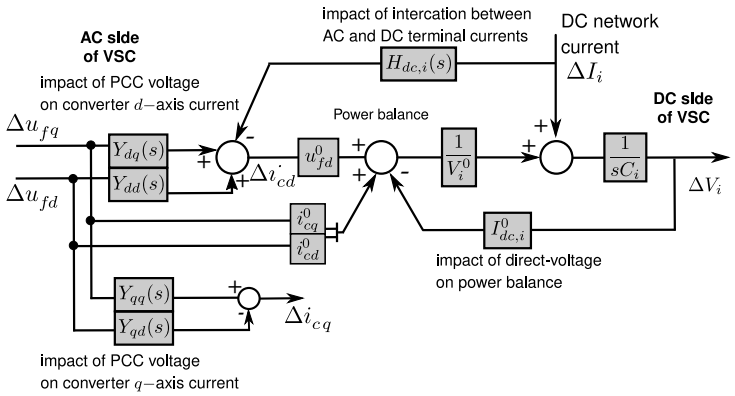

Figure 2.12: Equivalent block diagram of impedance modelling procedure

form as

$$\begin{pmatrix} \Delta i_{cd} \\ \Delta i_{cq} \\ \Delta V_{dc} \end{pmatrix} = \left(\begin{array}{cc|c} Y^{dp}_{dd}(s) & Y^{dp}_{dq}(s) & -H^{dp}_{dc}(s) \\ Y^{dp}_{qd}(s) & Y^{dp}_{qq}(s) & 0 \\ \hline H^{dp}_{dd}(s) & H^{dp}_{qq}(s) & Z^{dp}_{oc}(s) \end{array}\right) \begin{pmatrix} \Delta u_{fd} \\ \Delta u_{fq} \\ \Delta I_n \end{pmatrix}. \tag{2.45}$$

Fig. 2.11 suggests an equivalent circuit representation of the modelling procedures in this Section, showing the final input-output impedance models on both sides of the VSC and the isolated interaction functions between both sides. Fig. 2.12 depicts a block diagram of the modelling procedures as derived, showing how internal variables (from both sides of the VSC) are interconnected. The block diagram allows to easily derive impedance equivalents when information about one or more blocks is readily available.

Fig. 2.13 shows the frequency response of the impedance models of the active power/alternating-voltage controlled VSC as modelled in (2.45) with $R_{dc} = 0$ and the numerical verification (in red). In general, all trans-

fer functions are well damped. Fig. 2.14 shows the impedance models for an alternating-voltage/droop controlled active power with $R_{dc} = 2.5$ MW/kV. Fig. 2.15 shows the comparison of the frequency responses of impedance models for each of the three combination control strategies as derived. In general, droop/active power responses show better-damped responses compared to the direct-voltage strategy; particularly the interaction transfer functions between the alternating and direct-voltages. This confirms the previous discussions that the closed-loop DVC may be to blame for resonances. However, this is only a converter-level assessment. Network-level assessment may differ as resonant frequencies shift on interconnection with other subsystems. Additionally, DC feedback impedance responses Z_{oc} for active power and droop show high steady-state impedance. For droop control, this results in the well-known direct-voltage deviations in steady-state. As for active power controlled terminals, this deviation is significantly reduced by the terminal controlling the direct-voltage at the system-level. For direct-voltage controlled terminals, the Z_{oc} response may be used to assess the efficacy of direct-voltage control especially in steady-state. As can be seen, in steady-state, the impedance drops below 0 dB, thus in steady-state, the impedance vanishes and the measured direct-voltage is equal to the value imposed by the control V_{dc}^{*}.

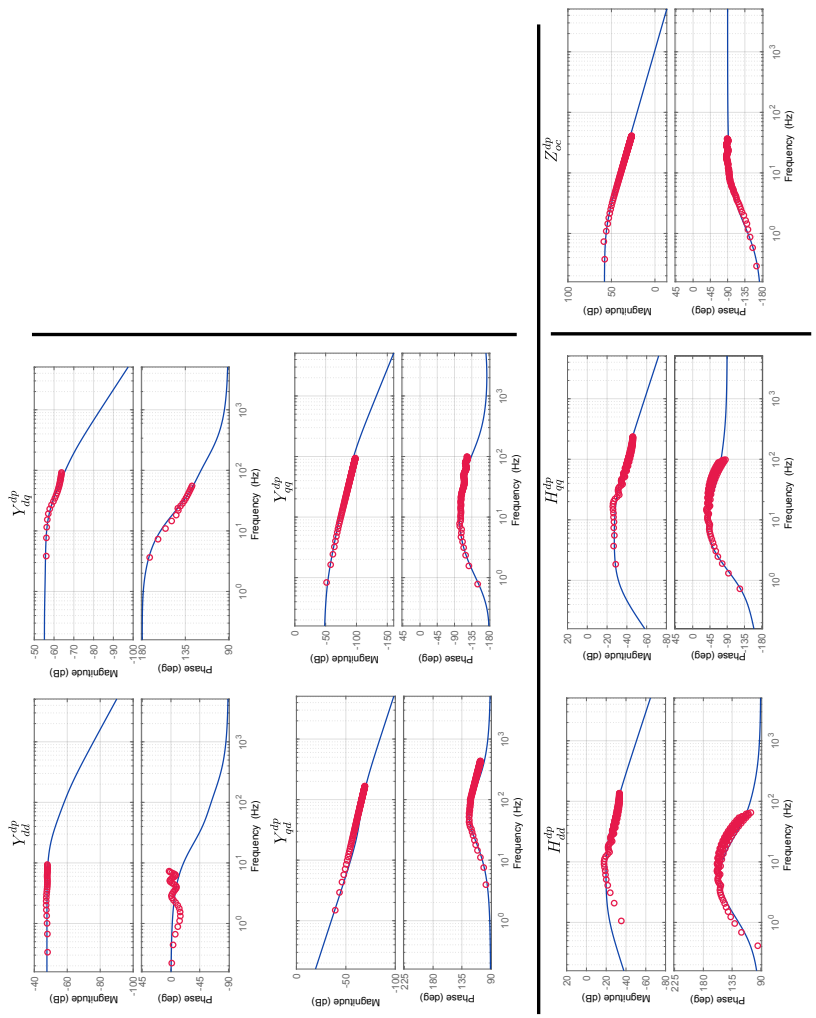

Figure 2.13: Output impedance models and verification response of the alternating-voltage/active power controlled VSC (Blue: Sequential derivation, Red: Numerical verification).

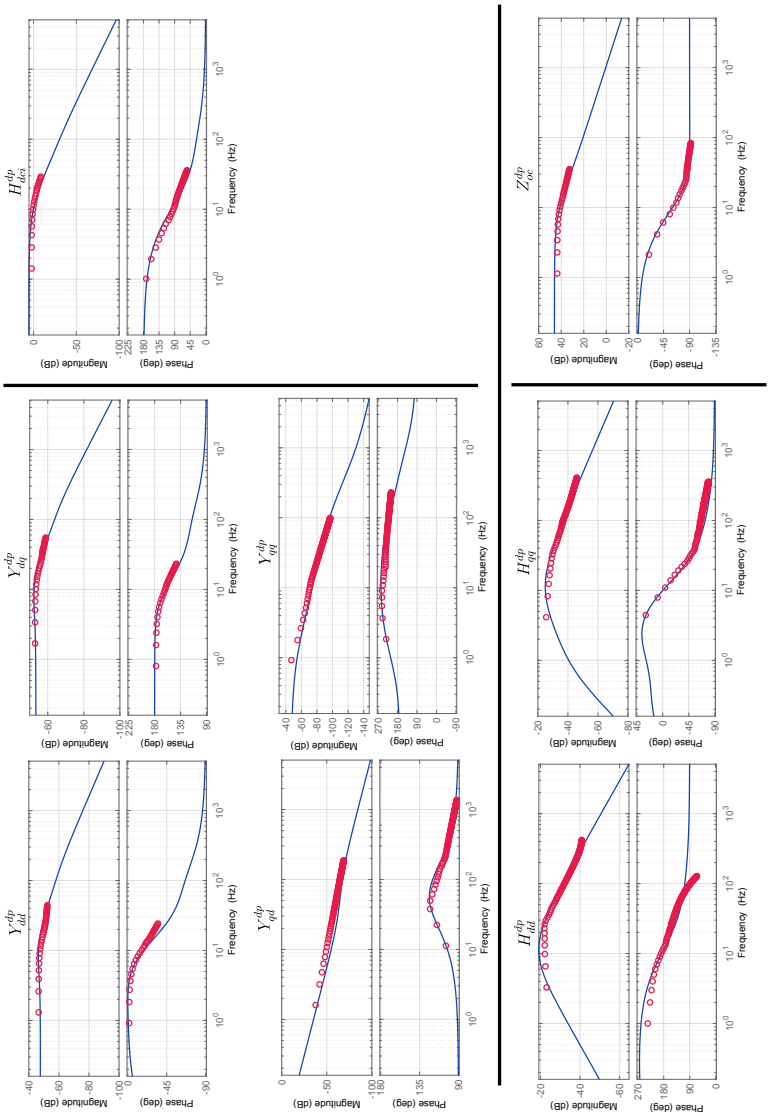

Figure 2.14: Output impedance models and verification response of the alternating-voltage/droop controlled VSC (Blue: Sequential derivation, Red: Numerical verification).

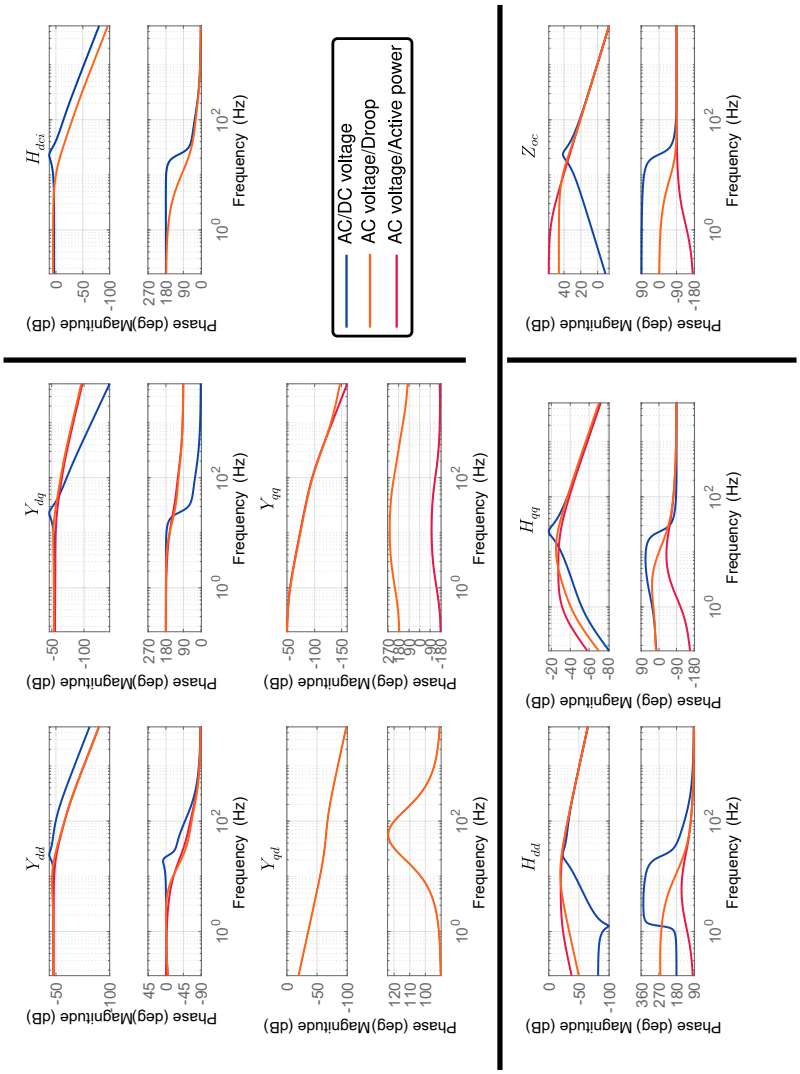

Figure 2.15: Comparison between the impedance response of the various combinations of control strategies

Fig. 2.16 depicts an overview of the impedance modelling framework for VSC.

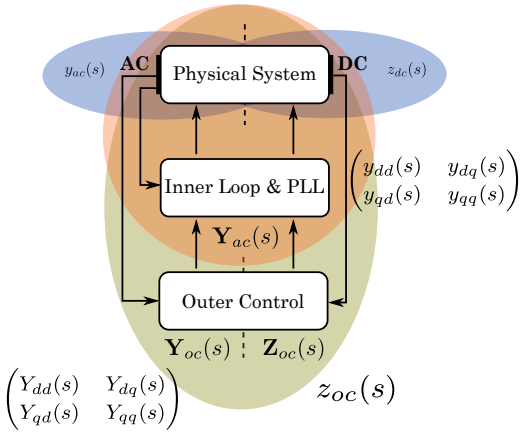

Figure 2.16: Overview of Impedance modelling framework for VSCs

2.3 Simplified Closed-loop Derivation of VSC Equivalents

The previous modelling procedures in Section 2.2 may appear daunting and time-consuming. A key advantage of the detailed procedure lies in it being a one-time procedure for each broad control strategy employed at the converter-level. Hence, it is easy to establish the impact of all internal variables of the converter to any detail. Secondly, it provides an easy means of isolating potential internal sources of resonance, and a handle on how internal variables are interacting as each control loop is open/closed. Thus, it is easy to establish the impacts of closed/open loop strategies amongst other parameters on the input-output impedance responses at the terminal-level.

Despite the advantages, it may well be desired to simply obtain the final input-output impedance response when certain assumptions hold without going through the detailed procedures of the previous section. This is especially the case for DC side studies where certain assumptions such as a fairly strong AC grid (SCR $>$ 3) or constant reactive power may hold. Therefore, interaction functions may be neglected, hence the AC and DC sides become partially decoupled (since either side may still depend on operating points from both sides). As a result, the imposed DC impedance becomes the most important transfer function (from the com-

pact impedance matrix of equations 2.33 and 2.45). As can be observed from equations (2.31) and (2.43), the DC impedance is relatively straightforward given the impacts of DVC and inner-current closed-loop transfer function. Therefore, closed-loop block diagrams can be adopted to simplify the derivations of the DC impedance subject to assumptions.

2.3.1 Direct-Voltage Controlled VSC

Given the following simplifying assumptions:

1. The AC grid is fairly strong; that is, short circuit ratio (SCR) is greater than or equal to 3. Then, it may be assumed that the PCC voltage magnitude U_f is constant at defined value, thus,

$$\begin{aligned} & u_{fq} \approx 0 \\ \implies & \Delta u_{fq} = u^0_{fq} = 0 \\ \implies & u_{fd} = U_f, \quad \implies \Delta u_{fd} \approx 0 \end{aligned} \tag{2.46}$$

   and the impact of AVC vanishes. Additionally, the impact of PLL can be neglected as well since the PLL deviation angle $\Delta\theta_p \approx 0$.
2. Reactive power reference can be assumed constant if there is no need for alternating-voltage control. This follows from (1). Thus,

$$\Delta i^*_{cq} = i^0_{cq} = 0. \tag{2.47}$$

Then, the inner-loop in (2.15) simplifies to

$$\Delta i_{cd} = h^i_{cl}(s)\Delta i^*_{cd}. \tag{2.48}$$

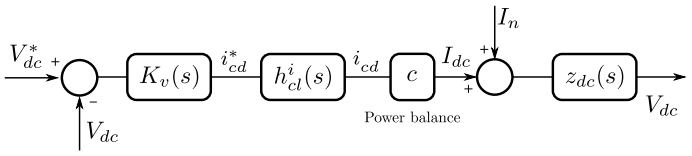

Figure 2.17: Simplified closed-loop block diagram of the DVC loop

It is important to note that most of these assumptions mainly decouple the AC and DC sides (hence the impedance models) of the converter by eliminating the connecting interaction transfer functions (off-diagonal elements of equations 2.33 and 2.45). Fig. 2.17 shows the block diagram of the outer-loop of the direct-voltage controlled VSC following the simplifying assumptions. The closed-loop expression can be simply derived from the block diagram as

$$V_{dc} = \underbrace{\frac{cK_v(s)z_{dc}(s)h^i_{cl}(s)}{1 + cK_v(s)z_{dc}(s)h^i_{cl}(s)}}_{H^v_{cl}(s)} V^*_{dc} + \underbrace{\frac{z_{dc}(s)}{1 + cK_v(s)z_{dc}(s)h^i_{cl}(s)}}_{Z_{oc}(s)} I_n \tag{2.49}$$

where

$$H_{cl}^{v}(s) = \frac{H_{ol}^{v}(s)}{1 + H_{ol}^{v}(s)}, \quad Z_{oc}(s) = \frac{z_{dc}(s)}{1 + H_{ol}^{v}(s)} = S(s)z_{dc}(s), \quad c = \frac{u_{fd}^{0}}{kV_{dc}^{0}},$$

where $S(s)$ is the sensitivity transfer function of the control system, $H_{cl}^{v}(s)$ is the closed-loop reference to output transfer function (vanishes after linearization), $H_{ol}^{v}(s)$ is the open-loop transfer function of the direct-voltage control, and $Z_{oc}(s)$ is the imposed DC impedance. Immediately, a parallel can be drawn between the DC impedances of equations (2.31) and (2.49). Importantly, the imposed DC impedance can be constructed from the open-loop transfer function or sensitivity transfer function of the control system. Fig. 2.18 shows the frequency response plot of the detailed DC impedance and the simplified derivation at an operating point. Both responses show an accurate match and any difference is negligible across the frequencies of interest despite the two-step procedure to derive the simplified impedance.

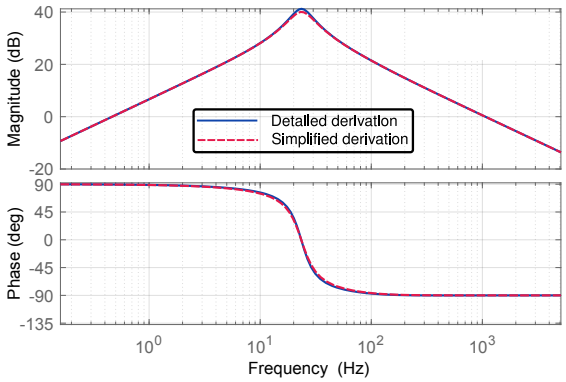

Figure 2.18: DC output impedance for a direct-voltage controlled VSC

2.3.2 Droop/Active Power Controlled VSC

Fig. 2.19 shows the block diagram of a droop/active power controlled converter with similar assumptions as previously. In addition to previous assumptions, the VSC can be assumed to be lossless in which case

$$P_{ac} = P_{dc} \tag{2.50}$$

where P_{dc} is the DC bus power. Due to the presence of the nonlinear power variable, linearization around an operating point must be done. Thus,

$$\Delta P_{ac} = \Delta P_{dc} = V_{dc}^{0}\Delta I_{dc} + I_{dc}^{0}\Delta V_{dc}. \tag{2.51}$$

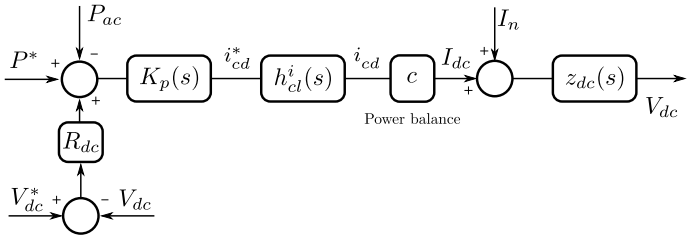

Figure 2.19: Simplified closed-loop block diagram of the droop/active power loop

Following a similar closed-loop derivation and linearization of variables and substituting for $\Delta P_{ac} = \Delta P_{dc}$, the impedance of the droop/active power controlled converter can be derived as

$$\begin{aligned}\Delta V_{dc} &= \frac{z_{dc}(s)\left(1+cK_p(s)h^i_{cl}(s)V^0_{dc}\right)}{\left(1+cK_p(s)h^i_{cl}(s)V^0_{dc}\right)+z_{dc}(s)\left(cK_p(s)h^i_{cl}(s)(I^0_{dc}+R_{dc})\right)}\Delta I_n \\ &= \underbrace{\frac{z_{dc}(s)}{1+z_{dc}(s)\left(\frac{cK_p(s)h^i_{cl}(s)(I^0_{dc}+R_{dc})}{1+cK_p(s)h^i_{cl}(s)V^0_{dc}}\right)}}_{Z^{dp}_{oc}(s)}\Delta I_n\end{aligned} \tag{2.52}$$

where $Z^{dp}_{oc}(s)$ is the imposed impedance by droop/active power control. Fig. 2.20 shows the frequency response comparison between the detailed droop derivation and the simplified derivation. It can be seen that both derivations match accurately. Hence, for DC side studies where the AC side can be neglected, the simplified derivation can be adopted.

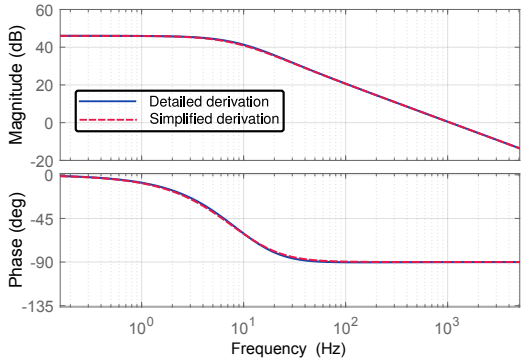

Figure 2.20: DC output impedance for the droop controlled VSC

2.4 Linearized State-space to Input-output Derivation

There are numerous cases where the internal structure of the VSC is too complex or order of states is too large to be modelled sequentially as done in Section 2.2. The state-space to input-output derivation can be adopted for such cases. However, the physical insights from sequential derivation including impacts of control (in open/closed loop) are lost. Additionally, it is difficult to isolate the output admittance models of the inner-loop and PLL, $\mathbf{Y}_{ac}(s)$ except derivations are done specifically for such a case. Furthermore, it becomes difficult to isolate internal sources of resonance as this method does not give access to auxiliary variables. Moreover, broad simplifications are difficult and require a proper understanding of internal processes; otherwise, a re-derivation is required. Therefore it is similar to the closed-loop derivation of Section 2.3, with an advantage to be as detailed as possible provided linearization is properly carried out. Linearization as applied in this section is based on the established notations and variables in previous sections.

For the alternating and direct-voltage controlled VSC, the open-loop equations of the physical system in (2.5) and (2.16), and all control systems can be linearized and expressed in the formal state-space notation as

$$\Delta \dot{x}_{ss} = \mathbf{A}\Delta x_{ss} + \mathbf{B}\Delta u \tag{2.53a}$$

$$\Delta y = \mathbf{C}\Delta x_{ss} + \mathbf{D}\Delta u \tag{2.53b}$$

where Δx_{ss}, u, and y are the state, input, and output vectors respectively, with elements

$$\begin{aligned} \Delta x_{ss} &= (\Delta i_{cd}, \Delta i_{cq}, \Delta V_{dc}, \Delta\theta_p, \Delta x_d, \Delta x_q, \Delta x_{id}, \Delta x_{iq}, \Delta x_{pll})^T \\ \Delta u &= (\Delta u_{fd}, \Delta u_{fq}, \Delta I_n)^T \\ \Delta y &= (\Delta i_{cd}, \Delta i_{cq}, \Delta V_{dc})^T \end{aligned} \tag{2.54}$$

and, $\mathbf{A}$, $\mathbf{B}$, $\mathbf{C}$, and $\mathbf{D}$ are the state, input, output, and feedforward matrices respectively, of appropriate dimensions. The detailed derivations of these matrices can be found in Appendix B.4. Other additional states such as those of the integrators of controllers can also be found in the Appendix. The impedance models of the VSC can then be obtained by isolating Δx_{ss} in (2.53a) (noting that $\Delta \dot{x}_{ss} = s\Delta x_{ss}$) and substituting into (2.53b) to obtain

$$\Delta y = \underbrace{\mathbf{C}\left(s\mathbf{I} - \mathbf{A}\right)^{-1}\mathbf{B}}_{\text{Impedance Models}}\Delta u \tag{2.55}$$

where $\mathbf{D} = 0$, and $\mathbf{I}$ is the identity matrix. The impedance models has the same structure as the matrix of (2.33) with similar inputs and outputs.

Fig. 2.21 shows the frequency response comparison between the impedance models as obtained for both the sequential derivation and state-space to input-output. It shows a good match between both derivations and any difference is quite negligible. Therefore, the state-space to input-output can be adopted if this information is readily available. However, this method only gives the final measurable input-output transfer functions.

For the alternating-voltage and droop/active power controlled converter, the physical system, input, and output remains the same. The states vector can be expressed as

$$\Delta x_{ss} = (\Delta i_{cd}, \Delta i_{cq}, \Delta V_{dc}, \Delta \theta_p, \Delta x_{pd}, \Delta x_{pq}, \Delta x_{id}, \Delta x_{iq}, \Delta x_{pll})^T \quad (2.56)$$

where x_{pd}, and x_{pq} are the states of the integrator of the active power compensator. The impedance models of the droop/active power controlled converter can be obtained by constructing the state-space matrices and following the state to input-output formulation in (2.55). The detailed derivations of each state can also be found in Appendix B.4.

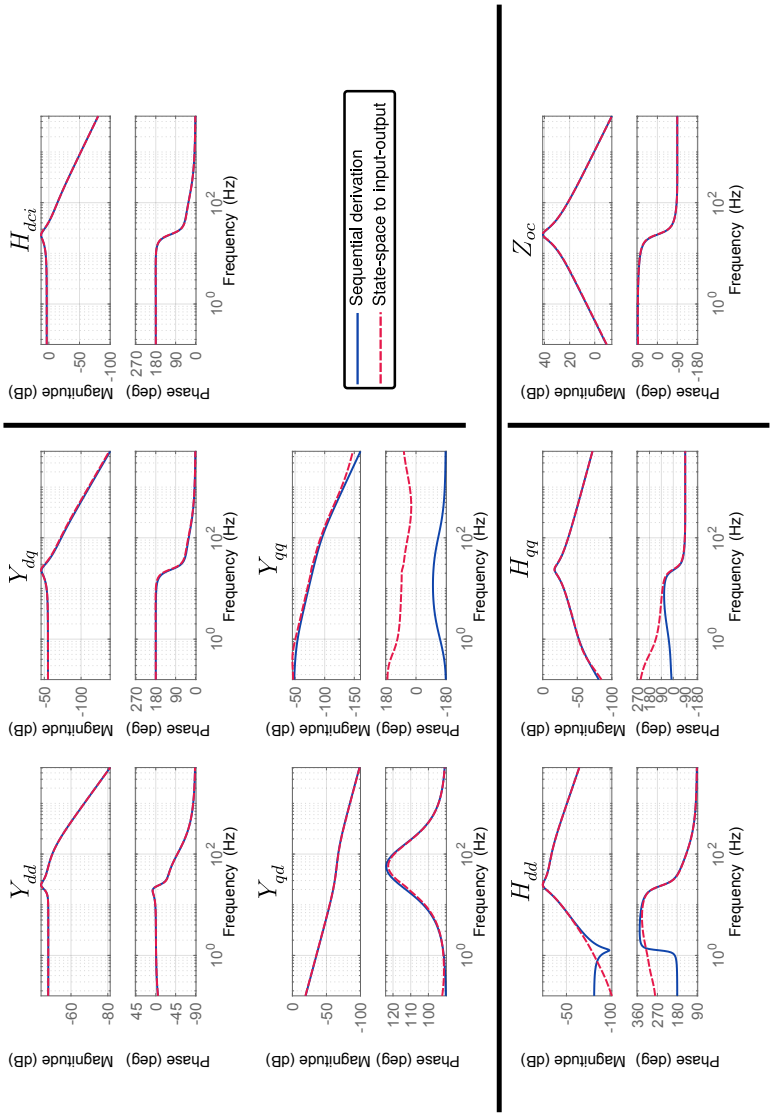

Figure 2.21: Comparison between frequency response of the sequential derivation and state-space to input-output for a direct-voltage controlled VSC

2.5 Impedance Equivalents of Synchronous Generators

The synchronous generator is the most important component of the conventional transmission infrastructure. Hence, they are still expected to contribute to the dynamics of hybrid AC/DC grids. Numerous models of the synchronous generator considering different studies have been proposed and adopted over decades. The objective here is not to re-derive the models of the synchronous generator; but instead, to derive the equivalent input-output impedance of a specific model with respect to output currents and imposed voltages suitable for system-level dynamics.

In this thesis, the impact of excitation system consisting of the automatic voltage regulator (AVR) and exciter, and potential interaction with the alternating-voltage controlled VSC through a network are of interest. Additionally, the equations in the natural dq framework of the generator are adopted since this allows ease of integration with the corresponding dq impedances of the converter. The linearized open-loop state differential equations for the synchronous generator in dq-frame can be expressed as [111]

$$\underbrace{\begin{pmatrix}\mathbf{L}_m & 0 & 0\\ 0 & -2H & 0\\ 0 & 0 & -1\end{pmatrix}}_{\mathbf{L}'_m}\frac{d}{dt}\begin{pmatrix}\Delta I_g\\ \Delta w_r\\ \Delta\delta\end{pmatrix}=\underbrace{\begin{pmatrix}\mathbf{R}_m & (2.58a) & 0\\ (2.58c) & (2.58b) & 0\\ 0 & 0 & 0\end{pmatrix}}_{\mathbf{R}'_m}\begin{pmatrix}\Delta I_g\\ \Delta w_r\\ \Delta\delta\end{pmatrix}+\begin{pmatrix}\Delta V_g\\ \Delta T\\ \Delta\delta\end{pmatrix} \tag{2.57}$$

where

$$I_g=\left(i_{sq},i_{sd},i_{kq1},i_{kq2},i_{fd}\right)^T,$$

$$V_g=\left(v_{sq},v_{sd},v_{kq1},v_{kq2},v_{fd}\right)^T,$$

$$\mathbf{L}_m=\begin{pmatrix}L_q & 0 & L_{mq} & L_{mq} & 0\\ 0 & L_d & 0 & 0 & L_{md}\\ L_{mq} & 0 & L_{kq1} & L_q & 0\\ L_{mq} & 0 & L_{mq} & L_{kq2} & 0\\ 0 & \frac{\omega_b L_{md}^2}{r_{fd}} & 0 & 0 & \frac{\omega_b L_{md}L_{fd}}{r_{fd}}\end{pmatrix},$$

$$\mathbf{R}_m=\begin{pmatrix}-r_s & -\omega_e L_d & 0 & 0 & -\omega_e L_{md}\\ \omega_e L_q & -r_s & \omega_e L_{mq} & \omega_e L_{mq} & 0\\ 0 & 0 & -r_{kq1} & 0 & 0\\ 0 & 0 & 0 & -r_{kq2} & 0\\ 0 & 0 & 0 & 0 & -\omega_e L_{md}\end{pmatrix},$$

$$-\omega_e L_d i_s^{d0}-\omega_e L_d i_f^{d0} \tag{2.58a}$$

$$-\omega_e L_q i_s^{q0} \tag{2.58b}$$

$$W = \left(\frac{3}{2} \left(L_{mq} i^0_{sd} - L_{md}(i^0_{sd} - i^0_{fd}) \right), \frac{3}{2} \left(-L_{md} i^0_{sq} + L_{mq} i^0_{sq} \right), \right. \\ \left. \frac{3\omega_e L_{mq} i^0_{sd}}{2}, \frac{3\omega_e L_{mq} i^0_{sd}}{2}, -\frac{3\omega_e L_{md} i^0_{sq}}{2} \right) \tag{2.58c}$$

$\mathbf{L}_m$ and $\mathbf{R}_m$ are the inductance and resistance matrices respectively, H is the inertia constant of the synchronous generator, I_g and V_g are vector of currents (stator, dampers, field) and corresponding voltages related to the generator respectively, w_r is the rotor speed, T is the electrical torque and δ is the rotor angle. The complete open-loop dynamic equation of the seventh order synchronous generator model can be written compactly as

$$\Delta \dot{x}_g = \underbrace{(\mathbf{L}_m^{'})^{-1} \mathbf{R}_m^{'}}_{\mathbf{A}_g} \Delta x_g + \underbrace{\mathbf{L}_m^{-1}}_{\mathbf{B}_g} \Delta u_g \tag{2.59a}$$

$$\Delta y_g = \mathbf{C}_g \Delta x_g + \mathbf{D}_g \Delta u_g \tag{2.59b}$$

where $\mathbf{A}_g$, $\mathbf{B}_g$, $\mathbf{C}_g$, $\mathbf{D}_g$, matrices of appropriate dimensions; $\mathbf{L}_m^{'}$, $\mathbf{R}_m^{'}$ are augmented inductance and resistance matrices respectively.

$$\begin{aligned} \Delta x_g &= (\Delta I_g^T, \Delta \omega_r, \Delta \delta)^T \\ \Delta u_g &= (\Delta V_g^T, \Delta T, \Delta \delta)^T \\ \Delta y_g &= \Delta I_g^T \end{aligned} \tag{2.60}$$

where x_g, u_g, y_g are the state, input, and output vectors.

Generator Excitation Control System

The excitation system's main function is to provide direct current to the rotor windings of the synchronous generator. Additionally, the excitation system improves the overall dynamic performance of the generator by controlling the field voltage, and thus current, and indirectly the output terminal voltage of the generator. Its is important to note that the excitation system may also contribute to poor performance at system-level depending on its own characteristics and that of the interconnected power system. The excitation system implemented in this thesis consists of a DC exciter and regulator shown in Fig. 2.22 [112]. The total transfer function of the excitation system can be expressed as

$$K_{ex}(s) = \frac{k_a}{(k_e + sT_e)(1 + sT_a)} \tag{2.61}$$

where k_a is the regulator gain, k_e is the exciter gain, T_a is the regulator time constant, T_e is the exciter time constant, and V_t is the terminal voltage of the generator given as

$$V_t = \sqrt{v_{sd}^2 + v_{sq}^2} \tag{2.62}$$

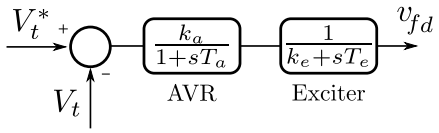

Figure 2.22: Excitation system of the synchronous generator

The linearized exciter and regulator expression is given as

$$\begin{aligned} \Delta v_{fd} &= K_{ex}(s)(\Delta V_t^* - \Delta V_t) \\ &= -K_{ex}(s)\Delta V_t \end{aligned} \tag{2.63}$$

where terminal voltage reference V_t^* is constant and

$$\Delta V_t = \frac{v_{sd}^0}{V_t^0}\Delta v_{sd} + \frac{v_{sq}^0}{V_t^0}\Delta v_{sd} \tag{2.64}$$

where terminal voltage reference V_t^* is constant. The impedance models of the synchronous generator with excitation control system is obtained as

$$\Delta y_g = \underbrace{\mathbf{C}_g \left(s\mathbf{I} - \mathbf{A}_g\right)^{-1} \mathbf{B}_g}_{\text{Impedance Models}} \Delta u_g. \tag{2.65}$$

The impedance models of the generator can be simplified further as required by eliminating corresponding variables from the state-space formulation.

Considering that the synchronous generator and AC side of the VSC are on separate dq frames, it is very important to transform both impedance models to a common reference frame before interconnection; in this thesis, preference is given to the VSC bus as the PLL aligns the voltage with the d-axis. Hence, the converter is chosen as the reference frame and transformation is done according to

$$\begin{pmatrix} d^c \\ q^c \end{pmatrix} = \begin{pmatrix} \cos\theta_c & \sin\theta_c \\ -\sin\theta_c & \cos\theta_c \end{pmatrix} \begin{pmatrix} d \\ q \end{pmatrix} \tag{2.66}$$

where dq^c are the expression in the chosen global reference frame (in this case, the VSC) and θ_c is the difference in angle between the global reference frame and the original reference frame. Fig. 2.23 shows the generator equivalent impedance responses.

2.5.1 Lines and Cables

A frequency-dependent series-parallel distributed Π cable as described in [113] with m series sections and n parallel branches per section shown

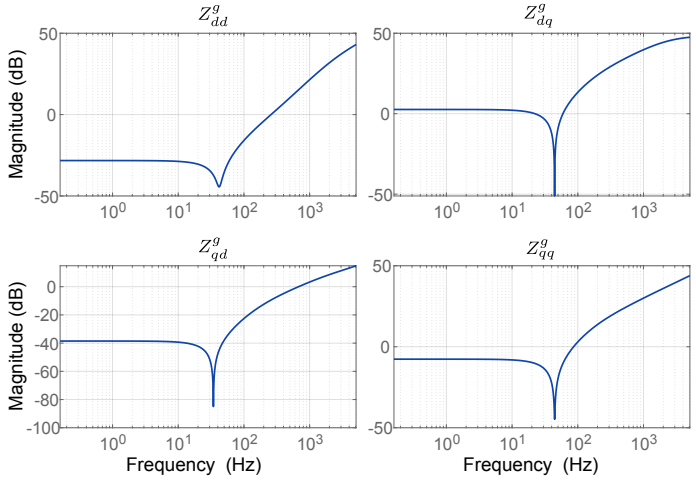

Figure 2.23: Generator equivalent input-output impedance

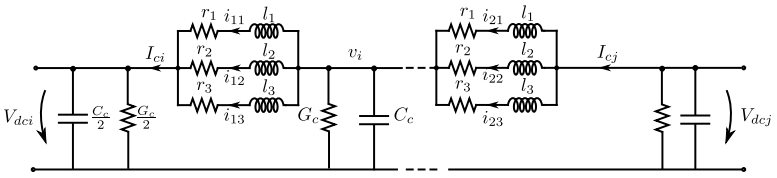

Figure 2.24: Frequency dependent distributed Π cable circuit

in Fig. 2.24 is adopted in this thesis. For a model with $n = 3$ branches as shown in Fig. 2.24, the state equations for each m series-parallel combination can be constructed as

$$\frac{di_{m1}}{dt} = \frac{v_m}{l_1} - \frac{V_{dci}}{l_1} - \frac{i_{m1}r_1}{l_1}, \qquad \forall m \tag{2.67a}$$

$$\frac{di_{m2}}{dt} = \frac{v_m}{l_2} - \frac{V_{dci}}{l_2} - \frac{i_{m2}r_2}{l_2}, \qquad \forall m \tag{2.67b}$$

$$\frac{di_{m3}}{dt} = \frac{v_m}{l_3} - \frac{V_{dci}}{l_3} - \frac{i_{m3}r_3}{l_3}, \qquad \forall m \tag{2.67c}$$

$$\frac{dv_m}{dt} = \frac{I_{cj}}{C_c} - \frac{I_{ci}}{C_c} - \frac{v_m G_c}{C_c}, \qquad \forall m \tag{2.67d}$$

where l_i, r_i are the branch inductances and resistances, i_{mn} are the branch currents, v_m are the mid-section voltages modelled by the mid-section cable capacitances C_c, and corresponding admittances G. Whereas, I_{cj} and

I_{ci} are the total cable currents at sending and receiving ends respectively. Each can be obtained as

$$I_{cj} = \sum_{n=1}^{3} i_{mn} = i_{21} + i_{22} + i_{23}$$
$$I_{ci} = \sum_{n=1}^{3} i_{(m-1)n} = i_{11} + i_{12} + i_{13}.$$

Equation (2.67) is sorted out for each cable according to

$$\Delta \dot{x}_c = \mathbf{A_c} \Delta x_c + \mathbf{B_c} \Delta V_c \tag{2.68a}$$

$$\Delta I_c = \mathbf{C_c} \Delta x_c \tag{2.68b}$$

where

$$x_c = (i_{m1}, i_{m2}, i_{m3}, v_m)^T \qquad \forall m$$
$$V_c = (V_{dci}, V_{dc,j})$$
$$I_c = (I_{ci}, I_{cj})$$

where x_c is the state vector of branch currents and mid-section voltages of the cable/line, V_c is the vector of input voltages to the cables/lines consisting of the sending and receiving end voltages, ΔI_c is the vector of currents flowing through the cable/line consisting of sending and receiving end currents. Whereas, $\mathbf{A_c}$, $\mathbf{B_c}$, and $\mathbf{C_c}$ are the state, input, and output matrices of corresponding dimensions. Transforming (2.68a) into Laplace and substituting for Δx_c in (2.68b)

$$\Delta I_c = \underbrace{\mathbf{C_c}(s\mathbf{I} - \mathbf{A_c})^{-1}\mathbf{B_c}}_{\mathbf{Y_c(s)}} \Delta V_c. \tag{2.69}$$

If the cable impedance is the same when viewed from either ends, then

$$\begin{aligned} \Delta I_{ci} &= \begin{pmatrix} -Y_{ci}(s) & Y_{ci}(s) \end{pmatrix} \begin{pmatrix} \Delta V_{dci} \\ \Delta V_{dcj} \end{pmatrix} \\ \Delta I_{ci} &= Y_{ci}(s)(\Delta V_{dcj} - \Delta V_{dci}) = \frac{\Delta V_{dcj} - \Delta V_{dci}}{Z_{ci}(s)} \end{aligned} \tag{2.70}$$

where $Z_{ci}(s) = Z_{cj}(s) = Z_{c,ij}$ is the input-output impedance of the cable in frequency domain as a subsystem and is a transfer function of order $2n + (m-1)$.

Table 2.1 provides a comparison between the different methods of derivations of the dq impedances as adopted in this thesis.

Table 2.1: Comparison between the methods for derivation of impedance models

	Analytical	State-space	Simplified
AC-DC analysis	+	+	−
AC-AC analysis	+	+	−
DC-DC analysis	+	+	+
Access to auxiliary impedances	+	−	−
AC/DC analysis	+	−	+
Internal sources of resonances	+	−	−
Complexity handling	−	+	+
Ease of derivation	−	+	+

2.6 Aggregation of System Level Impedance Models

The impedance derivations in Sections 2.2, 2.3, 2.4, and 2.5 was carried out for each component as unconnected subsystems. This is to facilitate modularity and flexibility of integration with an arbitrary grid architecture. In this section, impedance models of various subsystems are interconnected with an arbitrary grid and subsystem-level impedance formulations are extended to the entire system. Subsequently, the system-level equivalents of each subsystem given their location are obtained.

As previously remarked, the impedance models of the VSC were derived in a manner that decouples the AC and DC side. Hence, the system-level models for an arbitrary network on either side may be decoupled as well to allow for subnetwork aggregation on either side. However, the isolated interaction functions will determine how each subnetwork interfaced by the VSC will interact on a larger scale and this will be discussed in later Chapters.

2.6.1 Aggregation of DC Equivalents

Extension from One Terminal to n Terminals

For an interconnected n terminal DC network with an arbitrary number of lines/cables as shown in Fig. 2.25, Fig. 2.26 illustrates an interconnection of impedance equivalents of subsystems within the DC subnetwork as previously modelled. Recognizably, the entire subnetwork is composed of impedance equivalents. From the DC side of Fig. 2.11, the closed-loop expression for a VSC at an arbitrary terminal i can be generalized from

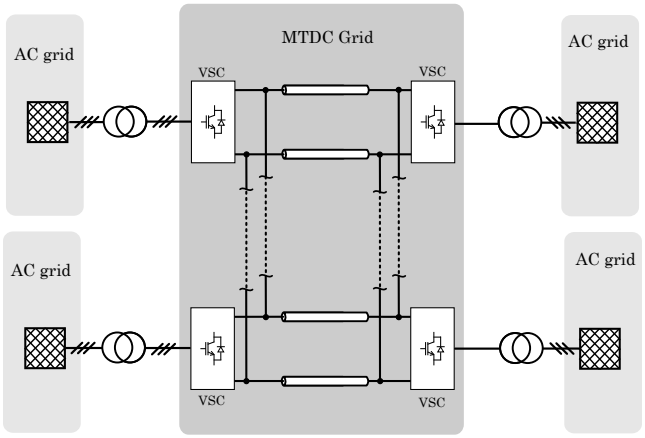

Figure 2.25: n terminal interconnected VSC-HVDC grid

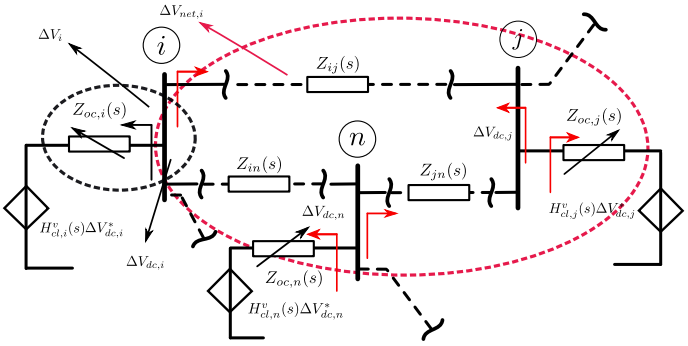

Figure 2.26: System level interconnection of DC side impedance models showing the rest of the network (in red) as seen from a terminal i with its local impedance

(2.49) as

$$V_{dci} = \underbrace{H^{v_i}_{cl}(s)V^{*}_{dc,i}}_{V^{0}_{dci}} + \underbrace{Z_{oc,i}(s)\Delta I_{ni}}_{\Delta V_i} \tag{2.71}$$

where V^{0}_{dci} is the control system imposed voltage and the operating point for direct-voltage, ΔV_i is the local disturbance response (illustrated in black dashed oval shape in Fig. 2.26), $H^{v_i}_{cl}(s)$ is the closed-loop reference to output transfer function of the i^{th} VSC. It is important to remark that for an active power controlled VSC $\Delta V^{*}_{dc,i} = 0$ by default since there is no direct control of voltage by the VSC. Although a formality, (2.71) is

simply linearized as

$$\Delta V_{dci} = H_{cl}^{v_i}(s)\Delta V_{dc,i}^{*} + \Delta V_i \tag{2.72}$$

where the $\Delta V_{dc,i}^{*}$ term is eliminated if direct-voltage reference is assumed constant. If the control system at the terminal level (without any network) is guaranteed stable (in a strict sense), then at a future time, ΔV_i will vanish, or in the worst case, all frequency components should vanish. The latter case is particularly true of droop controlled VSC and the corresponding steady-state deviation due to droop. Hence, during dynamics, ΔV_i dictates the evolution of the nodal direct-voltage of a VSC before connection with a grid. However, in an interconnected system where the observed responses are invariably coupled, response to disturbance at a terminal consist of local dynamics as described, and contribution from the rest of the system — the network and control systems from other terminals (see red oval shape in Fig. 2.26). At the global level, this implies the entire system is multi-input multi-output (MIMO) as opposed to the single-input single-output (SISO) local response equivalent.

In order to account for the impact of interconnection and other subsystems, (2.72) must be modified. To keep modularity of expressions, the modified linearized voltage equation at terminal i that accounts for the contribution from the network and other converters as illustrated in Fig. 2.26 can be generalized as

$$\Delta V_{dci} = \Delta V_i + \Delta V_{net,i} \tag{2.73}$$

ΔV_{dci} is the total voltage change measured at terminal i during disturbances considering the entire system, ΔV_i is the local contribution previously described, and $\Delta V_{net,i}$ is the total contribution from the rest of the network including impact of other converters as seen from the i^{th} terminal. That is,

$$\Delta V_{net,i} \neq \Delta V_{net,j}$$

except in the case of a ring topology with equal cable or line lengths. If there are no other converters, network, or the effects of both are neglected, or only resistive behaviour of the rest of the network is modelled, $\Delta V_{net,i} = 0$ or has no frequency components respectively, and (2.73) reverts to (2.72).

For linear systems where superposition principle applies, ΔV_{dci} at every terminal in the system can be obtained from the impedance aggregation based on well-established $\mathbf{Z}_{bus}$ method [114]. Therefore, the dynamic voltage responses to a disturbance at any interface in an n terminal network

can be generalized as

$$\underbrace{\begin{pmatrix}\Delta V_{dci}\\ \Delta V_{dcj}\\ \vdots\\ \Delta V_{dcn}\end{pmatrix}}_{\Delta \mathbf{V}_{dc}} = \underbrace{\begin{pmatrix} Z^{cl}_{ii}(s) & Z^{cl}_{ij}(s) & \cdots & Z^{cl}_{in}(s)\\ Z^{cl}_{ji}(s) & Z^{cl}_{jj}(s) & \cdots & Z^{cl}_{jn}(s)\\ \vdots & \vdots & \ddots & \vdots\\ Z^{cl}_{ni}(s) & Z^{cl}_{nj}(s) & \cdots & Z^{cl}_{nn}(s)\end{pmatrix}}_{\mathbf{Z}^{cl}_{dc}(s)} \underbrace{\begin{pmatrix}\Delta I_{ni}\\ \Delta I_{nj}\\ \vdots\\ \Delta I_{nn}\end{pmatrix}}_{\Delta \mathbf{I}} \tag{2.74}$$

where $\Delta \mathbf{V}_{dc}$ is the vector of bus voltage changes during disturbances, $\Delta \mathbf{I}$ is the vector of potential bus current changes, and $\mathbf{Z}^{cl}_{dc}(s)$ is herein referred to as the '*dynamic closed-loop impedance matrix*' of the DC grid. It consists of the impedance equivalent of each terminal and transfer-impedances from other terminals in the network as seen from the global level. Hence, during dynamics, the frequency components of the matrix are the frequency components of responses during disturbances.

The matrix predicts the evolution of voltages for disturbances, irrespective of internal converter characteristics and simply from transfer functions. Additionally, the matrix provides an external input-output view of the entire system given any control strategy employed at system-level. The element $Z^{cl}_{ii}(s)$ predicts the isolated response of direct-voltage at the i^{th} terminal for disturbances within the vicinity of terminal i in the absence of any other disturbances. Whereas, $Z^{cl}_{ij}(s)$ predicts the isolated response of direct-voltage at the i^{th} terminal to disturbances at j^{th} terminal in the absence of any other disturbance. $\mathbf{Z}^{cl}_{dc}(s)$ is a transfer function matrix of structure

$$\mathbf{Z}^{cl}_{dc}(s) = \frac{1}{Z(s)} \begin{pmatrix} a_{ii}(s) & a_{ij}(s) & \cdots & a_{in}(s)\\ a_{ji}(s) & a_{jj}(s) & \cdots & a_{jn}(s)\\ \vdots & \vdots & \ddots & \vdots\\ a_{ni}(s) & a_{nj}(s) & \cdots & a_{nn}(s)\end{pmatrix} \tag{2.75}$$

$$\left.\begin{aligned} a_{ij}(s) &= a_{ij,m}s^m + \cdots + a_{ij,1}s + a_{ij,0}\\ Z(s) &= z_n s^n + z_{n-1}s^{n-1} + \cdots + z_1 s + z_0 \end{aligned}\right\} \forall \{i,j\} \in n$$

where $a_{ij}(s)$ is the numerator of the transfer function of each element and $Z(s)$ is the denominator common to all elements.

The construction of the $\mathbf{Z}^{cl}_{dc}(s)$ is mathematically rigorous even for state-of-art symbolic computing considering the number of variables involved. The equivalent admittance matrix which is easier to construct can be inverted to obtain $\mathbf{Z}^{cl}_{dc}(s)$. However, such a crude method offers no physical interpretation and only eases the construction of the $\mathbf{Z}$ matrix by reducing the mathematical steps involved to two.

In general, the DC equivalent matrix contains the individual dynamics of the DC grid as an entity and shared dynamics with each connected AC grid

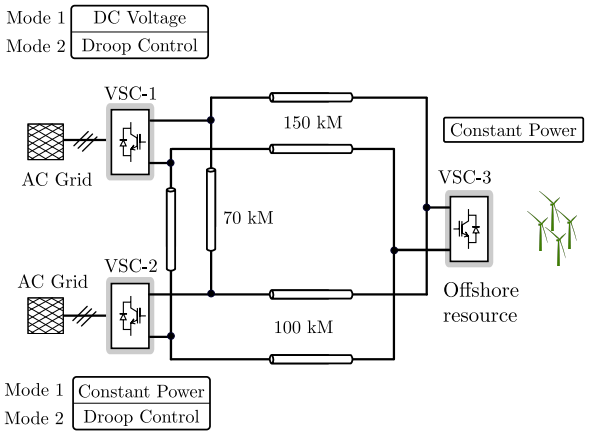

Figure 2.27: Three terminal VSC-HVDC grid with two possible system-level control modes

through the inner-current loop. In later sections, the exact contribution of other converters and the network through splitting of the $\mathbf{Z}_{dc}^{cl}(s)$ matrix according to (2.73) will be obtained. Such splitting applies to the design of coordinated supplementary controllers to improve robust performance and stability based on the manipulation of $\Delta V_{net,i}$.

To facilitate basic understanding and insights, the above derivations are applied to a three-terminal HVDC grid shown in Fig. 2.27. The grid integrates an offshore energy resource through a VSC that is in constant power mode at all times. Whereas, the other two VSCs are connected to onshore AC grid, with the possibility to switch between two corresponding control modes. Mode 1 is the well known master-slave strategy where one VSC controls the grid voltage as the master and others in constant power mode. Mode 2 is the droop control strategy whereas many VSCs can be equipped with this strategy.

The frequency response magnitudes of the system-level equivalent matrix $\mathbf{Z}_{dc}^{cl}(s)$ is shown in Fig. 2.28. Responses in similar colours are equivalent, that is the matrix is symmetrical about the principal diagonal. As can be seen, the three main dominant modes are around 17, 41, and 56Hz. However, some terminals show all three modes, whereas some show only two modes. Further analysis and clarifications will be presented later. Each element predicts the dynamic amplification for isolated disturbances from the corresponding terminal. The corresponding frequency response magnitudes for the droop control mode are shown in Fig. 2.29. The characteristic steady-state deviation due to droop interactions can be identified. Additionally, the major interaction modes in the system are at 37 and 47Hz.

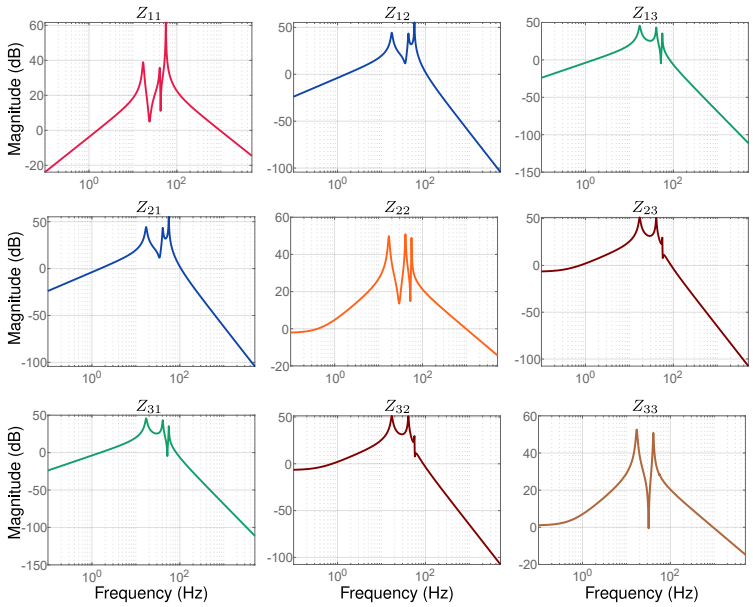

Figure 2.28: Frequency responses of system-level equivalents for the master-slave mode

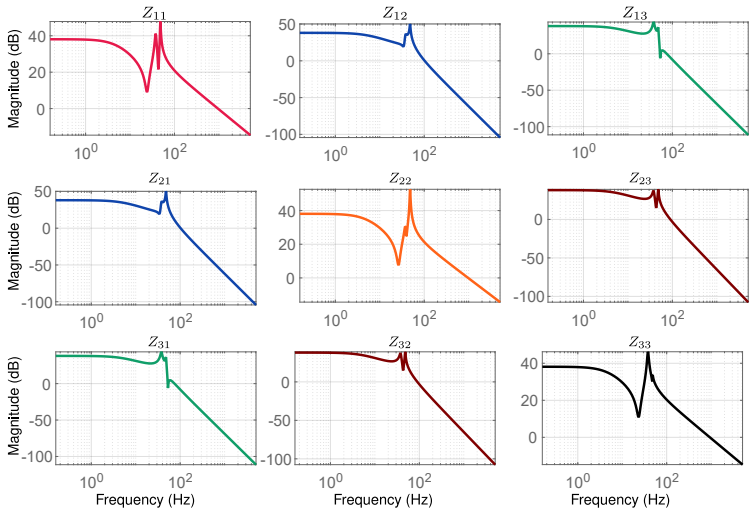

Figure 2.29: Frequency response of system-level equivalents for the droop mode

SISO to MIMO Equivalents

The SISO frequency response of the closed-loop dynamic matrix provides rich information on oscillatory behaviour and resonances contributed by each subsystem. In an uncoupled system, each element of the $\mathbf{Z}_{dc}^{cl}(s)$ matrix is the amplification and dynamic response contribution to the overall dynamics as measured at each terminal from a SISO perspective — that is, isolated behaviour. However, such SISO responses are difficult to interpret and may be erroneous when compared to physical time-domain simulations without any other supporting analysis. This is not to disregard the SISO frequency response, but to highlight that further analysis is required as the DC grid is a coupled system. Hence, disturbance at any interface results in almost simultaneous changes at all interfaces. A reason for this is that in the DC grid where the coupling parameter is voltage, any disturbance to bus currents at any interface elicits a voltage response at that interface and every other interface. This is a coupled MIMO response that SISO treatment cannot consistently interpret.

Despite the drawback of SISO equivalents, for simple first insight analysis, SISO may well provide all required information. But for system-level control design considering the entire system as a single entity, MIMO behaviour should be accounted for except otherwise proved. Therefore, $\mathbf{Z}_{dc}^{cl}(s)$ is a MIMO matrix rather than a collection of SISO transfer functions. Besides, SISO treatments cannot account for the influence of input directions on amplifications [115]. As aforementioned, well-established linear continuous-time system theory can be applied to $\mathbf{Z}_{dc}^{cl}(s)$. Hence, the MIMO frequency domain tools such as singular value decomposition (SVD) can be applied to obtain the principal gains that fully describe the system dynamic response as an entity.

The SVD is a powerful tool as it simultaneously reduces the number of important elements of the dynamic matrix from $\frac{n(n+1)}{2}$ SISO elements to n inclusive MIMO elements, sorted from worst-case dynamic amplification to best-case amplification [115, 116]. These can be applied to determine if existing control is effective or if additional control is required. The n resultant elements are often referred to as the principal amplification components [116]. SVD also directly relates to robust control approaches that allow bounds of acceptable responses to be placed on the singular values. This directly translates to robust performance improvements. The SVD of $\mathbf{Z}_{dc}^{cl}(s)$ can be obtained as

$$\mathbf{Z}_{dc}^{cl}(s) = U\Sigma V^H \tag{2.76}$$

where U and V are the output and input singular vectors respectively, H is the Hermittian operator, and Σ is the frequency dependent matrix of

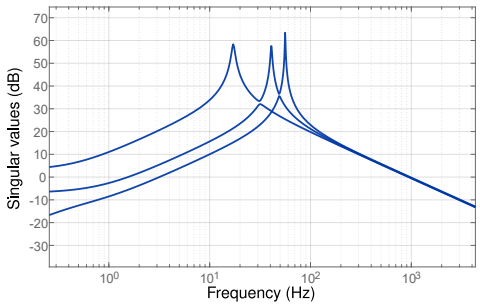

Figure 2.30: Singular value decomposition plot of the system-level equivalent matrix for the master-slave control mode

singular values sorted on the principal diagonal and given as

$$\Sigma = \begin{pmatrix} \sigma_1(s) & 0 & 0 & 0 \\ 0 & \sigma_2(s) & 0 & 0 \\ \vdots & \vdots & \ddots & \vdots \\ 0 & 0 & 0 & \sigma_n(s) \end{pmatrix} \tag{2.77}$$

with

$$\sigma_i(\mathbf{Z}_{dc}^{cl}(s)) = \sqrt{\lambda_i[(\mathbf{Z}_{dc}^{cl}(s))^H \mathbf{Z}_{dc}^{cl}(s)]} \tag{2.78}$$

where $\sigma_i(s)$ is the singular value of the i^{th} terminal contributing to the dynamic responses in the DC grid, and λ_i is the eigenvalue.

The MIMO responses based on SVD is shown for modes 1 and 2 in Figs. 2.30 and 2.31 respectively, indicating the principal components of responses and all potential interaction frequencies. The MIMO response also confirms all three frequencies identified in the SISO response. Additionally, MIMO responses also show that in the best-case scenario (indicated by the lowest singular value), only a single interaction frequency may be observed given the possible direction of inputs. MIMO responses correlate with time-domain responses, and the SVD provides information about potential magnitude responses that may require extra control effort, thus directly keys into control approaches to improve system behaviour.

In summary, $\mathbf{Z}_{dc}^{cl}(s)$ can be a matrix of any dimension including non-square. For instance, if a VSC is connected to the grid, but deemed not to contribute to the dynamic response, ΔI_i of that device can be set to zero, thus, $\mathbf{Z}_{dc}^{cl}(s)$ results to a non-square matrix for which SVD perfectly applies and the dynamic response excluding the eliminated device is revealed.

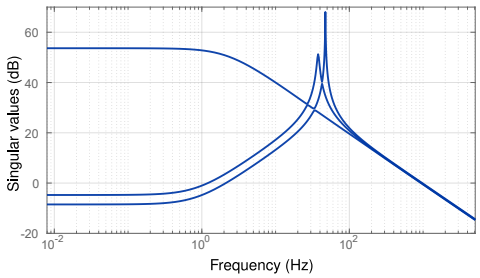

Figure 2.31: Singular value decomposition plot of the system-level equivalent matrix for the droop control mode

2.6.2 DC-DC Interactions and Stability Formulations

DC-DC Interactions Formulation

Despite the advantages of SVD responses, it still does not provide information on how subsystems are interacting at system-level if there is indeed any interaction. It is also difficult to establish the contribution to each frequency by each converter. For instance, in the SISO response of Fig. 2.28, out of the three potential interaction frequencies, the offshore resource (Z_{33}) is only contributing to two. This maybe easily identified for a relatively small system. However, it may be desired to establish how terminals are interacting on a large scale and which is contributing to each identified interaction frequency. This is important if coordinated system-level controllers are required to improve dynamic behaviour.

The frequency-dependent relative gain array (RGA) defined for MIMO systems is an extraordinary tool for interaction detection. It has been traditionally applied to the input-output pairing of variables for control [117] and later on as an interaction measure for decentralized controlled systems [118]. Here, it is desired to understand the mechanism of interaction between terminals, if interactions require supplementary control efforts to mitigate, and how to efficiently design these controllers.

Let $\mathbf{\Lambda}(s)$ evaluated at each frequency denote the corresponding RGA of $\mathbf{Z}_{dc}^{cl}(s)$ such that,

$$\mathbf{\Lambda}(s) = \mathbf{Z}_{dc}^{cl}(s) \otimes \left(\mathbf{Z}_{dc}^{cl}(s)\right)^{-T} \tag{2.79}$$

where $\otimes$ is the Hadamard product (element-wise multiplication) and $\mathbf{\Lambda}(s)$ is evaluated either at specific frequencies of interest or across a range of frequency.

In an n terminal system, the interaction between two or more terminals at a frequency is denoted by peaks in the corresponding diagonal and off-diagonal elements of the interacting terminals. Particularly, at certain interaction frequencies, corresponding elements show RGA magnitude peaks

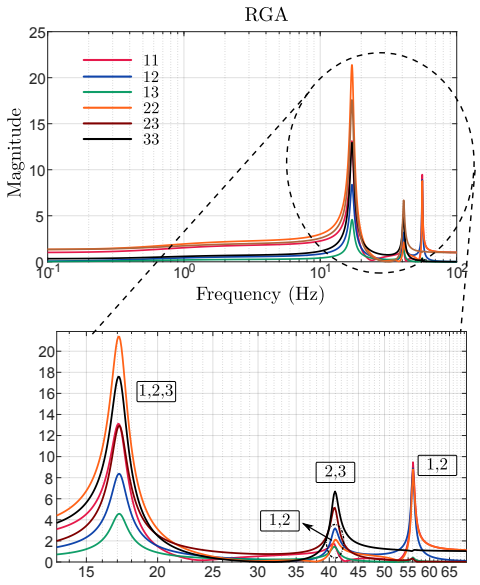

Figure 2.32: Frequency dependent relative gain array for master-slave control mode

higher than 1, while magnitudes $\gg 1$ indicate strong interaction. For an interaction-free system, $\mathbf{\Lambda}(s)$ approaches the identity matrix $\mathbf{I}$; that is, diagonal-elements approach 1 and off-diagonal elements approach 0.

Fig. 2.32 show the frequency-dependent RGA plot for the master-slave control mode discussed previously. The zoomed plot highlights the terminals contributing to each interaction frequency relative to their magnitudes. Several observations can be made. At the first peak, all terminals are significantly interacting with terminal 2 contributing the most to that interaction peak followed by terminal 3. This is the dominant frequency of the system from an interaction perspective. This analysis conflicts with the SVD plot of Fig. 2.30 that suggest the dominant mode is the third peak around 56Hz for which only terminals 1 and 2 are contributing to that frequency. Additionally, terminals 2 is interacting with terminals 1 and 3 and the mid-peak of 41Hz with terminal 1 contributing quite low. In summary, the RGA is most important when high-level control design is explored as it allows direct targeting of only the critical modes. For instance, it can be hypothesized from Fig. 2.32 that a single supplementary controller at terminal 2 designed to cover frequency ranges from $15-60$Hz is sufficient to eliminate interactions.

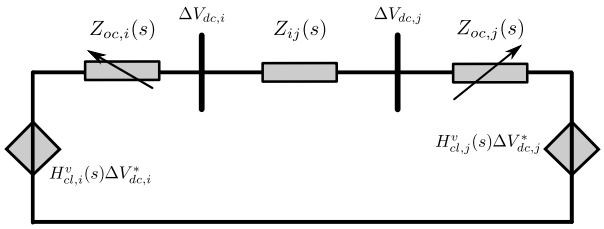

Figure 2.33: Impedance interconnection of an HVDC link

DC-DC Input-output Stability Formulation

From the view of each unconnected terminal in an n terminal VSC-HVDC system, each VSC as a subsystem is most often designed to have a guaranteed stability pre-connection. However, a guarantee of local stability of n independent VSCs does not imply system stability when they are interconnected through a network. For a MIMO system as presented, the problem becomes that of establishing input-output stability. The generalized Nyquist stability criterion for MIMO systems can be adopted to establish the input-output stability through the system return-ratio matrix [119]. This criterion has been extended to the impedance modelling framework in related literature [71, 91, 120–122].

For the impedance framework, the return-ratio function is often referred to as the impedance ratio given that each terminal has been partitioned into two parts — its local behaviour and the rest of the network as seen from that terminal. Then, the stability of that terminal with respect to the rest of the system can be established from the Nyquist of the impedance ratio function. It is important to remark that this is an alternative to the classical eigenvalue stability index and is often used to check the external input-output stability [123]. For frequency-dependent MIMO systems such as $\mathbf{Z}^{cl}_{dc}(s)$ the n frequency-dependent eigenvalues can be applied to construct n Nyquist plots and stability determined with Nyquist criterion. Previous works have applied the criterion to the analysis of stability on the AC side, and often to only one point of interconnection.

For an n terminal VSC-HVDC grid, the system impedance ratio matrix is a diagonal matrix consisting of n non-zero transfer functions. These can be derived from a two terminal network and extended to n terminals. Consider the impedance circuit diagram of a two terminal HVDC link shown in Fig. 2.33. The network can be partitioned from the view of any terminal i by considering the potential bus current changes as a current source in parallel with the equivalent impedance of the rest of the system as shown in Fig. 2.34 where

$$Z_{net,i}(s) = Z_{ij}(s) + Z_{oc,j}(s) \tag{2.80}$$

where $Z_{ij}(s)$ is the equivalent impedance of the cable/line, and $Z_{oc,j}(s)$ is the equivalent local impedance of the VSC at an arbitrary terminal j. If the reference voltage is assumed constant, the linearized voltage at terminal i can be rewritten as

$$\Delta V_{dci} = Z_{oc,i}(s)\frac{1}{1+\dfrac{Z_{oc,i}(s)}{Z_{net,i}(s)}}\Delta I_i. \tag{2.81}$$

The above equation as derived, holds all the information required to manipulate the behaviour of the DC network as seen from each terminal for robust stability and performance improvements. The right-most part of (2.81) is similar to the closed-loop transfer function of a control system with loop-gain given as

$$L_i(s) = \frac{Z_{oc,i}(s)}{Z_{net,i}(s)}. \tag{2.82}$$

Therefore, the Nyquist plot of $L_i(s)$ predicts the external stability of terminal i with respect to the rest of the global system. That is, the stability of any terminal with respect to the rest of the system is guaranteed if the Nyquist plot of $L(s)$ does not encircle the $(-1, j0)$ point. Additionally, network controllers can be designed by directly manipulating the tractable components of $L_i(s)$ as would be shown in later chapters. Fig. 2.35 depicts the feedback interconnection of the entire network as a closed-loop system based on the Nyquist criterion. Note that, $Z_{net,i}(s)$ holds the operating point information about the rest of the system.

Equation (2.82) can be extended to the n terminal network given the diagonal matrix of converter impedance equivalents $\mathbf{Z}_{oc}(s)$ and system-level equivalents of each terminal as the diagonal elements of $\mathbf{Z}_{dc}^{cl}(s)$ matrix, previously derived. The loop-gain matrix of the system $\mathbf{L}(s)$ can be derived

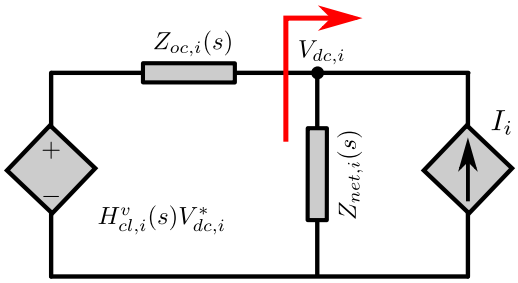

Figure 2.34: Subnetwork partition into two subsystems as seen from terminal i

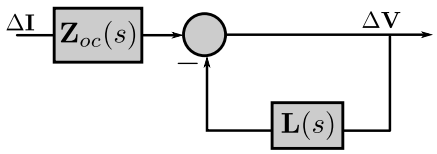

Figure 2.35: DC subnetwork feedback interconnection equivalent

compactly as

$$\mathbf{L}(s) = \mathbf{Z}_{oc}(s)\left(\mathbf{Z}_d(s)\right)^{-1} - \mathbf{I} \tag{2.83}$$

where $\mathbf{L}(s)$ is a diagonal matrix, $\mathbf{Z}_d(s)$ is the diagonal matrix consisting of the system-level terminal equivalents (diagonal elements of $\mathbf{Z}_{dc}^{cl}(s)$), and $\mathbf{I}$ is the identity matrix.

2.6.3 Aggregation of AC Equivalents

Given the equivalent impedance matrix of each active subsystem in the AC grid — converters, synchronous generators, compensators, etc. the generalized terminal equivalent formulation relative to imposed voltages and injected currents can be expressed as

$$\underbrace{\begin{pmatrix}\Delta u_d\\ \Delta u_q\end{pmatrix}}_{\Delta u_{dq}} = \underbrace{\begin{pmatrix}\Delta u_d^*\\ \Delta u_q^*\end{pmatrix}}_{\Delta u_{dq}^*} + \underbrace{\begin{pmatrix}Z_{dd}(s) & Z_{dq}(s)\\ Z_{qd}(s) & Z_{qq}(s)\end{pmatrix}}_{\mathbf{Z}(s)} \underbrace{\begin{pmatrix}\Delta i_d\\ \Delta i_q\end{pmatrix}}_{\Delta i_{dq}} \tag{2.84}$$

where Δu_{dq} is the vector of imposed voltages, Δi_{dq} is the vector of injected currents during disturbances, Δu_{dq}^* is the vector of control references, and $\mathbf{Z}(s)$ is the equivalent impedance of each subsystem. If constant voltage control is assumed, or voltage is not controlled, then, Δu_{dq}^* vector is eliminated. In the event current control is employed in an active device, then voltage and current vectors are interchanged in (2.84) and $\mathbf{Y}(s)$ is adopted. Nevertheless, this does not affect the results of stability and interaction analysis.

For an n terminal interconnected AC grid with at least one integrated VSC, Fig. 2.36 illustrates a generalized interconnection of impedance models of different active subsystems. This includes, current controlled converters, and voltage controlled subsystems such as static compensators, synchronous generators, alternating-voltage controlled converters, etc. The

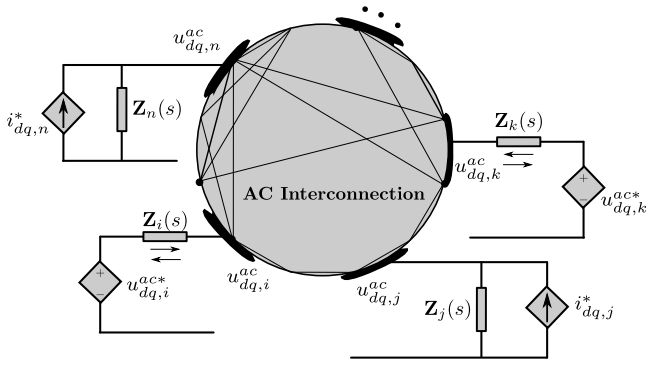

Figure 2.36: Interconnection of AC side impedance equivalents

dynamic voltage response can be generalized as

$$\underbrace{\begin{pmatrix}\Delta u^{ac}_{dq,i}\\ \Delta u^{ac}_{dq,j}\\ \vdots\\ \Delta u^{ac}_{dq,n}\end{pmatrix}}_{\Delta \mathbf{u}^{ac}_{dq}} = \underbrace{\begin{pmatrix}\mathbf{Z}^{cl}_{ac,ii}(s) & \mathbf{Z}^{cl}_{ac,ij}(s) & \cdots & \mathbf{Z}^{cl}_{ac,in}(s)\\ \mathbf{Z}^{cl}_{ac,ji}(s) & \mathbf{Z}^{cl}_{ac,jj}(s) & \cdots & \mathbf{Z}^{cl}_{ac,jn}(s)\\ \vdots & \vdots & \ddots & \vdots\\ \mathbf{Z}^{cl}_{ac,ni}(s) & \mathbf{Z}^{cl}_{ac,nj}(s) & \cdots & \mathbf{Z}^{cl}_{ac,nn}(s)\end{pmatrix}}_{\mathbf{Z}^{cl}_{ac}(s)} \underbrace{\begin{pmatrix}\Delta I_{dq,i}\\ \Delta I_{dq,j}\\ \vdots\\ \Delta I_{dq,n}\end{pmatrix}}_{\Delta \mathbf{I}_{dq}} \tag{2.85}$$

where $\mathbf{u}^{ac}_{dq}$ is a vector of voltage vectors at the point of connection of each active device (converters, synchronous generators, compensators, etc.), $\mathbf{I}_{dq}$ is the vector of current injected by each active device, and each element in $\mathbf{Z}^{cl}_{ac}(s)$ is a 2×2 matrix. Each dictate the dynamic responses at each terminal and between terminals during disturbances.

AC Impedance-based Stability Formulation

There are numerous ways in which a converter can be interfaced with an AC grid. For instance, an HVDC link may interconnect two distinct control areas in which case the impact of each converter on each corresponding network may be desired. On the alternative, an HVDC link may interconnect points within the same control area often termed as an embedded HVDC link, etc. To generalize stability formulations from an impedance perspective, it is assumed that the Thévenin equivalent of the rest of the network from any bus of interest in the AC network is available. That is information on $\Delta u^{ac}_{dq,i}$ at bus i is available in the form

$$\Delta u^{ac}_{dq,i} = \Delta u^{eq}_{dq,i} + \Delta u^{c}_{dq,i} \tag{2.86}$$

where $\Delta u^{eq}_{dq,i}$ is based on the Thévenin equivalent of the rest of the network as seen from terminal i (similar to $Z_{net,i}(s)$ on the DC side of the VSC) and

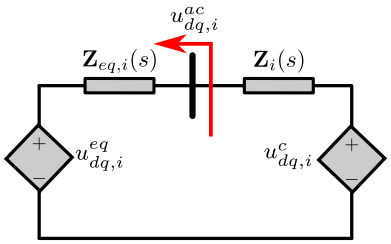

Figure 2.37: AC subnetwork partition at terminal i with a VSC interface

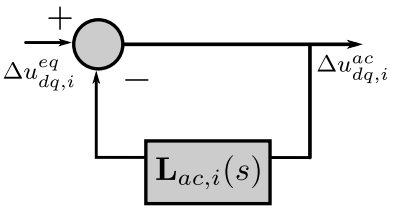

Figure 2.38: AC system feedback interconnection equivalent

Δu^{c}_{dq} is based on the equivalent impedance of the subsystem of interest as derived in (2.84) and shown in Fig. 2.37.

To establish the stability and potential interaction between an alternating-voltage or current controlled converter as shown in Fig. 2.37, $\Delta u^{dq}_{ac,i}$ considering the equivalent representation of network can be rewritten as [74]

$$\Delta u^{ac}_{dq,i} = \frac{\mathbf{Z}_i(s)}{\mathbf{Z}_i(s)+\mathbf{Z}_{eq}(s)}\Delta u^{eq}_{dq,i} = \frac{\mathbf{I}}{\mathbf{I}+\dfrac{\mathbf{Z}_{eq}(s)}{\mathbf{Z}_i(s)}}\Delta u^{eq}_{dq,i} \tag{2.87}$$

where $\mathbf{I}$ is the identity matrix in the case of a MIMO system, and

$$\mathbf{L}_{ac,i}(s) = \frac{\mathbf{Z}_{eq}(s)}{\mathbf{Z}_i(s)} \equiv \mathbf{Y}(s)\mathbf{Z}_{eq}(s). \tag{2.88}$$

where $\mathbf{L}_{ac,i}(s)$ is referred to as the *"minor loop gain"*. Hence, (2.87) can be drawn as feedback interconnection of the entire network as seen from terminal i is shown in Fig. 2.38. Therefore, the generalized multivariable Nyquist criterion is applied to establish stability and interaction between terminal i and the rest of the network.

2.7 Chapter Conclusions

This chapter establishes the details and basics of impedance modelling as adopted in this thesis. Several methods for the derivation of the models of each potential subsystem in the network were compared, verified, and demonstrated, with advantages and disadvantages highlighted. Particularly, the models of the AC/DC sides of the VSC as a subsystem were derived with modularity and scalability. It was also shown that it is possible to decouple the systems interfaced by the VSC into subnetworks while isolating the transfer functions that determine the bulk interactions between subnetworks. Subsequently, converter-level models of subsystems were aggregated and extended to subnetwork equivalents while keeping modularity.

Subnetwork level formulations which include DC-DC interactions, DC stability, and AC stability were introduced and established. Finally, several examples were applied to provide insights. Overall, the impedance modelling framework can be applied as a potent tool for system-level analysis of dynamic behaviour and potential control to improve behaviour across varying operating conditions.

3

Analysis and Control of VSC-HVDC Grids

This chapter presents an impedance-based approach for analysis and control of system-level interactions in HVDC grids. Through this approach, the mechanism of interactions within the DC grid and the potential impact of control on system-level behaviour is discussed. Furthermore, the subnetwork approach adopted allows obtaining insights into the control requirements of the DC grid that may differ with that of the AC grid as subnetworks. Finally, a methodology for high-level control design for multi-vendor converter HVDC grids to mitigate interactions without explicit knowledge of the internal architecture of any VSC is proposed and applied. This is important to guarantee robust stability in future power systems and mitigate detrimental interactions that may transfer to the entire system.

3.1 State-of-Art of Modelling and Control of VSC-HVDC Grids

In recent years, to solve the challenges brought about by the integration of solid-state devices into the power systems, the research community has been applying several methods from varying perspectives and tools for dynamic modelling and analysis. The well-established method of state-space modal analysis has been applied by numerous authors to HVDC grids to establish global stability [113, 124–127, 127–131]. However, even for stability-guaranteed power converters, the tight controls and small time constants employed contribute to an increase in coupling and interactions between the different elements of the network. More importantly, it may

be required to isolate the sources of disturbance efficiently to allow speedy mitigation without affecting the rest of the system. Nevertheless, the traditional state-space method is not sufficient in providing a complete picture of dynamics in the presence of these devices among other shortcomings.

Literature is extensive on the applications of the impedance modelling to AC side dynamics of the VSC [71,95,102,132]. Nevertheless, the impact of the DC side is often completely neglected. In a few of the cases where the DC side is the focus, results are specific to HVDC links [100, 104]. Hence, generalizations are difficult to systems with arbitrary structures and operating modes. On a final note, there is little to no literature on network-level interaction detection between VSCs and control design to mitigate such interactions when only black-box models are available. In this chapter, an impedance-based methodology is proposed for interaction analysis, input-output stability, and network control of VSC-HVDC grids.

3.2 Impacts of Control on DC-DC Interactions, and Stability

This section studies the impact of control on the global level impedance equivalents and corresponding impacts on input-output stability on a three-terminal VSC-HVDC grid shown in Fig. 3.1 (redrawn from Fig. 2.27). Two potential control modes are possible through the master-slave strategy — mode 1, and droop strategy — mode 2.

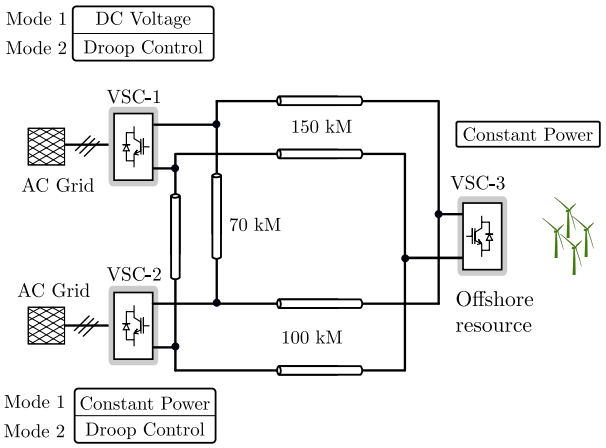

Figure 3.1: Three terminal VSC-HVDC grid with two possible system-level control modes

3.2.1 Impacts of DVC Bandwidth in Master-Slave Mode

Fig. 3.2 shows the impact of DVC closed-loop bandwidth variation on the global impedance responses in mode 1 of the three-terminal grid described. It is immediately clear the impacts of the closed-loop bandwidth of the DVC on the global impedance responses at each terminal (diagonal elements) and transfer responses (off-diagonal elements) in the system for the case of mode 1 (master-slave). The global impedance response at VSC-1 shows the most variation across the entire range of bandwidths. In general for low bandwidths, several interaction frequencies with significant peaks can be seen in all responses. As closed-loop bandwidth is gradually increased, several resonant frequencies damp out, indicating that a slightly faster bandwidth is desired of the direct-voltage controlling terminal at the global level. As bandwidth is significantly increased, the global impedance response at VSC-1 shows sufficient damping of all resonant frequencies. However, a new resonant point begins to develop in the high-frequency region (above 100Hz) not seen at other terminals. This is the result of self-interaction at VSC-1 between the direct-voltage control loop and the current loop, and further increase results to instability that transfers to the global system. This establishes the limit of allowable bandwidth of the DVC. In contrast, at other terminals, there is no significant impact of very high bandwidth of DVC beyond 40Hz. Moreover, increasing the bandwidth significantly simply shifts the existing interaction frequencies. In principle, this implies that the impacts of DVC closed-loop bandwidth diminish despite increasing its bandwidth. Therefore, any weakly damped

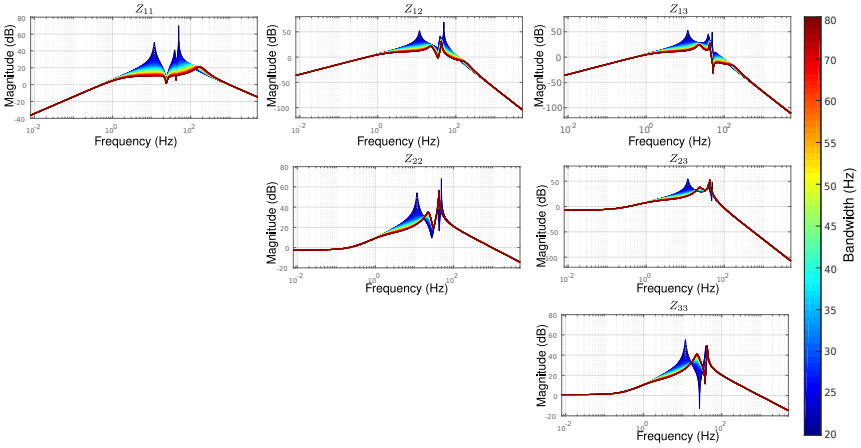

Figure 3.2: Impact of bandwidth variation of a three-terminal HVDC grid in master-slave mode

resonance will require additional control actions at the global level to mitigate if deemed necessary.

Fig. 3.3 shows the time-domain simulation in Matlab Simulink® of the impacts of bandwidth variation in mode 1 for a step increase in power injected into the DC at 1.5s from VSC-3. It can be observed that in the low bandwidth region, multiple frequencies can be identified in the time-domain responses matching the major peaks detected in Fig. 3.2. As bandwidth is gradually increased, these three peaks damp out with most damping occurring at VSC-1 controlling the direct-voltage as discussed in the frequency domain analysis. As bandwidth is significantly increased, existing resonances are shifted in frequency and phase at VSC-2 and VSC-3. These are control interactions and this confirms the previous discussions from frequency domain analysis where a significant increase in bandwidth only improves the responses at VSC-1 but worsens the responses at other terminals.

To further support the analysis previously made and to show the efficacy of frequency domain analysis, Fig. 3.4 shows the global impedance response for a selected bandwidth of 20Hz in mode 1. It shows clearly the

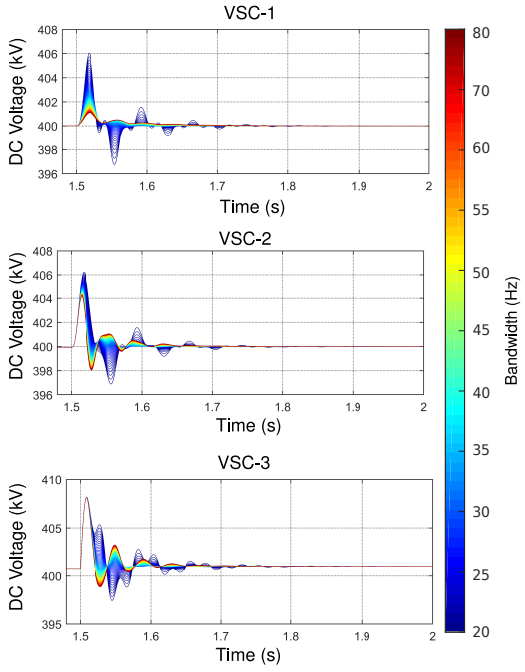

Figure 3.3: Time domain simulation of the impacts of closed-loop bandwidth variation in master-slave mode

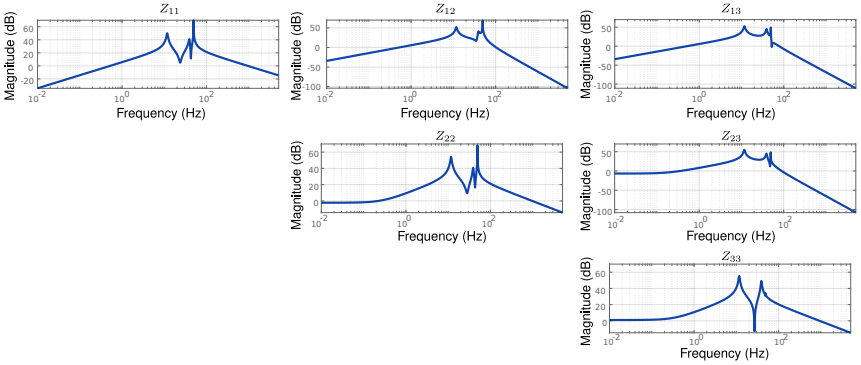

Figure 3.4: Global impedance responses in mode 1 for DVC closed-loop bandwidth of 20Hz

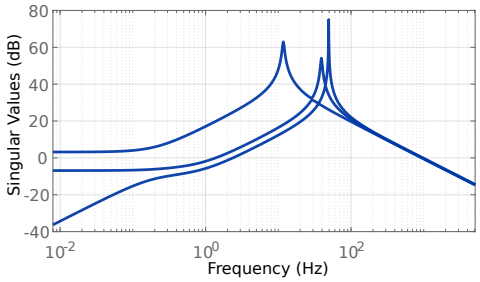

Figure 3.5: SVD response of global MIMO system in mode 1 for DVC closed-loop bandwidth of 20Hz

three major interaction frequencies at 11.7Hz, 39Hz, and 49.3Hz. Recall that in the example given in the previous chapter, it was explained that the SISO responses mainly identify the isolated resonance frequencies. However, these are worst-case interaction frequencies that do not necessarily consider the all potential directions of input. The MIMO SVD plot in Fig. 3.5 shows the collective responses from worst-case scenario to best-case scenario considering the possible direction of inputs (bus current changes) and confirms the interaction frequencies. Also, observe that in some of the global responses such as those at VSC-3 (Z_{33}), only two interactions frequencies can be seen compared to three frequencies at VSC-1. Hence, further analysis is required to isolate how these terminals are interacting or contributing to the interaction frequencies. This is important to establish any requirement for global control by decoupling these interactions.

Fig. 3.6 shows the RGA plot of mode 1 for the 20Hz DVC, showing the group of terminals interacting at each identified frequency. It shows

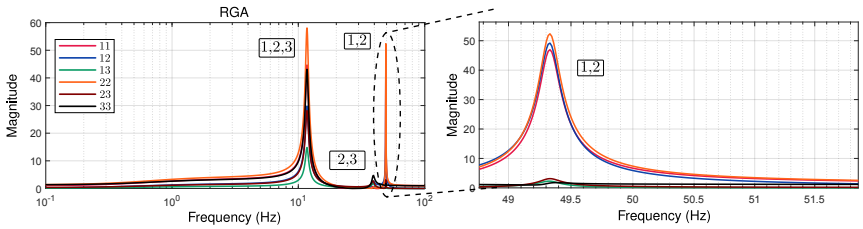

Figure 3.6: RGA magnitude plot of the global response in mode 1 for DVC closed-loop bandwidth of 20Hz

that despite three identified interaction frequencies, only two are significantly dominant at 11.7Hz and 49.3Hz. All terminals are interacting at 11.7Hz due to the equivalent capacitance of the global system and the direct-voltage controlled by VSC-1. At 49.3Hz, VSC-1 and VSC-2 are significantly interacting. Therefore, the time responses of VSC-1 and VSC-2 are expected to contain both 11.7Hz and 49.3Hz components. Whereas, VSC-3 will mainly consist of the 11.7Hz component and some residual components due to interactions with VSC-1 and 2 as seen by the small peaks at 49.3Hz. However, these are insignificant compared to the interaction occurring between VSC-1 and VSC-2. Fig. 3.7 shows the time-domain simulation confirming the preceding discussions. Oscillations in VSC-1 and VSC-2 consist of both the 11.7 and 49.3Hz components and VSC-3 mainly consists of the 11.7Hz components with well-damped residual components at 49.3Hz as RGA analysis predicts.

To ascertain the stability of this case, Fig. 3.8 shows the Nyquist plot of the impedance ratio based on the formulations derived in Equations (2.82) and (2.83) as seen from the voltage control terminal. Although the system is input-output stable from a classical sense, it can be observed from the plot that the system is marginally stable as the Nyquist plot is close to the $(-1, j0)$ stability margin. This confirms the sustained oscillations in steady-state in the time-domain simulations. To check the system input-output stability to a different operating point, Fig. 3.9 shows the Nyquist plot for a change in power direction; it can be seen that the system is unstable by crossing the stability margin. This is confirmed in the time-domain simulations shown in Fig. 3.10.

The preceding analysis underscores the need for collective tuning or retuning of controllers for optimal performance. If this is not possible such as for the independent design of local controls, or it is desired to improve the system-wide response, then supplementary controllers may be required at the system-level. Generally speaking, the DVC closed-loop bandwidth should not be too low to risk instabilities due to interactions (large peaks), nor high low to cause interaction with the inner loop that

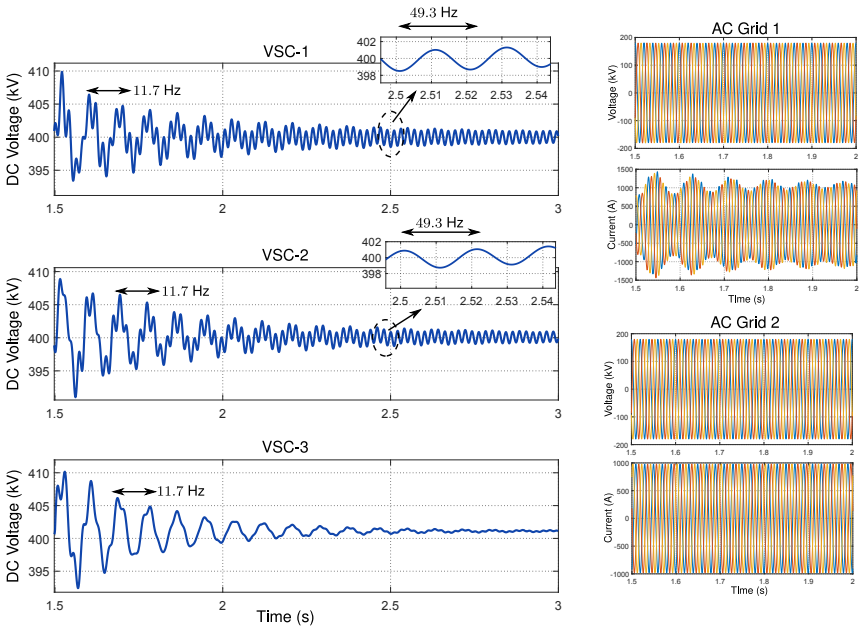

Figure 3.7: Responses for a step disturbance at VSC-3

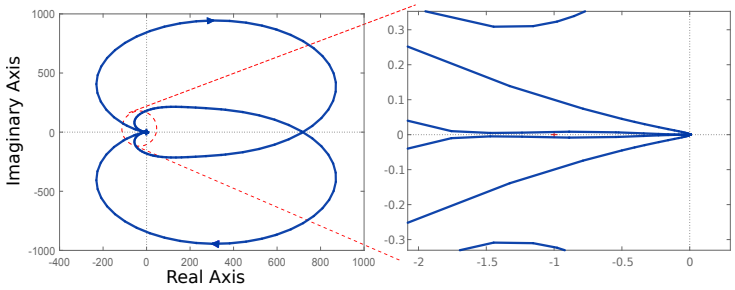

Figure 3.8: Nyquist plot of the of the impedance ratio as seen from VSC-1

eventually transfers to the AC grid and eventually the DC grid causing instability. Thus, a compromise based on potential self-interaction of the direct-voltage controlling terminal, AC and DC subnetwork interaction analyses are required in improving the global responses.

3.2.2 Impacts of PLL Bandwidth in Master-Slave Strategy

Following the modelling procedures in Sections 2.2.2, the cosine of PLL deviation angle ($\Delta\theta_p$) contributes to the imposed DC impedance derived

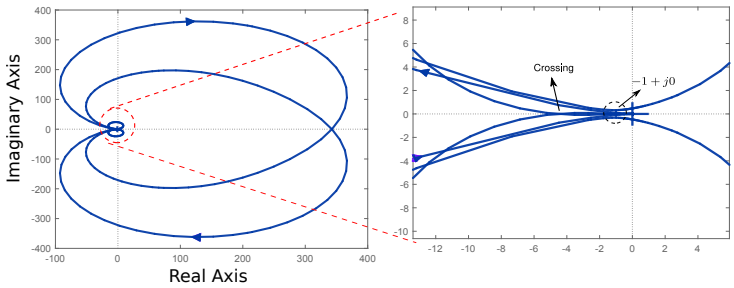

Figure 3.9: Nyquist plot of the of the impedance ratio as seen from the controlled terminal VSC-1 at a different operating point

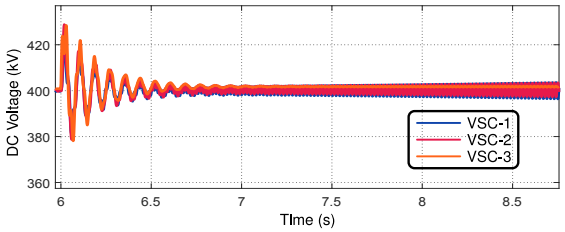

Figure 3.10: Simulation of unstable case

in (2.31) through the closed-loop transfer function of the inner loop $h^i_{cl}(s)$ derived in (2.15). Fig. 3.11 shows the impacts of the cosine of PLL deviation angle for varying PLL closed-loop bandwidths $(1-100\text{Hz})$ on the DC terminal voltages for a grid with SCR $= 5$. It can be observed that there is no considerable impact of the PLL deviation angle on DC side responses. It will be seen in the following chapter that this is relative to the strength of the connected AC grids. Therefore, for a fairly strong or strong AC grid (SCR > 3), the impacts of PLL on the DC grid can be neglected since the impact of AC voltage control is negligible and reactive power behaviour is fairly constant across operating points. However, for weak grids with severe requirements on reactive power, the coupling between the AC and DC side increases as reactive power can no longer be assumed constant and the impacts of AC voltage control is not negligible. Nevertheless, the DC impedance cannot provide information on the interactions with the connected AC grid. The off-diagonal elements in the impedance models of Equation (2.33) instead predict the interactions between the AC and DC sides depending on the topology of the DC grid.

Fig. 3.12 shows a plot of the PLL output angle obtained from nonlinear time-domain simulation with a strong AC grid against the closed-loop bandwidth frequency of the PLL. It shows that for a strong AC grid, the

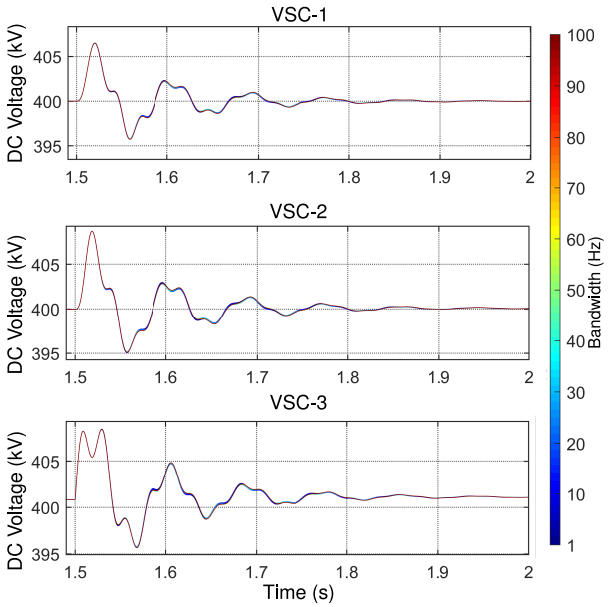

Figure 3.11: Impacts of PLL deviation angle on DC grid responses

impacts of PLL closed-loop bandwidth is quite negligible. Even for the slowest PLL bandwidth of 1Hz, the cosine of output angle which directly affects the feedback impedance is ≈ 1.

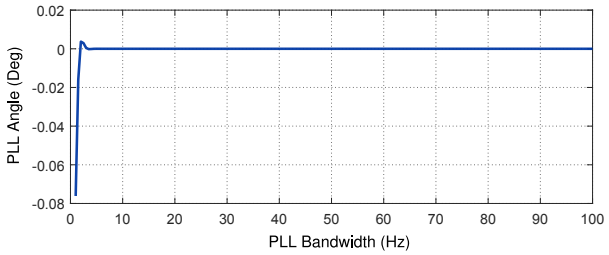

Figure 3.12: Impacts of PLL closed-loop bandwidths on PLL output angle for the interconnected HVDC grid

3.2.3 Impact Droop Gains in Droop Control Mode

Fig. 3.13 shows the impact of variation of droop gain at VSC-1 from 0 to 40MW/kV (which is quite high and unrealistic), whereas VSC-2 has a constant droop gain at the nominal value of 2.5MW/kV. It can be recognized

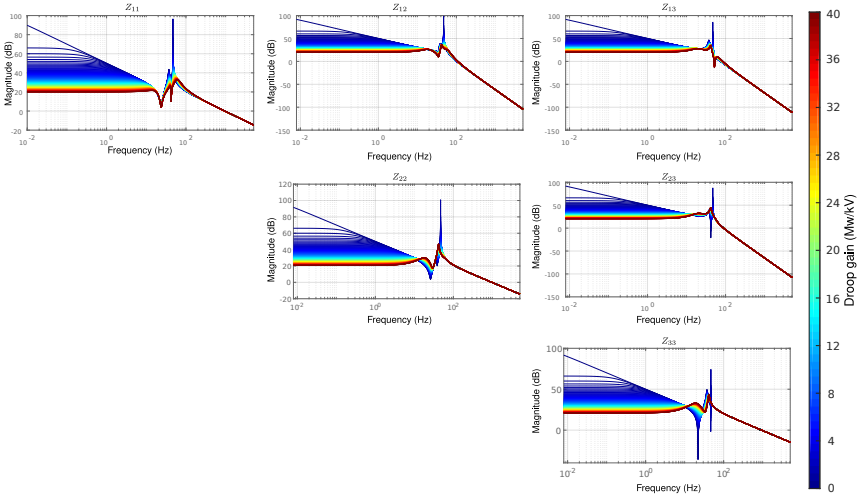

Figure 3.13: Impact of bandwidth variation of a three-terminal HVDC grid in droop mode

that large droop gain improves the performance by drastically reducing the impedance magnitude, at least in the low-frequency region. Increasing droop gain can also be interpreted as moving the system closer to a master-slave mode as the gain is significantly increased since a zero droop gain is equivalent to active power control and infinite droop gain to direct-voltage control [133]. However, considering that droop gains impact the overall system including the AC grids, and is limited by converter capability at an operating point, the impacts of high droop gain on the AC side cannot be established alone from the impedance response of the DC side. Nevertheless, despite the significant increase in droop gain, interaction frequencies are still observable as varying the droop gain has no significant effect on these frequencies. In contrast, very low droop gain results in high steady-state deviation and poor system dynamic response which may not be desirable. Fig. 3.14 shows the time-domain responses for a step change of 100 MW at 1.5s from VSC-3 in mode 2 similar to mode 1. This can be seen clearly in the time-domain responses shown in Fig. 3.14. The system is sluggish for very low gains, with multiple oscillation frequencies, and significant deviation despite only a change of 100 MW. Gradually increasing the gain immediately alleviates the steady-state deviation, but the oscillations are still present despite the increase.

To obtain insights into detailed behaviour similar to mode 1, Fig. 3.15 shows the global SVD response for equal droop gains of 2.5MW/kV in mode 2. As can be seen in the worst-case response, the droop response region in steady-state is obvious and two additional interaction frequen-

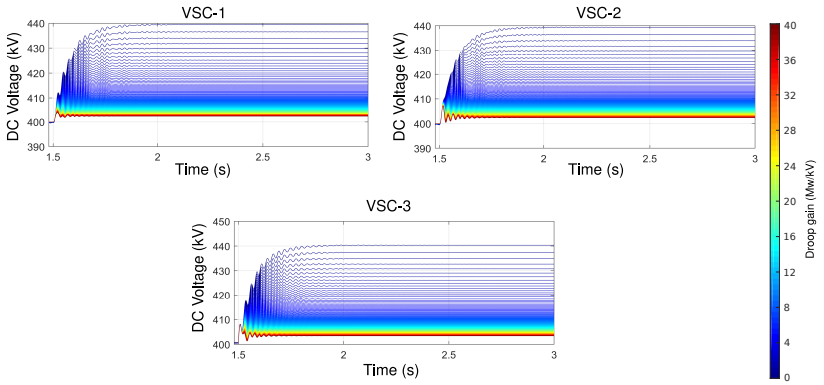

Figure 3.14: Time domain simulation of the impacts of closed-loop bandwidth variation in droop mode

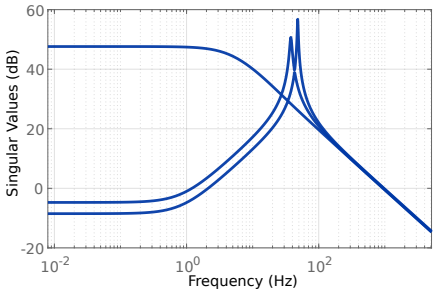

Figure 3.15: SVD response of global MIMO system in mode 2 for equal droop gains of 2.5MW/kV

cies at 37.8Hz, and 48.4Hz. Again, the SVD does not indicate terminal interactions and at first glance, it may be wrongly concluded that the peaks are a cause for concern as they are higher than the highest steady-state deviation. Fig. 3.16 shows the RGA frequency-dependent magnitude plot. Contrary to intuition, the interaction in the droop response region dominates significantly over the peaks. However, oscillations matching the peaks are still visible although well-damped. Fig. 3.17 shows the time-domain responses for a step disturbance at 1.5s similar to the previous cases. It is shown that the mid interaction frequency damps out within the first 500ms, while in general droop control dominates the time responses as predicted by the RGA.

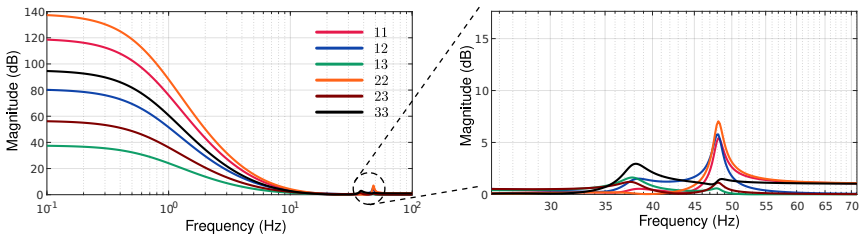

Figure 3.16: RGA magnitude plot of the global response in mode 2 for equal droop gains of 2.5 MW/kV at each droop terminal

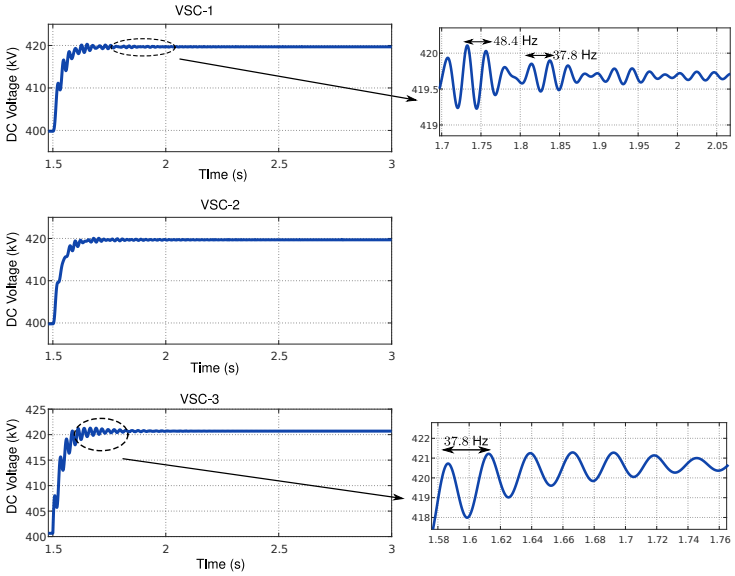

Figure 3.17: Simulations for a step disturbance at VSC-3 showing the damped mid interaction frequencies

3.3 Methodology for Supplementary Control Design in Multi-Vendor Converter HVDC Grids

In many of the cases such as those discussed in previous sections and chapter (See Figs. 2.32 and 3.6), network-scale interactions may be so critical to warrant additional control actions. In the same vein, such control actions may not be possible with local control as discussed in Section 3.2. Therefore, in a more realistic system, it may be required to design additional controllers that overlook the entire network. Additionally, given the low maturity of existing technologies and intellectual property concerns, it will be required to design these controllers without access to sensitive information about any converter. Sensitive information includes the adopted technologies, internal structure of converters, control, and related information. This is particularly expected of multi-vendor converter systems where different vendors apply in-house solutions and proprietary strategies based on varying experiences. For such a system where information is not shared, concurrent design of converter control is not possible. The ultimate consequences include unavoidable detrimental interactions.

As emerging literature suggests, designing network controllers to mitigate such unintended interaction is key to robust multi-vendor systems [134–137]. Nevertheless, vendors of converters are often willing and are required to share information in the form of black-boxes such as transfer functions that mask all sensitive information such as those aforementioned. Therefore, the methodology described in this section based on impedance transfer functions can be adopted for supplementary control action to guarantee robust performance and stability.

3.3.1 Requirements for Control Design

Supplementary controllers are designed in a manner that they 'over-look' the network either from each respective location or from a central location as desired. There are at least two broad and important information required a priori for any control design effort considering the existence of local control:

1. The input-output impedance models of each active device in the HVDC grid as a transfer function. These may be in any established form including continuous-time representation such as

$$Z(s) = \frac{\Delta V}{\Delta I} = \frac{b_m s^m + \cdots + b_1 s + b_0}{a_n s^n + a_{n-1} s^{n-1} + \cdots + a_1 s + a_0}$$

where the coefficients $b_m, \cdots, b_0$ and $a_n, \cdots, a_0$, are numbers. These can be obtained from established verification or system identification

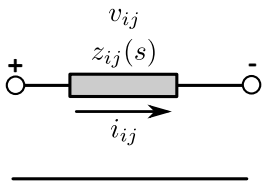

Figure 3.18: Circuit schematic of impedance models of passive devices

tests, provided directly from the manufacturer, or obtained from detailed black-box models that can be converted. However, it must be noted that the impedance models of VSCs depend heavily on operating point and control strategies as would be seen in the next chapter. Therefore, a set of transfer functions at several operating points across the expected range of operation of the device should be provided. Besides, the impedance models of all operating control modes must be provided.

2. The input-output models of all passive devices in the network are assumed to be available in the form of Fig. 3.18. The most important of these are the frequency-dependent impedance models of cables, lines, and passive devices. The level of detail of such models depends on the purpose and study at hand. However, models of different fidelities may be provided. For instance, Π models of cables may be sufficient up to a particular frequency and distributed Π may be better suited for studies beyond a range of frequencies. Low order equivalents of high fidelity models are encouraged. This is to prevent the total order of the system from being dominated by the order of passive components. Moreover, high fidelity models are typically suitable for analysis and protection coordination, rather than control design. The frequency range of models for control design may be limited to the bandwidth of the fastest control loop in the system; this loop is usually the inner current loop.
3. Network topology is assumed to be known. However, supplementary controller parameters may need to be re-optimized as network topology changes. Interaction frequencies typically shift in either direction as components are connected or disconnected from the grid.

It is important to remark that the problem of supplementary control design is a disturbance rejection problem. Hence, local controllers are assumed strictly stable. However, as it has been seen, the local stability of each converter does not necessarily imply global stability when interconnected with others.

3.3.2 Overall Objectives of Supplementary Control Design

The following objectives of the designed supplementary controllers provide the benchmark for assessing their performance after design.

1. Reduce the effect of feedback coupling (interaction) between active devices, and inherent network oscillations (dormant or otherwise) not considered during the independent design of local controllers.
2. Synthesized controllers should not interact with existing local controllers. Particularly, it is desired that synthesized controllers do not contribute to steady-state behaviour where local control is most active.
3. Improve the robust performance and stability in the event the existing system lacks any of these indices.

3.3.3 $\mathcal{H}_\infty$ Mixed-sensitivity Framework

Considering that tracking is not an issue as each local controller ensures this, the problem becomes that of minimizing $\Delta\mathbf{V}_{dc} = \mathbf{Z}_{dc}^{cl}(s)\Delta\mathbf{I}$ due to the interconnection and coupling with other subsystems according to equation (2.74). This is equivalent to simply minimizing the peaks of $\mathbf{Z}_{dc}^{cl}(s)$ as low as possible or shaping the impedance responses such that $\Delta\mathbf{V}_{dc}$ is acceptable. If this is possible, then the detrimental impacts of interactions are minimized at each location of an active subsystem. Constraints of control design include the maximum allowed/available control effort, order of synthesized controllers, structure, etc.

The minimization problem is both a frequency and magnitude problem and either one may be prioritized depending on several factors or a compromise between both as problem dictates. For example, at low to medium power ranges, damping of resonances may be prioritized over the magnitude of response; however, at high power, the magnitude of responses may be prioritized to avoid a breach of limits. Furthermore, a communicationless supplementary control action may be desired to mitigate any effect of latent delays and other related issues. Therefore, the overall problem is a mixed-sensitivity problem of disturbance rejection, control input, and fixed structure controllers. This directly fits into the established $\mathcal{H}_\infty$ decentralized fixed-structure framework [138].

Fig. 3.19 shows the defined problem in the standard $\mathcal{H}_\infty$ structure. $\mathbf{Z}_{dc}^{cl}(s)$ is the global closed-loop impedance matrix as derived in (2.74) at nominal power flow and random power flows introduced as uncertainty, $\mathbf{Z}_p(s)$ is a fictitious 'plant' model consisting of scalar gains α_{ii} corresponding to each active subsystem. The value indicates the relative priority of the location of the corresponding active subsystem. $\mathbf{W}_{\Delta v}$ is a frequency-dependent matrix that weights the system output vector $\Delta\mathbf{V}_{dc}$ which contains information about the disturbance; $\Delta\mathbf{I}_s$ is the supplementary control

output vector, and $\mathbf{W}_{\Delta I_s}$ is a frequency-dependent matrix that weights the controller outputs. The system input and outputs are the potential change in bus current vector $\Delta\mathbf{I}$ and $\mathbf{z}(s)$ respectively, and the supplementary controllers are sorted in $\mathbf{K}_s(s)$. The weights allow establishing the bounds on the corresponding input and output variables (See Appendix). All matrices except $\mathbf{Z}_{dc}^{cl}(s)$ are diagonal for the decentralized structure, with dimension equal to the number of active subsystems in the network. However, some matrices such as $\mathbf{K}_s(s)$ may contain null elements if the specified number of supplementary controllers is lower than the number of active subsystems.

The generalized closed-loop equation of the formulation in frequency domain can be derived from Fig. 3.19. Starting with the inner-most structure (red dashed box), the input-output expressions from $\Delta\mathbf{I}$ and $\Delta\mathbf{I}_s$ to z_1, z_2, and $\Delta\mathbf{V}$ can be derived as

$$z_1(s) = \mathbf{W}_{\Delta I_s}(s)\Delta\mathbf{I}_s \tag{3.1a}$$

$$z_2(s) = \mathbf{W}_{\Delta v}(s)\mathbf{Z}_{dc}^{cl}(s)\Delta\mathbf{I} + \mathbf{W}_{\Delta v}(s)\mathbf{Z}_p(s)\Delta\mathbf{I}_s \tag{3.1b}$$

$$\Delta\mathbf{V} = \mathbf{Z}_{dc}^{cl}(s)\Delta\mathbf{I} + \mathbf{Z}_p(s)\Delta\mathbf{I}_s \tag{3.1c}$$

The above expressions can be combined in a compact form as

$$\begin{pmatrix}\mathbf{z}\\ \Delta\mathbf{V}\end{pmatrix} = \underbrace{\left(\begin{array}{c|c} 0 & \mathbf{W}_{\Delta I_s} \\ \mathbf{W}_{\Delta v}\mathbf{Z}_{dc}^{cl} & \mathbf{W}_{\Delta v}\mathbf{Z}_p \\ \hline \mathbf{Z}_{dc}^{cl} & \mathbf{Z}_p \end{array}\right)}_{\mathbf{P}} \begin{pmatrix}\Delta\mathbf{I}\\ \Delta\mathbf{I}_s\end{pmatrix}; \quad \mathbf{z} = \begin{pmatrix} z_1 \\ z_2 \end{pmatrix} \tag{3.2}$$

where $\mathbf{P}$ is the augmented plant considering the weighting matrices as shown in Fig. 3.19. To include the controller(s) to be determined in the

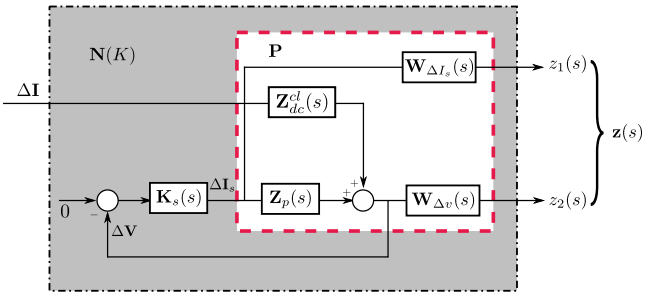

Figure 3.19: Decentralized fixed-structure supplementary control design in $\mathcal{H}_\infty$ framework

optimization framework and obtain the complete input to output transfer function, $\Delta\mathbf{I}_s = -\mathbf{K}_s\Delta\mathbf{V}$ is eliminated from (3.1) to become

$$z_1(s) = -\mathbf{W}_{\Delta I_s}(s)\mathbf{K}_s(s)\Delta\mathbf{V} \tag{3.3a}$$

$$z_2(s) = \mathbf{W}_{\Delta v}(s)\mathbf{Z}_{dc}^{cl}(s)\Delta\mathbf{I} - \mathbf{W}_{\Delta v}(s)\mathbf{Z}_p(s)\mathbf{K}_s(s)\Delta\mathbf{V} \tag{3.3b}$$

$$\begin{aligned} \Delta\mathbf{V} &= \mathbf{Z}_{dc}^{cl}(s)\Delta\mathbf{I} - \mathbf{Z}_p(s)\mathbf{K}_s(s)\Delta\mathbf{V} \\ \implies \Delta\mathbf{V} &= \underbrace{\underbrace{\frac{\mathbf{I}}{\mathbf{I}+\mathbf{Z}_p(s)\mathbf{K}_s(s)}}_{\mathbf{S}(s)}\mathbf{Z}_{dc}^{cl}(s)}_{\mathbf{Z}_{dc,new}^{cl}(s)}\,\Delta\mathbf{I} \end{aligned} \tag{3.3c}$$

where $\mathbf{Z}_{dc,new}^{cl}(s)$ is the modified closed-loop impedance matrix of the system after supplementary control action, $\mathbf{S}(s)$ is the sensitivity function of synthesized controllers. $\Delta\mathbf{V}$ from (3.3c) is eliminated from (3.3a) and (3.3b) to obtain

$$z_1(s) = -\mathbf{W}_{\Delta I_s}(s)\mathbf{K}_s(s)\mathbf{S}(s)\mathbf{Z}_{dc}^{cl}(s)\Delta\mathbf{I} \tag{3.4a}$$

$$z_2(s) = \mathbf{W}_{\Delta v}(s)\mathbf{S}(s)\mathbf{Z}_{dc}^{cl}(s)\Delta\mathbf{I} \tag{3.4b}$$

The above expressions can be written compactly as

$$\mathbf{z} = \mathbf{N}(K)\Delta\mathbf{I} \tag{3.5}$$

$$\mathbf{N}(K) = \begin{pmatrix} \mathbf{W}_{\Delta I_s}\mathbf{K}_s\mathbf{S}\mathbf{Z}_{dc}^{cl} \\ \mathbf{W}_{\Delta v}\mathbf{S}\mathbf{Z}_{dc}^{cl} \end{pmatrix}$$

where $\mathbf{N}(K)$ is the complete closed-loop system from input $\Delta\mathbf{I}$ to output $\mathbf{z}$, and $\mathbf{S}$ is a diagonal matrix. The optimization problem is then to minimize $\mathbf{N}(K)$ such that

$$\min_K ||\mathbf{N}(K)||_\infty \leq \gamma \tag{3.6}$$

where γ is the maximum allowed peak in frequency domain.

Design Preliminaries

1. Scaling: A key priority for a successful implementation is proper scaling to prevent potential skewing of the mixed-sensitivity problem. Scaling is done by determination of maximum expected change in bus currents (during disturbances), maximum allowed control input to reject disturbance, and maximum allowed voltage deviation for each converter. Scaling at each terminal can also emphasize the priority or role of that terminal. For instance, a maximum of 40kV deviation may be allowed at one converter, while only 25kV may

be allowed at another converter. The closed-loop impedance matrix $\mathbf{Z}_{dc}^{cl}$ and fictitious plant model $\mathbf{Z}_p$ are scaled according to

$$\begin{aligned} \mathbf{Z}_{dc,s}^{cl} &= \Delta\mathbf{V}_{max}^{-1}\mathbf{Z}_{dc}^{cl}\Delta\mathbf{I}_{max} \\ \mathbf{Z}_{p,s} &= \Delta\mathbf{V}_{max}^{-1}\mathbf{Z}_{p}\Delta\mathbf{I}_{s,max} \end{aligned} \tag{3.7}$$

where $\mathbf{Z}_{dc,s}^{cl}$ and $\mathbf{Z}_{p,s}$ are the scaled impedance matrix and plant model, $\Delta\mathbf{V}_{max}$ is the diagonal matrix of maximum allowed voltage deviation at each converter, $\mathbf{I}_{max}$ is the vector of maximum expected bus current change at each converter, and $\mathbf{I}_{s,max}$ is the vector of maximum allowed control input. The above scaling ensures the disturbance and plant model are scaled to 1 p.u. of disturbance in time and frequency domain.

2. Weight Selection and Justification: The choice of weights $\mathbf{W}_{\Delta v}(s)$ (objectives 1 and 3) and $\mathbf{W}_{\Delta I_s}(s)$ (objective 2) are influenced by the actual frequency domain responses, and iteration may be required in some cases to obtain the best weights.
   a) $\mathbf{W}_{\Delta v}(s)$: It can be observed in previous Sections that the global behaviour of each VSC terminal after interconnection is different from the local behaviour. However, the local behaviour before interconnection may be satisfactory in which case it may act as a reference for the selection of the elements of $\mathbf{W}_{\Delta v}(s)$ matrix. Therefore, initial weights may be chosen to force the global response to mimic the existing local response. Alternatively, in the event the local response is not adequate as a reference or it is desired to transfer some responsibilities to the supplementary control, then, an ideal weight can be selected.
   The disturbance rejection problem through control design is to have the sensitivity matrix $\mathbf{S}(s)$ in (3.5) sufficiently small (not necessarily zero). The smaller it is, the lower the system output $\mathbf{z}$ and control effort (all objectives combined). Hence, $\mathbf{W}_{\Delta v}(s)$ puts a maximum bound on $\mathbf{S}(s)$ according to [115]

$$\begin{aligned} &||\mathbf{S}(j\omega)|| \leq (||\mathbf{W}_{\Delta v}(j\omega)||)^{-1} \\ &\implies ||\mathbf{W}_{\Delta v}\mathbf{S}||_\infty \leq \mathbf{I} \end{aligned} \tag{3.8}$$

   where $\mathbf{I}$ is the identity matrix. If the above bound is satisfied, then (3.6) is easily satisfied based on the scaling of the system to 1 in (3.7). Hence, the optimized value of γ after controller synthesis indicates if the bounds are satisfied. It can be seen that the magnitude and frequency dependency of $\mathbf{W}_{\Delta v}(s)$ affects the synthesized $\mathbf{S}(s)$. Therefore, bandwidth and magnitude of each weight in the matrix should be chosen to reflect priority of each converter or coordination as obtained from the RGA plot. For

instance, the higher the magnitude of $\mathbf{W}_{\Delta v}(s)$ the tighter the bounds required of $\mathbf{S}(s)$. As for the frequency of $\mathbf{W}_{\Delta v}(s)$, this can be chosen based on the expected bandwidth of disturbance as shown in the SISO and MIMO response plots of the global impedance matrix. For an $\mathbf{S}$ that meet the bounds, the reshaped global impedance matrix $\mathbf{SZ}_{dc}^{cl}$ will indicate the overall improvements in performance and stability.

b) $\mathbf{W}_{\Delta I_s}$: Similar to the previous weighting matrix, this puts a bound on the allowed control effort to minimize the disturbance as measured at each terminal. It also puts a bound on the maximum bandwidth of synthesized controllers. This is important to prevent interactions with the inner loop which is usually the fastest loop in the system and the channel for the final command to the converter switches. Bounds are placed on $\mathbf{K}_s\mathbf{S}$ according to

$$\begin{aligned} &||\mathbf{K}_s(j\omega)\mathbf{S}(j\omega)|| \leq (||\mathbf{W}_{\Delta I_s}(j\omega)||)^{-1} \\ &\implies ||\mathbf{W}_{\Delta I_s}\mathbf{K}_s\mathbf{S}||_\infty \leq \mathbf{I} \end{aligned}. \tag{3.9}$$

The magnitude of the weights in $\mathbf{W}_{\Delta I_s}$ are then chosen based on the maximum available control effort. Whereas, the frequency is chosen to be below the bandwidth of the inner loop of each converter and the highest frequency component of the disturbance. In general, the weights are high pass filters that ensure components of frequencies higher than the bandwidth of the inner loop are minimized.

3. Model Reduction: Model reduction is a prerequisite to a successful design and simplicity, particularly if low order controllers are desired. Additionally, model reduction keeps the problem as tractable as possible by preventing numerical artifacts. Therefore, model reduction is sort for the key transfer function and synthesized controllers if desired. Several established methods are available in literature for model reduction. The Hankel balanced reduction method is adopted in this thesis [115].

3.4 Supplementary Control Design Examples

In previous chapter, the input-output stability of the HVDC grid was formulated as a collection of impedance-ratio functions in (2.81), rewritten as

$$\Delta V_{dci} = Z_{oc,i}(s)\frac{1}{1+L_i(s)}\Delta I_i; \quad L_i(s) = \frac{Z_{oc,i}(s)}{Z_{net,i}(s)}. \tag{3.10}$$

It was remarked that manipulating the behaviour of the DC grid is equivalent to manipulating $L_i(s)$ from each controllable terminal. Since $Z_{oc,i}(s)$

is based on existing control, $Z_{net,i}(s)$ becomes the tractable component. Supplementary controllers may then force $Z_{net,i}(s)$ to approach two possible limiting values; $Z_{net,i} \to 0$ or $Z_{net,i} \to \infty$. As would be shown in the following, the former is an impedance minimization problem, and the latter is an impedance matching problem. From the perspective of the $\mathcal{H}_\infty$ framework, the difference in both lies in the choice of weighting functions.

For $Z_{net,i} \to 0$,

$$\begin{aligned} & L_i(s) \to \infty \\ \implies & \Delta V_{dci} \to 0 \end{aligned}. \tag{3.11}$$

The above may apply to a case where the local response based on $Z_{oc,i}(s)$ is not acceptable (but strictly stable) or it is desired to share or transfer some responsibility to the global supplementary controllers. In which case, the supplementary controllers are simply required to minimize ΔV_{dci} as small as possible.

For $Z_{net,i} \to \infty$,

$$\begin{aligned} & L_i(s) \to 0 \\ \implies & \Delta V_{dci} \to Z_{oc,i}(s)\Delta I_i \end{aligned}. \tag{3.12}$$

Hence, supplementary controllers force the global response after interconnection to mimic the local behaviour before interconnection. Such is the case when the local behaviour is acceptable and can be adopted as a reference for which the global response is made to match. The following examples explore each of these cases described depending on the problem.

3.4.1 Case 1: Three Terminal Grid in Mode 1 Based on MIMO Global Impedance

This section designs decentralized supplementary control for the three-terminal system in Fig. 3.1 (mode 1) with poorly designed local controllers as described in Figs. 2.28, 2.30, and 2.32. Therefore, it is desired to transfer some of the local responsibility to the global controllers following the methodology described in Section 3.3. Hence, the entire elements of $\mathbf{Z}_{dc}^{cl}$ are required for a successful design — that is, the MIMO impedance response. Fig. 3.20 shows the analytical step responses of the elements of the global impedance matrix highlighting the frequency components of the components. Fig. 3.21 shows the simulation step responses of the nonlinear physical system in Matlab Simulink®. It shows the magnitude is not necessarily a problem, but the interaction frequencies are poorly damped. Therefore the output weighting matrix should have a tighter bound to target the interested frequencies.

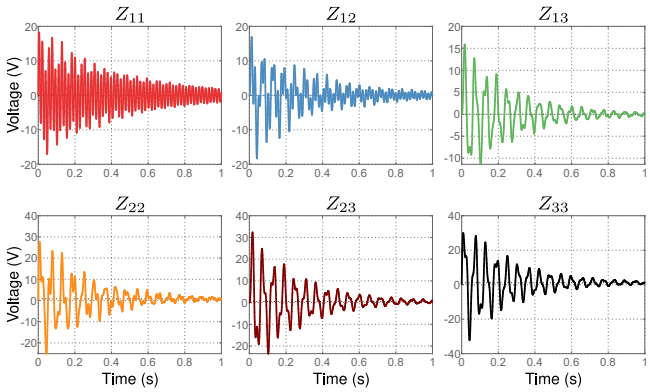

Figure 3.20: Analytical step responses of the distinct elements of the global closed-loop impedance matrix

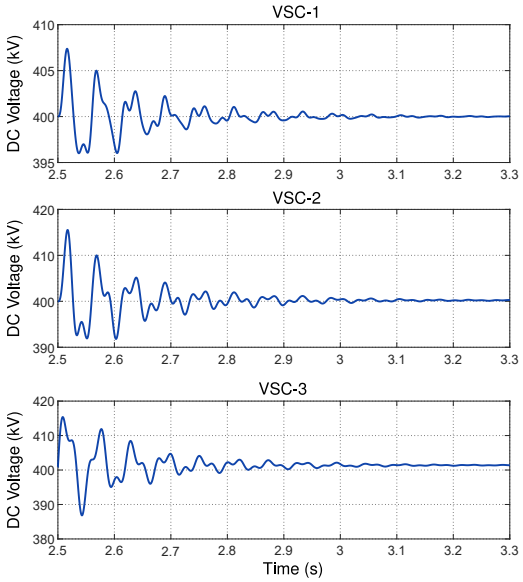

Figure 3.21: Nonlinear simulation of system responses for step change in power of 200MW from VSC-3 at 2.5s

Scaling

Following the block diagram of Fig. 3.19, $\mathbf{Z}_{dc}^{cl}$ is given as shown in Fig. 2.28 and $\mathbf{Z}_p = \alpha\mathbf{I}$. In this example, α is determined by iteration and to prevent the synthesis of a large gain controller. For each supplementary controller to be determined, $\alpha = [1 - 500]$ is adequate as this ensures the

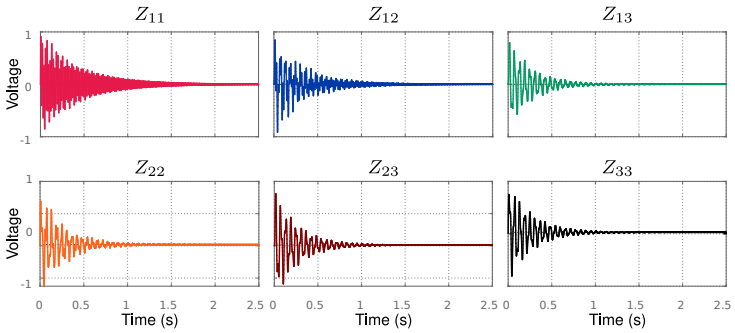

Figure 3.22: Scaled global impedance response

optimization problem is completely dominated by $\mathbf{Z}_{dc}^{cl}$. Subsequently, a similar scaling is applied at all converter locations for which supplementary control is desired. The scaling parameters are given in Table 3.1 and Fig. 3.22 shows the scaled global impedance response. Based on the choice of scaling, the magnitude is acceptable as it is within the maximum deviation (± 1) set for the maximum bus current changes expected. Hence, significant improvements are not expected in magnitude after controllers are synthesized.

Table 3.1: Scaling Factors

Parameter	Value	Comments
ΔV_{max}	20 kV	Maximum allowed voltage deviation
$\Delta I_{s,max}$	0.8 kA	Maximum allowed control input
ΔI_{max}	1 kA	Maximum expected bus current changes

Weighting Matrices

As previously stated, the weighting functions are selected to emphasize the desired control actions to the selected frequency response. Table 3.2 lists the components of each weighting matrix and Fig. 3.23 show the frequency responses of the output and control weights respectively. The output weight magnitudes can be increased as necessary to ensure that the poorly damped interaction peaks are inside the envelope.

Model Reduction

Model reduction is a prerequisite especially if low order controllers are desirable. Fig. 3.24 shows the contribution of the states to the dynamics

Table 3.2: Design Weights

	$W_{\Delta v}$	$W_{\Delta I_s}$	$f_{\Delta v}$ (Hz)	$f_{\Delta I_s}$ (Hz)
VSC-1	$0.5\frac{s+2\times 2\pi f_{\Delta v1}}{s+\frac{2\pi f_{\Delta v1}}{500}}$	$0.75\frac{s}{s+2\pi f_{\Delta I_{s1}}}$	65	90
VSC-2	$0.45\frac{s+2\times 2\pi f_{\Delta v2}}{s+\frac{2\pi f_{\Delta v2}}{450}}$	$0.65\frac{s+2}{s+2\pi f_{\Delta I_{s2}}}$	65	75
VSC-3	$0.45\frac{s+2\times 2\pi f_{\Delta v3}}{s+\frac{2\pi f_{\Delta v3}}{450}}$	$0.65\frac{s}{s+2\pi f_{\Delta I_{s3}}}$	65	60

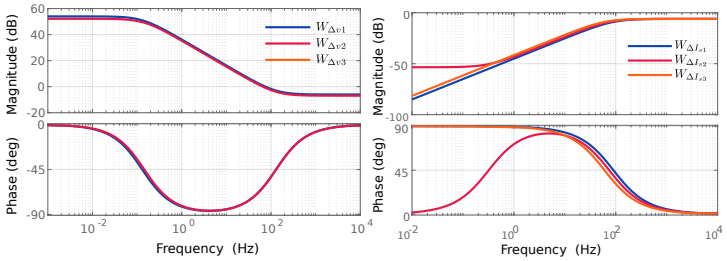

(a) Output weights (b) Control weights

Figure 3.23: Frequency responses of system weights

of the system through Hankel singular values. Based on the singular value plots, the model can be reduced from a total order of 35 to 7. Fig. 3.25 shows the response of the original and reduced system showing an accurate match without loss of dynamics.

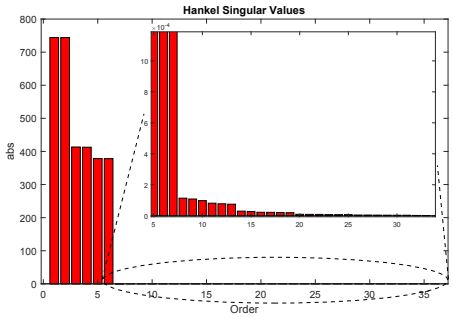

Figure 3.24: Hankel singular values of dominant states in the system

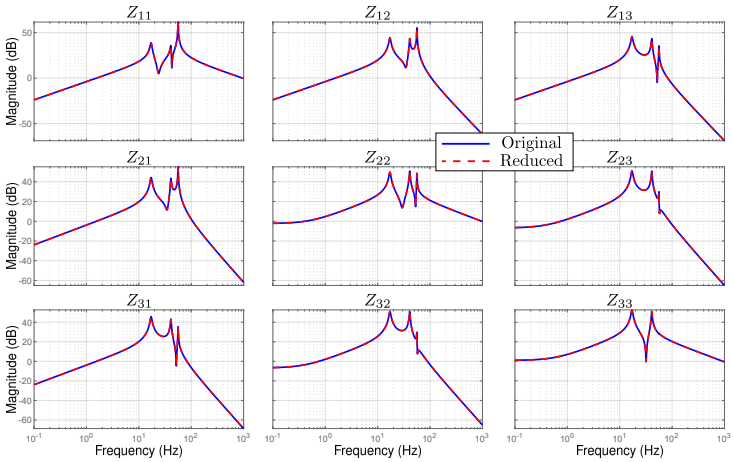

Figure 3.25: Frequency response of the original and reduced global impedance response

MIMO Control Design

Decentralized controllers of fixed orders are desired to demonstrate the possibility for low order controllers and to prevent issues related to communication requirements. The problem described by equation (3.6) is solved subject to a stabilizing controller such that the maximum peak of $\gamma \leq 1$. The `hinfstruct` algorithm in Matlab® is adopted with maximum order of controllers fixed to three.

The decentralized supplementary controllers take in voltage deviation as inputs at the instant of disturbances and output corresponding current signals to damp oscillations due to interactions. Hence, they are additional feedforward terms considering the interconnection. Fig. 3.26 shows the position of the synthesized controllers relative to the local controllers.

Fig. 3.27 shows the frequency responses of synthesized controllers with the algorithm returning $\gamma = 0.891$ as the peak gain achieved. This indicates that synthesized controllers meet the maximum bounds sets in the frequency domain. It is shown that the controllers are band-pass filters with the active region around the interaction frequencies as seen from each converter. As desired, the controllers are not active outside of the band of frequencies of the disturbances. Hence, this limits unintended interactions with the local controllers especially in the low-frequency region where local controllers are active.

Aforementioned previously, in practical cases it may be desired to implement supplementary controllers only at specific locations in the system. For instance, for the three-terminal case discussed in this example, it may

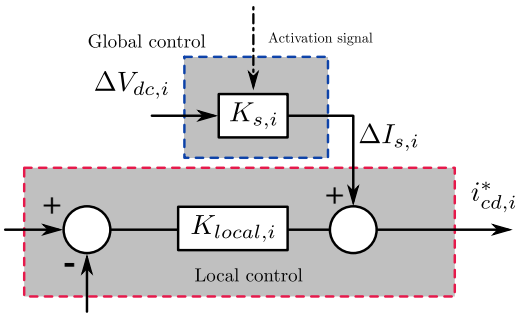

Figure 3.26: Block diagram of synthesized controllers relative to local control

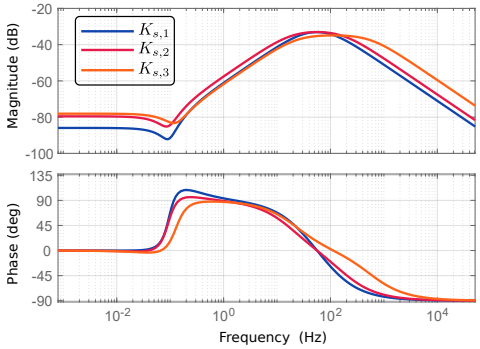

Figure 3.27: Frequency response of synthesized controllers

be desired to have supplementary controllers only in the connected AC grids. That is, the converter terminals that integrate alternative energy resources may not be deemed fit for supplementary actions. Hence, supplementary controllers designed are less than the number of converters. However, it may be desired to include some information about the entire grid including the terminal where control action is not required. This can be directly included in the formulation by simply setting the controller at that terminal to *zero* at the expense of slightly degraded performance. That is, in the framework shown in Fig. 3.19, the supplementary controller not required is set to 0 in the $\mathbf{K}_s(s)$ matrix. However, the grid information as seen from that terminal where additional control is not possible is included in the $\mathbf{Z}^{cl}_{dc}(s)$ matrix.

Fig. 3.28 shows the frequency response for two supplementary controllers at VSC-1 and VSC-2. As can be observed, the magnitude of response is nearly a decade higher than those of Fig. 3.27 to compensate for the lack of supplementary action at terminal 3.

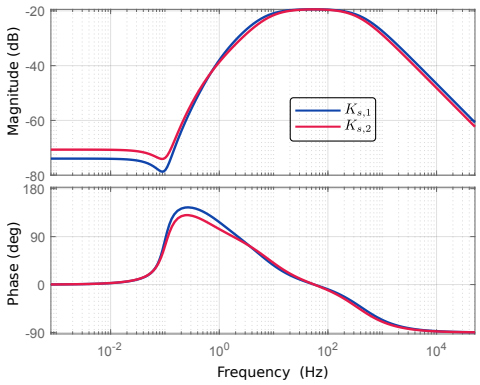

Figure 3.28: Frequency response for two synthesized controller

Modified Frequency and Interaction Responses

After the implementation of the high-level supplementary controllers to decouple the system, Fig. 3.29 shows the comparison of the SISO response with and without supplementary control (compared with Fig. 2.28). The elimination of detrimental interactions and the shaping effect of the global supplementary controllers can be immediately seen. The new responses are considerably improved over the responses without supplementary control.

The MIMO characterization of the modified system with supplementary control compared to the existing system is shown in Fig. 3.30. The peaks of the maximum singular value have been reduced, and the minimum singular has been significantly reduced compared to without supplementary action. This indicates an overall improved behaviour of the system. To establish the new interaction behaviour as indicated by the RGA response, Fig. 3.31 shows the frequency-dependent RGA for the case with supplementary control. Compared to the existing control in Fig. 2.32 with clear interactions at three frequencies (indicated by the gain $\gg 1$), the modified system is almost interaction-free. The residual interaction around 10Hz between VSC-2 and VSC-3 is however negligible compared. Outside of this frequency, the diagonal elements approach 1 and the off-diagonal elements approach 0, indicating an interaction-free system.

Time Domain Simulations and Verification of Performance

Several nonlinear detailed time-domain simulations scenarios have been carried out to demonstrate the performance of the supplementary controllers. For a change in power injected into the DC grid by the offshore resource at VSC-3 for the base case, Fig. 3.32 shows the time-domain simulation in Matlab Simulink® of synthesized controllers and compari-

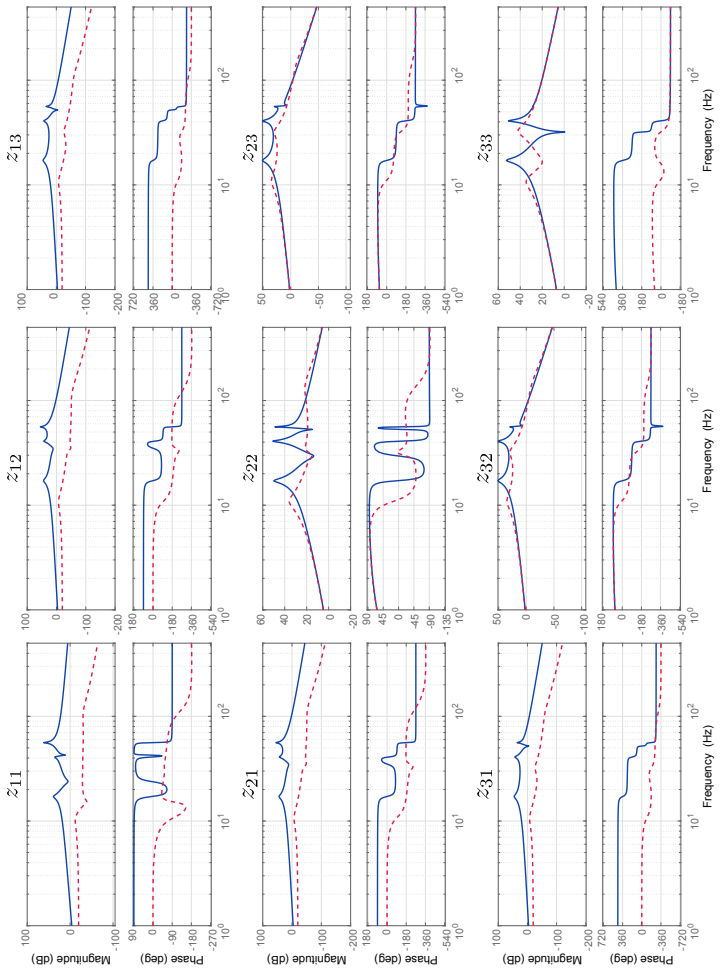

Figure 3.29: SISO frequency responses with and without supplementary control

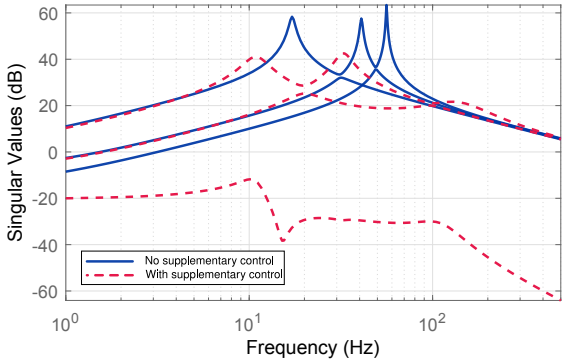

Figure 3.30: SVD MIMO frequency response with and without supplementary control

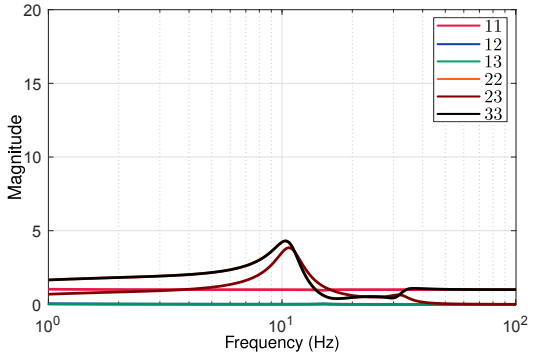

Figure 3.31: Frequency dependent relative gain array with supplementary control

son existing case showing significant improvements. The controllers were able to quickly decouple the system as seen from each terminal and damp out the interaction oscillations within the expected time frame. For the case where only two controllers are designed, Fig. 3.33 shows the comparison between three and two designed controllers. As expected, there is a slight degradation in performance, particularly at VSC-3 compared to three controllers. However, the performance is tolerable and significantly better than without supplementary control. Fig. 3.34 shows the control effort of the designed controllers indicated by the output current to damp oscillations in voltages. As can be seen, controllers only act during disturbances and their outputs in steady-state are negligible.

To further demonstrate the robustness of synthesized controllers (two decentralized) in a more stringent scenario, Fig. 3.35 depicts the time

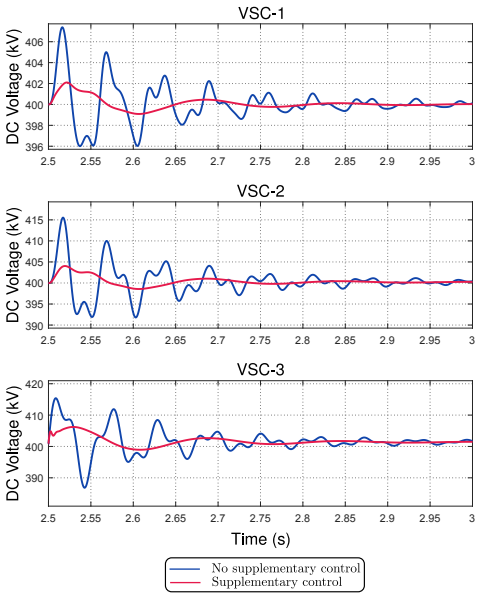

Figure 3.32: Time domain validation and comparison of performance of supplementary control

response comparison to persistent step changes from the offshore resource between two controllers and without any additional controller. Observe that in the case with only local control, the system lost stability when there was a sudden loss of a significant amount of power. Furthermore, the identified limits of $380 - 420$kV were breached. Whereas, with two supplementary controllers at VSC-1 and VSC-2, the system maintained robust stability and performance. Significant improvements can be seen in both frequency content and magnitude. As expected at the offshore resource, the lack of a supplementary location led to a breach of limit. However, the performance is quite better and acceptable despite the lack of additional control actions.

3.4.2 Case 2: Four Terminal Grid in Mode 2 Based on SISO Equivalent of Global Impedance

In a more realistic case of a multi-vendor converter system, vendors of these devices are often held to standards [58, 139]. That is, at the local level before connecting to any grid, a converter is designed to behave optimally and predictably across the expected operating range. Therefore, this pre-connection guarantee can be exploited as a reference to design network-wide supplementary controllers with the methodology outlined.

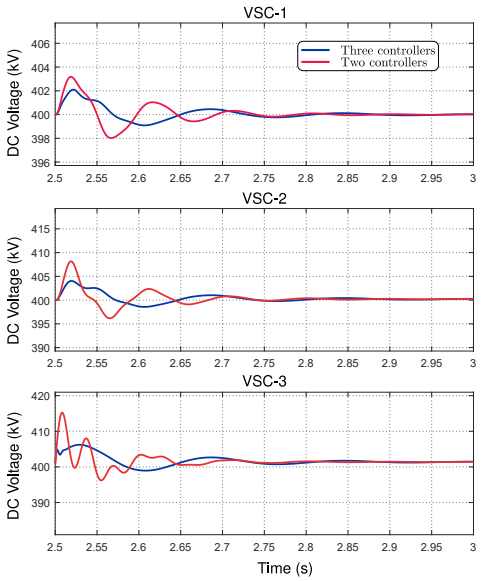

Figure 3.33: Time domain validation for two designed supplementary controllers

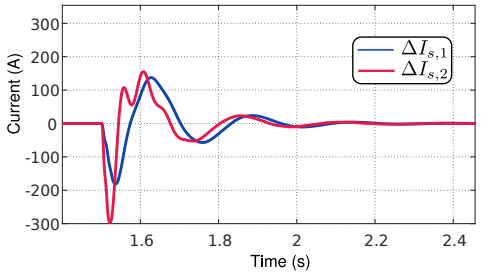

Figure 3.34: Output of controllers during disturbance

This example differs from the previous in that local controllers are properly designed and have an acceptable response before connection to the grid. As a result, the control design stage is remarkably simplified with the potential for significant flexibility. In contrast, a four-terminal HVDC grid shown in Fig. 3.36 is adopted. The grid is an extension of two initial HVDC links with one offshore resource at VSC-3 in constant power mode and others interconnecting conventional AC grids in droop control mode. Initially, VSC-2 and VSC-3 are injecting power into the grid, whereas, VSC-1 and VSC-4 are extracting power from the grid.

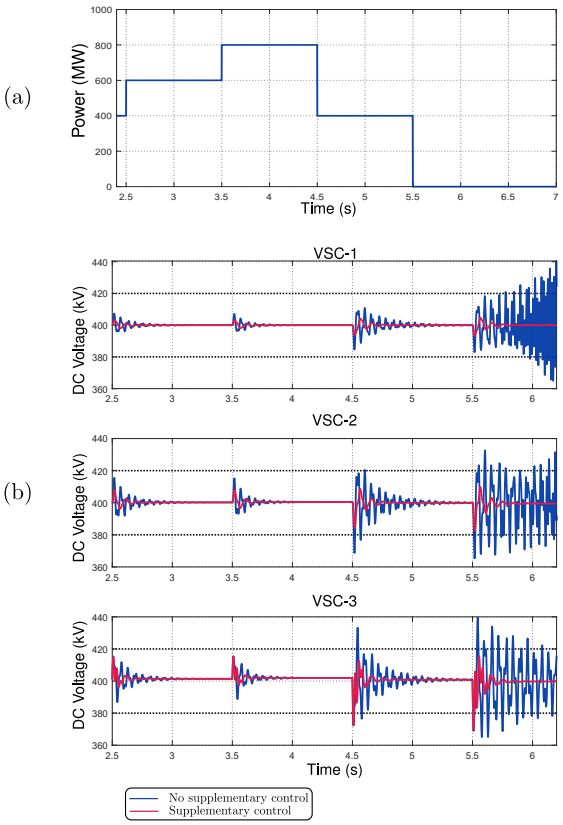

Figure 3.35: (a) step disturbances at subsystem 3 (b) time-domain response of system

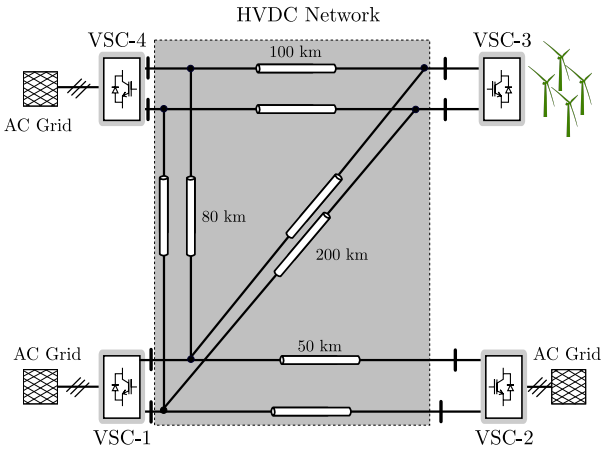

Figure 3.36: Four terminal droop controlled HVDC Grid

Simplified Design of Converter Controllers Pre-connection

Due to different experiences of each converter designer, the active power loops of VSCs-1, 2, 4 are designed with first-order responses of 15ms, 4ms, and 30ms respectively. However, the inner loop is assumed standardized across all converters with a time response of 1ms. Note, however, that these response times are arbitrary and may differ from real implementations.

The impacts of droop control are more visible at the global level rather than at the local level. Hence, the appropriate droop gains before connection that meet specific system-level requirements (such as a power-sharing formula) may not be known ahead of time during the independent design phases of each converter. However, a converter designed to provide droop response should meet minimum requirements set by the owner of the converter (e.g. a network operator). Such requirements can be transformed into frequency domain requirements based on the impedance framework described in this thesis. Given a maximum expected voltage deviation ΔV^{max} p.u. of each converter from rated voltage following droop response, and the maximum expected bus current change ΔI p.u. of rated DC current, the bounded frequency domain requirement can be computed from the DC side impedance model as derived in equations (2.43) and (2.52) as [128]

$$Z_{oc,i}^{max} = 20 \log_{10} \left(\frac{\Delta V_i^{max} \times V_{rat}}{\Delta I_i \times I_{rat,i}} \right) \text{dB} \tag{3.13}$$

where $Z_{oc,i}^{max}$ is the maximum allowed impedance response magnitude imposed by droop control, ΔV_i^{max} is the maximum allowed voltage deviation

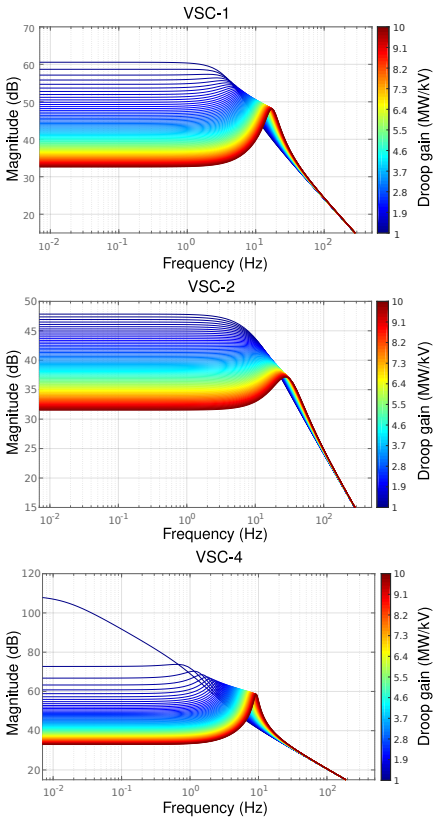

Figure 3.37: Converter specific terminal impedance response at an operating point for varying droop gains

in p.u. at the i^{th} VSC, V_{rat} is the rated direct-voltage of the grid, ΔI_i is the maximum expected bus DC current change in p.u., $I_{rat,i}$ is the rated DC current of the i^{th} VSC.

As an example, for a maximum allowed voltage deviation of 0.15p.u. and maximum expected change in DC bus current of $\Delta I = 0.25$p.u. at each VSC (equivalent to the contribution of 25% of rated power to droop response) from rated direct-voltage of 400kV and rated current of 2kA, the maximum bound can be calculated as

$$Z_{oc}^{max} = 20\log_{10}\left(\frac{0.15 \times 400}{0.25 \times 2}\right)\text{dB} \approx 42\text{dB} \tag{3.14}$$

thus, a bound of $\approx$ 42dB is established in the frequency domain as the maximum allowed steady-state impedance; the droop gains that meet this bound are selected. Due to the inherent differences in the first-order re-

Table 3.3: Droop Gains

Vendor	Droop gain (MW/kV)
1	4.12
2	3.38
4	4.86

sponses of each converter, the droop gains that meet the bounded frequency response will differ as well. To determine the required droop gain at each converter that meets the bounded frequency requirement, Fig. 3.37 shows the frequency response of the equivalent input-output impedance of each VSC to sensitivity in droop gains from $1 - 10$MW/kV. In general, for all converters, increasing droop response reduces the steady-state gain below 1Hz where droop response is most active. Additionally, for VSCs 1 and 3 where the active power responses are orders slower than VSC-2, increasing the droop gain also isolates low-frequency resonances that may be aggravated after interconnection despite the reduction in steady-state gain. Therefore, the droop gain should not be unnecessarily high to prevent resonances, or too low to avoid breaching steady-state limits. Given this sensitivity analysis, VSC-2 is expected to have the lowest droop gain and negligible oscillatory response for the same bounds compared to VSC-1 and VSC-4; on the other hand, VSC-4 is expected to have the highest gain and the most oscillatory response before interconnection. The approximate droop gains of each vendor equipped with droop control that meets the defined bound are presented in Table 3.3.

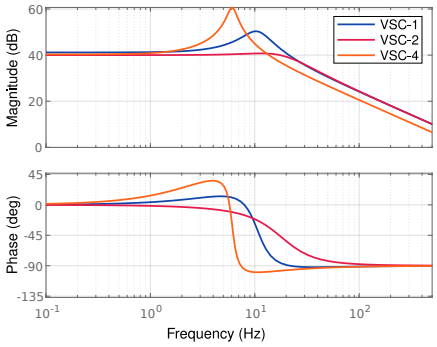

Figure 3.38: Converter specific impedance response corresponding to selected droop gains

It is worth to remark that in a real system, different physical bounds

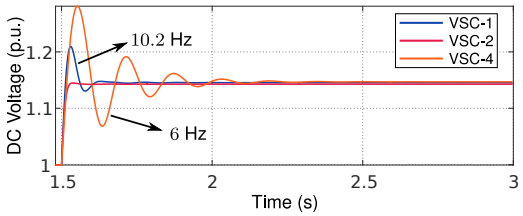

Figure 3.39: Converter specific nonlinear time response of local behaviour to terminal changes

may be set on each converter as seen at the network-level. Moreover, actual deviation margins will be lower than that obtained at the local level after interconnection depending on network resistances, and interaction with other droop gains. To verify that the selected droop gain satisfies the requirements pre-connection, Fig. 3.38 shows the impedance response of each converter corresponding to the droop gains that meet the requirements. These are the equivalent DC impedance models of each converter before connection and can be supplied as is by a manufacturer or obtained from the time-domain simulation of black-box models. Fig. 3.39 shows the nonlinear time-domain responses to a step change of 200MW ($\approx 25\%$ of rating) at the terminals of each converter obtained as shown in Fig. 3.40. As can be observed, all steady-state deviations meet the bounded requirement of 1.15p.u. maximum of direct-voltage. Furthermore, the observed resonances match the expected local behaviour as seen from Fig. 3.38. Specifically, VSC-4 has the most oscillatory behaviour, whereas, VSC-2 presents the least. The oscillatory behaviour is not necessarily of concern at the local level as actual oscillatory frequencies may shift on interconnection, and the role of the global level controller is to mitigate these.

To summarize, these responses are in general acceptable. However, local oscillatory behaviour as seen from frequency responses may encourage a manufacturer to retune locally before interconnection.

Interconnection of Converters and Global Response Models

Following the interconnection of each converter impedance response model and the network, Fig. 3.41 shows the global MIMO response based on SVD. The MIMO response indicates bound satisfaction of the global system such that for any violation of the bounds, additional control actions are required to 'push down' the peaks. Four interaction frequencies can be identified; a well-damped mode around 10Hz, slightly damped mode around 33Hz, and poorly damped modes at 44.2Hz and 73Hz confirmed

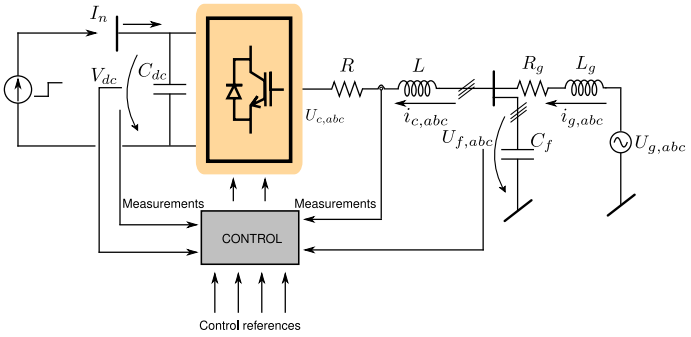

Figure 3.40: Schematic circuit for terminal response behaviour

by the SVD response. Hence, there is a need for supplementary controllers to mitigate these interactions. Therefore, further analysis with the RGA is required to determine how these converters are interacting and to provide information on how controllers should be coordinated.

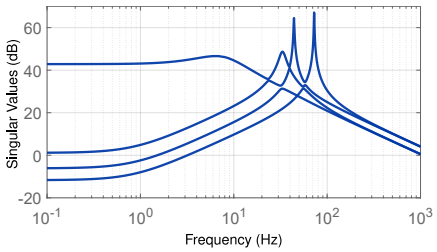

Figure 3.41: MIMO SVD response of interconnected system as a single-entity

Interaction Analysis

The frequency-dependent RGA magnitude plot of $\mathbf{Z}_{cl}(s)$ is illustrated in Fig. 3.42. The interaction pairing of vendors and their contributions to each identified interaction frequency is clearly shown. Interaction at a frequency is indicated by peaks in corresponding diagonal and off-diagonal elements.

In this case, all terminals are strongly interacting in steady-state with VSC-1 expected to have the highest steady-state deviation margin followed by VSC-4, 2, and 3 respectively. This is an expected effect of droop control and further analysis using the RGA may be adopted to improve the steady-state droop response. In the oscillatory region and at the first fairly damped 33Hz resonance, VSC-1 and VSC-2 are interacting. At

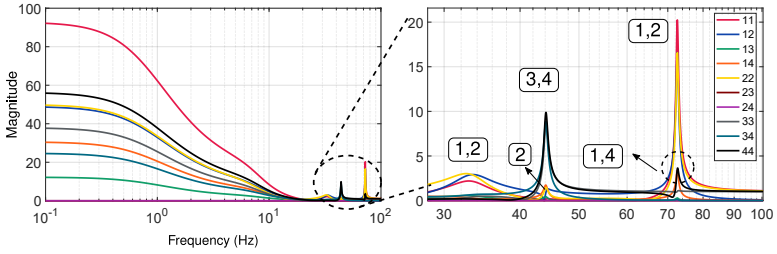

Figure 3.42: Frequency dependent relative gain array for interaction detection

44.2Hz VSC-3 and VSC-4 are the main contributors to this interaction frequency, whereas, VSC-1 and VSC-2 are significantly contributing to the resonance at 73Hz. It can be observed that VSC-1 is the highest contributor to oscillatory behaviour in the system, and small disturbances at that terminal may aggravate the system response. However, in a realistic system, constant disturbances will be mainly expected from VSC-3 where an intermittent power resource is connected. Therefore, on this basis, the main frequency component of oscillations in the system will be around 44.2Hz. For changes at VSC-1, all three frequency components may be observed. To summarize, the RGA plot indicates the best way to coordinate designed supplementary controllers by pairing up terminals. Therefore, for the described case, two supplementary controllers 'overlooking' the network from the location of VSC-1 and VSC-4 (if VSC-3 is not deemed fit for supplementary action) are sufficient to decouple the system and mitigate the impact of interactions.

The direct-voltage responses for a change in power injected into the DC grid from the offshore resource at VSC-3 is shown in Fig. 3.43. It can be observed that the frequencies of oscillations match with one or more of those identified in Fig. 3.41. As predicted by the RGA, for disturbances at VSC-3, the dominant frequency is 44.2Hz. This is the case particularly for the responses at VSC-2 and VSC-3, and VSC-4 where 44.2Hz is dominant (with lower magnitude at VSC-2). At VSC-1 the responses are more distorted as a result of VSC-1 contributing to multiple frequencies in the system. Notwithstanding, the dominant mode remains at 44.2Hz with a lower magnitude compared to VSC-3 and VSC-4. For a different source of disturbance, Fig. 3.44 shows the time-domain responses for step disturbance at VSC-1. As previously remarked, the dominant frequency predicted from the RGA plots for disturbances at VSC-1 is 73Hz with VSC-2 interacting strongly with VSC-1. This is can be observed from the voltage responses as the dominant frequency is 73Hz. Additionally, it confirms the interaction between VSC-1 and VSC-2 as the major contrib-

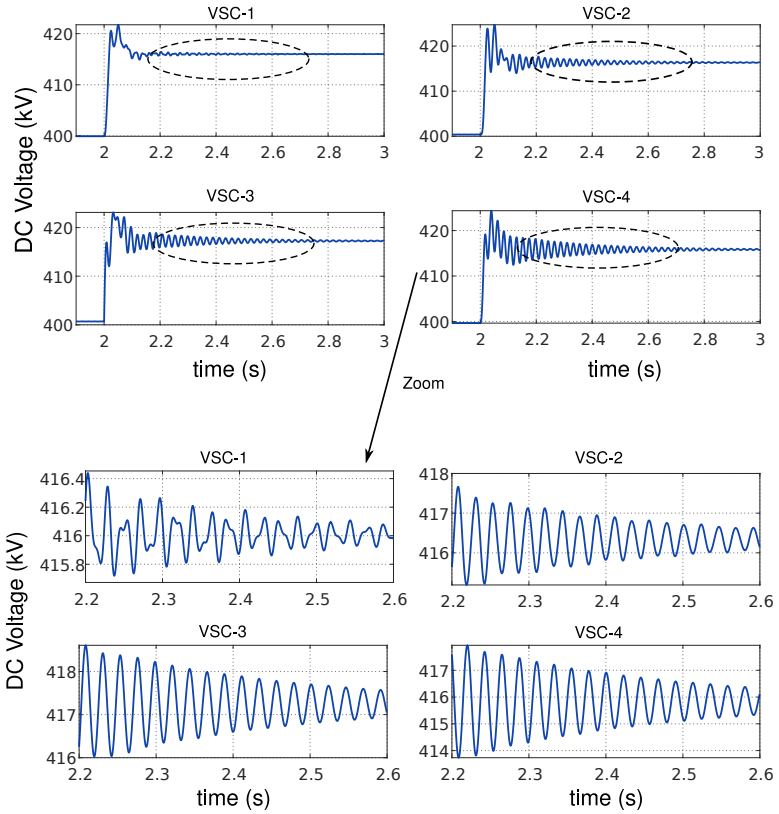

Figure 3.43: Direct-voltage responses for a step disturbance at VSC-3

utors, with VSC-4 only slightly at this frequency as indicated by the RGA plots.

Fig. 3.45 shows the time responses for simultaneous disturbances at VSCs 1 and 3. It shows that at VSC-3 and VSC-4, the dominant frequency is at 44.2Hz as previously highlighted. At VSC-1, both the 44.2Hz and the 73Hz components are present with the 73Hz component more dominant also as predicted by the RGA plot, whereas at VSC-2 multiple frequency components are present, with the 73Hz more dominant.

Decomposition of MIMO Problem to N SISO Problems

It was highlighted at the converter design phase that the local impedance model of the VSC is acceptable. Given this guarantee, the global supplementary controllers may be designed specifically to force the global impedance responses at specified VSC locations to mimic the local impedance

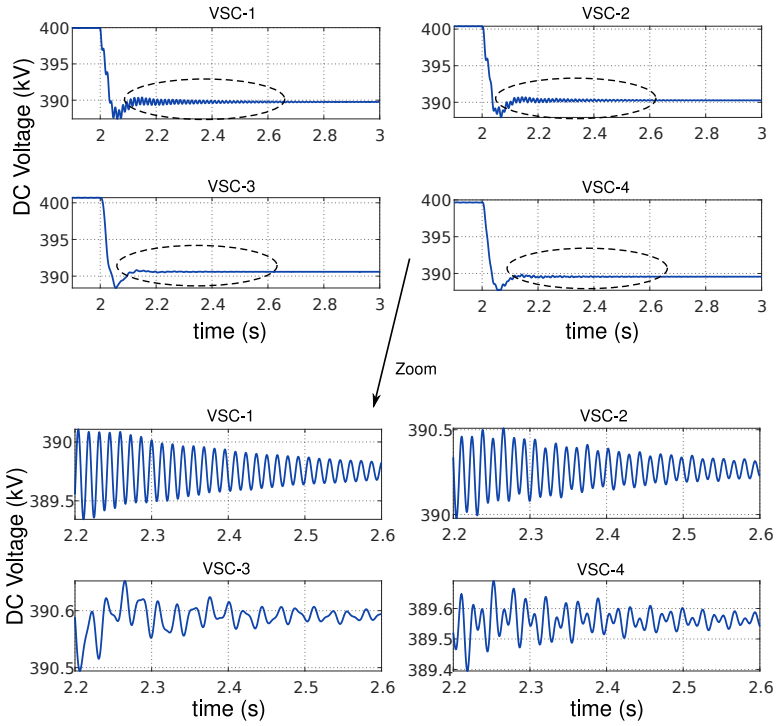

Figure 3.44: Direct-voltage responses for a step disturbance at vendor VSC-1

response that those locations. Hence, the global impedance response after supplementary design should at least approximate or better the pre-connection impedance model of each converter. Therefore, the full elements of the global impedance response are not required as the reference impedance model for each converter are SISO equivalents. Decomposing the global MIMO problem into equivalent SISO problems involves splitting the $\mathbf{Z}_{dc}^{cl}(s)$ matrix into local response based on $Z_{oc,i}$ (Fig. 3.38) and transferred response from the rest of the network $Z_{net,i}(s)$ as seen from the i^{th} terminal based on equation (2.73). Extending from the point-to-point HVDC link shown in Fig. 2.33 to an arbitrary system, the global impedance response Z_{ii} of terminal i can be derived as

$$Z_{ii}(s) = \frac{Z_{oc,i}(s)Z_{net,i}(s)}{Z_{oc,i}(s) + Z_{net,i}(s)} \tag{3.15}$$

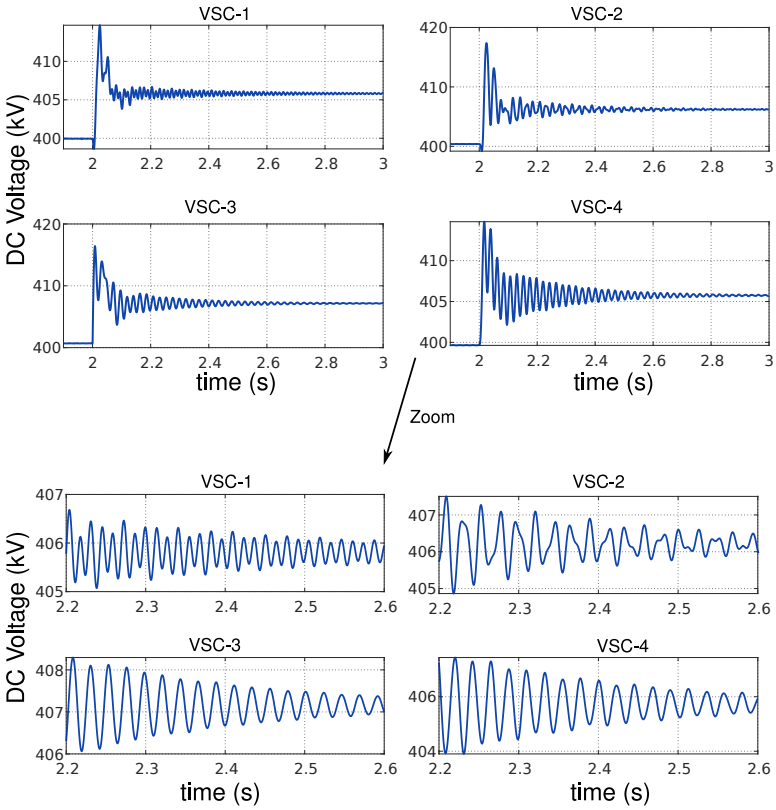

Figure 3.45: Direct-voltage responses for simultaneous disturbances at VSC-1 and VSC-3

where $Z_{net,i}(s)$ is the rest of the network as seen from terminal i. Therefore, at any terminal

$$Z_{net,i} = \frac{Z_{ii}(s)Z_{oc,i}(s)}{Z_{oc,i}(s) - Z_{ii}(s)}. \tag{3.16}$$

Since the local impedance model $Z_{oc,i}(s)$ is acceptable, then it is desired that the rest of the network as seen from that terminal $Z_{net,i} \to \infty$. If this strictly holds, then the global impedance as seen from each terminal simply reverts to the impedance model pre-connection which is agreed as acceptable as expressed in (3.12). Therefore, robust stability and performance is guaranteed from (3.16) if, $Z_{ii}(s) = Z_{oc,i}(s)$. As it is seen, the entire problem reduces to an impedance matching problem. Subsequently, supplementary controllers are adopted to shape $Z_{ii}(s)$ into $Z_{oc,i}(s)$ at the corresponding locations through the sensitivity of controllers $S_{ii}(s)$ to be

obtained such that

$$\begin{aligned} S_{ii}(s)Z_{ii}(s) &= Z_{oc,i}(s) \\ \implies S_{ii}(s) &\approx \frac{Z_{oc,i}(s)}{Z_{ii}(s)} \end{aligned} \tag{3.17}$$

where $S_{ii}(s)$ is the target sensitivity transfer function of the controllers to be obtained. If only m supplementary controllers are required, only the corresponding diagonal elements are required from the $\mathbf{Z}_{dc}^{cl}(s)$ matrix. Therefore in the framework shown in Fig. 3.19, all transfer matrices are now reduced to corresponding SISO transfer functions. Hence, the optimization problem can be solved independently for each supplementary controller required. This is in contrast to the previous example where $\mathbf{Z}_{dc}^{cl}(s)$ is not diagonal and here the selection of system output weighting matrix is significantly simplified since there is a target sensitivity for each controller required.

Next, the control synthesis problem can be formulated as all related information are available. For the case discussed, only two supplementary controllers are required. However, due to the fully decentralized SISO structure, three controllers can be designed and any activated as required.

Scaling for Control Synthesis

The bounds established in previous discussion $\Delta V_d^{max} = 0.15$ p.u., and $\Delta I = 0.25$ p.u. directly determine the limits within which supplementary controllers can act. In addition to these bounds, the maximum allowed control effort for each supplementary controller to match global impedance response with local response must be determined. For this design example, the control effort is chosen based on insight from the RGA analysis, and the maximum control effort, defined in terms of current, are $\Delta I_{s1,max} = 0.3$, $\Delta I_{s2,max} = 0.3$, and $\Delta I_{s4,max} = 0.2$p.u., for each supplementary control respectively. Each of these parameters could be chosen to reflect the desired response from each terminal distinctly or depending on operational parameters. Therefore, the three parameters are adopted to scale the system according to (3.7). Fig. 3.46 shows the scaled nominal system in time-domain. As in the previous case, this is not a magnitude problem, but that of frequency components.

Weight Selection

The most important phase of the control design through $\mathcal{H}_\infty$ is the selection of system output weighting matrix, $\mathbf{W}_{\Delta v}(s)$ which is already simplified. Standard weights can be selected for $\mathbf{W}_{\Delta I_s}(s)$ if the maximum allowed control bandwidth is known. This is important to prevent interactions, especially with the inner loop. On the other hand, selection of $\mathbf{W}_{\Delta v}(s)$ is significantly simplified through equation (3.17) since Z_{ii} and

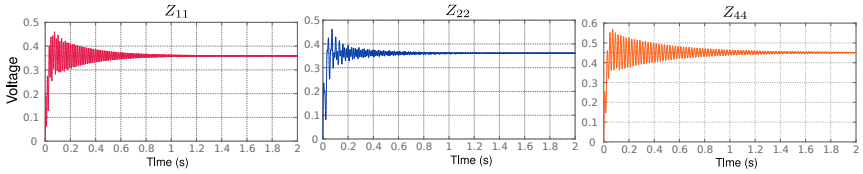

Figure 3.46: Scaled nominal system at each converter location at nominal power

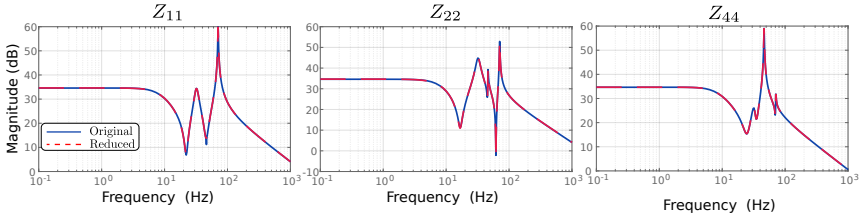

Figure 3.47: Frequency response of original models and reduced impedance models

$Z_{oc,i}$ are known. Each weighting function in the matrix $\mathbf{W}_{\Delta v}(s)$ is simply chosen based on the approximate target sensitivity function $S_{ii}(s)$, with room for flexibility on the order of weights relative to desired complexity. The weighting functions for each controller to be determined are shown in Table 3.4.

Table 3.4: Weighting transfer functions

Location	w_{Δ_v}	$w_{\Delta I_s}$
1	$\frac{1131s}{s^2+1.885s+0.03553}$	$\frac{0.5s}{s+2\pi f_1}$; $f_1 = 70$Hz
2	$\frac{741s}{s^2+1.662s+0.02763}$	$\frac{0.5s}{s+2\pi f_2}$; $f_2 = 70$Hz
4	$\frac{944.5s}{s^2+1.885s+0.03553}$	$\frac{0.5s}{s+2\pi f_4}$; $f_4 = 70$Hz

Model Reduction

The impedance response at each location is reduced similarly to the previous case using the Hankel norm. Figs. 3.47 and 3.48 shows a comparison plot of original models and reduced models, and the Hankel norm plots showing the contribution of states. Table 3.5 shows the initial model order and reduced order.

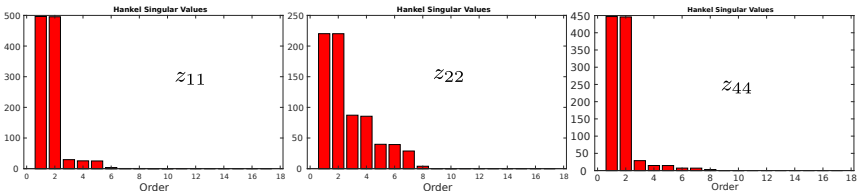

Figure 3.48: Hankel singular values of dominant states in the system

Table 3.5: Model reduction order

Vendor	Initial order	Reduced order
1	18	6
2	18	8
4	18	8

Control Design

The optimization problem of (3.6) is solved for each supplementary controller to be synthesized subject to constraints and fixed controller order of three. For each synthesized controller at each location — VSCs 1, 2, and 4, the realized γ are given as $0.472, 0.209, 0.618$ respectively. Hence, the bounds are satisfied for the nominal model and one hundred random power flows as a family of models.

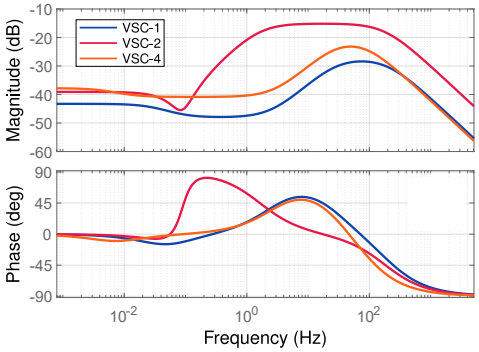

Figure 3.49: Decentralized supplementary controllers at corresponding vendor locations

The frequency response of each controller at the corresponding locations are shown in Fig. 3.49. It can be seen that the controllers are bandpass filters and it is worth to note that they do not impact in steady-state. The

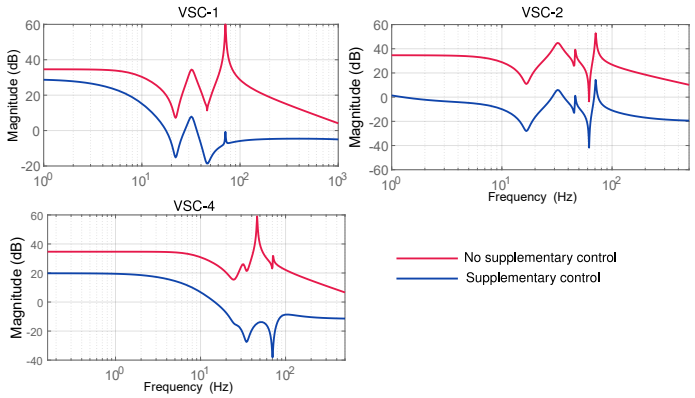

Figure 3.50: Reshaped global impedances at each supplementary control terminal

supplementary controller at VSC-1 peaks at 73Hz around the same region as the dominant frequency identified in Fig. 3.16 for VSC-1. Whereas, the supplementary control at VSC-4 peaks at 44Hz similar to its dominant frequency identified in Fig. 3.42. The supplementary controller at VSC-2 covers the entire region from $30 - 100$Hz. This is the result of the global response at VSC-2 having two peaks around 33 and 70Hz and the low order approximation of target sensitivity. An ideal controller VSC-2 should have a low peak at the first interaction frequency and a higher peak at the second interaction frequency. However, this will result in a higher-order controller at VSC-2 which is unnecessary. Thus, it is not recommended to have a supplementary controller at VSC-2 to prevent large control effort and since the dominant frequency at VSC-2 is covered by the controller at VSC-1.

Modified Frequency and Interaction Responses

To verify any improvements over the terminal global responses shown in Fig. 3.47, the reshaped global impedances before and after supplementary control are illustrated in Fig. 3.50. As can be seen, the original peaks in the global responses have been damped out significantly. This equates to a significantly lower ΔV_{dci} at each terminal where supplementary control is located. Additionally, the synthesized controllers were able to closely approximate the local impedances at VSC-1 and VSC-4 and improve on the local responses. However, at VSC-2 the approximation was poor as expected from the preceding discussion. Notwithstanding, this is not an issue as the magnitude of oscillatory frequencies has been significantly reduced and the dominant frequency at VSC-2 is dealt with by VSC-1.

Similarly, Fig. 3.51 shows the MIMO response of the system with and without supplementary control (with all three controllers online). Interestingly, in the event all three controllers are activated, it is seen that all singular values of the system are well-below the previously established maximum of 42dB. This indicates an improved decoupling of interactions between converters as established by the modified RGA plot in Fig. 3.52. Compared to Fig. 3.42, it is can be observed in the dynamic interaction region that all diagonal elements approach 1 and all off-diagonal elements approach 0. This indicates a complete decoupling of interactions in the system (excluding the expected interaction below 1Hz attributed to droop) and the efficacy of global controllers in decoupling the system.

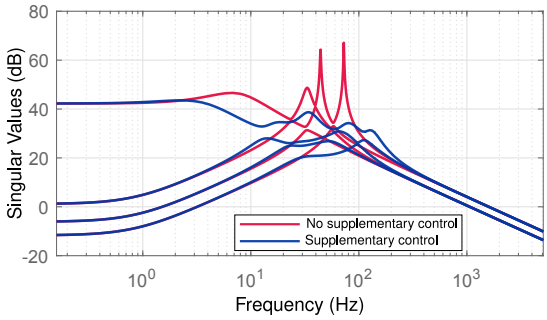

Figure 3.51: MIMO SVD responses with and without supplementary controllers

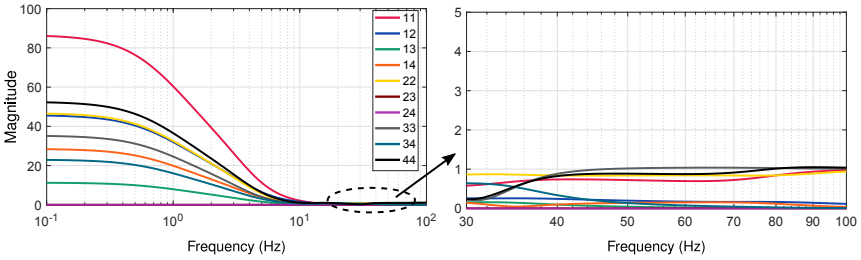

Figure 3.52: Modified RGA plot with all three supplementary controllers activated

Case Studies

Case studies are performed on the four-terminal to establish the efficacy of several combinations of supplementary controllers at different locations. The main goal is to establish any improvements in interaction induced

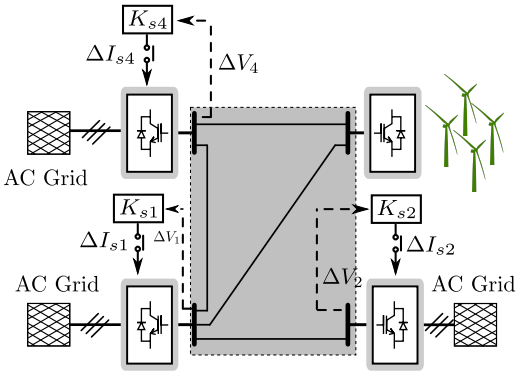

Figure 3.53: Location of supplementary controllers relative to the HVDC grid

responses of Figs. 3.43, 3.44, and 3.45. The locations of the supplementary controllers in relation to the entire grid are illustrated in Fig. 3.53.

Fig. 3.54 shows the time-domain simulation of the HVDC grid for simultaneous disturbances at VSC-1 and VSC-3 at 2s (step increase power extracted and injected respectively) with only one supplementary controller activated at VSC-1. To obtain insights into the responses shown, recall that for disturbances from terminals VSC-1 and VSC-3 the dominant interaction frequencies in the system are at 73Hz and 44.2Hz respectively. However, since the controller at VSC-1 was designed considering the dominant mode as seen from VSC-1 only the 73Hz component will be damped leaving the 44.2Hz component undamped. This can be seen from the time-domain simulation in Fig. 3.54 where there is only improvement in the responses is at VSC-1 whereas, at VSC-3 and VSC-4 there is no improvement as the dominant mode is at 44.2Hz. Additionally, the second dominant mode at VSC-1 at 44.2Hz due to a slight interaction with VSC-3 is left undamped for the same reasons discussed.

For another test case of a single supplementary controller located instead at VSC-4 Fig. 3.55 shows the responses for disturbance from offshore resource providing significant improvement. This is due to the supplementary controller designed to mitigate interactions between VSC-3 and VSC-4 and residual interactions with other terminals for disturbances from VSC-3. Moreover, for VSC-1 only the 44.2Hz component is eliminated; hence only partial improvements. Therefore, to cover all potential sources of disturbances in this system, at least two supplementary controllers are required particularly at VSC-1 and VSC-4, or VSC-1 or 2, and VSC-4.

To verify the hypothesis made in previously, two supplementary controllers at VSC-1 and VSC-4 are activated to cover all sources of distur-

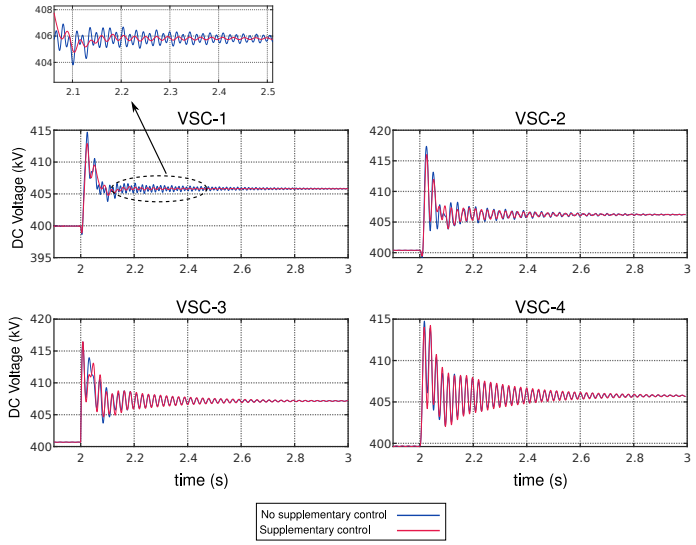

Figure 3.54: Network direct-voltage responses for supplementary controller located at vendor VSC-1 for simultaneous step disturbances at offshore resource and VSC-1

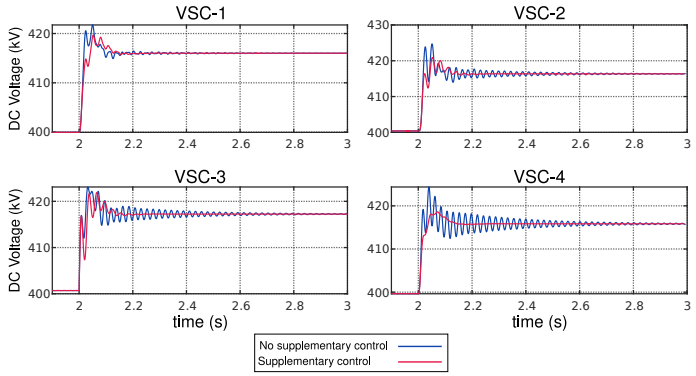

Figure 3.55: Network direct-voltage responses for supplementary controller located at VSC-4 for step disturbances at offshore resource

bances. The direct-voltage responses for simultaneous disturbances from VSC-1 and VSC-4 are shown in Fig. 3.56. The improvements over the case without any supplementary controllers are clear as the dominant interaction modes in the system have been damped out. Additionally, despite the lack of a supplementary controller at VSC-2 and the offshore

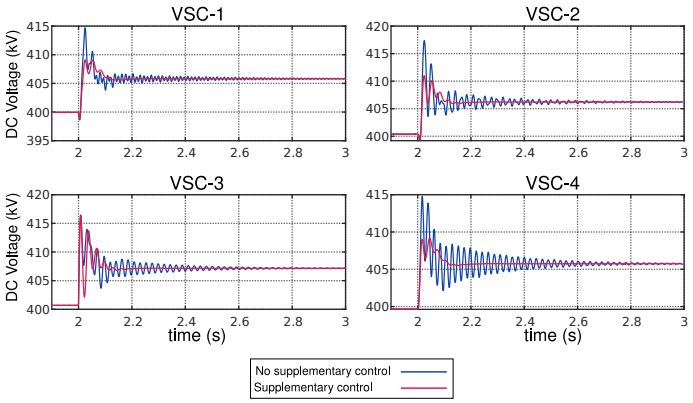

Figure 3.56: Network direct-voltage responses for two supplementary controllers located at VSC-1 and VSC-4 and simultaneous disturbances at offshore resource and VSC-1

resource at VSC-3, the response is much improved compared to without the supplementary controller. This demonstrates the influence of only two supplementary controllers in covering the entire range of potential interaction frequencies. Hence, any additional supplementary controller will simply be redundant with negligible effects. Fig. 3.57 shows the plot of direct-voltage responses for the same conditions explained, but all three supplementary controllers are activated. It can be seen that there is no significant improvement of the responses with two supplementary controllers activated and this verifies that only two supplementary controllers are indeed required. A third controller will result in unnecessary control effort without any improvements.

3.5 Recommendations on Impedance Models For Control Design

There are certain details required for a successful analysis and control design based on the impedance framework that is not immediately obvious. The following recommendations are proposed to allow easy adoption and overall verification.

1. Impedance models of devices, especially the VSC should be provided as a set of transfer functions rather than one transfer function. A set of transfer function consists of the impedance models at discrete steps of operating points across the entire range of operation. The impact of varying operating points on the DC impedance of the

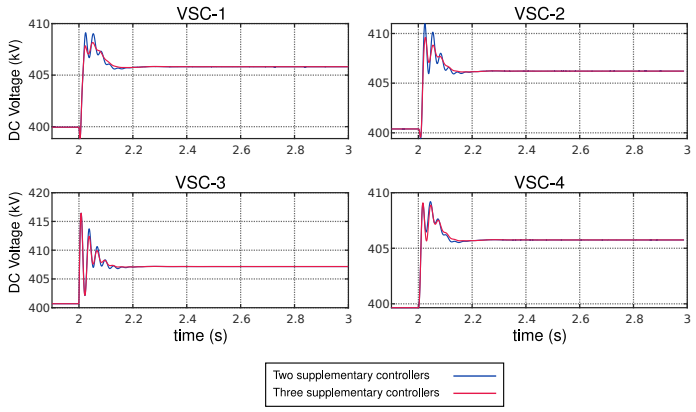

Figure 3.57: Network direct-voltage responses for three supplementary controllers as designed and simultaneous disturbances at offshore resource and VSC-1

direct-voltage controlled VSC rated at 800MW from inversion to rectification is shown in Fig. 3.58. The impacts of operating point do not appear significant at the device level for this control mode. The differences are highlighted on interconnection where arbitrary power flows are possible. Fig. 3.59 illustrates a similar plot for an active power controlled converter. Significant differences can be seen in the phase from inversion through to rectification. Hence, such a set of transfer functions should be provided.

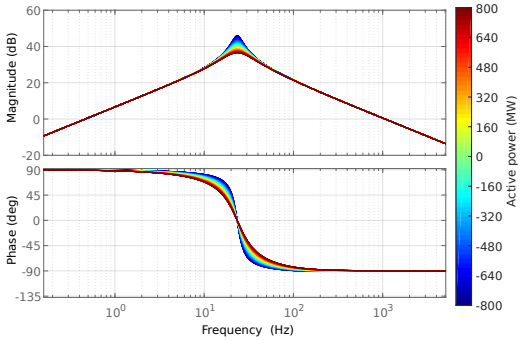

Figure 3.58: Sensitivity of DC impedance to varying active power operating points for a direct-voltage controlled VSC

The steps should be as low as 0.1 MW to ensure that when models are aggregated at the network-level, based on power flow, the correct

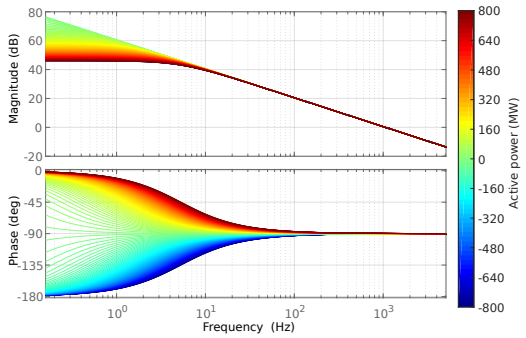

Figure 3.59: Sensitivity of DC impedance to varying active power operating points for an active power controlled VSC

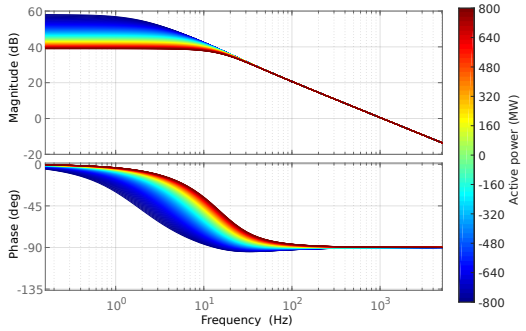

Figure 3.60: Sensitivity of DC impedance to varying active power operating points for a droop controlled VSC

impedance model can be chosen without loss of significant accuracy.

2. In addition to the above, models must be provided separately for each different combination of control modes as impedance models of different control modes differ significantly.
3. A network operator may mandate the designer of each converter to have additional control channels for supplementary control actions. This is similar to the implementation of power system stabilizers (PSS) in synchronous generators. Subsequently, it is the responsibility of the operator to determine when to activate the controllers depending on location and initial interaction studies.
4. Re-optimization of control parameters is required if system topology changes or additional devices are connected to the system and in a practical setting, adaptability should be inherent.
5. Despite the adoption of transfer functions that mask internal information about a device, some basic information is required. For

example, information about the inner loop (often the fastest loop and provides the final command to switches) is required in the form of its bandwidth. To prevent any requirement to provide explicitly this information, the bandwidth of the inner loop may be standardized and a minimum bandwidth recommended to all converter designers. Then external controllers can adopt the declared minimum bandwidth when designing supplementary controllers. Otherwise, the interaction between the inner-loop and supplementary controllers may defeat the original purpose of additional control. On the alternative, a device manufacturer can simply specify a forbidden range of frequencies for which any additional control action external to the device should not cross.

3.6 Chapter Conclusions

This chapter proposes a potential application of the impedance framework to analyse the system-level behaviour of VSC-HVDC grids as a subnetwork subject to control. The impact of different control strategies and parameters on interactions and stability of the system was presented. In general, it was observed that a compromise on control bandwidth is required for minimum stability margins. Specifically, controllers with too low or too high bandwidths are not desired. In the event compromises are not achievable, then, supplementary control actions may be required depending on the information available. Furthermore, analytical formulations previously derived were applied to concisely determine how converters are interacting in the DC subnetwork, at each identified interaction frequencies through their relative contributions. It was shown how this may assist as a tool in the coordinated design of controllers if so desired.

Then, supplementary control design was proposed as a problem of minimizing impedances or matching by manipulating the stability formulation of the system as seen from any terminal. Two design examples based on both approaches show the effectiveness of the proposed methodology in decoupling interactions and improving overall dynamic response and stability of the DC grid. Additionally, the flexibility, scalability, and tractability of methodology and designed controllers was demonstrated. Most importantly, it was shown that it is possible to design these controllers without knowledge of sensitive information about the converter which is often not available.

Finally, recommendations were proposed for applications of the impedance framework in large-scale analysis and control of HVDC grids as subnetworks.

4 Control of VSC-Interfaced AC Grids

This chapter presents the control of a VSC-interfaced AC grid as opposed to the DC grid. Similar to the previous chapter, the mechanism of dynamics and interactions between the converter and an arbitrary AC grid separate from the DC grid is systematically presented. The impedance-based approach is applied as a tool for understanding the interaction between the controlled VSC and the physical system. The insights obtained from the detailed analysis are then applied to modify existing controllers that take into consideration the interactions as analysed. As a result, proposed modifications are remarkably simple and easily extended to as many interconnected converters. Furthermore, the potential conflicts of control requirements relative to the knowledge obtained from the DC grid in the previous chapter are highlighted. This directly keys into required trade-offs for a stable hybrid AC/DC grid as a whole.

4.1 State-of-Art of Impedance-based Approach for AC Side Dynamics of a VSC

The application of impedance-based modelling to analysis and control of VSC-interfaced AC grids is quite extensive as highlighted in previous chapters. The direction today is towards the application of the impedance framework to analysis and control of large-scale multi-converter interfaced AC grids; that is, more than one converter on the AC side [74]. However, given the potential size of such a system, literature is lacking in systematic approaches that allow extending a single converter system to a multi-converter system. More so, the interactions between the converter

and physical system are not completely understood particularly with special cases such as AC grids with high impedance characteristics. Such cases could stem from long transmission lines, unique grids such as offshore AC grids, or weak points in the existing AC system [140, 141]. For such cases with vector controlled VSCs, there are still certain challenges in stable integration. According to literature, the stability limit is severely limited to 0.6p.u. of converter rated power [142, 143]. The causes have a direct relationship with the interactions between the control loops of the VSC and the dynamics at the point of common coupling (PCC).

One major control loop often blamed under such conditions is the PLL as reported in [122, 144–146]. As a way to improve the performance of the PLL and overall system, different implementations and tuning methods have been proposed for the PLL [144, 147–152]. In other studies, the problem was tackled by eliminating the vector current control (VCC) and the necessity for PLL [142]. However, the VCC was suggested as a back-up in case of emergencies where the VCC is better.

Another potential cause of limited power capability is the complex interactions introduced by the outer loops of the vector controlled VSC [88, 153–155]. Therefore, a retuning, redesigning, or modifying of the outer-loops seems to provide relief. However, many of these solutions neglect the mechanism of interaction as seen from the PCC through to the converter, rather than just considering the control loops. As a result, proposed solutions are specific, too complex to adopt, and cannot cater for varying conditions. In another effort, it was proposed to synchronize the converter to another bus where the perceived grid impedance is lower [152, 156]. However, this is physically complicated to implement due to communication requirements considering potential remoteness of the "artificial-bus."

In this chapter, an analysis of the complete behaviour of the VSC as a subsystem under varying operating points, conditions, and different components before interconnection is presented. Then, based on analyses a modification of the existing control is proposed to allow the integration of the vector controlled VSC to any arbitrary AC grid, with extensibility to any number of converters. Additionally, a systematic approach is followed in problem definition in a manner that allows the DC grid (meshed or otherwise) to support weak AC grids as necessary.

4.2 Alternating/Direct-Voltage Controlled VSC Under Varying Conditions

It has been established in the previous chapter that the impedance modelling framework involving VSCs depends heavily on operating conditions

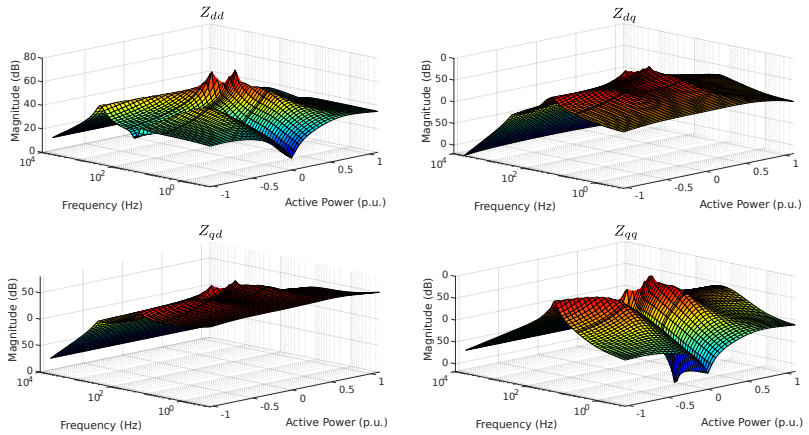

Figure 4.1: VSC impedance magnitude response with all-pass filters and PLL bandwidth of 1Hz

and active components within the VSC. Numerous research endeavours applying the impedance framework have focused on a single operating point. However, the behaviour of the VSC differs significantly from one operating condition to another, the direction of power (inverting or rectification), control mode, active components such as PLL, filters, etc. Therefore, a complete insight into the converter behaviour through the shape of impedance response relative to the different components is fundamental to performance improvements of the VSC.

4.2.1 Characterization of AC Impedance Response

This subsection focuses on the dynamic characterization of the alternating and direct-voltage controlled VSC under varying operating conditions and bandwidth of active components such as PLL and filters.

Impact of PLL on Impedance Responses

For a VSC with all-pass filters on the PCC feedforward voltage $\mathbf{u}^c_{fd,q}$; $F_d(s) = F_q(s) = 1$, and a PLL bandwidth of 1Hz, Fig. 4.1 shows the magnitude response of the impedance equivalent of the AC side admittance. The figure illustrates the most remarkable influence of operating point across the range of frequencies. The characterization illustrated intuitively indicates the relative ease of transitioning from one operating point to another and how the behaviour will vary as the VSC is interconnected to an AC grid. The sharp peaks around the low power region are parallel resonant points between filter bus and VSC. Such points result in

voltage jumps which the PLL and the alternating-voltage controller may aggravate.

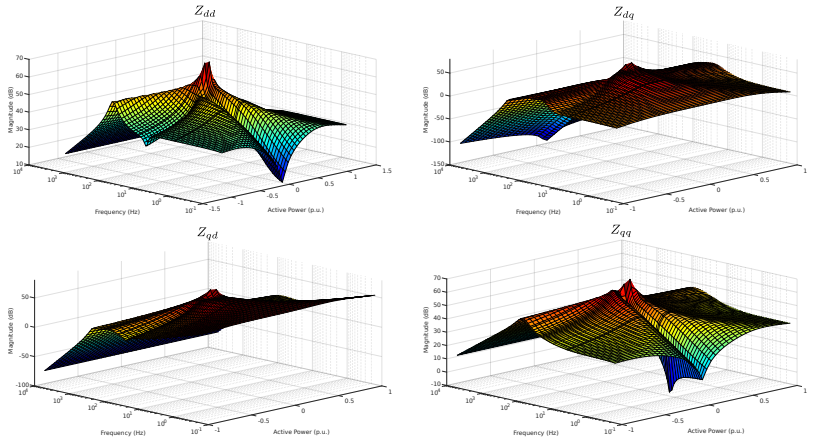

Figure 4.2: VSC impedance magnitude response with all-pass filters and PLL bandwidth of 20Hz

Fig. 4.2 shows the magnitude response for the same conditions as previously with a PLL bandwidth of 20Hz. Immediately, the impact of increasing the PLL bandwidth can be seen. The magnitude of the *qq* component has been reduced by more than 20dB compared to the case with a PLL bandwidth of 1Hz, and the overall magnitude of off-diagonal elements are also reduced. Additional, only one peak can be observed in the *dd* components compared to two in the case with a PLL bandwidth of 1Hz. To verify fully the impacts of the PLL and add support to the previous observation, Fig. 4.3 shows the impedance response for the same conditions as previously discussed, but with an increased PLL bandwidth of 50Hz. It can be seen that all peaks have damped out and an argument may be made to adopting a faster PLL bandwidth as this improves the dynamics of the VSC. This is related to the location of undamped poles within the VSC for which increasing the closed-loop bandwidth of the PLL ensures the poles are within the reach of the PLL. This is also the result of the PLL's behaviour as an extra filter to damp resonances and oscillatory behaviours [150]. However, it is worth noting that these impedance responses only show the isolated behaviour of the VSC as a standalone system without any interconnection. The actual behaviour depends on the characteristics of the grid connection and the ensuing interaction as seen from the PCC.

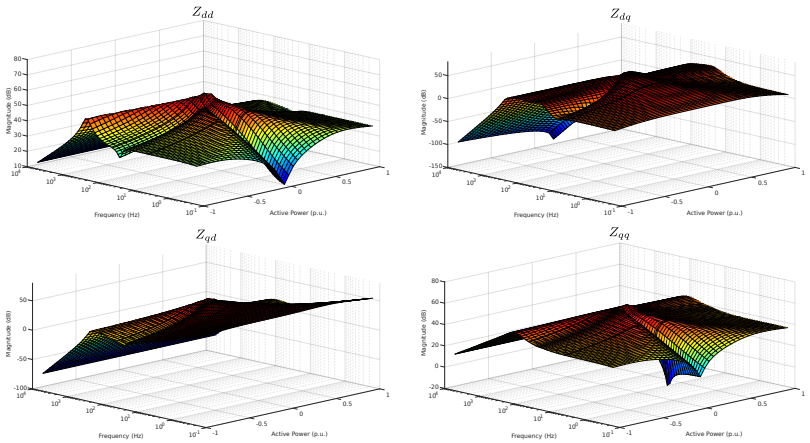

Figure 4.3: VSC impedance magnitude response with all-pass filters and PLL bandwidth of 50Hz

Impact of Feedforward Filter Bandwidth on Impedance Responses

Fig. 4.4 shows the magnitude response of the impedance of the alternating and direct-voltage controlled VSC for a PLL bandwidth of 1Hz and feedforward filter cut-off frequency of 50Hz. It can be seen that the feedforward filter has the most effect on the d-axis and mainly in the inversion region by damping out one of the resonance peaks. There is no significant improvement on the q-axis of the VSC in any operating region since most of the peaks in the rectification region are in the low-frequency range below the reach of the filters. Fig. 4.5 shows the magnitude response when the feedforward filter bandwidth is increased to 100Hz. It can be observed that the responses are largely similar except for a new resonant point in the inversion region around 21Hz. In general, the feedforward filters only show improvements in the inversion region by introducing a valley where high-frequency dynamics dominate. Therefore, the feedforward filter assist in filtering out these high-frequency dynamics. However, it also isolates the low-frequency dynamics in the rectification region and care must be taken as filters may aggravate low-frequency dynamics.

General Observations on the Impedance Responses

In general, several observations can be made from these plots:

1. It is clear how the impedance response behaves as a range of peaks, valleys (dips), and plateaus (flat). Generally speaking, this response indicates the ease of transition between operating points.
2. In the diagonal impedances (dd and qq), the peaks range from inver-

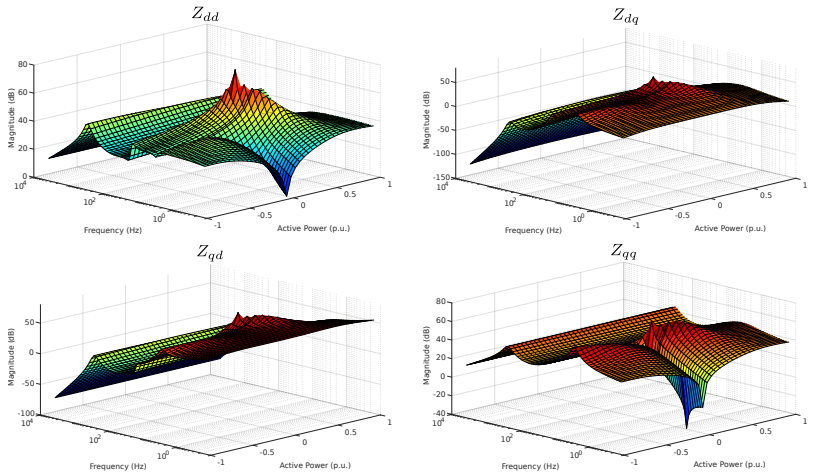

Figure 4.4: VSC impedance magnitude response with PLL bandwidth of 1Hz and feedforward filters with cut-off frequency of 50Hz

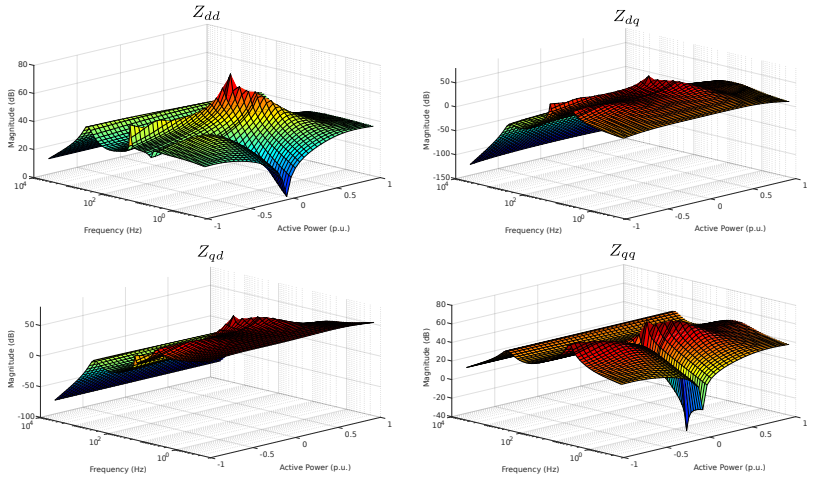

Figure 4.5: VSC impedance magnitude response with PLL bandwidth of 1Hz and feedforward filters with cut-off frequency of 105Hz

sion in the high-frequency region to rectification in the low-frequency region. That is, for operating points in the inversion region, high-frequency dynamics dominate; whereas under the same conditions, in the rectification region, low-frequency dynamics dominate. Therefore, the converter behaves distinctly across operating points.

3. The impact of PLL on the peaks can be observed. These peaks are regions of potential alternating-voltage dynamics that may influence the behaviour of the converter.
4. In steady-state, all regions are plateaus which are typically expected of steady-state behaviour.
5. Under the same conditions for the *dd* impedance, the *qq* impedance shows significantly higher magnitude low-frequency dynamics across the operating range. This is the result of the PLL and alternating-voltage control on that axis.

4.2.2 Interconnected Behaviour of the Alternating/Direct Voltage Controlled VSC

The frequency response plots shown in previous subsections do not by themselves predict the overall behaviour of the converter and system when interconnected to an AC grid. As an example, under a very strong AC grid, the grid impedance may be too low for the converter impedance at the PCC to play any role in the overall system behaviour. The converter does contribute to some dynamics; notwithstanding, stability is guaranteed in the linear region under small grid impedances according to (2.87) from Fig. 2.37. However, under poor grid conditions in which the grid impedance is comparable to the converter's, then an interaction between the grid and converter at the PCC ensues depending on the crossing points between both impedances. Fig. 4.6 depicts a VSC connected to an arbitrary AC grid. Fig. 4.7 shows a snapshot of time-domain responses for step changes in the inversion and rectification stages. It can be observed that in inversion, the oscillations are of high-frequency in nature ($f_1 < f < 2f_1$) as indicated in the frequency responses of the VSC impedances. In contrast, in rectification, oscillations are of low-frequency in nature ($f < f_1$).

Impacts of PLL on the Interconnected System

For an all-pass feedforward filter on PCC voltage, Fig. 4.8 shows the actual active power capability curve of the interconnected VSC in alternating and direct-voltage control mode under varying PLL closed-loop bandwidths and changing SCRs from very weak (1) to very strong (9). It is worth noting that for each case shown, the magnitude of PCC alternating-voltage is within $\pm 0.5\%$ of the reference value.

Numerous observations can be made:

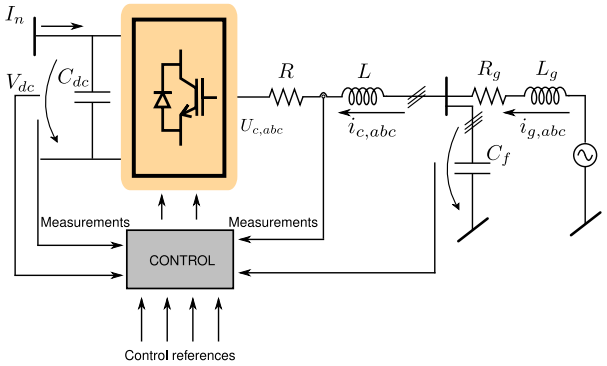

Figure 4.6: Interconnected AC grid

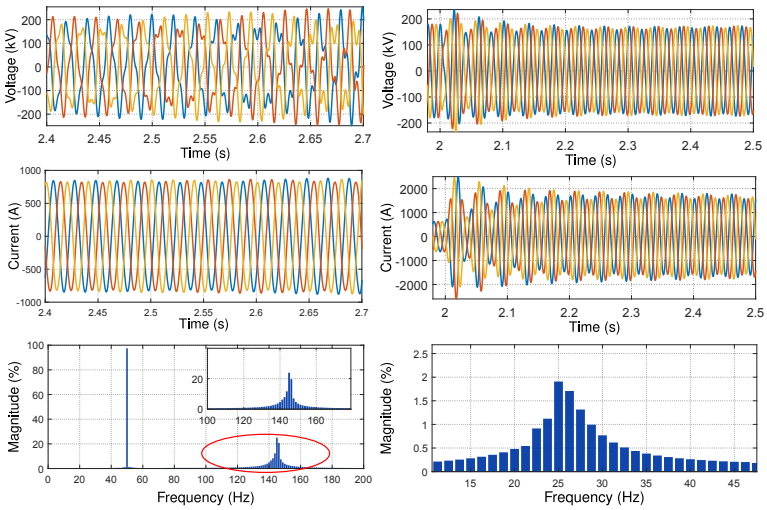

(a) Near-synchronous oscillations for step changes in inversion

(b) Subsynchronous oscillations for step changes in rectification

Figure 4.7: Time domain snapshot for inversion and rectification stage showing tendencies for near- and subsynchronous oscillations

1. At SCR of 1, active power injection/absorption is only possible with the slowest PLL closed-loop bandwidth of 1Hz. Besides, active power capability is limited to -0.15p.u. in inversion to 0.5p.u. in rectification. The system is unstable for any increase beyond this limit.
2. For increasing PLL closed-loop bandwidth beyond 20Hz, the active power capability is 0 for all SCRs less than 2.
3. The active power capability limit increases as the SCR increases.

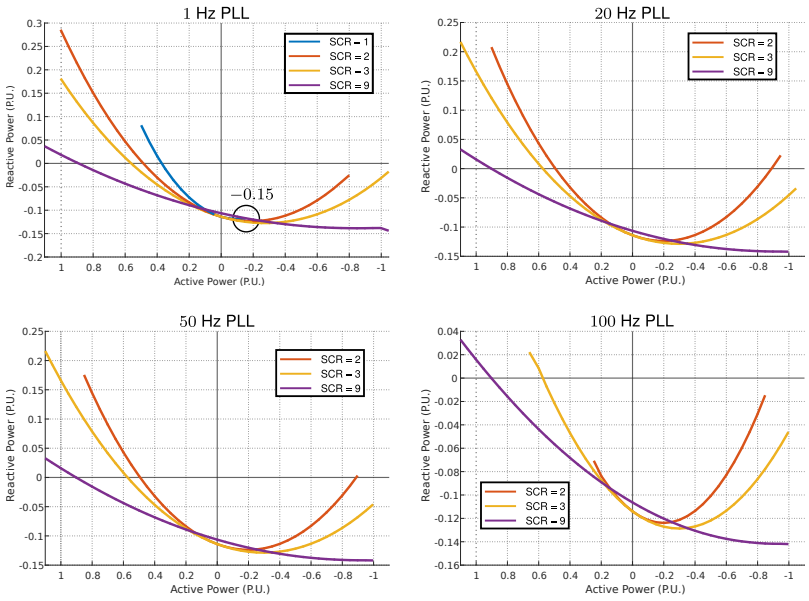

Figure 4.8: Dynamic capability curves for varying PLL closed-loop bandwidths under changing SCR conditions in alternating/direct-voltage control mode

That is, at a fixed PLL bandwidth, active power capability increases as the grid becomes stronger since the reactive power demand reduces allowing more active power.

4. Most severe limits are imposed when SCR is less than 3 where the grid can be described as weak to extremely weak. For SCRs greater than 3 the entire range of active power through ±1p.u. can be observed irrespective of PLL bandwidth. For SCRs greater than 9 up to 1.1p.u. in rectification is possible as reactive power demand is very low allowing the full range of active power.
5. The curves are not symmetrical about the reactive power axis. This implies that inverter behaviour is different from rectifier behaviour. A case for adaptive control could be made; however, one control in either one of rectification or inversion is adequate. This confirms the same analysis from the impedance response.
6. Observe that at closed-loop bandwidth of 100Hz the active power capability limit at SCR of 3 (fairly strong grid) reduces to 0.65p.u. in rectification and system is unstable beyond this limit. Hence, a very high bandwidth PLL is not desired.

Fig. 4.9 shows a clearer view of the interconnected behaviour considering the stability of the entire system and active power capability for each specified SCR and the impact of increasing PLL bandwidths. For SCR of 1 the system can only inject/absorb active power with a PLL closed-loop bandwidth of as low as 1Hz with still limited capability. The system lost stability for any PLL bandwidth greater than 20Hz. For increasing SCRs as seen, increasing PLL closed-loop bandwidth reduces the active power limits.

In general, the interconnected system suggests that a faster PLL bandwidth is detrimental to the closed-loop stability of the entire system. This is counterintuitive to the frequency domain analyses on the VSC impedance response as a subsystem. At the VSC level, an argument can be made for increasing the PLL bandwidth as this improves the overall response of the VSC. This does not seem to hold when the VSC is connected to particularly weak AC grids as an interaction between the VSC and grid ensues and stability is challenged.

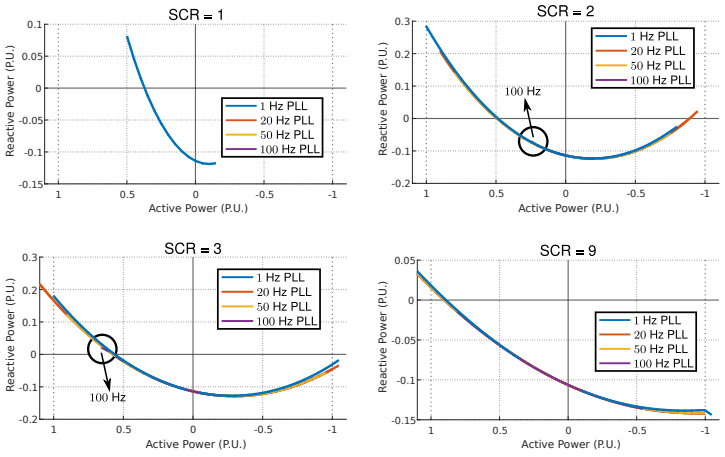

Figure 4.9: Impacts of PLL closed-loop bandwidth on active power capability under the same SCR

The characteristic loci of the minor loop gain of the AC side based on generalized Nyquist as derived in (2.88) for an AC grid with SCR = 9 is shown in Fig. 4.10. It is seen that for such a relatively high SCR, the system remains stable for any PLL bandwidth and in any power direction by not encircling the $(-1+j0)$ point. However, for a faster PLL bandwidth of 50Hz as shown in the bottom subplots Fig. 4.10a and b the characteristic loci are close to the point $(-1+j0)$ point slight disturbance may move the system to instability. This correlates with the observations

from Fig. 4.9 where for an SCR = 9, active power is possible across the entire range up to a PLL bandwidth of 100Hz. The time-domain responses of physical variables on both AC and DC sides for SCR of 9 are shown in Fig. 4.11. As discussed previously, there is no noticeable difference for a PLL bandwidth of 1Hz or 50Hz in either inversion or rectification.

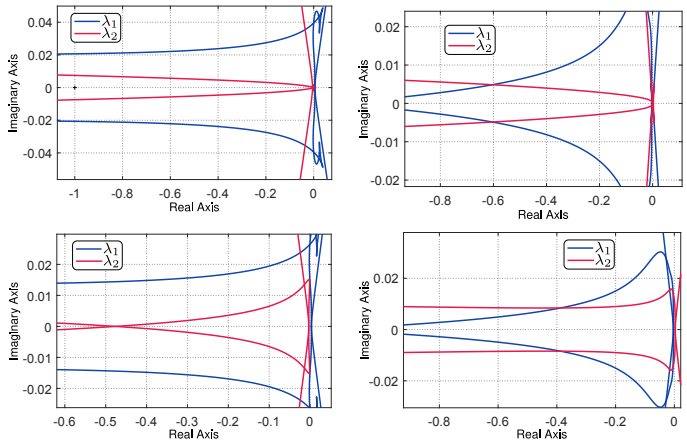

(a) Inversion (PLL bandwidths **top**: 1Hz, **bottom**: 50Hz)

(b) Rectification (PLL bandwidths **top:** 1Hz, **bottom:** 50Hz)

Figure 4.10: Characteristic loci of the impedance ratios based on generalized Nyquist

For very weak grid conditions at SCR = 1, Fig. 4.12 shows the characteristic loci of the minor loop gain. As expected, for a PLL bandwidth of 1Hz and 50Hz, the system is unstable in inversion. Whereas in rectification, the system is stable but close to instability for a PLL bandwidth of 1Hz and unstable for a PLL bandwidth of 50Hz. The time-domain responses of phase voltages, currents, and direct-voltages are shown in Fig. 4.13. As predicted by the characteristic loci, the inversion stage is unstable in both cases of PLL bandwidth and for rectification, the system is unstable for PLL bandwidth of 50Hz.

Impacts of Feedforward Filter on the Interconnected System

Fig. 4.14 shows the impact of a filter on the PCC feedforward voltage for a fixed PLL bandwidth of 1Hz at each SCR as analysed previously. It can be observed that the feedforward filter plays a negligible role as the curves for varying filter cut-off frequencies are largely similar for each SCR. This is a consequence of a very low bandwidth PLL that acts as an efficient low

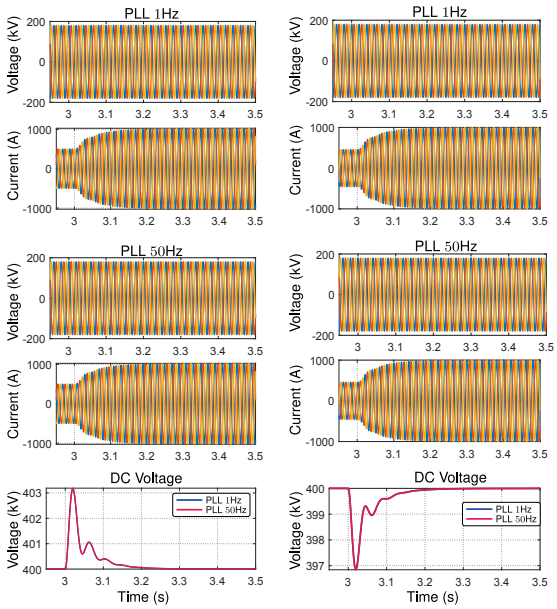

(a) Inversion (b) Rectification

Figure 4.11: Time domain shot of physical variables

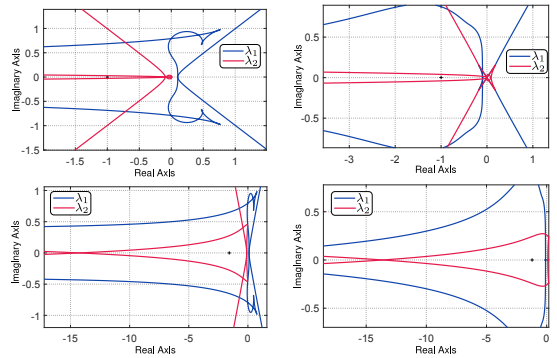

(a) Inversion (PLL bandwidths **top**: 1Hz, **bottom**: 50Hz)

(b) Rectification (PLL bandwidths **top:** 1Hz, **bottom:** 50Hz)

Figure 4.12: Characteristic loci of the impedance ratios based on generalized Nyquist

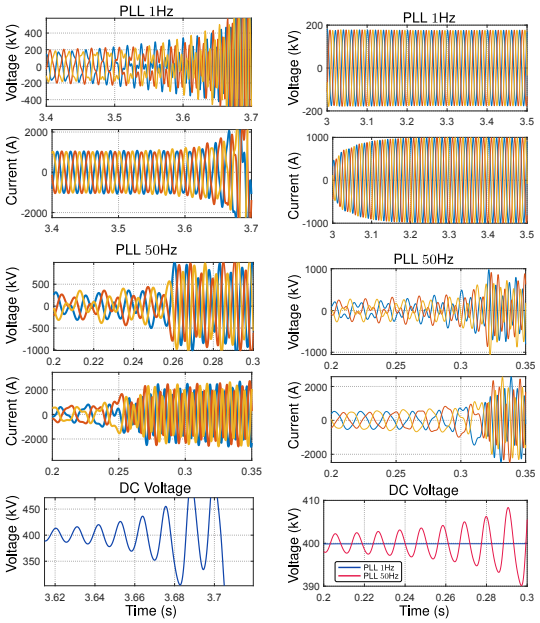

(a) Inversion (b) Rectification

Figure 4.13: Time domain shot of physical variables

pass filter for which it is no longer necessary to have a feedforward filter. Additionally, the feedforward filter at the given cut-off frequency only attenuates dynamics above the cut-off frequency. Therefore, the filter will only play a role when the bandwidth of PLL is increased beyond the feedforward filter cut-off frequency. However, it has already been shown from the magnitude response of the VSC impedance that the feedforward filter only improves the response in the inversion region where high-frequency dynamics dominate.

4.3 Alternating-Voltage and Active Power Controlled VSC Under Varying Conditions On the AC Side

This section discusses the impedance response of the alternating-voltage and active power controlled VSC as a different control mode that may be applied.

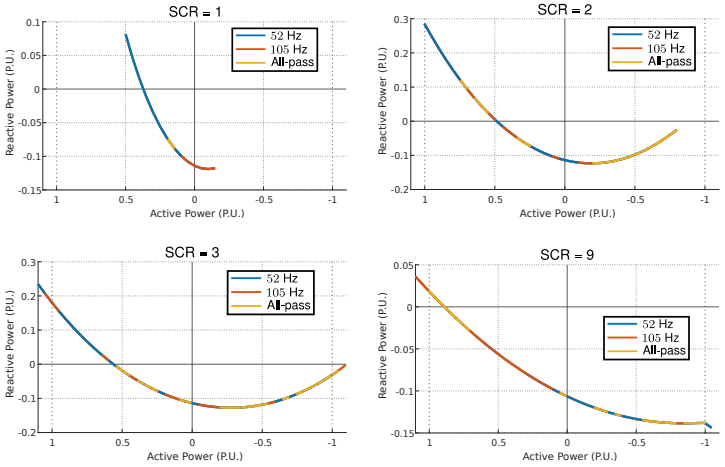

Figure 4.14: Impacts of filter cut-off frequency on active power capability under the same SCR for a PLL closed-loop bandwidth of 1Hz

4.3.1 Characterization of AC Impedance Response

This section discusses the dynamic characterization of the alternating-voltage/Active power controlled VSC as a possible control mode.

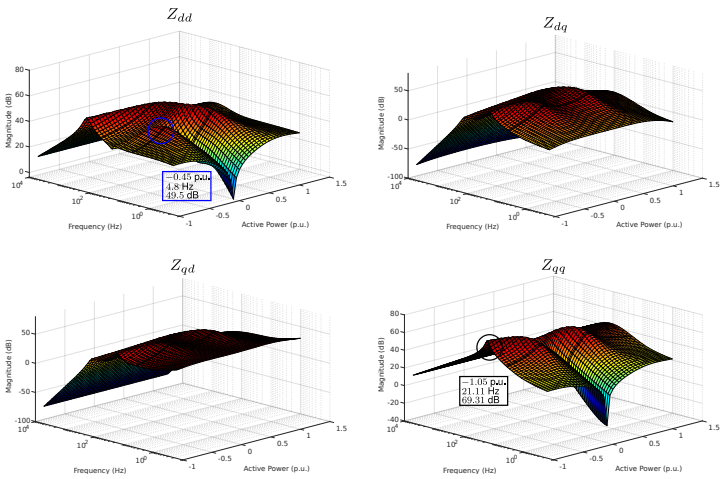

Figure 4.15: VSC impedance magnitude response with all-pass filters and PLL bandwidth of 1Hz

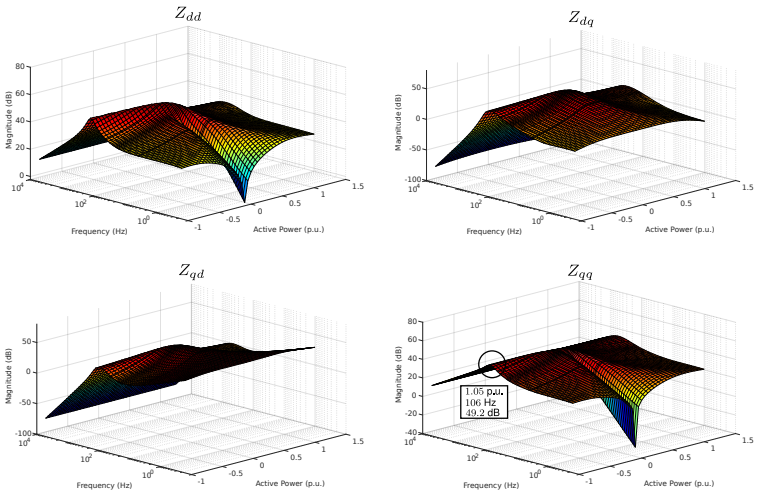

Figure 4.16: VSC impedance magnitude response with all-pass filters and PLL bandwidth of 20Hz

Impact of PLL on Impedance Response

Similarly to the alternating and direct-voltage controlled converter, Fig. 4.15 shows the AC side impedance magnitude response with an all-pass feedforward filter on $\mathbf{u}^c_{fd,q}(s)$, a PLL bandwidth of 1Hz, over varying operating points as derived in (2.45) ($R_{dc} = 0$). The impedance response of the active power controlled shows a smoother surface in all components compared to the direct-voltage control case and this indicates easier transitions. This a consequence of direct control of active power injected and extracted from the AC grid. Figs. 4.16, 4.17 show the impedance response for the same conditions with PLL bandwidth increased to 20Hz and 50Hz respectively. In general, it can be observed that the responses are largely similar; high-frequency dynamics around the inversion region, and low-frequency dynamics dominantly in rectification. Additionally, at very low PLL bandwidth, a low-frequency resonance is detected in the inversion region (indicated by the blue circle in the *dd* components of Fig. 4.15). However, this is damped out as the PLL bandwidth is increased. On the *qq* component, an increase in PLL bandwidth damps the high power resonance and shifts the resonance from 21Hz on the low-frequency side to 313Hz at the highest PLL bandwidth. Considering that the magnitude is lower for the high-frequency resonance, this is not expected to be an issue. Compared to the direct-voltage controlled converter, the active power responses are in general smoother and flatter.

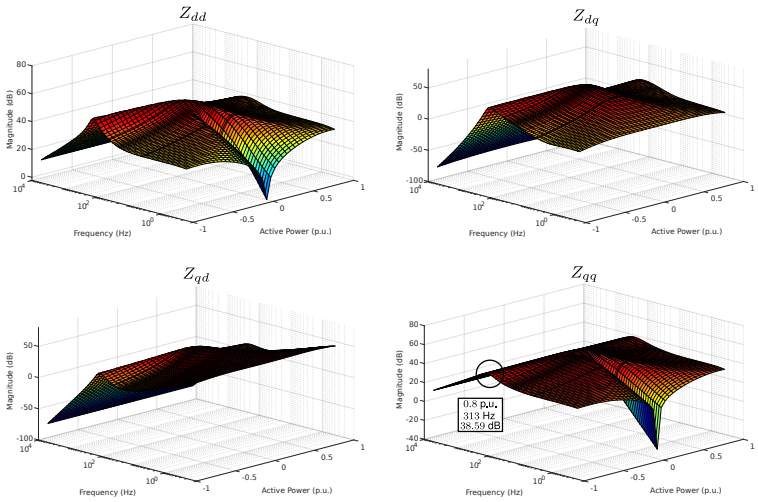

Figure 4.17: VSC impedance magnitude response with all-pass filters and PLL bandwidth of 50Hz

Impact of Feedforward Filter Bandwidth on Impedance Response

Fig. 4.18 shows the impedance responses for a PLL bandwidth of 1Hz and a feedforward filter bandwidth of 50Hz. It is seen that the filter assists in significantly damping the high-frequency resonance in the inversion region of *dd* and *qq* components. However, similarly to the case of the direct-voltage controlled VSC, the filter has no impact on the rectification side. Further increase in bandwidth of feedforward filter has no impact on the impedance responses as shown in Fig. 4.19.

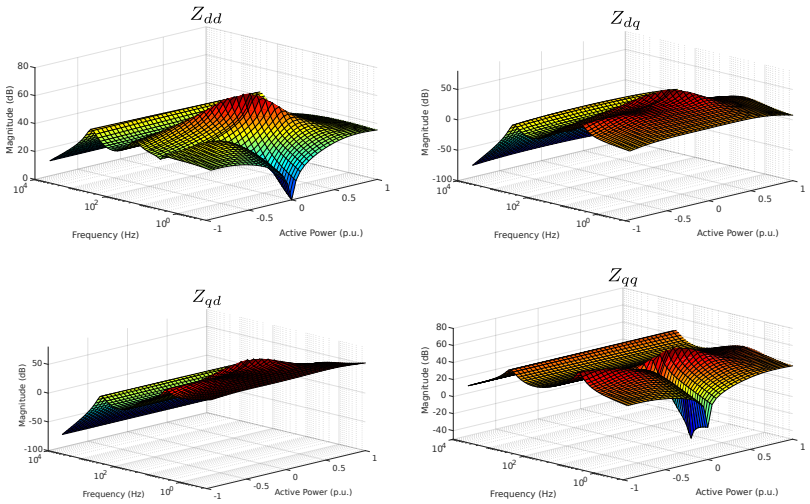

Figure 4.18: VSC impedance magnitude response with PLL bandwidth of 1Hz and feedforward filters with cut-off frequency of 50Hz

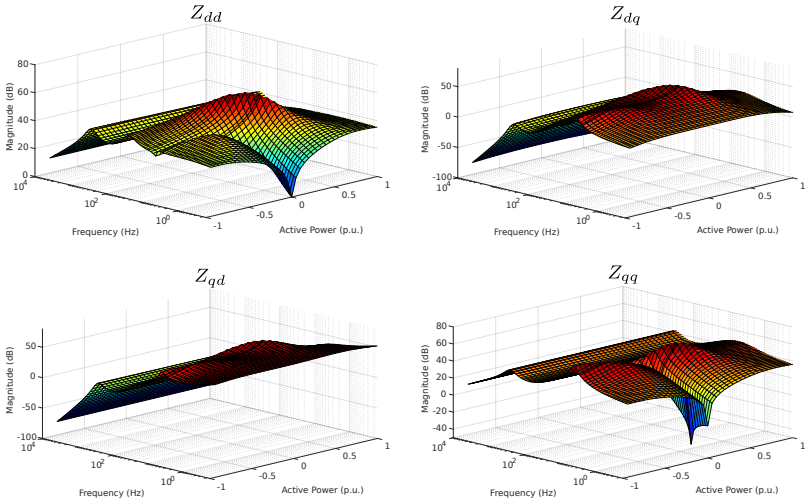

Figure 4.19: VSC impedance magnitude response with PLL bandwidth of 1Hz and feedforward filters with cut-off frequency of 100Hz

4.3.2 Interconnected Behaviour of the Alternating-Voltage/Active Power Controlled VSC

Impacts of PLL on the Interconnected System

For an all-pass feedforward filter on the PCC voltage, Fig. 4.20 shows the impact of varying PLL closed-loop bandwidths on different SCR from very weak to very strong for an active power controlled VSC. Similar to previously, the PCC alternating-voltage magnitude is maintained within $\pm 0.5\%$.

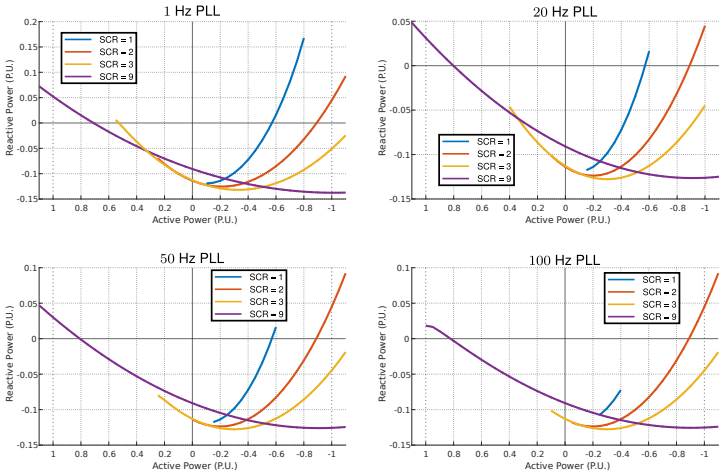

Figure 4.20: Dynamic capability curves for varying PLL closed-loop bandwidths under changing SCR conditions in alternating-voltage/active power control mode

An immediate comparison between the direct-voltage controlled case shows some similarity. For instance, increasing the PLL closed-loop bandwidth generally results in reduced active power capability for SCR ≤ 3. Additionally, active power capability increases for each PLL closed-loop bandwidth as SCR is increased. At a PLL closed-loop bandwidth of 100Hz, the VSC can barely rectify (except for a very strong grid) despite a smoother impedance response of the active power controlled VSC. This is the result of a faster active power closed-loop bandwidth which gives priority to active power dynamics over reactive power dynamics. That is, the faster closed-loop bandwidth improves active power dynamics. However, this constrains the dynamics of the reactive power (through alternating-voltage control and implemented limiting strategy) that is extremely needed under weak grid conditions.

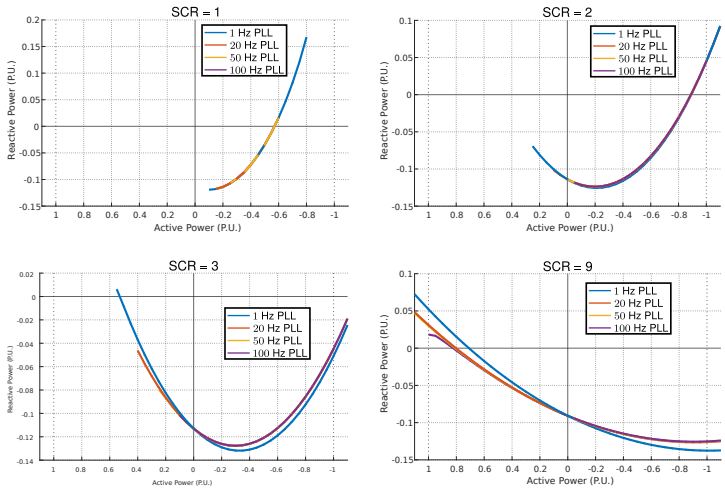

Figure 4.21: Impacts of PLL closed-loop bandwidth on active power capability under the same SCR

Fig. 4.21 shows the same power capability curves but instead for varying PLL closed-loop bandwidths under each SCR. Observe that for very low SCRs (less than 3) most of the capability curve lies in the inversion region. This points to a characteristic difficulty in rectification for an active power controlled VSC.

Impacts of Feedforward Filter on the Interconnected System

Fig. 4.22 shows the impact of varying cut-off frequency of the PCC feedforward filter. In general, the feedforward filter has a negligible impact across all SCRs except for the case of SCR = 3 where there is an improvement in active power capability for cut-off frequencies of 52Hz and 105Hz compared to Fig. 4.20. For a PLL closed-loop bandwidth of 1Hz and an all-pass filter with SCR of 3, the active power is limited to 0.55p.u. However, the introduction of a filter of specified cut-off frequency improves the active power capability to the entire range of the VSC.

4.3.3 Comparison Between Direct-Voltage and Active Power Controlled VSC

Fig. 4.23 shows the active power capability plot of the direct-voltage and active power controlled VSCs for a fixed PLL closed-loop bandwidth of 1Hz. One difference is remarkable; observe that in weak to very weak

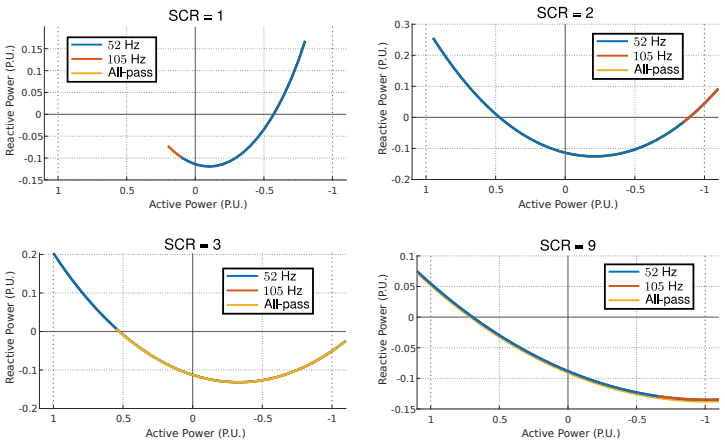

Figure 4.22: Impacts of filter cut-off frequency on active power capability under the same SCR for a PLL closed-loop bandwidth of 1Hz

grids, the direct-voltage curve lies about the rectifying region and the active power curve lies about the inversion region. This indicates a relative difficulty in inversion for direct-voltage controlled VSCs; whereas a relative difficulty in rectification for active power controlled VSCs. Hence, an active power controlled VSC integrating a weak grid performs better in inversion mode than rectification mode and vice-versa for the direct-voltage controlled VSC. This behaviour is largely independent of the PLL bandwidth as shown in Fig. 4.24 for a PLL closed-loop bandwidth of 100Hz as the same interpretation can be made. Notwithstanding, the direct-voltage controlled VSC performed better than the active power controlled VSC. However, this comparison is difficult to establish as the bandwidth of both controllers for stable operation under the same conditions may be different.

4.4 Performance Enhancement of a VSC Connected to Grids of Arbitrary Strength

The preceding discussions in Sections 4.2 and 4.3 showed the most noteworthy impacts of auxiliary active components such as PLL and filter under varying operating points and grid conditions. For the PLL, a faster closed-loop bandwidth is desired at the converter level as this improves the device level behaviour of the VSC. However, on interconnection with a particularly weak AC grid (SCR < 3), a very slow closed-loop bandwidth

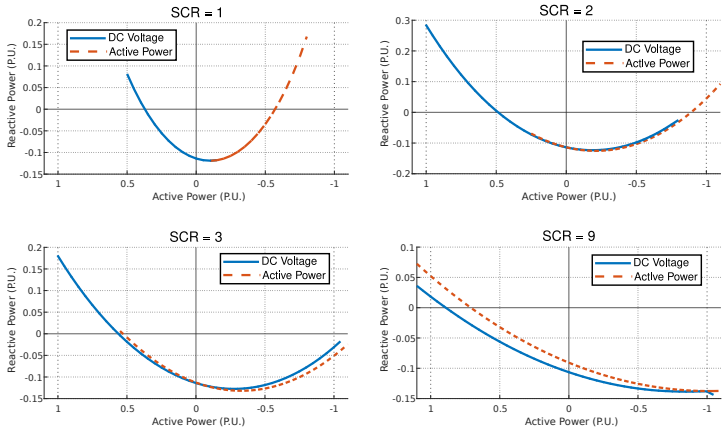

Figure 4.23: Comparison between the interconnected behaviour of the direct-voltage and active power controlled VSCs for a PLL closed-loop bandwidth of 1Hz

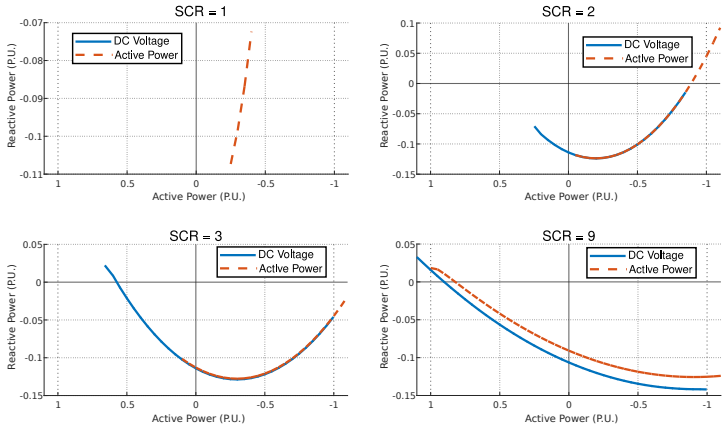

Figure 4.24: Comparison between the interconnected behaviour of the direct-voltage and active power controlled VSCs for a PLL closed-loop bandwidth of 100Hz

is desired of the PLL to transfer any amount of power. It is shown that despite a reduction to a PLL closed-loop bandwidth as low as 1Hz the power capability is still severely limited. For the direct-voltage controlled converter, this limit is 0.5p.u. in rectification and -0.15p.u. in inversion. Whereas, for an active power controlled converter the limit the limits are

much severe as it is only possible to invert between -0.15p.u. to -0.8p.u.

In this section, a detailed analysis of VSC input admittance is presented to understand the interactions between the VSC at the PCC and the dynamics of existing control under weak grid conditions. This is to obtain insights into physical variables that may contribute to the detrimental behaviour of the VSC under weak grid conditions and then eliminate them through a modification of the existing control. Hence, the active power capability is significantly improved beyond the limitations described for any arbitrary SCR, particularly very low SCRs.

4.4.1 Passivity Based Analysis of the Input Admittance of a Direct-Voltage Controlled VSC

Passivity criterion establishes that if the VSC can be designed such that the input-output admittance described by $\mathbf{Y}(s)$ is passive at all frequencies $s = j\omega$, the VSC will remain stable under any condition [77, 78]. That is

$$\mathrm{Re}\{\mathbf{Y}(s)\} \geq 0, \quad \forall \omega > 0. \tag{4.1}$$

However, due to the collection of controllers, active components implemented, and the inherent complexity of the VSC, it is impossible to guarantee passivity across all frequencies [78]. Nevertheless, if passivity can be guaranteed in certain frequency ranges, then destabilization will not occur [157]. In other words, simply reducing the area of negativity to a minimum is sufficient to significantly improve the performance of a vector controlled VSC connected to an ac grid of arbitrary strength.

The VSC admittance on the AC side $\mathbf{Y}(s)$ as derived in equation (2.33) is described by

$$\mathbf{Y}(s) = \begin{bmatrix} Y_{dd}(s) & Y_{dq}(s) \\ Y_{qd}(s) & Y_{qq}(s) \end{bmatrix} \tag{4.2}$$

where $\mathbf{Y}(s)$ is an asymmetric MIMO complex matrix. However, test of positivity of a matrix only applies to symmetric matrices. Therefore $\mathbf{Y}(s = j\omega)$ must be transformed to an equivalent symmetric real-valued matrix from linear algebraic theory such that,

$$\mathbf{Y}(j\omega) + \mathbf{Y}^H(j\omega) = \begin{bmatrix} A & C^* \\ C & B \end{bmatrix} \tag{4.3}$$

with elements

$$\begin{aligned} A &= 2\mathrm{Re}\{Y_{dd}(j\omega)\} \\ B &= 2\mathrm{Re}\{Y_{qq}(j\omega)\} \\ CC^* &= \left(Y_{dq}^*(j\omega) + Y_{qd}(j\omega)\right)\left(Y_{dq}(j\omega) + Y_{qd}^*(j\omega)\right) \\ &= \mathrm{Re}\{Y_{dq}(j\omega) + Y_{qd}(j\omega)\}^2 + \mathrm{Im}\{Y_{dq}(j\omega) - Y_{qd}(j\omega)\}^2 \end{aligned} .$$

The matrix on the right hand is a symmetric matrix and test of positivity of the real part of the matrix is a check of positive definiteness and this holds if both conditions below hold [158]

$$\begin{aligned} A > 0, \quad B > 0 \\ AB > C^*C \end{aligned} . \tag{4.4}$$

It is worth noting that a strict positivity is not necessary and the above conditions may be relaxed to include positive semi-definite in which case $A \geq 0$, $B \geq 0$. Additionally, due to the squares involved, $CC^* \geq 0$ for all intent and purposes. Hence, (4.4) can be relaxed to

$$\begin{aligned} A \geq 0, \quad B \geq 0 \\ AB \geq C^*C \end{aligned} \tag{4.5}$$

The following assumptions are made in the scope of this section to keep the problem as compact as possible. However, where necessary, the impact of assumptions are indicated.

- The grid impedance is assumed to consist of passive R, L, and/or C components. This allows to directly neglect the grid characteristic since it is already passive by this definition. Hence, only the converter admittance is required in the analysis.
- A slow closed-loop bandwidth of PLL of 1.5Hz is applied except otherwise stated.
- The q-axis filter voltage at an operating point $u_{fq}^0 \approx 0$. This holds for nearly all cases since the PCC voltage magnitude is maintained below $\pm 0.5\%$ of the reference value. In the worst case, the impact of u_{fq}^0 almost always appear as u_{fq}^0/U_f^0 which is negligible. Hence, $U_f^0 \approx u_{fd}^0$.
- The above implies that $P^0 = u_{fd}^0 i_{cd}^0/k$.
- The PLL deviation angle at an operating point $\Delta\theta_p^0 = 0$. This follows from previous assumptions.
- The magnitude of the closed-loop transfer function of the inner current loop $h_{cl}^i(s) = 1$. This holds strictly up till the cut-off frequency of the inner loop designed to be around 105Hz.

4.4.2 Decomposition of VSC Admittance Components

Each of the d and q-axes components of the matrix in (4.2) are further decomposed into variables. This is for ease of insights into the corresponding contributions to the passivity of the system based on the conditions in (4.5).

Decomposition of $Y_{dd}(s)$

From equation (2.32) of a direct-voltage controlled VSC,

$$Y_{dd}(s) = y_d^d(s) - y_{dc}^d(s) H_{dd}(s) \tag{4.6}$$

where

$$\begin{aligned} y_d^d(s) &= y_{dd}(s) - \frac{k h_{cl}^i(s) P^0}{(u_{fd}^0)^2}, \\ y_{dc}^d(s) &= \frac{k K_v(s) V_{dc}^0 h_{cl}^i(s)}{u_{fd}^0}, \\ H_{dd}(s) &= \frac{z_{dc}(s)\left(u_{fd}^0 y_d^d(s) + u_{fq}^0 Y_{qd}(s) + i_{cd}^0\right)}{k V_{dc}^0 + z_{dc}(s)\left(u_{fd}^0 y_{dc}^d(s) + k I_{dc}^0\right)}. \end{aligned}$$

Substituting the expressions for $y_{dd}(s)$ from (B.5), $Y_{qd}(s)$ from (2.29), $y_d^d(s)$, y_{dc}^d, $H_{dd}(s)$, and applying the assumptions, $Y_{dd}(s)$ can be decomposed as

$$Y_{dd}(s) = a_{d1}(s)\left(F_d(s) - 1\right) + a_{d2}(s)\left(1 - F_d(s)\right) - a_{d3} \tag{4.7}$$

with coefficients

$$\begin{aligned} a_{d1}(s) &= \frac{y_{ac}(s) K_v(s) V_{dc}^0}{(K_c(s) y_{ac}(s) + 1)(s C_{dc} V_{dc}^0 + K_v(s) V_{dc}^0 + I_{dc}^0)}, \\ a_{d2}(s) &= \frac{y_{ac}(s)}{K_c(s) y_{ac}(s) + 1}, \\ a_{d3} &= \frac{i_{cd}^0}{u_{fd}^0}, \end{aligned}$$

where $y_{ac}(s)$ is the primitive admittance of the VSC consisting of R and L components. To guarantee $\mathrm{Re}\{Y_{dd}(j\omega)\} \geq 0$,

$$\begin{aligned} &[\mathrm{Re}\{a_{d1}(j\omega)\} \cdot \mathrm{Re}\{F_d(j\omega) - 1\} - \mathrm{Im}\{a_{d1}(j\omega)\} \cdot \mathrm{Im}\{F_d(j\omega)\}] \\ &+[\mathrm{Re}\{a_{d2}(j\omega)\} \cdot \mathrm{Re}\{1 - F_d(j\omega)\} - \mathrm{Im}\{a_{d2}(j\omega)\} \cdot \mathrm{Im}\{F_d(j\omega)\}] - a_{d3} \geq 0 \end{aligned} \tag{4.8}$$

For an all-pass filter

$$\begin{aligned} \mathrm{Re}\{F_d(j\omega)\} &= 1, \quad \forall \omega > 0 \\ \mathrm{Im}\{F_d(j\omega)\} &= 0, \quad \forall \omega > 0 \end{aligned} \tag{4.9}$$

therefore, a_{d1} and a_{d2} cancel out and

$$\mathrm{Re}\{Y_{dd}(j\omega)\} = -a_{d3} = -\frac{i_{cd}^0}{u_{fd}^0} \tag{4.10}$$

Clearly, the real part of $Y_{dd}(j\omega)$ would depend on a_{d3}. Hence, in rectification (where $i^0_{cd} > 0$), $\text{Re}\{Y_{dd}(j\omega)\} < 0$, whereas in inversion (where $i^0_{cd} < 0$), $\text{Re}\{Y_{dd}(j\omega)\} > 0$.

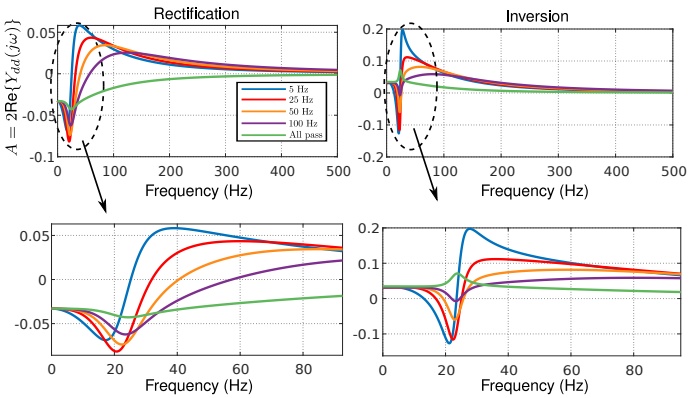

Figure 4.25: Impact of feedforward filter on $A = 2\text{Re}\{Y_{dd}(j\omega)\}$

For a first-order low pass filter with bandwidth less than or equal to that of the closed inner loop, Fig. 4.25 shows the impacts of different cut-off frequencies of $F_d(s)$ on A element of the symmetric matrix in (4.3) at rated operating points for inverter and rectifier operation ($-1 \leq P^0 \leq 1$). In general, for a feedforward filter with a cut-off frequency less than or equal to the cut-off frequency of the inner current loop, the filters ensure that A is positive for all frequencies above the cut-off frequency of the inner loop. That is, the filter with a cut-off frequency improves the passivity of the system particularly in the rectification region where $A < 0$ for an all-pass filter. However, observe that in the low-frequency region (below the cut-off frequency of inner loop) the filter contributes to negativity in the near/sub-synchronous region ($< 2f_1$). This is the region where resonances usually appear in very weak grids [153, 159]. In the inversion stage where $A > 0 \quad \forall\omega$ the filter introduces negativity in the low-frequency. Hence, the filter is detrimental to the overall system behaviour in this region. Although a low cut-off frequency filter provides a smaller negative area in the near-synchronous region ($f \leq 2f_1$), a low cut-off feedforward filter introduces more negativity in the same region compared to an all-pass filter.

In summary, the feedforward filter introduces detrimental interactions below the synchronous frequency, despite significant improvements they provide above this frequency. One solution to improve the capabilities of the VSC is to adopt a feedforward filter of cut-off frequency well below the synchronous frequency in rectifier operation and switch to an all-pass filter in inversion. For a case where $u^0_{fq} \neq 0$, for an all-pass feedforward

filter, $Y_{dd}(s)$ can be decomposed as

$$Y_{dd}(s) = \frac{K_u(s)K_v(s)V_{dc}^0 u_{fq}^0}{\left(sC_{dc}V_{dc}^0 + K_v(s)V_{dc}^0 + I_{dc}^0\right)U_f^0} - a_{d3} \tag{4.11}$$

without further simplifications, it can be easily conjectured from (4.11) that reducing the bandwidth of the direct-voltage control loop and increasing the bandwidth of the alternating-voltage control loop may reduce the area of negative conductance. However, this depends on the actual value of u_{fq}^0 and the cross-coupled admittances which depend on AVC. For optimal behaviour, any changes to AVC bandwidth should be done relative to the DVC bandwidth.

Fig. 4.26 shows the curves for the impact of closed-loop bandwidth direct-voltage control with an all-pass filter while the bandwidth of the AVC is kept constant. For rectifier operation, although the conductance is negative for all frequencies, in the near synchronous region the slower the bandwidth of direct-voltage control, the smaller the area of negative conductance. Moreover, if an acceptable operation can be guaranteed without the integral gain, the resulting reduction in negative area can improve the behaviour. A suggestion is to adopt a slower DVC at a cost of performance degradation of direct-voltage, however, a compromise may be found. For inverter operation, the conductance remains positive as long as an all-pass filter is employed. The impact of the AVC bandwidth is shown in Fig. 4.27 while keeping the DVC bandwidth constant. For both operations, the AVC bandwidth has negligible impact, at least on the d-axis (even for $u_{fq}^0 \neq 0$).

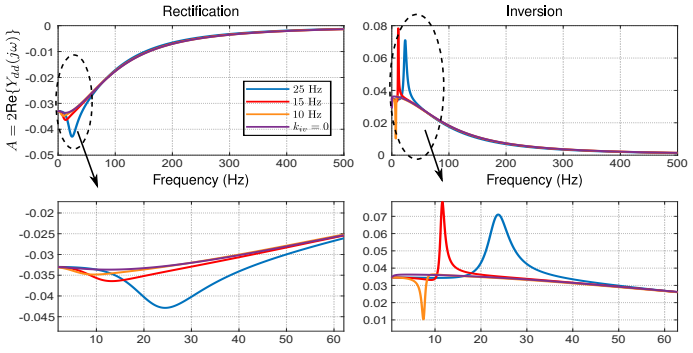

Figure 4.26: Impact of bandwidth of the DVC on $A = 2\mathrm{Re}\{Y_{dd}(j\omega)\}$

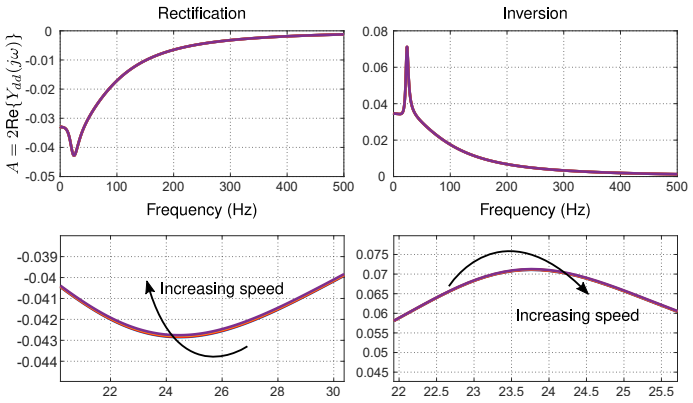

Figure 4.27: Impact of bandwidth of AVC on $A = 2\mathrm{Re}\{Y_{dd}(j\omega)\}$

Decomposition of $Y_{qq}(s)$

From equation (2.29) of a direct-voltage controlled VSC,

$$Y_{qq}(s) = y_q^q(s) = y_{qq}(s) - \frac{K_u(s)h_{cl}^i(s)u_{fq}^0}{U_f^0} \tag{4.12}$$

Substituting for $y_{qq}(s)$ from (B.5) and applying the assumptions

$$Y_{qq}(s) = y_{qq}(s) = a_{q1}(s) + a_{q2}(s)\left(1 - F_q(s)\right) + a_{q3}(s)\left(u_{fd} - u_{cd}\right) \tag{4.13}$$

with coefficients

$$\begin{aligned} a_{q1}(s) &= \frac{y_{ac}(s)K_c(s)K_{pll}(s)i_{cd}^0}{(K_c(s)y_{ac}(s)+1)(u_{fd}^0K_{pll}(s)+s)}, \\ a_{q2}(s) &= \frac{y_{ac}(s)s}{(K_c(s)y_{ac}(s)+1)(u_{fd}^0K_{pll}(s)+s)}, \\ a_{q3}(s) &= \frac{y_{ac}(s)K_{pll}(s)}{(K_c(s)y_{ac}(s)+1)(u_{fd}^0K_{pll}(s)+s)}. \end{aligned} \tag{4.14}$$

To guarantee $\mathrm{Re}\{Y_{qq}(j\omega)\} \geq 0$,

$$\begin{aligned} \mathrm{Re}\{a_{q1}(j\omega)\} + [\mathrm{Re}\{a_{q2}(j\omega)\} \cdot \mathrm{Re}\{1 - F_q(j\omega)\} - \mathrm{Im}\{a_{q2}(j\omega)\} \cdot \mathrm{Im}\{F_q(j\omega)\}] \\ +\mathrm{Re}\{a_{q3}(j\omega)\}\left(u_{fd} - u_{cd}\right) \geq 0 \end{aligned} \tag{4.15}$$

For an all-pass filter or filter with cut-off frequency greater than that of inner loop, a_{q2} cancels out and

$$\mathrm{Re}\{Y_{qq}(j\omega)\} = \mathrm{Re}\{a_{q1}(j\omega)\} + \mathrm{Re}\{a_{q3}(j\omega)\}\left(u_{fd} - u_{cd}\right). \tag{4.16}$$

Therefore,

$$\mathrm{Re}\{Y_{qq}(j\omega)\} \geq 0 \iff \mathrm{Re}\{a_{q1}(j\omega)\} \geq 0,\ \mathrm{Re}\{a_{q3}(j\omega) \geq 0,\ \left(u^0_{fd} - u^0_{cd}\right) \geq 0$$

$\mathrm{Re}\{a_{q1}(j\omega)\}$, is dependent on active power operating point, whereas the difference $(u_{fd} - u_{cd})$ is dependent on the reactive power requirements demanded by the converter under any grid conditions. This sets the major difference between the passivity of $Y_{dd}(s)$ and $Y_{qq}(s)$ where the former depends mainly on active power operating point (in rectifier), but the latter on both active power and reactive power demands in any direction.

More importantly, under fairly strong grids where the reactive power requirements can be easily managed and fairly constant across operating points, the difference $(u_{fd} - u_{cd})$ is positive. In rectification, if the difference is negative at all, the negativity is mitigated by the positivity of $a_{q1}(s)$; thus, $\mathrm{Re}\{Y_{qq}(j\omega)\} > 0$. However, under weak grids, the difference becomes negative with increasing active power due to severe reactive power requirements demanded from the converter. Hence, the negativity increases with increasing active power leading to instability when the positivity due to $a_{q1}(s)$ (since its positivity is limited by rated current) is lower than the negativity due to $(u_{fd} - u_{cd})$. In inversion, the negative sign of i^0_{cd} makes $\mathrm{Re}\{Y_{qq}(j\omega)\} < 0$, and this is further compounded by the negativity of $(u_{fd} - u_{cd})$ under weak grids. This explains why it is still possible to rectify some active power under weak grids as shown in Fig. 4.8 but inversion is not possible at all.

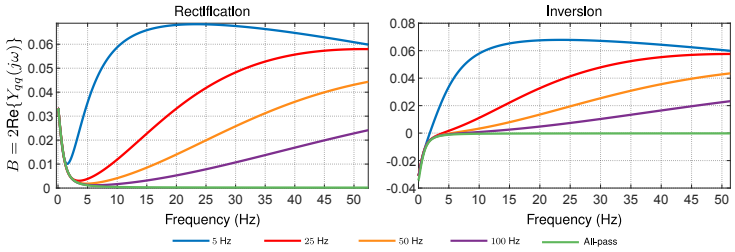

Figure 4.28: Impact of feedforward filter on $B = 2\mathrm{Re}\{Y_{qq}(j\omega)\}$ when $(u_{fd} - u_{cd} > 0)$

Fig. 4.28 shows the impact of different cut-off frequencies of the feedforward filter $F_q(s)$ on B in rectifier and inverter operation when the difference $(u_{fd} - u_{cd}) > 0$. For rectifier operation, $\mathrm{Re}\{Y_{qq}(j\omega)\} > 0$ for all frequencies of interest and for any feedforward filter due to $\mathrm{Re}\{a_{q1}(j\omega)\} > 0$ and $\mathrm{Re}\{a_{q3}(j\omega)\} > 0$. Whereas in inverter, $\mathrm{Re}\{Y_{qq}(j\omega)\} < 0$ for all frequencies with an all-pass filter. However, significantly less negative with a low cut-off frequency feedforward filter. This generally suggests that a feedforward filter should be adopted. However, due to potential negativ-

ity of $(u_{fd} - u_{cd})$ under very weak grid conditions and high power, the feedforward filter only marginally improves the capabilities.

Decomposition of $Y_{dq}(s)$ and $Y_{qd}(s)$

Fundamentally, due to the squares involved, CC^* is always semi-definite (i.e. $CC^* \geq 0$). Based on the conditions established in (4.5), it is desired that CC^* is as small as possible, preferably close to zero since any $CC^* \gg 0$ puts a higher bound on AB. Hence, this imposes difficulty in reducing the negativity of A or B, or improving their positivity. For instance, if $CC^* \approx 0$, then it is desired that $AB \approx 0$, which is relatively easier to obtain than $AB \gg 0$. According to (4.3) both $Y_{dq}(s)$ and $Y_{qd}(s)$ contribute to CC^*; therefore, both are decomposed into components to reveal their contributions.

From equation (2.32)

$$Y_{dq}(s) = y_{dq}(s) - y_{dc}^{d}(s) H_{qq}(s) \tag{4.17}$$

where

$$H_{qq}(s) = \frac{z_{dc}(s)\left(u_f^{d0} y_{dq}(s) + u_f^{q0} Y_{qq}(s) + i_c^{q0}\right)}{kV_{dc}^0 + z_{dc}(s)\left(u_f^{d0} y_{dc}^{d}(s) + kI_{dc}^0\right)}.$$

Substituting the expressions for $y_{dq}(s)$ from (B.5), $Y_{qq}(s)$ from (2.29), $y_{dc}^{d}(s)$, $H_{qq}(s)$, and with the assumptions, $Y_{dq}(s)$ can be decomposed as

$$Y_{dq}(s) = a_{dq1}(s)\frac{V_{dc}^0 i_{cq}^0}{u_{fd}^0} + a_{dq2}(s) u_{cq}^0 + a_{dq3}(s) i_{cq}^0 \tag{4.18}$$

with coefficients

$$a_{dq1}(s) = \frac{-K_v(s)\left(s(K_c(s)y_{ac}(s)+1) + K_{pll}(s)u_{fd}^0\right)}{(K_{pll}(s)u_{fd}^0 + s)(K_c(s)y_{ac}(s)+1)\left(V_{dc}^0(sC_{dc} + K_v(s)) + I_{dc}^0\right)},$$

$$a_{dq2} = \frac{K_{pll}(s)y_{ac}(s)\left(sC_{dc}V_{dc}^0 + I_{dc}^0\right)}{(K_{pll}(s)u_{fd}^0 + s)(K_c(s)y_{ac}(s)+1)\left(V_{dc}^0(sC_{dc} + K_v(s)) + I_{dc}^0\right)},$$

$$a_{dq3}(s) = \frac{-K_{pll}(s)K_c(s)y_{ac}(s)}{(K_{pll}u_{fd}^0 + s)(K_c(s)y_{ac}(s)+1)}.$$

It is clear that $Y_{dq}(s)$ depends on a complex interplay between reactive power, closed direct-voltage control, and PLL closed-loop control. Similarly, from (2.29)

$$Y_{qd}(s) = y_{qd}(s) - \frac{K_u(s)h_{cl}^{i}(s)u_{fd}^0}{U_f^0} \tag{4.19}$$

substituting for $y_{qd}(s)$ from (B.5) and we obtain

$$Y_{qd}(s) = -K_u(s). \tag{4.20}$$

Clearly, $Y_{qd}(s)$ depends on the closed alternating-voltage controller $K_u(s)$. Particularly, $\mathrm{Re}\{Y_{qd}(j\omega)\}$ depends on the proportional gain, and $\mathrm{Im}\{Y_{qd}(j\omega)\}$ depends on the integral gain of the AVC. To obtain $CC^* \approx 0$, it is required that

$$\begin{aligned} (\mathrm{Re}\{Y_{dq}(j\omega)\} + \mathrm{Re}\{Y_{qd}(j\omega)\})^2 &\approx 0 \\ (\mathrm{Im}\{Y_{dq}(j\omega)\} - \mathrm{Im}\{Y_{qd}(j\omega)\})^2 &\approx 0 \end{aligned}. \tag{4.21}$$

It was suggested from the passivity checks in the previous case, to adopt a low bandwidth DVC to reduce the negativity of the system. For a reduced DVC bandwidth to around 15Hz, Fig. 4.29 depicts the impact of varying PLL closed-loop bandwidths in both rectification and inversion (top-left subplot) on each component, $\mathrm{Re}\{Y_{dq}(j\omega)\} + \mathrm{Re}\{Y_{qd}(j\omega)\}$ and $\mathrm{Im}\{Y_{dq}(j\omega)\} - \mathrm{Im}\{Y_{qd}(j\omega)\}$. In rectification, it is seen that increasing PLL closed-loop bandwidths result in an increase in the real and imaginary parts about the zero line. However, the sums remain very low as

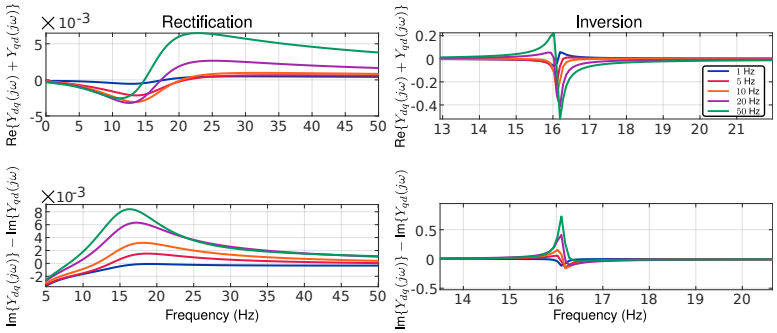

(a) sum of each component

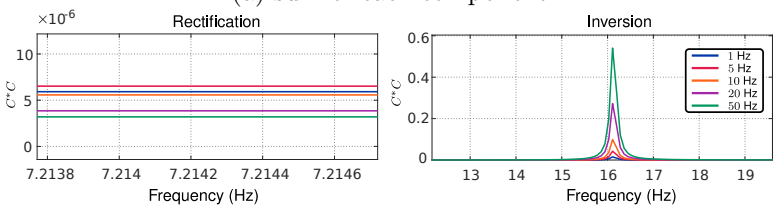

(b) sum of squares of components

Figure 4.29: Detailed view below f_1 for varying PLL closed-loop bandwidths on CC^* in rectification and inversion **(a)** sums **(b)** sum of squares

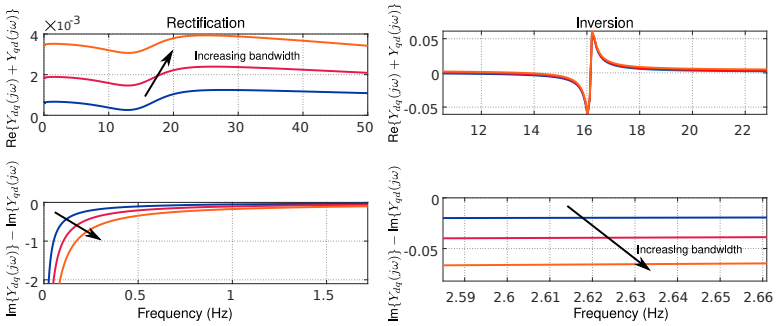

(a) sum of each component

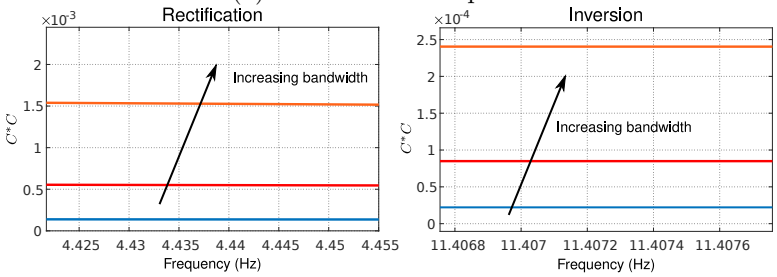

(b) sum of squares of components

Figure 4.30: Detailed view below f_1 for varying alternating-voltage control bandwidths on CC^* in rectification and inversion **(a)** sums **(b)** sum of squares

well as the sum of squares of each component depicted in the lower-left subplot of Fig. 4.29. In inversion (top-right subplot), the impact of varying PLL closed-loop bandwidths for a reduced DVC bandwidth. Peaks and dips can be seen around the bandwidth of the DVC with increasing absolute magnitude as the PLL closed-loop bandwidth is increased. That is, a reduced DVC bandwidth puts stringent conditions on the diagonal elements through the off-diagonal elements as shown by the sum of squares in the bottom-right subplot of Fig. 4.29. This is contrary to the benefits of reduction of the bandwidth for the DVC from the case of the Y_{dd} component especially for a high bandwidth PLL. Hence, a slow bandwidth PLL should be adopted to obtain $CC^* \approx 0$ as much as possible, or the dynamics of the direct-voltage could be improved with additional terms.

The impacts of varying bandwidth of the AVC similar to previously in rectification (left subplots) and inversion (right subplots) for a fixed PLL closed-loop bandwidth of 1.5Hz are shown in Fig. 4.30. In rectification, the component $\mathrm{Re}\{Y_{dq}(j\omega) + Y_{qd}(j\omega)\}$ is quite low; however, the absolute magnitude of $\mathrm{Im}\{Y_{dq}(j\omega) - Y_{qd}(j\omega)\}$ is larger than zero below 1Hz.

Notwithstanding, the sum of squares shown in the lower-left subplot of Fig. 4.30 is still relatively low. A similar analysis is observed for the inversion stage, where the impacts of the AVC bandwidth are not significant other than the peaks due to the reduced bandwidth of the DVC.

4.4.3 Proposed Modification of the VSC Control

Physically, the main control challenge of a VSC under a weak grid is an effort by the converter to force the AVC to perform two strongly coupled functions — PCC voltage magnitude control and reactive power management through the same control channel and input. Under grids with SCR greater than three, reactive power management is not directly required as this is fairly constant over the operating range. Therefore, the closed AVC loop performs the designed function of simply controlling the voltage through the reactive current. However, under very weak grids, the reactive power demand causes the alternating-voltage at PCC to change abruptly which the AVC tries to regulate through the reactive current. This causes further abrupt changes in the alternating-voltage at PCC eventually leading to loss of stability. This is further compounded by an inherent limitation imposed by the speed of the PLL and the direct-voltage control loop that constrains the reactive loop in favour of active current.

The major proposition mainly involves an additional open-loop feedforward (on the q-axis of outer loop) of the difference between u_{fd} and u_{cd} thereby decoupling the discussed functions. This difference implicitly encodes the actual grid impedance and reactive current required relative to the operating point, without the requirement to estimate the grid impedance nor explicitly include the operating point as suggested in literature. In addition to this, the bandwidth of the direct-voltage control is reduced relative to the AVC bandwidth. However, this reduction in the bandwidth results to the poor performance of alternating-voltage control under weak grids. To compensate for the loss of damping due to bandwidth reduction, a bandpass filter active only around the frequencies of interest (as obtained from Fig. 4.1) can be adopted to improve direct-voltage dynamics. To avoid the use of the bandpass filter, a faster PLL can be adopted.

The described modification of outer loops of vector current control is shown in Fig. 4.31. The proposed modification acts as a reactive current forcing term to relief this requirement from the AVC especially under weak grid where this is coupled with the AVC. Hence, the dual responsibilities demanded by the AVC are shared between the existing and added loop. A similar strategy is often employed in conventional generators where the internal voltage of the generator (u_{cd} in this case) is used as a feedback signal. However, this is simply an open-loop implementation. This significantly improves the active power capability under weak grid without

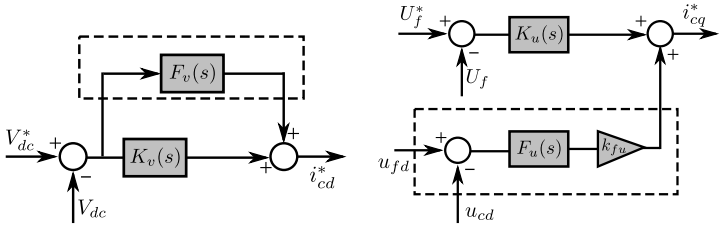

(a) Modification on d-axis (b) Modification on q-axis

Figure 4.31: Modified outer loops of vector current control

complicating the existing vector control structure. The overall modification on both axis can be described by

$$\begin{aligned} i_{cd}^* &= (V_{dc}^* - V_{dc})\,(K_v(s) + F_v(s)k_{fv}) \\ i_{cq}^* &= K_u(s)\left(U_f^* - U_f\right) + F_u(s)\,(u_{fd} - u_{cd})\,k_{fu} \end{aligned} \tag{4.22}$$

where k_{fv} and k_{fu} are constant gains, $F_v(s)$ is a bandpass filter, and $F_u(s)$ is a low pass filter with structures described by

$$F_v(s) = \frac{\frac{\omega_{v0}}{Q}s}{s^2 + \frac{\omega_{v0}}{Q}s + \omega_{v0}^2}, \quad F_u(s) = \frac{\omega_u}{s + \omega_u} \tag{4.23}$$

where ω_{v0} is the midpoint of frequencies of interest, and ω_u is the cut-off frequency of the low pass filter $F_u(s)$ of the additional feedforward term $(u_{fd} - u_{cd})$; ω_u should be chosen well below the bandwidth of the inner loop.

The modified magnitude response of the VSC impedance equivalents is shown in Fig. 4.32. In comparison to the magnitude response of Fig. 4.1 for the same conditions, it can be seen that the modified response has a significantly smoother surface, lower in magnitude, and almost constant impedance across operating points, indicating easier transitions. Furthermore, better improvements can be seen in the inversion region compared to the rectification region. Fig. 4.33 shows a comparison between the passivity with and without modifications for the case of all-pass feedforward filters. As expected, slight improvements on the d-axis in rectifying operation and better improvement in the inverting operation on q-axis.

4.4.4 Time Domain Simulation and Analysis

The previous sections relied on analytical derivations and frequency domain analysis. Nonlinear time-domain simulations are adopted to support previous analysis and validate the proposed modifications and exact capability limits. Several scenarios are simulated for both inverter and rectifier

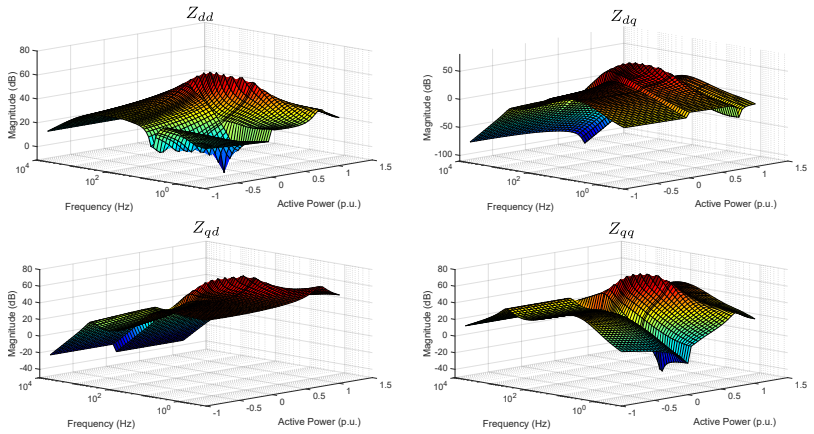

Figure 4.32: Impedance characterization of the direct-voltage controlled VSC with PLL bandwidth of 1Hz after modifications

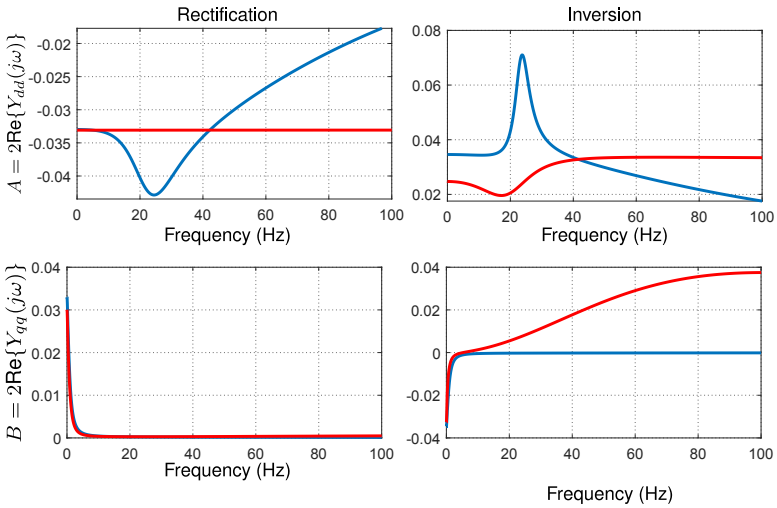

Figure 4.33: Comparison between the passivity with and without modifications of the vector controlled VSC (a) $A = 2\text{Re}\{Y_{dd}(j\omega)\}$ (b) $B = 2\text{Re}\{Y_{qq}(j\omega)\}$

operations. Simulations are developed first for an ac grid of SCR = 1. In later cases, capabilities under any arbitrary grid strength are demonstrated.

Comparisons with Conventional Vector Control

Fig. 4.34 shows the comparison of responses between the conventional vector control and the proposed modifications. It is very clear the significant improvement over the existing structure particularly for inverter operation considering the simplicity of modifications. Inverter operation is poorer than rectification due to the increased negative conductance in inversion as a result of the current sign. Whereas rectification with the existing vector controlled system shows an improvement better than inversion due to the positive sign of current up to a region where negative conductance cannot be mitigated by the positive current sign. In the case of inversion, stability is lost around 0.3p.u. with the conventional vector control, and around 0.6p.u. in the case of rectification. Figs. 4.35 and 4.35 depict the time-domain snapshot of the unstable cases with the conventional vector control showing growing oscillations.

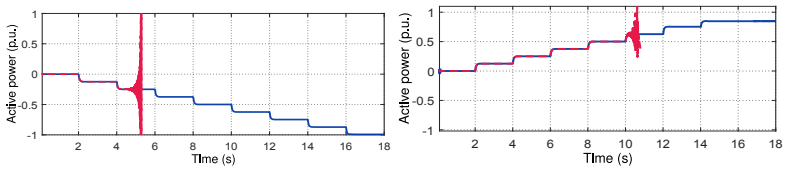

(a) Inversion (b) Rectification

Figure 4.34: Comparison between conventional vector control and proposed modification operation

Capability Under Varying Operating Conditions

To demonstrate the capabilities of the modified vector current-controlled VSC, Fig. 4.37 shows the time-domain responses of active power, alternating and direct-voltages, and converter ac currents over persistent step changes in dc link power across in inverter operation. It shows the efficacy of variables in tracking the desired references up to -1p.u. active power limit within a response time of 20ms. It is also seen that although the alternating and direct-voltage responses consist of slight oscillations and magnitude deviation during the instant of step changes, deviations are well within 1% for the direct-voltage and 1.5% for the alternating-voltage, and oscillations are well-damped without significant degradation. Fig. 4.38 shows a snapshot of time responses of physical variables external to the converter. It can be seen that responses are as expected without degradation in the steady-state nor breach of limits.

Likewise for the rectifier operation, Fig. 4.39 shows the similar responses. As can be observed, with the proposed modification, rectification

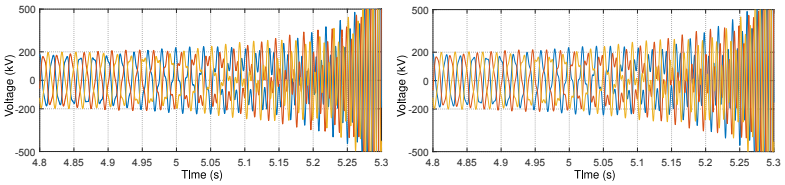

(a) Converter voltages (b) PCC voltages

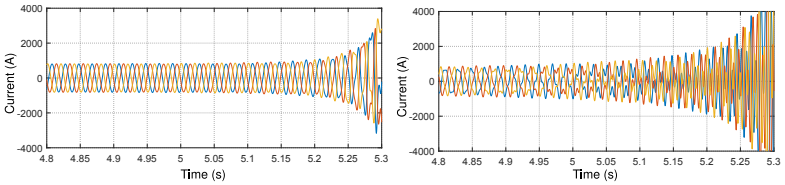

(c) Converter currents (d) grid currents

Figure 4.35: Time domain snapshot of physical variables of the grid with the conventional vector control in inversion stage

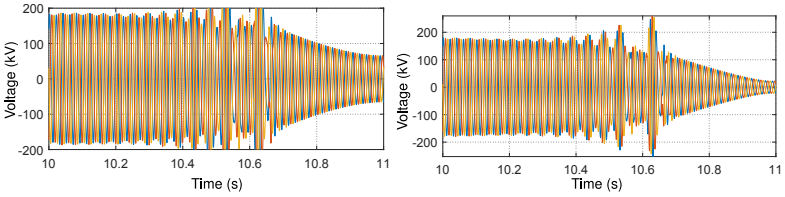

(a) Converter voltages (b) PCC voltages

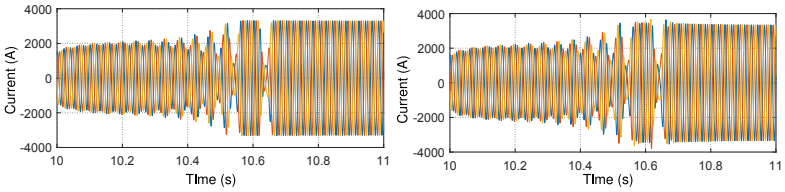

(c) Converter currents (d) grid currents

Figure 4.36: Time domain snapshot of physical variables of the grid with the conventional vector control in rectification stage

is only possible up to 0.84p.u. The Inability to go further is the result of severe reactive power requirements under in rectifier operation compared to inverter operation. Fig. 4.41 shows the comparison between the reactive power requirements under inverter and rectifier operation, showing a significant difference for rectifying operation under similar conditions,

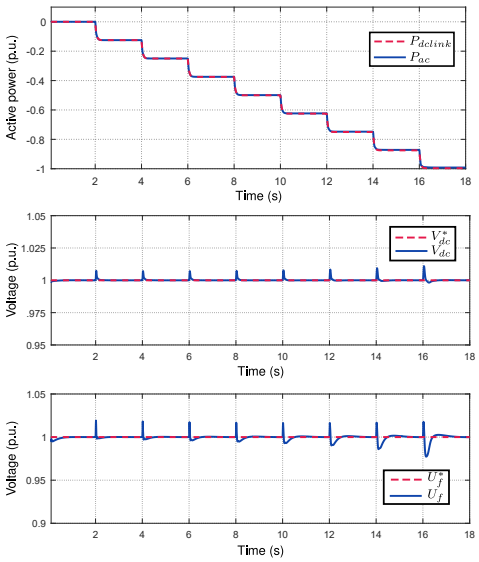

Figure 4.37: Responses of controlled variables under varying operating points in inverter operation with the proposed modifications (a) active power (b) direct-voltage (c) alternating-voltage

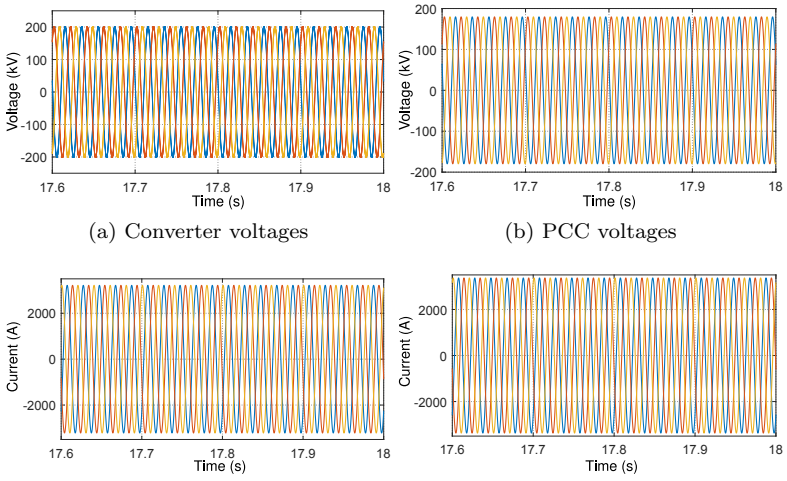

(a) Converter voltages (b) PCC voltages

(c) Converter currents (d) grid currents

Figure 4.38: Time domain snapshot of physical variables of the grid with the modified outer loops in the inversion stage

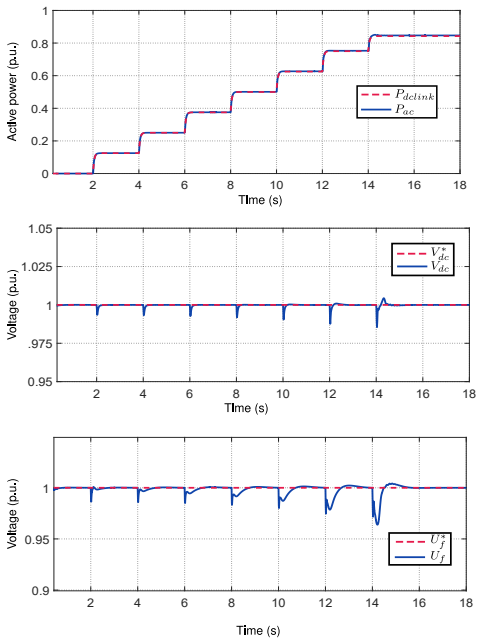

Figure 4.39: Responses of controlled variables under varying operating points in rectifier operation with the proposed modifications (a) active power (b) direct-voltage (c) alternating-voltage

thus limiting the active power capability. This implies that reactive current limit is reached faster in rectifier than in inverter operations such that the maximum active power capability is reduced if stability is to be kept. Additionally, the grid resistance plays more role in rectification than in inversion, and the voltage drop across it may not be negligible, thus, the PCC voltage is affected as a result as the voltage drop cannot be compensated without grid estimation.

To further demonstrate the active power capabilities with the proposed modifications in rectifier operation under an improved grid strength, Fig. 4.42 shows the comparison of active power capabilities under SCR = 1 and SCR = 1.5 showing that the rated power capability is possible with SCR = 1.5. This is due to a considerable reduction in reactive requirements under SCR = 1.5 allowing more room for active power.

Reactive Behavior under Changing Grid Conditions

Fig. 4.43 demonstrates the converter reactive behavior with proposed modifications under changing grid strength in inverter operation. It shows

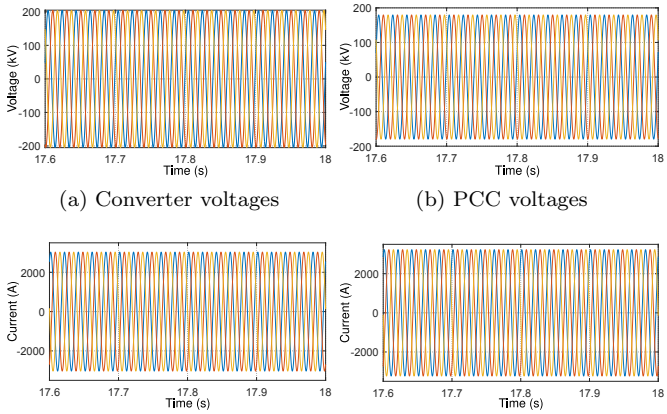

(a) Converter voltages (b) PCC voltages

(c) Converter currents (d) grid currents

Figure 4.40: Snapshot of physical variables of the grid with the modified outer loops in the rectification stage

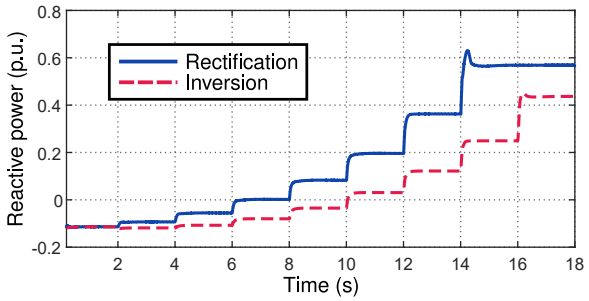

Figure 4.41: Reactive power requirements in inverter and rectifier operations

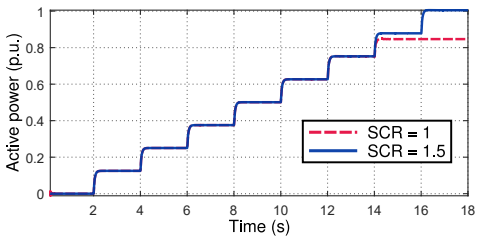

Figure 4.42: Active power capabilities under SCRs 1 and 1.5

clearly in Fig. 4.43a the reactive requirements demanded from the con-

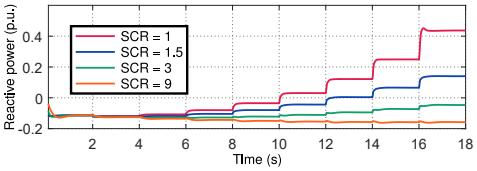

(a) Reactive power

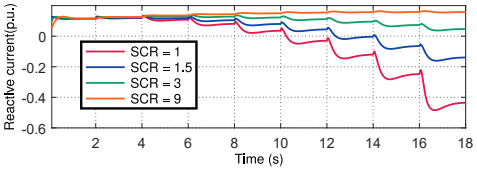

(b) Reactive current

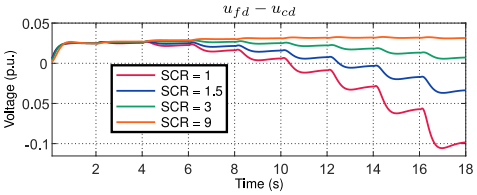

(c) voltage difference ($u_{fd} - u_{cd}$)

Figure 4.43: Reactive behavior under varying grid condition in inversion

verter under SCR = 1 compared to SCR = 1.5 given both grids are till relatively very weak. As grid conditions improve towards a stronger grid, reactive support required of converter drops considerably. Additionally, subplot Fig. 4.43c supports the analysis in previous section on the sign of $(u_{fd} - u_{cd})$ in weak grids. As can be observed, for a fairly strong to strong grid (SCR > 3), the difference is positive across all operating points and reactive requirements are easily managed. However, the difference becomes negative at (SCR < 3) as the grid is severely weakened and the magnitude of negativity increases with increasing active power. The same behavior applies to rectifier operation.

To demonstrate the coordination between the existing AVC and the added reactive power loop, Fig. 4.44 shows the contributions to reactive current from the existing AVC and the additional feedforward term. The figure demonstrates the ability of the additional feedforward term to force reactive power, in most cases providing more reactive current compared to the AVC loop. Additionally, it demonstrates inherent coordination and sharing of responsibility between both channels as the alternating-voltage control maintains the voltage at the reference set point.

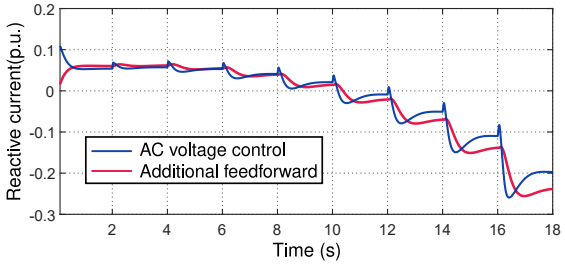

Figure 4.44: Reactive current contributions of AVC and proposed reactive feedforward term

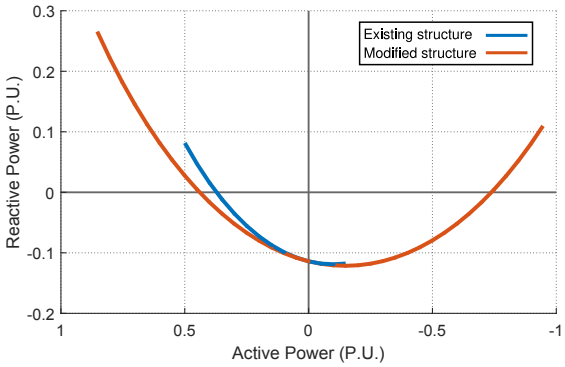

Figure 4.45: Active power capability curve for the existing and proposed modifications

In summary, it has been demonstrated how the simple modification proposed significantly improves the active power capability. Active power capability is improved up to -1p.u. from -0.15p.u., and up to 0.85p.u. from 0.5p.u. without the modifications in the worst case condition (SCR = 1). Fig. 4.45 shows a comparison between the static power capability curve with and without the modifications. It shows the significant improvements with the proposed modifications. It is also demonstrated that once SCR improves to as low as 1.5 which is still a very weak grid, active power capability is possible across the entire operating range of -1p.u. to 1p.u. without losing stability. Results also indicate the performance under any arbitrary grid strength and it shows that complex strategies are not necessarily required to improve the active power capability.

4.5 Chapter Conclusions

The static and dynamic behaviour of the controlled VSC has been characterized across varying conditions and parameters. Varying conditions included operating conditions across the expected range of converter capability, and parameters of controllers, and auxiliary components. It was found that in general, the resonance behaviour of the VSC varies across the operating conditions and parameters. However, its behaviour can be grouped into inversion and rectification behaviour.

Additionally, it was observed that a faster bandwidth is desired of controllers and auxiliary components at the subsystem-level. However, after interconnection with an AC grid and depending on the grid conditions, detrimental interactions ensue at the PCC which requires a compromise in control bandwidth. Generally speaking, low bandwidth of controllers and components is desired. This particularly conflicts with the requirements for the DC grid for instance which require fairly fast bandwidth controllers. Furthermore, it was observed expectedly that if the connected grid is strong, then the bandwidth of control does not play a significant role in stability and eventual capability of the VSC. Therefore, an overall compromise and modification of existing control is required for significant improvements in performance, stability, and thus active power capability in any grid conditions, including weak grids.

Subsequently, a passivity-based approach was leveraged to obtain insights into variables and parameters for which under strong grids do not necessarily provide information about system behaviour. Nevertheless, under very weak grids the evolution of these same variables determines the detrimental behaviour of the VSC when interconnected. Then, a solution was proposed to feedforward these variables to the converter among other compromises as analysed to obtain a tradeoff in controller requirements. More importantly, proposed modification is simple, easy to adopt, and scale to any converter.

Finally, the converter was re-characterized to consider the modification which shows improvement over the characterization with existing controls. The efficacy of the modified controller in significantly improving the behaviour, stability, and thus active power capability was demonstrated.

5

Analysis and Control of Interconnected Hybrid AC/DC Grids

This chapter delves into the mechanism of interaction between AC and DC subnetworks of an interconnected hybrid AC/DC grid. Specifically, the functions that predict interactions between variables on either side are analysed considering the impacts of different components. Further, the impacts of the characteristics of each connected subnetwork on the ensuing interaction are discussed. After this, solutions are proposed to mitigate interactions and improve the capability of a typical AC/DC grid. Finally, interactions between a VSC interconnected on both sides, with a synchronous generator on the AC side are analysed and solutions proposed to mitigate detrimental interactions.

5.1 Introduction

The fast-changing energy landscape, the need for connecting divers resources, bulk power transmission, the limits of existing infrastructure, and long distances have meant that hybrid AC/DC grids are the most feasible solution in future systems. The future of transmission infrastructure has been anticipated as a system that leverages both AC/DC technologies [160]. Literature on applications and control of hybrid AC/DC microgrids is quite comprehensive and vast, and many strategies have been studied [161–165]. However, microgrids are more suited to shorter distances and isolated networks, with sparse structures. For bulk power transmission interconnecting different networks of different characteristics

and interconnecting topologies, interactions are complex and many factors contribute in elaborate ways.

As previous chapters discussed, the analysis and control of hybrid AC/DC grids can be considered as control of several subnetworks interfaced by converters. Notwithstanding, subnetworks are expected to be in constant interaction with each other which cannot be neglected. Although, in some cases, the interaction may be inconsequential and thus, may be ignored. In other cases, this may not hold and it is desired to obtain insights into how several components contribute to the interaction between the AC and DC sides as opposed to only within either one. Then, it becomes straightforward to determine cases where the subnetworks can be safely assumed to be decoupled and cases where such an assumption may not hold. As presented in Chapter 2, the implemented controllers, components, etc., contribute to the interaction gains, in addition to the characteristics of the connected network on either side as will be seen.

5.2 Interactions in AC-DC grids

In Chapter 2, the impedance models for both the AC and DC sides of a VSC were derived as subsystems with an equivalent circuit diagram shown in Fig. 2.11. In the subsequent chapters, the impedance models of both sides were applied in analysing the system-level behaviour and interaction on either side (AC-AC, DC-DC). The interaction between the AC and DC sides can be predicted by adopting the interaction transfer functions described by the off-diagonal elements in (2.45). Particularly, the interaction transfer functions between the alternating and direct-voltages. Then, imposing the equivalent of the interconnected networks as seen from any arbitrary terminal as shown in Fig. 5.1.

For a direct-voltage controlled terminal from (2.31) (re-written for ref-

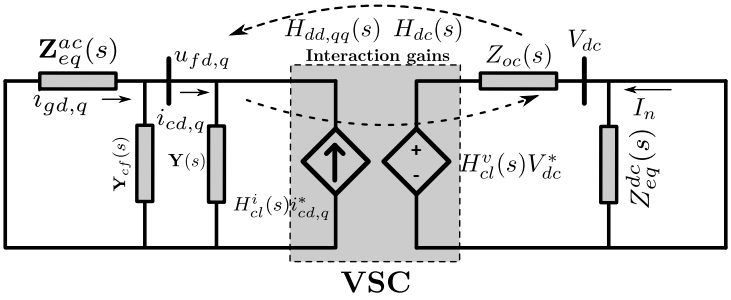

Figure 5.1: Schematic circuit of interconnected AC-DC grid as seen from any arbitrary terminal with a VSC interface

erence),

$$\Delta V_{dc} = H_{dd}(s)\Delta u_{fd} + H_{qq}(s)\Delta u_{fq} + Z_{oc}(s)\Delta I_n. \tag{5.1}$$

Including the bus capacitor (if available) and the interconnection with the AC grid, the PCC voltage vectors consisting of Δu_{fd} and Δu_{fq} can be obtained as

$$\Delta \mathbf{u}_f = \frac{\mathbf{Z}_{cf}(s)}{\mathbf{Z}_{cf}(s) + \mathbf{Z}^{ac}_{eq}(s)}\Delta \mathbf{u}_g - \frac{\mathbf{Z}_{cf}(s)\mathbf{Z}^{ac}_{eq}(s}{\mathbf{Z}_{cf}(s) + \mathbf{Z}^{ac}_{eq}(s)}\Delta \mathbf{i}_c \tag{5.2}$$

where

$$\Delta \mathbf{u}_f = \begin{pmatrix}\Delta u_{fd} & \Delta u_{fq}\end{pmatrix}^T,\ \Delta \mathbf{i}_c = \begin{pmatrix}\Delta i_{cd} & \Delta i_{cq}\end{pmatrix}^T,\ \Delta \mathbf{u}_g = \begin{pmatrix}\Delta u_{gd} & \Delta u_{gq}\end{pmatrix}^T$$

are the PCC voltages, converter currents, and grid voltage (behind the impedance), respectively. Whereas, $\mathbf{Z}_{cf}$ and $\mathbf{Z}^{ac}_{eq}$, are the impedance of the filter capacitor and AC grid respectively. If a capacitor is not available or disconnected, $\mathbf{Z}_{cf} = \infty$ and its impact cancels out. Substituting for $\Delta \mathbf{u}_f$ into (5.1) and assuming an infinite AC grid voltage source

$$\Delta V_{dc} = -H_{dd}(s)\frac{Z_{cf,dd}(s)Z^{ac}_{eq,dd}(s)}{Z_{cf,dd}(s) + Z^{ac}_{eq,dd}(s)}\Delta i_{cd} - H_{qq}(s)\frac{Z_{cf,qq}(s)Z^{ac}_{eq,qq}(s)}{Z_{cf,qq}(s) + Z^{ac}_{eq,qq}(s)}\Delta i_{cq} + \frac{Z_{oc}(s)Z^{eq}_{dc}(s)}{Z_{oc}(s) + Z^{eq}_{dc}(s)}\Delta I_n. \tag{5.3}$$

The first term is the equivalent AC impedance on the d-axis reflected on the DC grid, the second term is the corresponding q-axis impedance, and the last term is the equivalent DC impedance as seen on the DC side (this is the same as Z_{ii} derived in Chapter 2). These terms predict how the DC grid interacts with the AC grid given the characteristics of the AC grid and vice-versa. For instance, on first observation, if the AC grid is very strong, $Z^{ac}_{eq,dd} \to 0$, then, the AC impedances cancel out and there is no interaction with the DC grid as ΔV_{dc} only consists of the DC impedance. This can be easily conjectured from the analyses detailed in Chapter 3. On the alternative, if either one of the interaction gains $H_{dd,qq} \approx 0$ then the AC impedances also cancel out. However, considering the complexity of the VSC, it may be difficult to obtain $H_{dd,qq} \approx 0$ and also difficult to quantify how low they should be. Both H_{dd} and H_{qq} depend on all implemented controllers and passive components on both AC and DC sides (See Chapter 2). The same procedure can be adopted for any other control strategy as implemented in the converter.

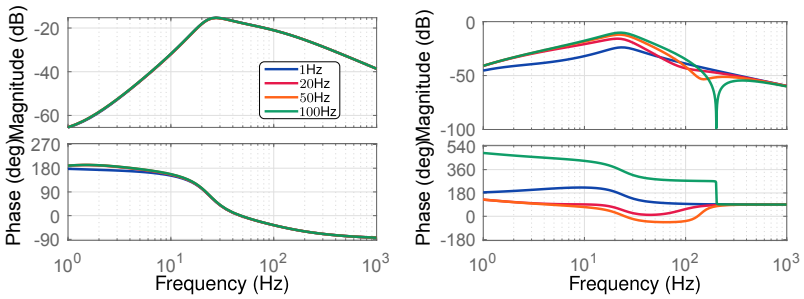

(a) Interaction gain H_{dd} (b) Interaction gain H_{qq}

Figure 5.2: Impact of varying PLL bandwidths on the interaction gains between AC and DC sides

5.2.1 Impact of PLL on Interaction and Reflected Impedances

For a DC network interconnected with an AC grid as illustrated in Fig. 4.6, the impact of varying PLL bandwidths on the interaction gains between the AC and DC sides, as a component of the reflected impedances is illustrated by the frequency responses shown in Fig. 5.2. It can be observed that the impact of PLL bandwidths is negligible on the d-axis. On the q-axis, increasing bandwidth of the PLL increases the interaction gain which in turn impacts the interaction between the AC and DC sides. As PLL bandwidth is further increased, an interaction between the PLL and the inner loop (with a bandwidth of 105Hz) ensues, shown by the sudden dip in the interaction function. A clearer impact of the PLL bandwidth is obtained when the characteristic of the AC grid is included.

The frequency responses of the reflected impedances from the AC side on the DC as derived in (5.3) for different SCRs for a PLL bandwidth of 50Hz is shown in Fig. 5.3. In general, increasing SCR simply shifts the existing resonance at the PCC to the high-frequency side while reducing the magnitude. As discussed in Section4.4, these can be easily mitigated using the PCC voltage feedforward filters with a cut-off frequency of the inner loop. Recall that, it was discussed that feedforward filters with a bandwidth equal to that of the inner current loop ensures positivity above $2f_1$ by damping out those resonances.

Further, observe that the magnitude of the low-frequency resonance on the q-axis impedance around 20Hz in Fig. 5.3b is high for low SCRs, and reduces significantly as SCR increases; nearly a decade higher at SCR of 1 compared to 9. This directly indicates more interactions between the AC and DC sides when the AC grid has a high impedance characteristic.

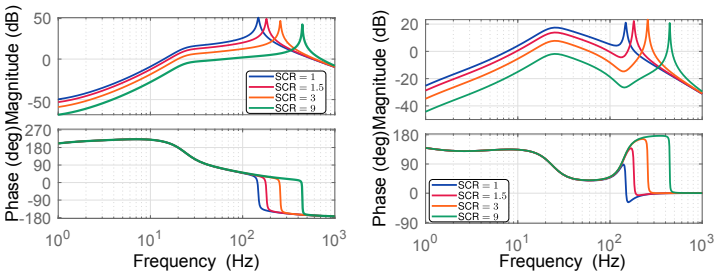

(a) Reflected impedance on d-axis (b) Reflected impedance on q-axis

Figure 5.3: Impact of varying SCR on the reflected impedances for a PLL bandwidth of 50Hz

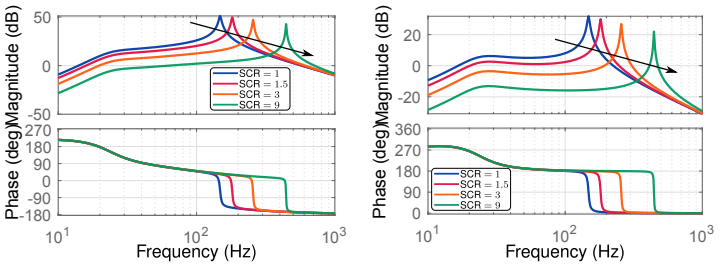

(a) Reflected impedance on d-axis (b) Reflected impedance on q-axis

Figure 5.4: Impact of varying SCR on the reflected impedances for a PLL bandwidth of 1Hz

However, these low-frequency interactions cannot be mitigated by feedforward filters as it was discussed in the previous chapter that a feedforward filter of low bandwidth may potentially destabilize the low-frequency resonance. Hence, such interaction studies must be carried out to have an insight into the impacts of different components.

For a reduced PLL bandwidth of 1Hz, the frequency responses of the reflected impedances are shown in Fig. 5.4. It can be seen that the low-frequency resonance is damped and this explains the slightly improved capability obtained for a low bandwidth PLL. Additionally, the d-axis impedance and high-frequency resonance remain unchanged. In summary, it can be conjectured that the q-axis is responsible for most of the interactions induced by the PLL as d-axis interaction gain and impedance do not show significant changes.

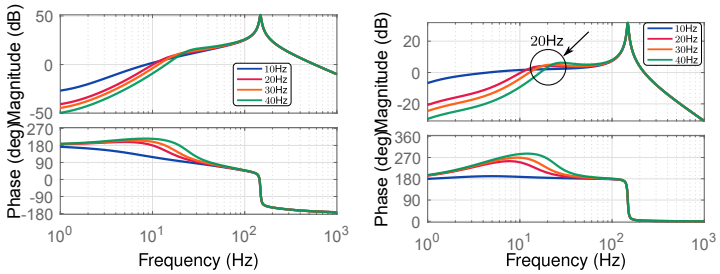

(a) Reflected impedance on d-axis (b) Reflected impedance on q-axis

Figure 5.5: Impact of varying bandwidths of the DVC for SCR = 1 on the reflected impedances for a PLL bandwidth of 1Hz

5.2.2 Impact of Direct-Voltage and Control

The impacts of varying bandwidths of the DVC on the reflected impedances are shown in Fig. 5.5 for a PLL bandwidth of 1Hz and SCR = 1. As can be seen, most of the impact occurs in the low-frequency side below 20Hz. As the $q-$axis impedance shows, a slightly slower DVC is desired. However, these impacts are not so significant. It is important to note that this impact is related to interactions between the AC and DC side, rather than on any side. The time-domain responses of the PCC alternating-voltage magnitude and direct-voltage magnitude are shown in Fig. 5.6 for varying bandwidth of the DVC. As expected, the bandwidth of the DVC only significantly affects the direct-voltage on the DC side, but this can only be detected from the DC impedance model. Although there is appears to be an impact around 20Hz as shown in Fig. 5.5b, the impact on the PCC voltage magnitude is insignificant.

For an increase in the DC capacitance model from the initial value of 150μF by a factor of 10, Fig. 5.7 shows the corresponding impacts on the reflected impedances for an AC grid of SCR = 1 and PLL bandwidth of 1Hz. Although a higher capacitance reduces the impact of the high-frequency resonance above $2f_1$, it also introduces a low-frequency resonance which with a potential risk since in weak grid conditions, resonances below the fundamental frequency f_1 dominates. Hence, the DC capacitance should be as low as to prevent the risk of low-frequency resonance that is aggravated in a weak grid. This was shown previously that, while a higher DC capacitance improves the direct-voltage dynamics, it also introduces a low-frequency risk with the AC side. Similar to the previous subsection, the high-frequency resonance above $2f_1$ can be easily mitigated. Since changing the equivalent DC capacitance also changes imposed DC impedance, Fig. 5.8 shows the frequency responses of the

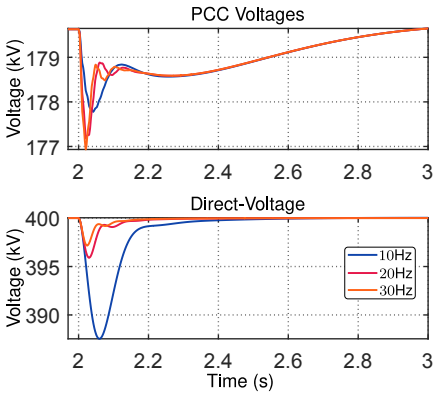

Figure 5.6: PCC voltage and direct-voltage responses for varying bandwidth of the DVC

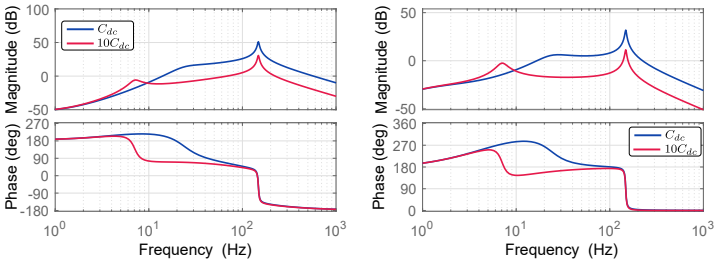

(a) Reflected impedance on d-axis (b) Reflected impedance on q-axis

Figure 5.7: Impact of DC capacitances on the reflected impedances

reflected impedances and the DC impedance. It shows the increased DC capacitance in Fig. 5.8b, a common low-frequency resonance between the AC and DC sides. This may occur in an interconnected DC side with more than one terminal, in which the equivalent capacitance of the grid as whole impacts on any terminal controlling the direct-voltage (as described in Chapter 3). The time-domain responses are shown in Fig. 5.9 verifying the low-frequency resonances in both AC and DC system quantities for the case of higher DC capacitances.

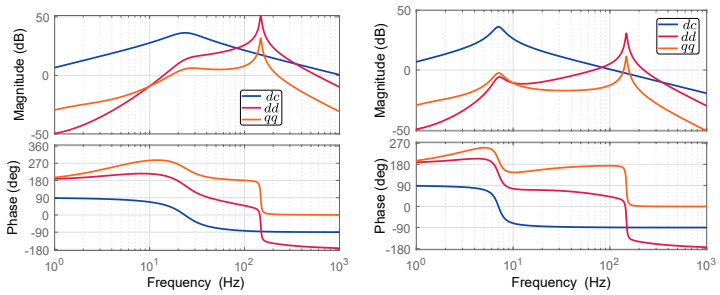

(a) C_{dc} (b) $10C_{dc}$

Figure 5.8: Comparison between the reflected impedance and DC impedances for different DC capacitances

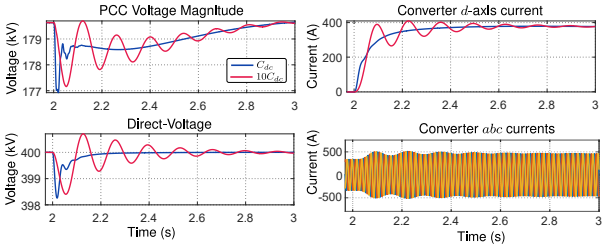

Figure 5.9: AC and DC system responses for varying DC capacitance

5.3 Interconnection of Two Weak AC Grids Through an HVDC Link

5.3.1 System Level Interaction Analysis

The previous chapter highlighted the challenges of integrating a VSC to a weak grid. This section presents the analysis of interactions in an HVDC system interconnecting two weak AC grids. Then, the solutions proposed in the previous chapter are adopted to improve the active power capability of the system. The interconnected HVDC system is illustrated in Fig. 5.10 where it is shown the potential path in which interactions could occur. Regardless, the DC grid will be the major channel for interactions. The VSC-HVDC link is operated in master-slave mode with VSC-1 in direct-voltage control mode.

The reflected impedances between each AC and DC subnetworks at each terminal and the DC grid equivalent at each terminal can be derived from

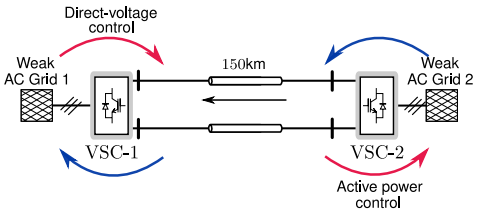

Figure 5.10: Interconnected weak grids through VSC-HVDC Link

(5.1) as

$$\Delta V_{dc,1} = Z^{ref}_{dd,1}(s)\Delta i_{cd,1} + Z^{ref}_{qq,1}(s)\Delta i_{cq,1} + Z_{11}(s)\Delta I_1 \tag{5.4a}$$

$$\Delta V_{dc,2} = Z^{ref}_{dd,2}(s)\Delta i_{cd,2} + Z^{ref}_{qq,2}(s)\Delta i_{cq,2} + Z_{22}(s)\Delta I_2 \tag{5.4b}$$

where $Z_{11}(s)$ and $Z_{22}(s)$ are obtained from the aggregation of the DC subnetwork given as

$$\mathbf{Z}^{cl}_{dc}(s) = \begin{pmatrix} Z_{11}(s) & Z_{12}(s) \\ Z_{21}(s) & Z_{22}(s) \end{pmatrix} = \begin{pmatrix} \frac{Z_{oc,1}Z_{net,1}}{Z_{oc,1}+Z_{net,1}} & \frac{Z_{oc,1}Z_{oc,2}}{Z_{oc,1}+Z_{net,1}} \\ \frac{Z_{oc,2}Z_{oc,1}}{Z_{oc,2}+Z_{net,2}} & \frac{Z_{oc,2}Z_{net,2}}{Z_{oc,2}+Z_{net,2}} \end{pmatrix} \tag{5.5}$$

with

$$Z_{net,1}(s) = Z_{oc,2}(s) + Z_{cab,12}(s)$$
$$Z_{net,2}(s) = Z_{oc,1}(s) + Z_{cab,12}(s)$$

where $Z_{oc,1}$ and $Z_{oc,2}$ are the DC impedance models of each VSC.

The frequency responses of the reflected impedances of the AC side on the DC side of each terminal and the DC impedance equivalent for weak grids with SCR = 1.5 on both sides is shown in Fig. 5.11. Multiple crossings can be detected at both terminals between the reflected impedances and the DC equivalent especially in the low-frequency region below approximately 105Hz which is the bandwidth of the inner loop. Hence, detrimental interactions at these crossings will result in instability.

The phase voltages and currents for a step-change in active power at terminal 2 at 2s are shown in Fig. 5.12 in the case where both AC grids are weak. Since the step-change is initiated at terminal 2, instability occurred first at this terminal, which is then transferred to the DC grid through the direct-voltage controlled by VSC-1. It can be seen from Fig. 5.12b that the phase currents are distorted, while the phase voltages are distorted with multiple resonances.

For strong grids with SCR = 9 on both sides of the HVDC network, Fig. 5.13 shows the frequency responses of the reflected impedances and the DC equivalents at each terminal. For such a strong grid, it can be seen

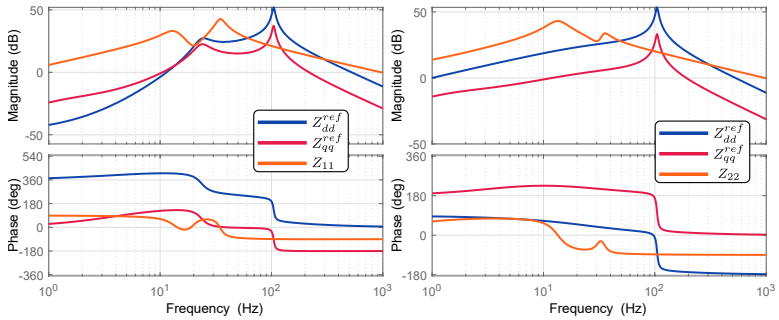

(a) Terminal 1 (b) Terminal 2

Figure 5.11: Frequency responses of the reflected impedances and DC equivalents for weak AC grids

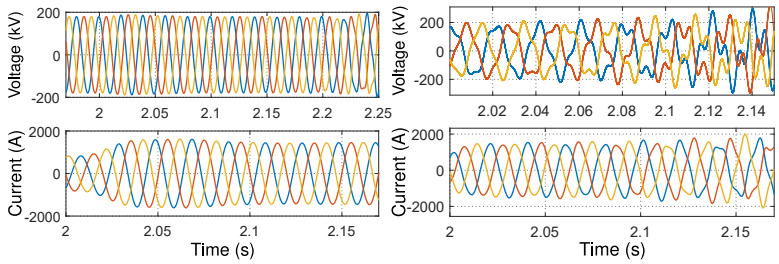

(a) Terminal 1 (b) Terminal 2

Figure 5.12: Phases voltages and currents for the interconnected weak AC grids

that crossings between the reflected impedances and DC equivalents are restricted to the high-frequency region far away from typical resonances of the system and all impedances, especially the reflected impedances are low.

The corresponding phase voltages and currents for a step-change in active power similar to the previous is shown in Fig. 5.14 for strong AC grids. Voltages and currents are as expected in both AC grids demonstrating an interaction-free system. The direct-voltage responses for both cases of strong and weak AC grid are shown in Fig. 5.15 showing the instability due to interactions. This occurred through interactions at terminal 2 that transferred to the direct-voltage through the interaction transfer functions and subsequently to the direct-voltage controlling terminal at terminal 1.

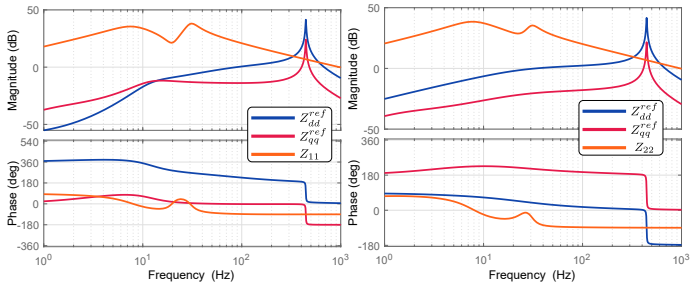

(a) Terminal 1 (b) Terminal 2

Figure 5.13: Frequency responses of the reflected impedances and DC equivalents for strong AC grids

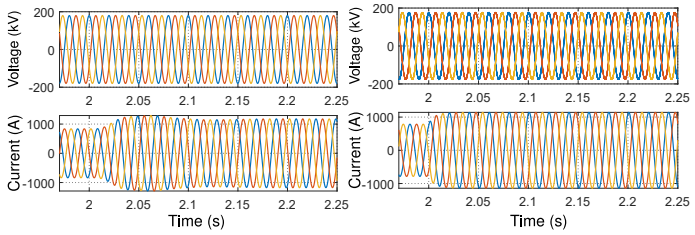

(a) Terminal 1 (b) Terminal 2

Figure 5.14: Phases voltages and currents for the interconnected strong AC grids

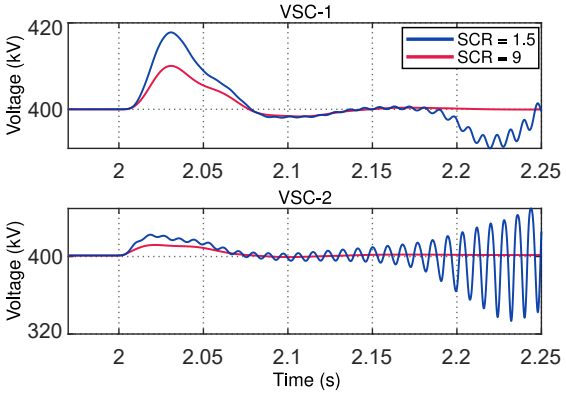

Figure 5.15: Direct-voltage responses for both strong and weak cases

5.3.2 Network Decoupling Through Impedance Shaping

The previous subsection highlighted the interaction behaviour of interconnected hybrid AC/DC grids as predicted by the interaction functions and reflected impedances. The system impedances can be decoupled through impedance shaping. Previous research efforts have mainly focused on impedance shaping through modification of controller bandwidth. In this work, impedance shaping through the use of extra feedforward terms as detailed in Chapters 3 and 4 is adopted. This is to accommodate practical cases in which direct modification of existing controllers may not be possible.

On the DC side, it was proposed in Section 4.4 to reduce the DVC bandwidth and feedforward the direct-voltage on the $d-$axis. This is similar to the proposal for meshed DC grids in Chapter 3. However, the system is fairly small and the methodology described is not necessary. The controller is a bandpass filter with a centre frequency $\omega_{v0} = 22.5$Hz. This is implemented in the direct-voltage controlling station of Fig. 5.10, similar to the block diagram of Fig. 4.31a. This effectively decouples the direct-voltage controlling station from the active power terminal. On the AC side of each VSC where the PCC voltage magnitude is controlled, and the grid is weak (with SCR $= 1.5$), it was proposed similarly in Chapter 4 to feedforward the difference $(u_{fd} - u_{cd})$ on the $q-$axis through a low-pass filter. Here, the cut-off frequency of the filter $\omega_u = 8$Hz and gain $k_{fu} = 0.04$ as shown in Fig. 4.31b. This is implemented in both VSCs as supplementary signals since both AC grids are weak. The structures of the controllers and filters remain the same as in Fig. 4.31.

The frequency responses of the interaction transfer functions between the alternating and direct-voltages of VSC-1 is shown in Fig. 5.16. The interaction functions of the modified control loops are lower compared to the existing control loops. This indicates fewer interactions according to

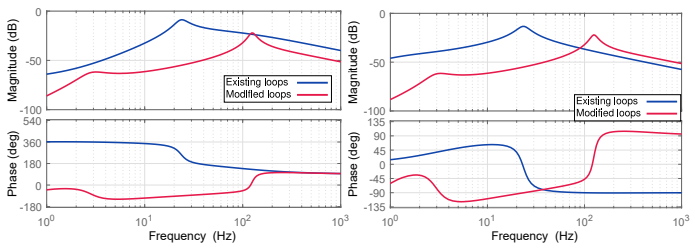

(a) $d-$axis interaction function (b) q-axis interaction function

Figure 5.16: Interactions functions of existing and modified control loops (Direct-voltage controlled)

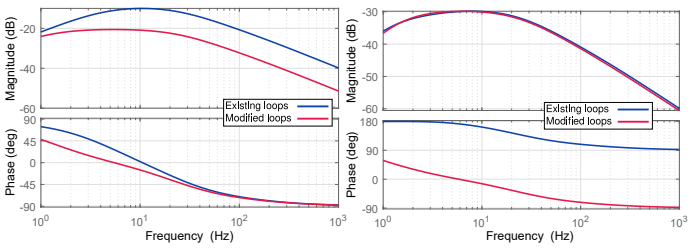

(a) $d-$axis interaction function (b) q-axis interaction function

Figure 5.17: Interactions functions of existing and modified control loops (Active power controlled)

(5.3), depending on the conditions of the connected grid. The corresponding frequency responses of the interaction functions of the active power controlling terminal at VSC-2 is shown in Fig. 5.17. Similar conclusions can be made, except for the $q-$axis where there is no significant difference in magnitude, but rather in phase.

For a complete picture of the impact of interactions considering the weak grid at VSC-1, Fig. 5.18 compares the frequency responses of the reflected impedances on either axes for the existing and modified loops. Expectedly, the magnitudes of the impedances have been reduced especially in the low-frequency region where the effect of weak grids is most felt. The additional feedforward terms succeeded in targeting the low-frequency interaction resonances. Additionally, the phase margin of both axes has been improved. Similarly, Fig. 5.19 shows the frequency responses of the reflected impedances at VSC-2. It is shown that improvement is not significant compared to VSC-1, particularly in magnitude. This is due to only modifying the $q-$axis. However, improvement is seen in the phase margin of the q-axis response.

The combined frequency responses of the reflected impedances and the DC terminal equivalents as seen from each terminal after modification is shown in Fig. 5.20. Comparing with the case without the feedforward terms in Fig. 5.11, the interaction points especially in the low-frequency region on both terminals have been effectively eliminated.

5.3.3 Time Domain Simulations

Time domain simulations have been carried out to verify the frequency domain analysis and predictions for several cases.

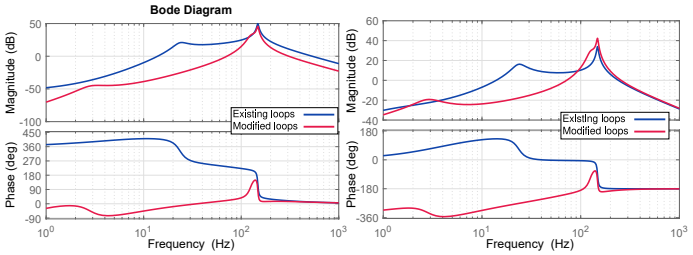

(a) Reflected impedance on $d-$axis(b) Reflected impedance on $q-$axis

Figure 5.18: Reflected impedances of existing and modified control loops—VSC-1

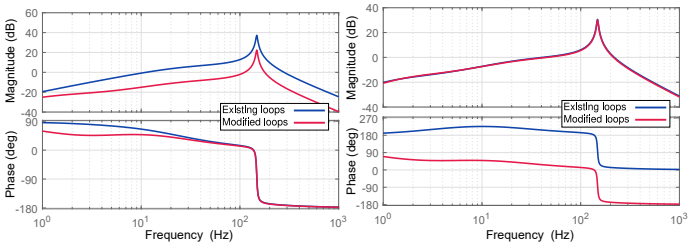

(a) Reflected impedance on $d-$axis(b) Reflected impedance on $q-$axis

Figure 5.19: Reflected impedances of existing and modified control loops—VSC-2

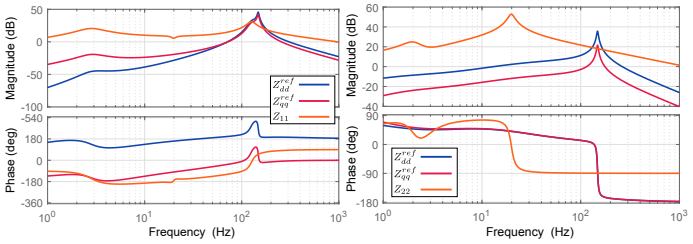

(a) Terminal 1 (b) Terminal 2

Figure 5.20: Frequency responses of the reflected impedances and DC equivalents

Impact of Supplementary Loops on Oscillations

In the first instance, the proposed feedforward signals are only implemented in the direct-voltage controlling terminal, VSC-1. The three-phase

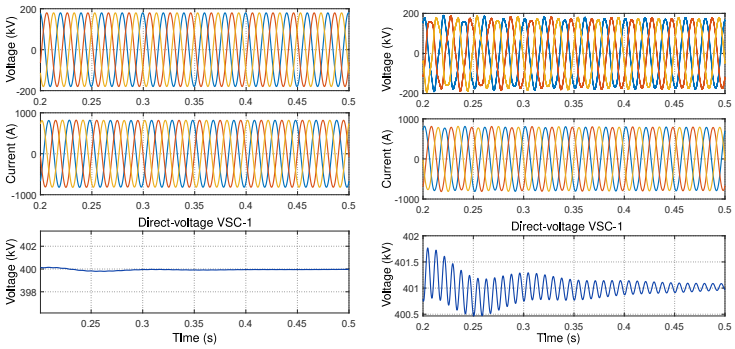

(a) VSC-1 (b) VSC-2

Figure 5.21: Time domain responses for SCR = 1.5 in each connected AC grid with supplementary controls only at VSC-1

voltages and currents, and the direct-voltage responses at each of VSC-1 and VSC-2 for AC grid SCR of 1.5 are shown in Fig. 5.21. As can be seen, since VSC-1 has been partially decoupled from VSC-2 through the direct-voltage, VSC-1 is oscillations-free and stable. However, residual oscillations from VSC-2 can still be seen due to the direct-voltage control action of VSC-1. At VSC-2, although the system is stable, both low and high-frequency oscillations can be seen. This is the effect of the weak grid of VSC-2, for which VSC-1 has been partly decoupled. The time-domain responses for supplementary controllers in both terminals are shown in Fig. 5.22. As it can be seen, responses at both terminals are without resonances as each supplementary loops on either axis mitigate interactions on either side of the VSC.

Capability Improvement under Weak Conditions

As discussed in the previous section and chapter, the capability of the VSC with existing controllers is limited. Here, we demonstrate that the proposed solutions can improve the capability of the interconnected hybrid AC/DC grid. The time responses for a step-change in active power to 400MW from VSC-2 at 2s is shown for an SCR of 1.5 without the supplementary is shown in Fig. 5.23. The system is unstable with interactions of varying frequencies. Although VSC-1 attempted to control the direct-voltage, the growing oscillations in VSC-2 relative to its weak grid are transferred to the VSC-1.

For supplementary loops implemented in both terminals, Fig. 5.24 shows the time-domain responses for the same conditions. As can be seen, the interactions have been mitigated and the system transitions as

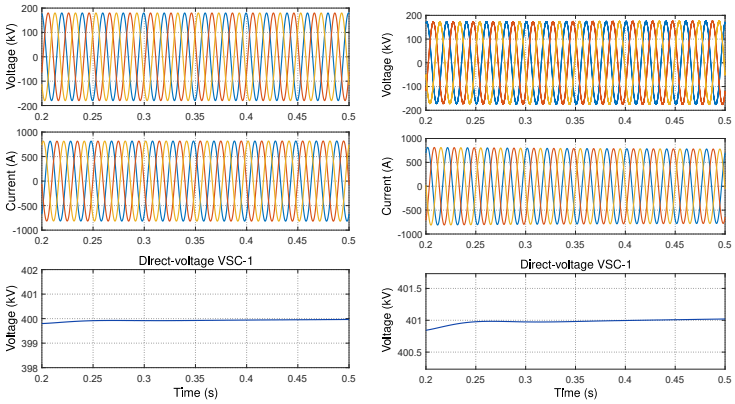

(a) VSC-1 (b) VSC-2

Figure 5.22: Time domain responses for SCR = 1.5 in each connected AC grid with supplementary control in both terminals

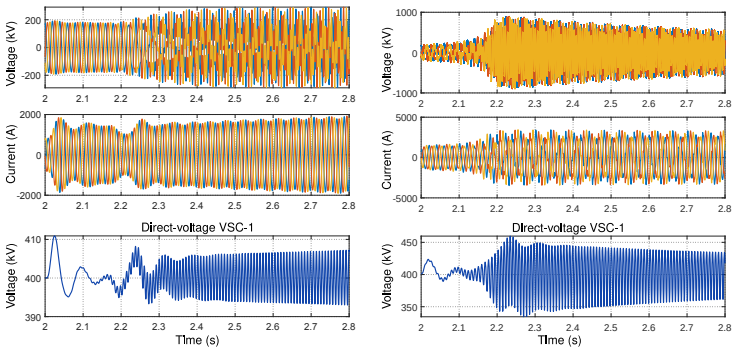

(a) VSC-1 (b) VSC-2

Figure 5.23: Time domain responses for SCR = 1.5 in each connected AC grid without supplementary control

expected. The residual oscillation seen is a consequence of the equivalent DC grid capacitance. Nevertheless, this is a well-damped oscillation as AC responses show and should not present any challenges. To demonstrate that the added supplementary loops are robust to changes in SCR, Fig. 5.25 shows the response to the same conditions as previous for SCR of 9 in both AC grids. It can be observed that the system operates stably without oscillations. Hence, supplementary loops simply share responsibilities with the existing control, indicating flexibility to any grid conditions.

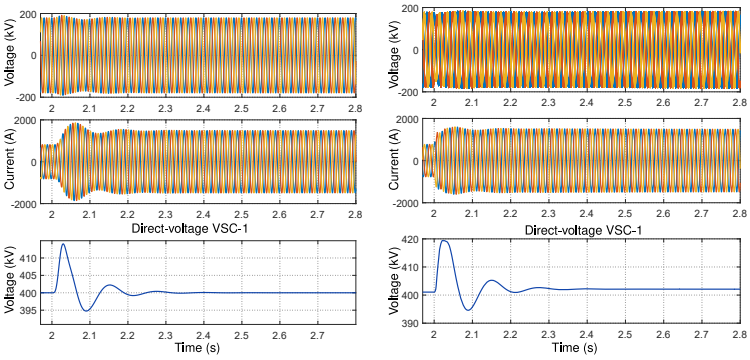

(a) VSC-1 (b) VSC-2

Figure 5.24: Time domain responses for SCR = 1.5 in each connected AC grid with supplementary controls

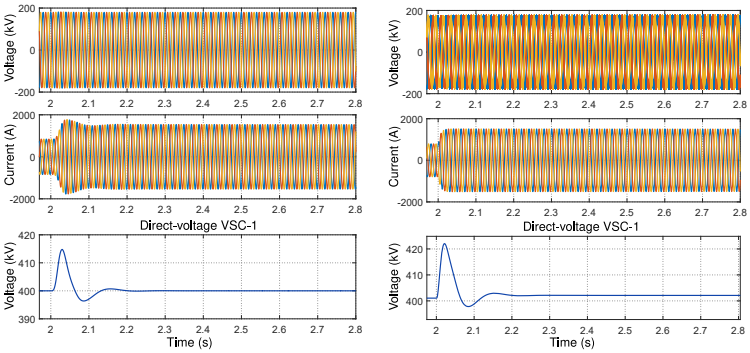

(a) VSC-1 (b) VSC-2

Figure 5.25: Time domain responses for SCR = 9 in each connected AC grid with supplementary controls

5.4 Interactions in Hybrid AC-DC grids with Synchronous Generator

Much has been discussed about future transmission systems and the domination of power electronic interfaced hybrid AC/DC grids. Regardless, it is expected that conventional synchronous generators will still form a considerable part of hybrid AC/DC grids including power electronic devices. Hence, interactions between both devices are anticipated given the inherent differences between them, such as time scale of control. There-

fore, it is of interest to understand potential sources of interactions when these devices are connected over a network. A simplified single-line diagram of a hybrid AC/DC grid interconnecting a VSC and a synchronous generator is illustrated in Fig. 5.26. The network integrates two offshore resources through the DC grid, and the onshore converter connects with the generator through the AC grid with both controlling the AC voltages at their respective buses.

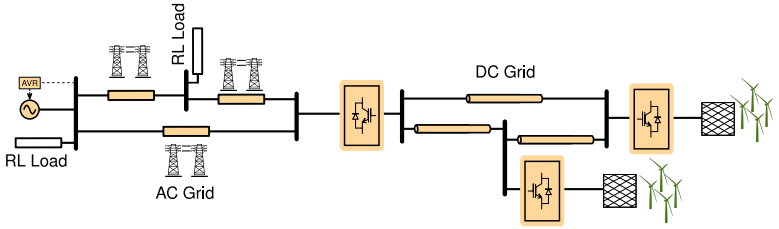

Figure 5.26: Single-line diagram of a hybrid AC/DC grid with a controlled synchronous generator

Following the modelling procedures highlighted in Chapter 2, Fig. 5.27 illustrates the interconnection of subsystems of interest and their corresponding control modes and the equivalent matrices.

5.4.1 Subsystem Sensitivity to Controller Parameters

The magnitude response of the impedance models of the synchronous generators to varying gains of the excitation control system from $5 - 250$ is shown in Fig. 5.28. Here, it can be observed that at the generator terminal level, the impact of the amplifier gain is a frequency shifting behaviour. However, the true impact of the AVR amplifier is most observed on interconnection with the network and the network's topology.

On the converter AC side, Fig. 5.29 shows the sensitivity of converter output impedance to varying droop gains. It can be seen at the terminal level that increasing droop gain results in increasing the magnitude of resonances and shift towards the high-frequency side. As droop gain is significantly increased the magnitude of resonances seems to decrease. This is the result of the VSC having a behaviour closer to a direct-voltage controlled converter which may not be desired. The response of the DC side impedance of the VSC is shown in Fig. 5.30 for a similarly increasing droop gain shows the opposite behaviour. For increasing droop gain, the steady-state gain reduces. This is equivalent to a lower steady-state deviation as expected. Furthermore, although a similar frequency shifting is observed, the increasing droop gain steadily reduces the magnitude of resonance. This suggests a low droop gain is desired on the AC side and

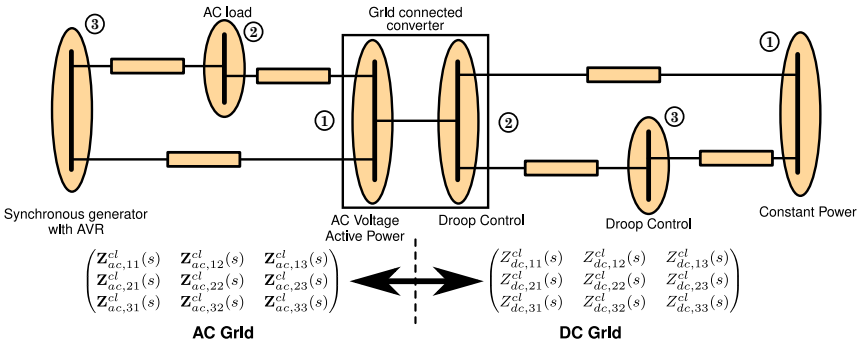

Figure 5.27: Interconnection of equivalent subsystems of the hybrid AC/DC grid

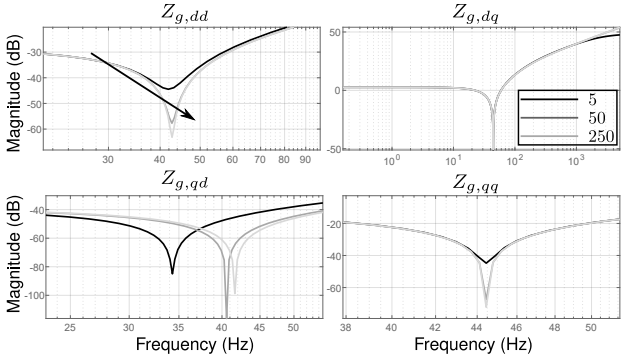

Figure 5.28: Frequency response of generator equivalent impedance with varying amplifier gains

a slightly higher gain on the DC side. Proper operation thus requires a trade-off considering the entire system responses (on both AC and DC sides).

5.4.2 Interconnected Responses of the Network

After the aggregation efforts of each subnetwork, Fig. 5.31 shows the frequency response plot of total impedance equivalents at the controlled buses 1 (converter) and 3 (generator), and the transfer impedance between them for nominal droop gain and AVR gains given in Table 5.1. At the converter terminal, the converter AC impedance has been reshaped and new resonances introduced around 225Hz and a slightly damped resonance around 7 Hz. Whereas on the generator side, the 225Hz resonance is clear and the 7Hz resonance has a higher magnitude as seen from this bus.

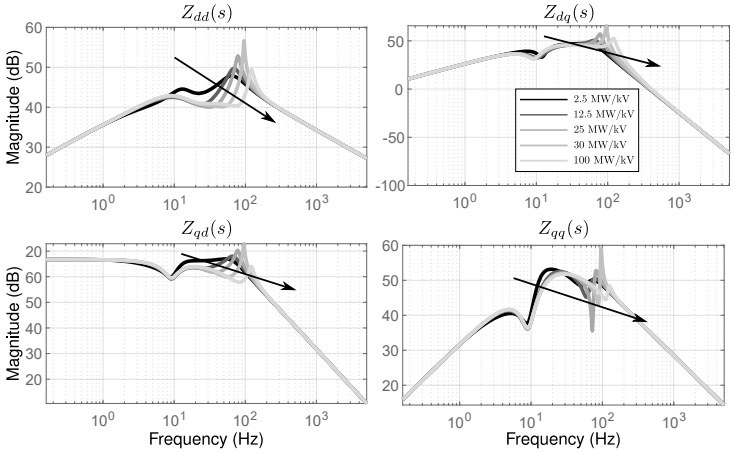

Figure 5.29: Frequency response of the equivalent AC impedance of the VSC with varying droop gains

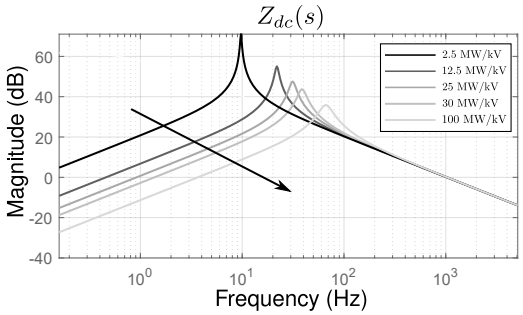

Figure 5.30: Frequency response of the equivalent DC impedance of the VSC with increasing droop gain

Similarly for the DC subnetwork, Fig. 5.32 shows the frequency response of diagonal elements of the DC equivalent matrix showing clearly the resonances seen from each terminal. It can be observed that all terminal in the DC grid have one common resonance frequency around 53 Hz not related to the AC grid, with VSC-3 showing the highest contribution to this frequency, and other distinct frequencies slightly shifted from each other. The low-frequency resonance in the AC grid is shifted slightly to around 9 Hz on the DC grid. This is an interaction point between the AC and DC grids.

Figs. 5.33 shows the time-domain simulation of voltages on the AC side showing distorted waveform with both high and low-frequency resonances as can be observed in the frequency response plot, whereas Fig. 5.34 show

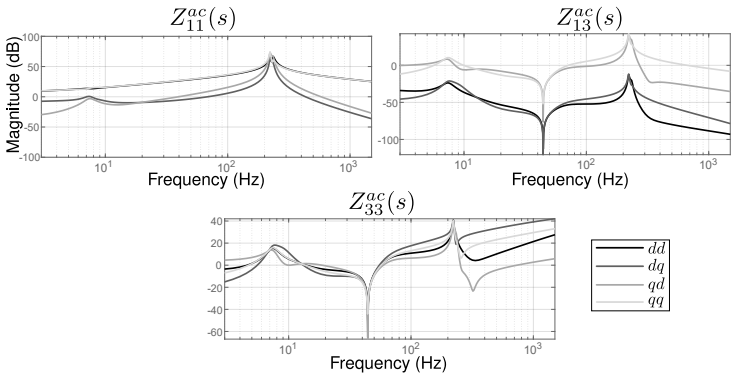

Figure 5.31: Frequency response of equivalent impedances at buses 1 and 3

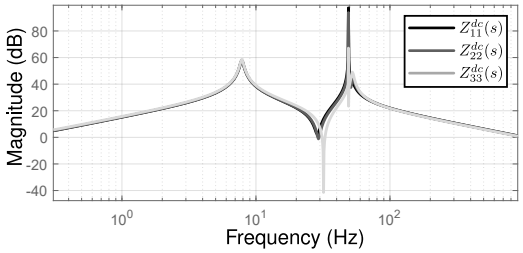

Figure 5.32: Frequency response of terminal impedances of the DC grid

the corresponding DC voltages responses matching the identified resonance frequencies in the response plot. The shown responses are not acceptable as clearly the synchronous generator was not considered in the choice of droop gain in the DC grid. Therefore, either the AVR/exciter gain or DC droop gain must be reduced to minimize the impact of the low-frequency resonance around $5 - 10$Hz. Similarly, the dominant resonance in the DC system not related to the AC grid must also be managed by simply utilizing a damping scheme based on the identified frequencies by simply minimizing the matrix $\mathbf{Z}_{cl}^{dc}(s)$.

For a high droop gain, Fig. 5.35, illustrate clearly the impact of high droop for a step-change in active power in the MTDC grid from the constant power VSC at $t = 3$s. It can be seen that the step-change resulted in the loss of stability in both the AC and DC grids. Therefore, a reduction in droop gain is sort as a compromise. For a reduction in droop gain and exciter regulator gain, Fig. 5.36a depicts the alternating-voltages after a reduction in gain showing an acceptable performance on the AC side. On the DC side, Fig. 5.36b shows the comparison of the responses

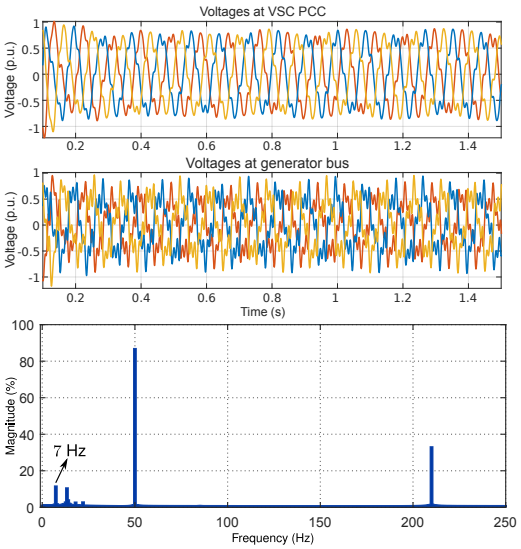

Figure 5.33: Time domain simulation of AC voltages and FFT at VSC PCC and generator bus showing the impacts of generator regulator gain

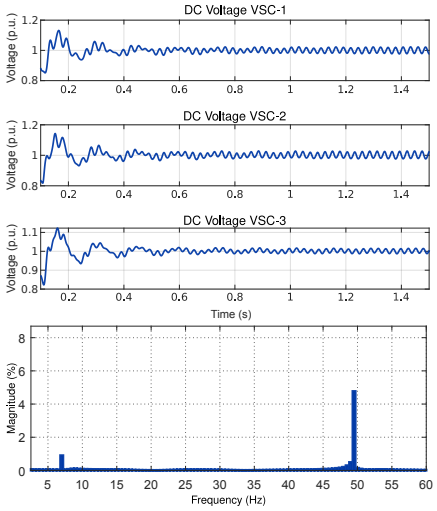

Figure 5.34: Time domain simulation of direct-voltages showing the impact of generator regulator gain and DC side oscillations

of the direct-voltages for a reduction in droop gain with the synchronous generator connected and the default droop gain at that terminal when the

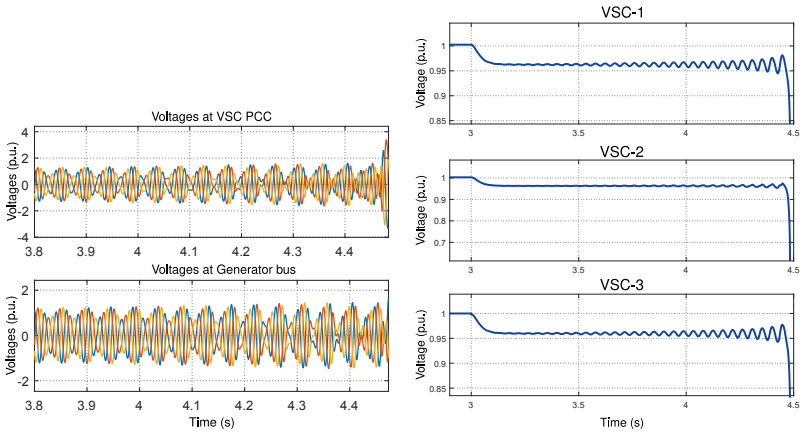

(a) Alternating-voltages (b) Reflected impedance on q-axis

Figure 5.35: Impact of DC droop gain on system responses

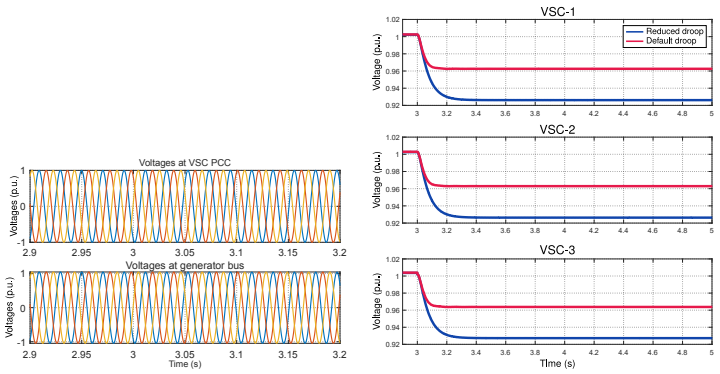

(a) Alternating-voltages (b) Reflected impedance on q-axis

Figure 5.36: Impact of reduced DC droop gain on system responses

generator is disconnected. Particularly, it is shown how that despite the reduced droop gain improving the dynamics on the AC side, it results in a higher deviation in voltages compared to a higher droop gain without a synchronous generator. This demonstrates the required trade-offs in performance required of hybrid AC/DC grids due to conflicting requirements.

Table 5.1: AC-DC Grid Parameters

DC Grid Parameters		
Parameter	**Value**	**Units**
Rated Power	250	MVA
Reference direct-voltage	400	kV
C_{dc}	150	μF
L_{cab}	2.6	mH/km
C_{cab}	0.1908	μF/km
R_{cab}	0.0141	Ω/km
Cable length (12,13,23)	$70, 150, 100$	km
AC Grid Parameters		
Parameter	**Value**	**Units**
Nominal alternating-voltage	± 220	kV (p-p)
L_{cab} (+ve seq.)	0.0011	mH/km
R_{cab} (+ve seq.)	0.028	Ω/km
Cable length (12,13,23)	$123, 200, 115$	km
L	42	mH
C_f	10	μF
R	0.242	Ω
Stator (L_d, L_q, R_s)	4.9825, 4.85, 0.0031	mH, Ω
k_a, k_e, T_e	200, 1, 1.25s	

5.5 Chapter Conclusions

This chapter set out to obtain insights into the mechanism of interactions between the AC/DC sides of an interconnected hybrid AC/DC grids. The impacts of the bandwidth of internal components such as controllers, on subnetwork to subnetwork interactions were investigated. Further, it was demonstrated how these interactions can be mitigated.

The results indicate the mechanism of detrimental interactions and it was shown that supplementary signals through feedforward of relevant variables from both sides of the VSC can improve the overall behaviour. In order cases, a retuning of controllers was simply adequate. One of the most important contributions to existing knowledge is a method to access interactions in hybrid AC/DC grids of arbitrary structures with tractability and ease. Further, it was shown that the main factor for interactions between subnetworks is first dependent on the broad characteristics of each, and several important subsystems. Ultimately, findings contribute in several ways to the understanding of network-level interactions, rather within subnetworks.

6

A Statistical-Physics Approach to Analysis of Coherency in Large-scale HVDC Grids

This chapter explores a fundamental yet advanced modelling and analysis concepts borrowed from molecular and statistical physics for collective modelling and analysis of large-scale and complex systems. In the context of this thesis, this concept is applied to the analysis of coherency to dynamic perturbations in large-scale HVDC grids as a single-entity both in steady-state and during dynamics. The major questions answered include, how fast can the system be transitioned from an incoherent state to a coherent state and vice versa within constraints, the impact of control on state transitions of the network, and coherency of the grid.

6.1 State-of-Art of Modelling for Coherency Studies in HVDC Grids

In the introductory chapter of this thesis, the expected pervasiveness of large HVDC grids was motivated. As subsequent chapters show, the emergence of such networks will drastically change the dynamics of power systems as it is known today. Therefore, more effort is needed in completely understanding the behaviour of large-scale HVDC networks on a macroscopic scale, rather than from the view of any specific device or terminal.

As a precursory analogy, the atoms of diamonds as the hardest naturally occurring material could barely be persuaded to lose their basic structure and attraction (coherency) under temperatures exceeding $3000°C$. Whereas water molecules completely loose their coherency (vaporizes) at

temperatures exceeding $100°C$. The phase transition plots of these two materials are indicative of the underlying structures of each material themselves and all possible states between coherency and full incoherency will become clear. This is the precursory analogy to the method employed in this work.

It is well-established that the most important control variable in DC networks is the nodal voltages. In a well-functioning DC network, there is an expectation of cohesiveness of nodal voltages at all terminals both in steady-state and particularly during dynamics for typical perturbations. Perturbations can be dynamic such as constant changes in the evolution of the system or structural such as changes in the network topology. In traditional power systems, the stability of nodal voltages has been indicted in many power system stability incidents pertaining to slow varying voltage oscillations that could worsen if not arrested [166, 167]. With large-scale DC grids been planned and implemented in both microgrids and large-scale HVDC grids, the risks and consequences of coherency or lack thereof for voltages are even more severe considering that voltage is the synchronization parameter. That is, the direct-voltage is an indication of power imbalance in the DC grid and voltage instability in one node could easily transfer to every node in the grid within a matter of microseconds. Hence, the coherency of direct-voltages indicates the collective properties under perturbations relative to a given topological structure. Furthermore, it is of interest to understand how the dynamics of the nodal voltages would transition under the influence of controllers from a coherent phase to an incoherent phase and vice versa under dynamic perturbations.

One of the most classical frameworks for studying such coherency in power system literature is the widely applied Kuramoto model [168–176]. These works often revolve around synchronization in complex networks and literature is extensive on this topic as acknowledged in the survey articles [177, 178]. However, the DC grid does not directly fit into the framework of oscillators for obvious reasons. More recent works focusing on DC grids can be found in [179–182]. In an effort to model the HVDC from a dynamic networked systems point of view, [179] considered the problem of bounded voltages during disturbances as a bounded synchronization problem whilst considering droop control law with saturation constraints on controller included. However, this does not provide a systematic method for understanding how coherency emerges in HVDC grids. Therefore, generalizations to any arbitrary grid or disturbances are challenging to make.

In this chapter, we focus on steady-state and dynamic coherency of nodal voltages in a large HVDC grid, by borrowing notions from molecular and statistical mechanics to study the collective behaviour of large-scale systems under an external disorder parameter. Readers are referred to the

early work in [183], and more recent works in [184–186], for background study. Coherency as the property of a system is defined as the ability of the system defined by parameters to stay within pre-defined values during and/or after disturbances. The study of coherency has been applied for decades to fields with truly large-scale networks ranging from the electrical power system, communications, statistical mechanics, and molecular networks. Most recently, this notion has been applied to the macroscopic description of collective phenomena in power grids with respect to the underlying topological structure [187], and decentralized power grids with distributed resources [188].

Subsequently, the full picture of coherency can be observed from the phase transition plots between coherent and incoherent regions, relative to the degree of external disorder (line impedances) — herein referred to as the order or disturbance parameter. Here, the transition to a state of incoherency from coherency may indicate potential weaknesses of that system given its structure and controller dynamics. Information about the macroscopic properties of the system may be obtained directly from these phase plots using appropriate statistical techniques.

Therefore, this chapter offers an alternative to the rich body of literature by modelling the HVDC as a network of feedback-controlled subsystems and subsequently employing a statistical approach to provide insights into certain macroscopic properties. This includes the coherency (or lack thereof) of nodal voltage responses to external disorder for a statistical network considering the implemented global feedback strategy.

6.2 Preliminaries

6.2.1 Coherency as a Measure of Distance and Dispersion

As previously mentioned, the direct-voltage is the synchronization parameter in the DC grid. Hence, the coherency (or lack thereof) of direct-voltages directly translates to the coherency of the system as an entity. Coherency as a metric applied in this chapter is, therefore, the measure of the dispersion of nodal voltages about the mean voltage of the system.

Given n vectors of nodal voltages of equal lengths, the coherency is computed based on the Euclidean distance about the system average, given as

$$\mathcal{L}_2(V_i(t), \cdots, V_n(t)) = \frac{1}{n} \sum_{i=1}^{n} \left(V_i(t) - \overline{V}(t) \right)^2 \tag{6.1}$$

where V_i are the nodal voltages, and $\overline{V}$ is the system average voltage. Hence, coherency is a measure of the variance of nodal voltages. The lower the variance, the more coherent the system is, and the higher the

variance, the more incoherent.

6.2.2 Complex Networks

A generic HVDC grid of arbitrary structure is shown in Fig. 6.1, with potential to interconnect diverse resources across long distances. The HVDC grid can be described as a connected graph defined by

$$\mathcal{G} = (\mathcal{V}, \mathcal{E}, \mathcal{A}) \tag{6.2}$$

consisting of $\mathcal{V} = \{1, 2, \cdots, n\}$ nodes (each node described by a set of differential equations), $\mathcal{E}$ are the edges — the lines and/or cables, and the node-edge adjacency matrix $\mathcal{A}$ describing the underlying topology and interconnections.

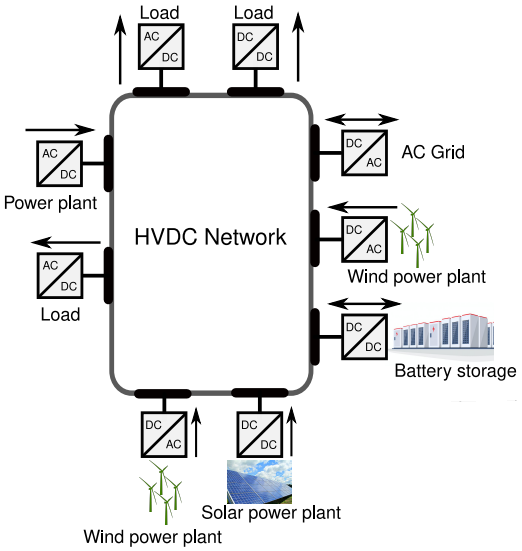

Figure 6.1: Structure of a large-scale multi-terminal HVDC grid

6.3 Aggregate Modelling of VSC-HVDC Grids

In previous chapters, the impedance modelling framework was broadly applied to analysis from component to system-level considering both the AC and DC grids; with examples for fairly small-sized grids with disturbance sources limited to linear functions. In this chapter, a state-space approach is applied to model a fairly large HVDC grid for system-level generalizations using random perturbation techniques. Since the focus is

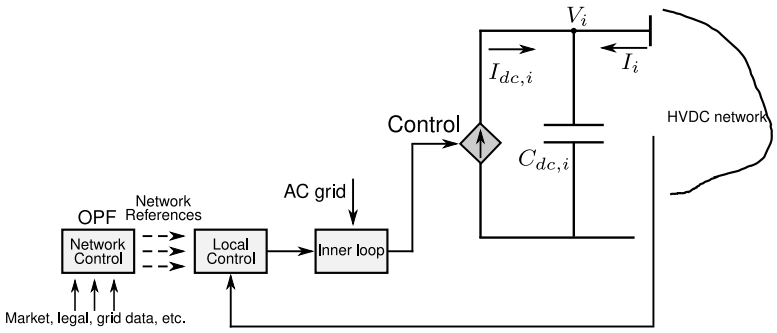

Figure 6.2: System level overview of control strategy

on the DC grid, the AC grid is neglected. In the following, each node is modelled with two states viz. its voltage and injected current from power balance in the case of controlled dynamics. And one state per node in the case of uncontrolled dynamics and steady-state studies. Since only nodal dynamics are of interest, the network of cables is modelled by resistance equivalents. Therefore, the network is modelled by RC equivalents.

6.3.1 Controlled Dynamics of the VSC-HVDC Grid

In a feedback-controlled network of subsystems, the dynamics of constraining the network based on control objectives is of most interest. In such cases, the collective dynamics of the network will be governed by the controllers, passive components, and the network topology. For HVDC grids, the controllers are often decentralized at each node with a collective response at the global level. These controllers typically utilize local information to control the voltages at their respective buses [49]. However, the direct-voltage may be controlled following different strategies. For terminals where the voltages are directly controlled in closed-loop, the current injections at each terminal are controlled based on the measured voltages. For terminals where voltages are not directly controlled, current injections are constant. These are called 'constant current terminals.' Fig. 6.2 depicts an overview of the grid and control strategy as described. In this work, the inner loop is assumed much faster than the outer loops and their dynamics are disregarded to keep simplicity.

Constant Direct-Voltage Controlled Node

For a constant direct-voltage controlled node with a proportional-integral (PI) compensator K_v, the control law for balancing the nodal voltage

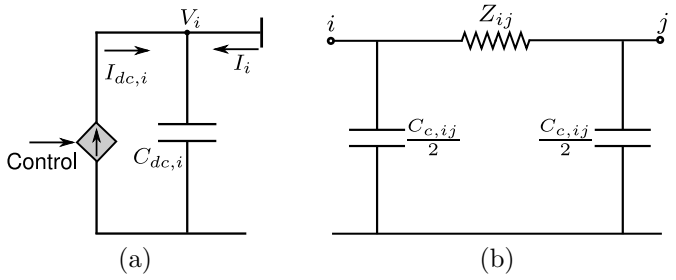

Figure 6.3: Equivalent terminal models of converter and cables/lines **(a)** converter **(b)** cable

variation can be expressed as

$$I_{dc,i} = K_v(V_i^* - V_i) + I_i^* \tag{6.3}$$

where V_i^*, I_i^* are the network level voltage and current references obtained from power flow, and $I_{dc,i}$ is the controlled current injection as shown in Fig. 6.3a (hence, a state) [49].

Constant Power/droop Controlled Node

An alternative to a voltage controlled node is either constant power or droop control mode. This is based on a combination of a proportional (droop) compensator R_{dc} and a PI (active power) compensator K_p for active power. The objective of the proportional compensator is to regulate its nodal direct-voltage by adjusting the constant power reference (as shown in Fig. 2.19). Therefore, the constant power controlled node can be viewed as special case of the power-based droop where the proportional gain is zero. The control law can be described by

$$I_{dc,i} = I_{ac,i} = K_p\left(P_i^* - P_{dc,i} + R_{dc,i}(V_i^* - V_i)\right) + I_{ac}^* \tag{6.4}$$

where $I_{ac,i}$ is the current flowing through the connected AC grid, $R_{dc,i}$ is the droop gain, I_{ac}^* is the network level AC reference. For simplicity, if the active power is balanced between the AC and DC grids, then a node in active power control where $R_{dc} = 0$ is simply a constant current node.

Nodal Dynamics

Considering a cable network of RC components as shown in Fig. 6.3b, the DC nodal dynamics is dictated according to

$$C_i\frac{dV_i}{dt} = I_{dc,i} + I_i = I_{dc,i} + \sum_{\substack{i=1\\ i\neq j}}^{n_c} I_{ij} \tag{6.5}$$

where $I_{dc,i}$ is the injection as obtained from (6.3) or (6.4), I_i is the network current flowing through node i determined by the network Laplacian matrix $\mathbf{G}$ given in (6.8), I_{ij} is the cable current between nodes i and j ($\in n$), n_c is the number of cables connected to node i, and C_i is the total capacitance at node i, expressed as

$$C_i = C_{dc,i} + 0.5 \sum_{\substack{i=1 \\ i \neq j}}^{n_c} C_{c,ij} \tag{6.6}$$

where $C_{dc,i}$ models the nodal capacitance, and $C_{c,ij}$ is the capacitance of the DC cable between nodes i and j. The network currents at each node are obtained according to

$$\mathbf{I} = \mathbf{G}\mathbf{V} \tag{6.7}$$

where

$$\mathbf{G} = \mathcal{A}\mathbf{Y}_b\mathcal{A}^T \tag{6.8}$$

$$\mathbf{Y}_b = \text{diag}(g_{ij}) \quad \forall i = j \in \mathbb{R}^{m \times m}$$

$\mathcal{A}$ is the incident matrix that defines the network interconnection, $\mathbf{I}$ is the vector of nodal currents, $\mathbf{V}$ is the vector of nodal voltages, $g_{ij} \in \mathbb{R}^{m \times m}$ are the edge weights between nodes i and j (admittance of the cable/line), and m is the number of cables in the system. Combining the expressions given in (6.3)-(6.5), the aggregated dynamics of a controlled n node network in state-space can be expressed in the standard form as

$$\frac{d}{dt}\begin{pmatrix}\mathbf{V} \\ \mathbf{I}\end{pmatrix} = \underbrace{\begin{pmatrix}\mathbf{A}_{11} & \mathbf{A}_{12} \\ \mathbf{A}_{21} & \mathbf{A}_{22}\end{pmatrix}}_{\mathbf{A}_{net}}\begin{pmatrix}\mathbf{V} \\ \mathbf{I}\end{pmatrix} + \underbrace{\begin{pmatrix}\mathbf{B}_{u_{11}} & \mathbf{B}_{u_{12}} \\ \mathbf{B}_{u_{21}} & \mathbf{B}_{u_{22}}\end{pmatrix}}_{\mathbf{B}_{net}}\begin{pmatrix}\mathbf{I}^* \\ \mathbf{V}^*\end{pmatrix} \tag{6.9}$$

with

$$\begin{aligned}\mathbf{V} &= (V_1, V_2, \cdots, V_N)^T \\ \mathbf{I} &= (I_1, I_2, \cdots, I_N)^T \\ \mathbf{V}^* &= (V_1^*, V_2^*, \cdots, V_N^*)^T \\ \mathbf{I}^* &= (I_{dc,1}^*, I_{dc,2}^*, \cdots, I_{dc,n}^*)^T\end{aligned}$$

where $\mathbf{I}$ is related to the state of the integral control, $\mathbf{A}_{net}$ is the network state matrix, and $\mathbf{B}_{net}$ is the network input matrix with elements defined

as

$$\begin{aligned}
\mathbf{A}_{11} &= -\mathbf{C}^{-1}\mathbf{G}_{aug} && \in \mathbb{R}^{n\times n} \\
\mathbf{A}_{12} &= \mathbf{C}^{-1} && \in \mathbb{R}^{n\times n} \\
\mathbf{A}_{21} &= -\mathbf{G}_I && \in \mathbb{R}^{n\times n} \\
\mathbf{A}_{22} &= 0 && \in \mathbb{R}^{n\times n} \\
\mathbf{B}_{u_{11}} &= \mathbf{C}^{-1} && \in \mathbb{R}^{n\times n} \\
\mathbf{B}_{u_{12}} &= \mathbf{C}^{-1}\mathbf{G}_P && \in \mathbb{R}^{n\times n} \\
\mathbf{B}_{u_{21}} &= \mathbf{0} && \in \mathbb{R}^{n\times n} \\
\mathbf{B}_{u_{22}} &= \mathbf{G}_I && \in \mathbb{R}^{n\times n} \\
\mathbf{G}_P &= \mathrm{diag}(k_{p_1}, \cdots, k_{p_n}) \\
\mathbf{G}_I &= \mathrm{diag}(k_{i_1}, \cdots, k_{i_n}) \\
\mathbf{G}_{aug} &= \mathbf{G} + \mathbf{G}_P
\end{aligned} \tag{6.10}$$

where $\mathbf{C}$ consists of the equivalent nodal capacitances sorted on the diagonal, $\mathbf{G}_I$ consist of the integral control gains at each node, $\mathbf{G}_P$ consist of the proportional control gains at each node, $\mathbf{G}_{aug}$ is an augmented Laplacian matrix consisting of the sum of proportional control gains at each node, and the network Laplacian matrix. It is worth to note that, $\mathbf{G}_{aug}$ is not a strict Laplacian.

6.3.2 Uncontrolled Dynamics of HVDC Grids

It is theoretically interesting to obtain insights into the dynamic coherency of an uncontrolled network. This establishes the basis for controlling the dynamics and potential trade-offs required between control efforts. In this case, the system determines the appropriate nodal voltages for a balanced current injection. Therefore, (6.9) reduces to

$$\frac{d\mathbf{V}}{dt} = -\mathbf{C}^{-1}\mathbf{G}\mathbf{V} + \mathbf{C}^{-1}\mathbf{I}^{*} \tag{6.11}$$

However, such results are only of theoretical interest as steady-state values may breach material limits or unrealistic values. Furthermore, such a system cannot respond to constant changes that are expected in normal operation.

6.3.3 Steady-state Coherency of HVDC Grids

In steady-state where dynamics have decayed and time is no longer a factor, the network resistances and thus admittances dictates the values of nodal voltages. Steady-state coherency reveals the natural intrinsic behaviour of the system when time is not of essence. The left hand side

of (6.11) decays to zero and the terminal voltage responses are obtained by solving the power flow equation of the DC grid given in (6.7).

6.4 Order Parameter Analysis

An understanding of the collective dynamics of large-scale HVDC grids requires a knowledge of how transitions occur between the coherent (ordered) and incoherent (disordered) states. The order parameter provides a low-level understanding of the phase transitions mainly governed by the system structure and dynamics — controlled and otherwise. That is, the order parameter allows to determine these states, the transitions between, and the basic shape of transitions [185, 186, 189, 190].

The control parameter effectively controls the changes between these states by acting as a perturbation source. The aim is to derive theoretical indices from which conclusions can be drawn on the collective behaviour of the system in any state. That is, to find necessary and sufficient conditions for which coherency is fulfilled, and how the system can be brought from one state to another in a given time frame.

The idea behind the order parameter as applied in this work is that the network impedances—edge weights hold the underlying information about the correlation between nodal voltages. The stronger the coupling between nodes through the edges, the more ordered or synchronized the system will become and act collectively. In contrast, the weaker the coupling strength, the more the disorder in the system where each node behaves arbitrarily [183], under constraints imposed by dynamics. Therefore, the order parameter is relative to the edge weights (network impedances). Then, the dispersion between variables of interest about their expected mean, and/or the mean of the system determines the coherency or lack thereof.

A deterministic control parameter $r(t_f) \in \{0, 1\}$ is discretized in the described range to ensure smoothness; t_f is the element index. $r(t_f)$ can be compared to a temperature regulator, where $r(1) = 0$ implies absolute zero temperature where characteristically the energy of the system is zero. Hence, there is complete order in the system — variables of interest are the closest, and $r(t_f) = 1$ implies infinite temperature where characteristically the energy of the system is infinitely large. Hence, maximum disorder in the system — variables of interest are dispersed.

To study how the voltages become coherent when the line resistances vary we perform a statistical study using a control parameter. If the parameter value is high, all the resistances are dissimilar, being randomly chosen or if it is low, all the resistances are equal to the control parameter itself. Then we solve the equations and assess the coherency of the voltages by measuring their 2-norm, max-norm, distance from the mean, etc.

6.4.1 Implementation of Order Parameter Analysis

The application of the order parameter goes to the core of statistical mechanics by first describing a supposed set of all possible systems [185]. In this work, this set is described by a collection of $N \in \mathbb{R}$ random edge-weight vectors (impedances) that make up a network. The steps highlighted below are followed as implemented in this work.

(a) Define the appropriate basis, in this case, per unit (p.u.).
(b) Define a balanced power flow vector in the chosen basis.
(c) Define all variables — incidence matrix $\mathcal{A}$, nodal capacitances, controller parameters, and solver parameters.
(d) Generate an evenly discretized deterministic vector of the control parameter $r \in \{0, 1\}$ in t_f discretizations[1].
(e) Generate N uniformly distributed random row vectors within the interval $\{0, 1\}$, which may be denoted by

$$R_N = \{r_{Nj}\}_{j=1,\cdots,m} \quad \in \mathbb{R}^m \tag{6.12}$$

where m is the total number of edges (cables/lines in the system). Therefore, for N random systems each consisting of R_N row vectors, the entire statistical system can be combined as

$$\mathbf{R}_s = \begin{bmatrix} \{R_i\} \\ \vdots \\ \{R_N\} \end{bmatrix}_{i=1,\cdots,N} \quad \in \mathbb{R}^{N\times m} \tag{6.13}$$

(f) Apply the order parameter to perturb the underlying properties of the system by applying the law

Algorithm 1 Algorithm for order parameter analysis

```
for k = 1 : t_f do
    if R_s(i, j) > r(t_f),   ∀(i, j) then
        R_s(i, j) = r(t_f)   ∀t_f
    end if
end for
```

(g) Obtain the new matrix of perturbed system $\mathbf{R}_s^p \in \mathbb{R}^{N\times m\times t_f}$.
(h) Delete the first page corresponding to zero resistances.
(i) For each perturbed m set $\in \mathbb{R}^{N\times m\times t_f}$, construct the Laplacian matrix $\mathbf{G}$. This results to $N \times t_f$ distinct systems.
(j) For steady state analysis,

[1] t_f should be large enough for smoothness, but not too large to complicate solution time.

- solve the $n-1$ unknown voltages, and compute the second moment $||V||_2$, $||V_e||_2$ of the nodal voltages and edge voltages respectively
- plot of $||V||_2$,$||V_e||_2$ and derivative of each against the vector $r(t_f)$.

(k) For dynamic analysis with or without control (constant power sources),

- from (i), construct all matrices detailed in Sections 6.3.1 and 6.3.2 — $\mathbf{A}_{net}$, $\mathbf{B}_{net}$ for each system.
- Define the vector of nodal voltage set-points (reference trajectories).
- Solve the dynamic equations at discretized time steps t_s for $t \in \{0, t_{final}\}$ and initial conditions from power flow, resulting in a solution matrix $\in \mathbb{R}^{t \times 2n \times N \times t_f}$ (n instead of $2n$ without control.)
- Compute the norm at each time τ

$$||V_{i,N}(\tau, N)||_\infty \quad \forall (i \in n) \tag{6.14}$$

- Apply (6.1) to the results of (6.14) for each t_f.
- Alternatively, compute $|v_i - v_i^*|$ ($v_i^* = 1$ or the voltage reference of node i). Thus variances are computed from mean of 1 p.u. or from the voltage reference of each node.
- Show the three dimensional plot of the $\mathcal{L}_2$ as computed from (6.1), against t, and t_f vectors.

To facilitate an easier understanding, Fig. 6.4 depicts a vectorized overview of the steps as implemented in this work. Fig. 6.4a illustrates the implementation of the order parameter algorithm as in (f)-(h) above. Fig. 6.4b illustrates the construction of the Laplacian matrices $\mathbf{G}$ for each statistical system $\in N$, and discretized disturbance parameter t_f as in (i). Then, the $\mathbf{A}_{net}$ and $\mathbf{B}_{net}$ matrices are obtained given $\mathbf{G}$ and the controller parameters as in (k). Subsequently, the system of ODEs (Ordinary Differential Equations) is solved for a specific case to obtain a system of solutions as shown in Fig. 6.4c. Then, the ∞-norm is applied over all solutions of the statistical system to obtain the worst-case solution at each τ as shown in Fig. 6.4d. Finally, the variance between all nodal voltages at each time step τ is computed for each disturbance parameter to obtain Fig. 6.4e.

6.5 Analysis of a Physical VSC-HVDC Grid

An adapted Cigŕe VSC-HVDC benchmark model is considered in this thesis [191]. The HVDC grid consists of 12 nodes and a network of 18 cables/lines. The network interconnects several offshore wind farms which

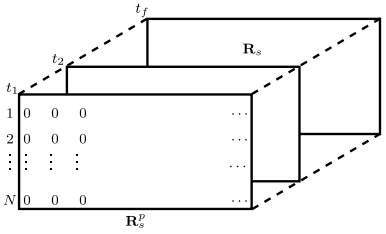

(a) Vectorized implementation of the order parameter law

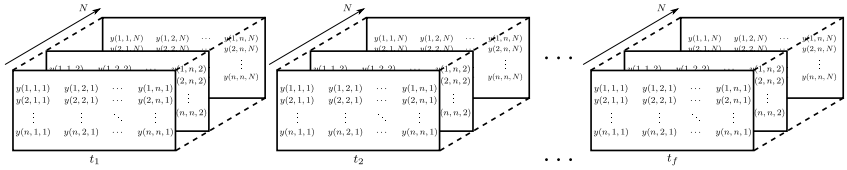

(b) Construction of the Laplacian matrices of the network

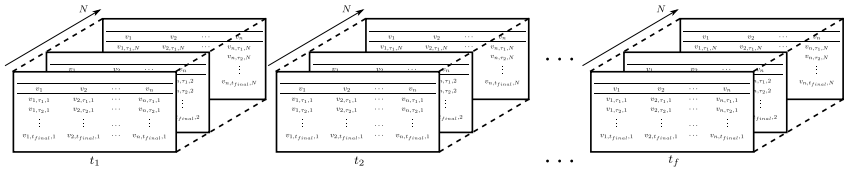

(c) Solution of the system of ODEs

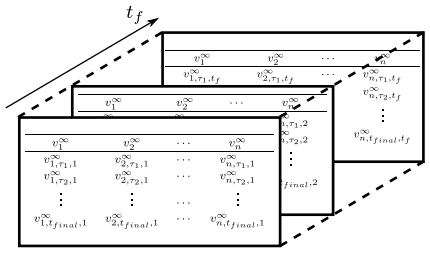

(d) $||.||_\infty$-norm over all N

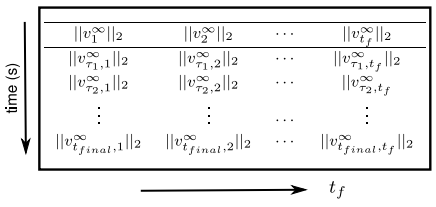

(e) $||.||_2^2$-norm over all n

Figure 6.4: Illustrative overview of the order parameter analysis as implemented in vectorized form

are modelled as constant power sources, and grid side converters which are modelled as either constant power, constant voltage, or droop controlled depending on the network level strategy. The planar network structure is shown in Fig. 6.5 and Fig. 6.6 shows the connected graph representation of the same network showing the nodes and connected edge weights. The system base parameters are provided in Table 6.1, the initial system parameters are given in Table 6.2, and line lengths are given in Table 6.3. The active power direction reference used in this work is that loads are negative injections and sources are positive injections. At this juncture, it is worth remarking that the analysis employed in this chapter is based on a statistical approach. Hence, these parameters as provided are only for references.

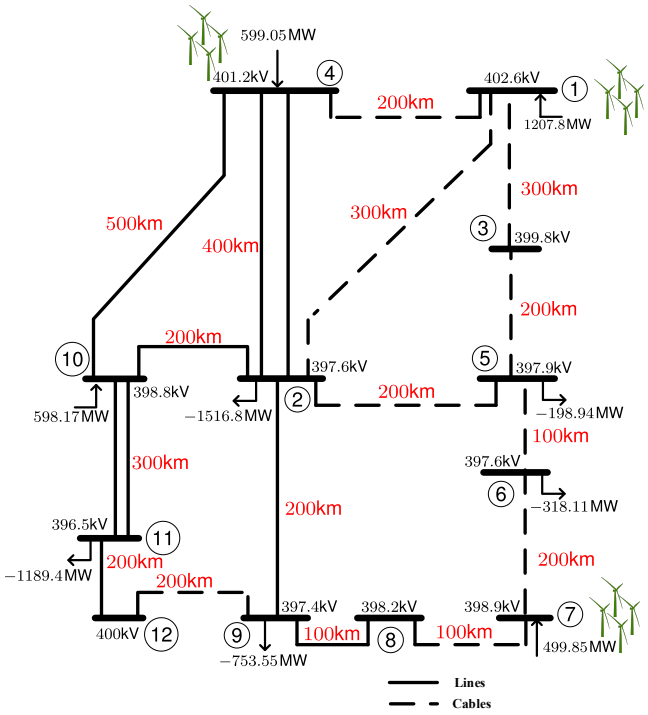

Figure 6.5: Network structure and steady-state initialization of the modified Cigré VSC-HVDC Grid

For the case of droop control strategy as applied in this chapter, the grid side converters are in droop mode and the wind farm converters simply inject power into the grid.

This section aims to understand the behaviour of a controlled and uncontrolled physical HVDC grid including the voltage dynamics under time

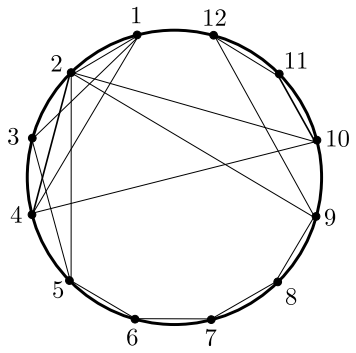

Figure 6.6: Connection graph of Cigré HVDC Grid

Table 6.1: System Base Parameters

Parameter	Value
Power	1500MW
Voltage	400kV
Cable resistance	0.011Ω/km
Nodal capacitance	150μF

Table 6.2: Nodal Parameters

Node Tag	Node Type	V_i^* (kV)	$I_{dc,i}^*$(kA)	P^*(MW)
1	Wind farm	402.6	3000	1207.8
2	AC grid	397.6	−3815	−1516.8
3	Substation	399.8	0	0
4	Wind farm	401.2	1493	599.05
5	AC grid	397.9	−500	−198.94
6	AC grid	397.6	−800	−318.11
7	Wind farm	398.9	1253	499.85
8	Substation	398.2	0	0
9	AC grid	397.4	−1896	−753.55
10	AC grid	398.8	1500	5985.17
11	AC grid	396.5	−3000	−1189.4
12	AC grid	400	2765	1106

considerations as opposed to a random network. However, the time range of simulations is chosen to reflect typical time constants of dynamics in an

Table 6.3: Line Parameters of the HVDC Grid

Line	Nodes	Length	Line	Nodes	Length
1	$1-3$	300km	10	$10-11$	300km
2	$3-5$	200km	11	$2-10$	200km
3	$5-6$	100km	12	$4-10$	500km
4	$2-5$	200km	13	$2-4$	400km
5	$6-7$	200km	14	$2-4$	400km
6	$7-8$	100km	15	$1-4$	200km
7	$8-9$	100km	16	$11-12$	200km
8	$9-12$	200km	17	$1-2$	300km
9	$10-11$	300km	18	$2-9$	200km

HVDC grid ($<$ 1s for primary voltage control and balancing, and $<$ 10s for secondary voltage control [57]). To establish a reference case, basic results are given for the physical grid shown in Fig. 6.5 in contrast to the random networks in subsequent analysis.

6.5.1 Uncontrolled dynamics of the Physical HVDC Grid

The dynamic equations of (6.11) are solved. In this case, there is no influence of controller and network references. Therefore, such a case is only of theoretical interest. Zero power flow is initially assumed before power injection was initiated at 5ms with the same power injection as the current references given in Table 6.2. Fig. 6.7 depicts the theoretical responses of the uncontrolled HVDC grid for a balanced power flow. Although the responses have little practical significance, it illustrates the inherent natural stabilizing self-control exhibited by the DC grid in the absence of control with a steady-state guarantee. This is due to the large equivalent capacitance of the DC grid and the resistive damping. In this case, the voltages are well-around the typical voltage value at 1p.u. However, in other cases, the voltages may breach material limits as the system is allowed to determine the nodal voltages without any constraints.

6.5.2 Controlled Dynamics of the Physical HVDC Grid

For the controlled case of the HVDC in the reference case, the dynamic equations of (6.9) are solved.

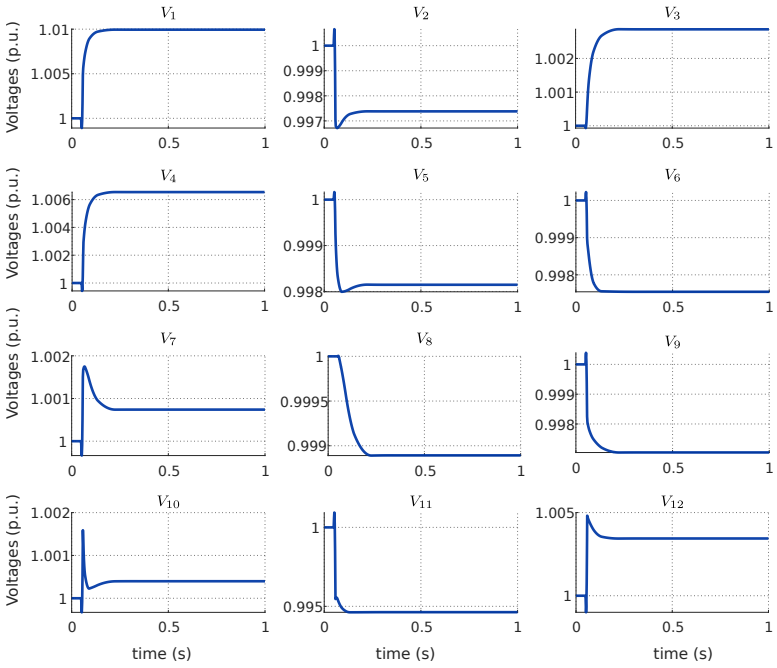

Figure 6.7: Theoretical voltage responses of an uncontrolled HVDC grid for step changes in power

Master-slave Control Strategy

In this case, the master-slave control strategy is implemented and one controller performs the primary voltage control and balancing in the DC grid, whereas others are in constant power mode. Here, the controller is implemented at node 12 and it operates by controlling the voltage at its bus to 1p.u. thereby regulating the network direct-voltage. Fig. 6.8 shows the comparison between the controlled (red) and uncontrolled responses (blue) with similar conditions. The cost of control and its advantages is immediately clear compared to an uncontrolled system. For instance, from Fig. 6.8, the subplot of V_{12} controlling the direct-voltage tracks the reference 1 p.u. in steady-state despite the oscillations. Oscillations due to interactions between the control and network and the balancing action of the voltage control terminal can be observed.

Since only one converter carries out voltage balancing, its behaviour is dependent on its location and required balancing power among other things. The voltage responses for a step change at 0.05s from zero power flow for voltage control located at three locations — nodes 2, 6, and 12 is shown in Fig. 6.9. It can be seen that node 2 is oscillatory due to the high

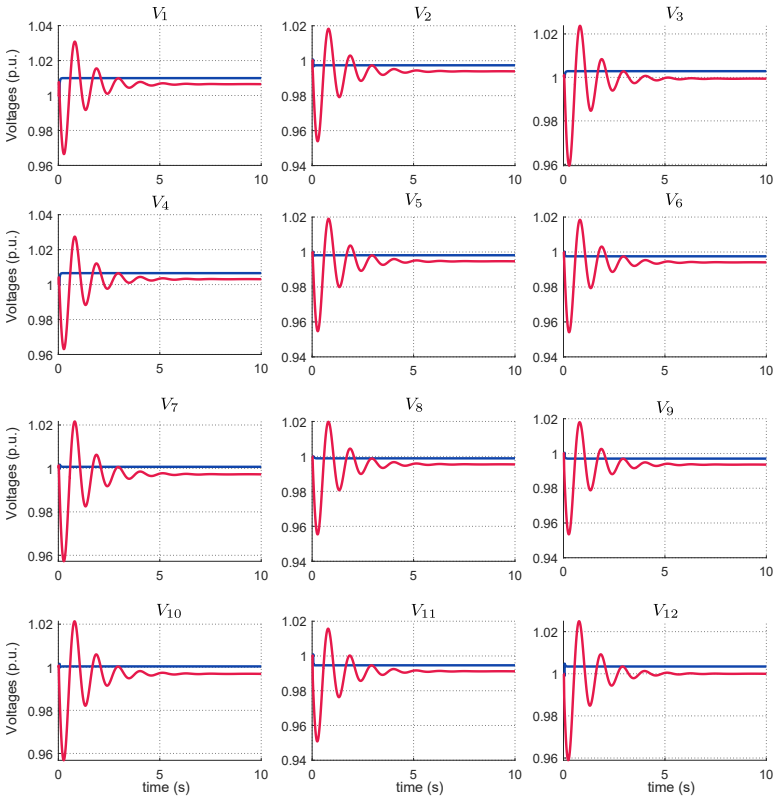

Figure 6.8: Comparison of dynamic voltage responses of the uncontrolled and master-slave controlled HVDC grid at node 12. Uncontrolled grid (blue), controlled grid (red)

balancing current required at that node and its location (see Fig. 6.5). Node 2 is connected to 5 out of the 12 terminals, hence the oscillatory behaviour that persists for more than 10s is due to interactions with other nodes and low damping. Thus, the high-balancing current required results in repeated saturation of the control system shown in Fig. 6.10. On the contrast, for the voltage control located at node 6, interactions are damped in the first 2s due to the low balancing power required at that terminal and its isolated location in the system.

Fig. 6.10 shows the balancing current from the controller for each location with saturation limit set at ± 1.2p.u. The controller saturation at node 2 can be observed resulting in the oscillations in the direct-voltage that transfers to the rest of the system. This verifies that the oscillations are both controller and system-induced.

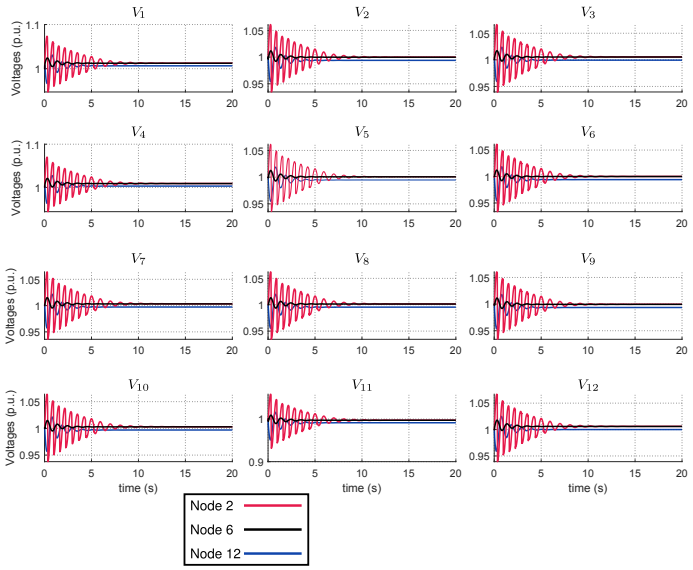

Figure 6.9: Comparison of dynamic voltage responses for different location of voltage control for master-slave strategy

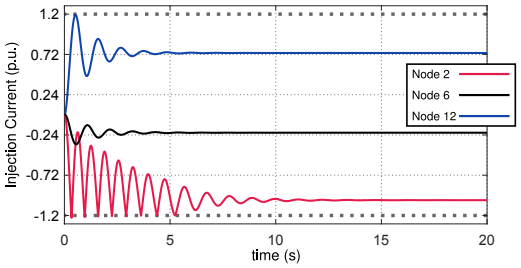

Figure 6.10: Comparison of controller balancing current for different location of voltage control for master-slave strategy

Droop Control Strategy

Here, several nodes collectively control the direct-voltages of the system through the droop control strategy. Fig. 6.11 shows the system droop response of the system for a complete loss of power at node 4 supplying power into the DC grid. The voltage deviations are the effects of droop control action at the secondary level. Fig. 6.12 shows the converter current response to the complete loss of node 4. It can be seen how the droop controlled nodes (2, 5, 6, 9, 10, 11, 12) responded by varying their power to accommodate the loss.

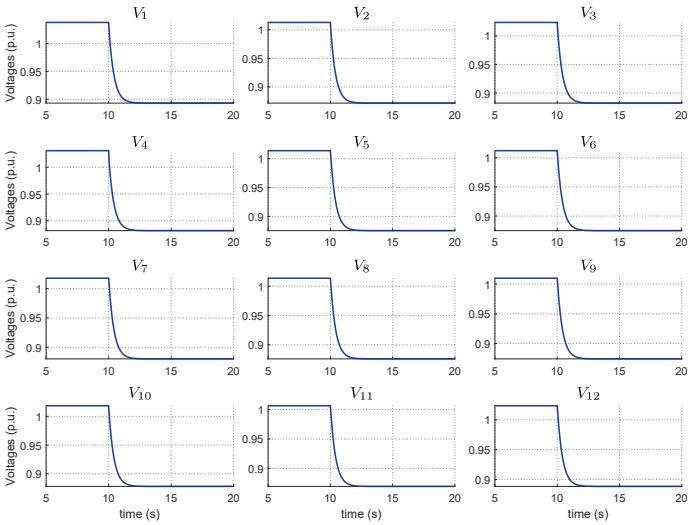

Figure 6.11: Droop responses for a loss of active power at node 4

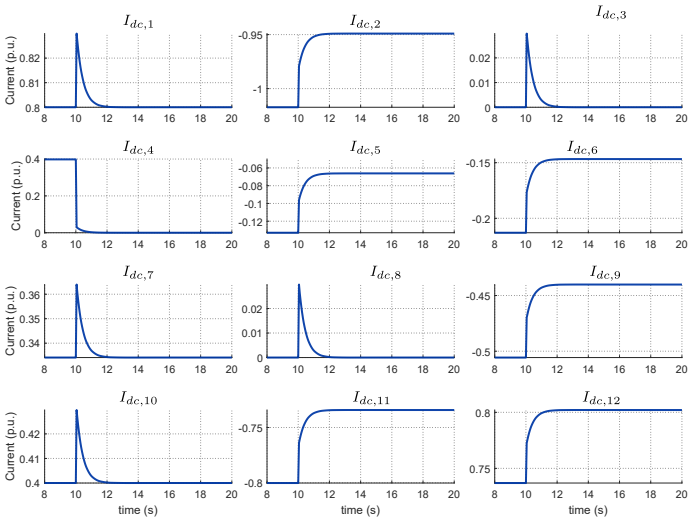

Figure 6.12: Converter currents for a complete loss of active power source at node 4

6.6 Characterization of Dynamic Coherency in HVDC Grids

In the preceding section, the typical dynamics of a physical HVDC grid with typical distances were analysed. However, it is difficult to make generalizations from this analysis to an arbitrarily large HVDC grid. Moreover, it is more difficult to make system-level generalizations through nodal responses as shown previously. This section aims to provide a method to obtain insights into the collective dynamics of the system as one entity through the use of variance as a measure of coherency. The statistical parameters as applied in this thesis are provided in Table 6.4.

6.6.1 Coherency During Initialization

Initially, there is no power flow in the DC grid. Then at 0.05s, the grid is initialized with the power flow as specified in Fig. 6.5 with the same system parameters, except otherwise mentioned.

Fig. 6.13 depicts several views of the three dimensional phase transition plot over time and disturbance parameter r with voltage controller located at node 12 as discussed. The transition plot is plotted by using the mean of nodal voltages to compute the nodal variances. The shape is, in general, sigmoidal with three distinct regions namely; the coherent region where the nodal voltage variances approach 0, the next is the phase transition region where the variances depart from 0, and the incoherent region where the variance diverges or is maximum. Each region can be identified from the choice of the colour bar where the dark blue region indicates the coherent region, the dark red region indicates the incoherent region, and the transition region is indicated with the cyan, greenish-yellow, and yellow. The length of the tail of the sigmoidal distribution (where the variance is ≈ 0) is indicative of the relative ease of the system in evolving towards incoherency. The longer the tail, the better the system and vice versa. Additionally, the length of the blue region (where variances are low but not necessarily zero) is indicative of the coherency of the system.

Table 6.4: Statistical parameters

Parameter	Value	Remarks
t_f	101	number of discretizations
N	500	number of statistical networks
n	12	number of nodes in the network
m	18	number of cables

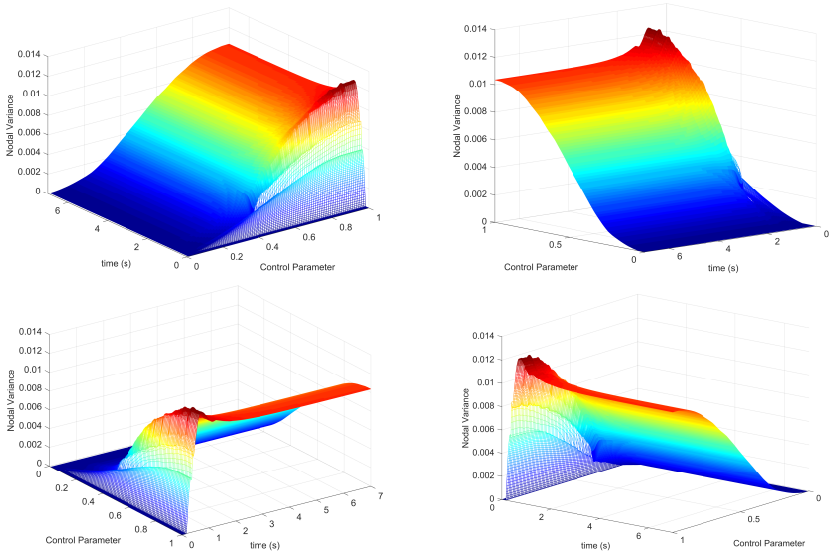

Figure 6.13: Basic three-dimensional shape of the phase transition of the HVDC network over time and order parameter for voltage controller located at node 12 with different views

It is particularly challenging to view the phase transition plot from three-dimensional plots as this depends on the view. Since the basic shape of the phase transition plot has been established, a two-dimensional top view relative to the magnitude is henceforth adopted. Fig. 6.14 depicts the same phase transition plot as Fig. 6.13, however, from a two-dimensional top view which is representative and clearer. The darkest shade of red is the region with the highest variance; in this case the region of overshoot after initialization. Whereas, the darkest shade of blue is the region with variances close to zero; for example, the region between $0 - 0.05$s has zero variance as the system was not yet initialized. Hence, the direct-voltages are closed. Therefore, the blue-coloured region establishes the threshold to maintain coherency or order in the system. In the same manner, the multi-coloured region represents the region in which both the coherent and incoherent states theoretically coexists. The red-coloured region establishes the region of complete disorder or less coherency.

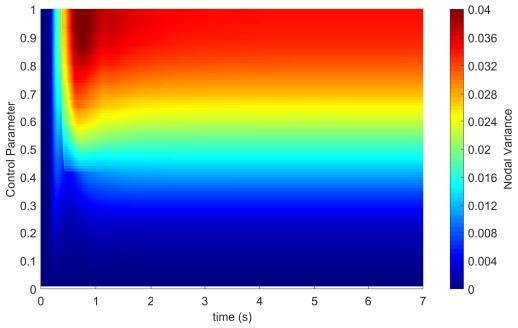

Figure 6.14: Two dimensional top view of the phase transition plot of disturbance parameter against time for DVC implemented at node 12

6.6.2 Impact of Different locations of the Voltage Controller

Fig. 6.15 depicts the phase transition plots for three different locations of the DVC in the master-slave strategy namely, nodes 2, 6, and 12 respectively. The DVC implemented in node 2 shows a better coherency behaviour, with coherency region up to 0.5 of the control parameter compared to the DVC implemented in nodes 6 and 12 where the coherency region is limited to around 0.25 of the control parameter. Additionally, it has the lowest variance in the less region. This contradicts the observations from the physical system where the DVC implemented at node 2 shows the worst response followed by nodes 12 and 6.

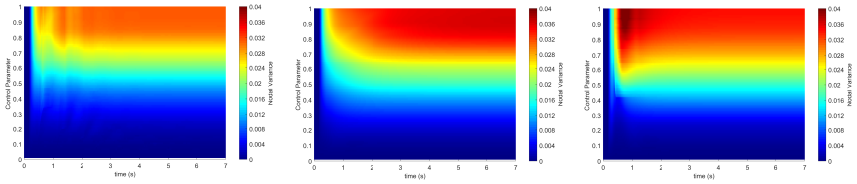

(a) DC voltage control implemented at node 2 (b) DC voltage control implemented at node 6 (c) DC voltage control implemented at node 12

Figure 6.15: Top view of phase transition plot of nodal variance for direct-voltage control at different locations

Node 2 is directly connected to five out of ten controllable nodes and is thus the centroid of the system. Hence, node 2 directly controls the voltage in half of the controllable terminals in the system. Therefore, it has

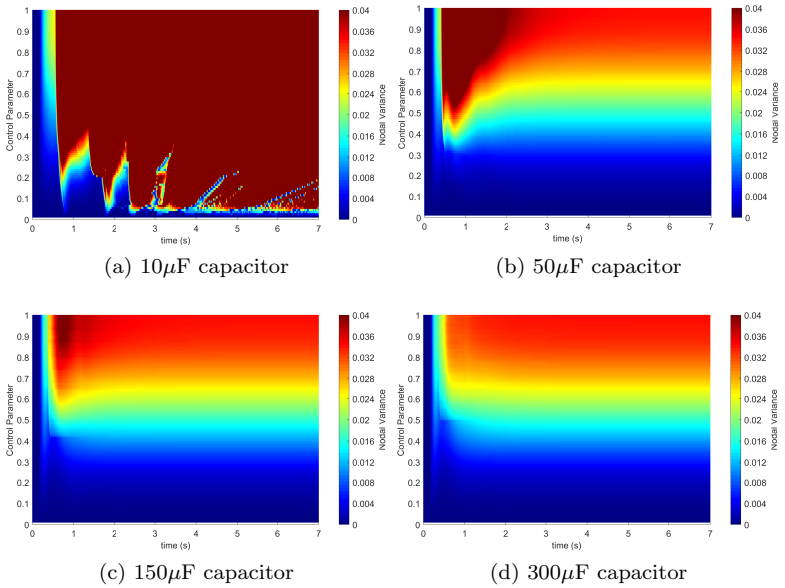

(a) 10μF capacitor (b) 50μF capacitor

(c) 150μF capacitor (d) 300μF capacitor

Figure 6.16: Top view of phase transition plot of nodal variance for sensitivity to varying capacitances at voltage control node 12

the most influence on the system behaviour relative to voltage dynamics. However, the DVC implemented at node 6 is well-isolated from the rest of the network and has little influence in balancing actions required during disturbances; whereas node 12 shows it is particularly vulnerable given its connection to only two nodes and the high balancing power required. Notwithstanding, node 6 has the least oscillatory behaviour due to the low balancing power required for this case and node 2 is the most oscillatory as expected.

6.6.3 Impact of Nodal Capacitances on Coherency

The phase transition plots for varying nodal capacitances at the voltage control node, in this case, implemented at node 12, while others are kept constant is illustrated in Fig. 6.16. It is desired to obtain insights into the interaction between the implemented controller and the nodal capacitance on the system coherency. It can be seen that for very low capacitance, the system is much less coherent as the behaviour is strongly dominated by the highest nodal variance and this indicates a fast transition to a state with less coherence. As the capacitance is increased to 50μF the less coherent phase becomes limited to the first few seconds after initialization

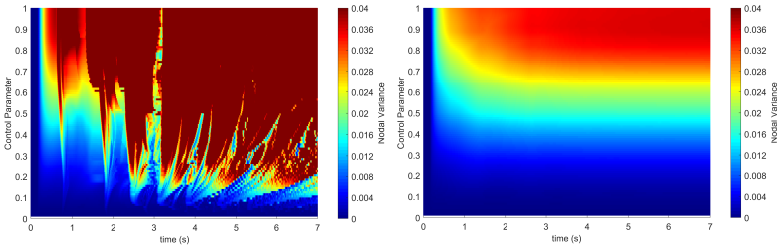

(a) DC voltage control implemented at node 2

(b) DC voltage control implemented at node 6

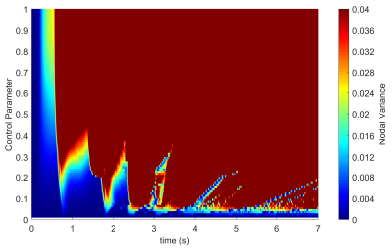

(c) DC voltage control implemented at node 12

Figure 6.17: Top view of phase transition plot of nodal variance for direct-voltage control at different locations and 10μF capacitance at controlled node

for the control parameter larger than 0.5. Additionally, the transition from coherent phase to incoherent phase is slower given the length of the coherent phase. Further increase in the capacitance reduces the maximum variance over time and control parameter but the transition remains the same.

This is due to the location of node 12 relative to the rest of the system (only direct connection to two nodes) and the power required in balancing and reaching steady-state compared to node 2 which has five connection and thus higher equivalent capacitance (this can be observed from Fig. 6.6). This is shown in Fig. 6.17 comparing the case for 10μF nodal capacitance at each of nodes 2, 6, and 12. Node 2 shows a better coherency since, for the same capacitance, the equivalent capacitance at node 2 is higher than for node 12. Node 6 does not show any difference compared to the nominal capacitance in Fig. 6.15b because the steady-state power and balancing power required is lower compared to other controlled nodes (see Fig. 6.10). Thus, this terminal exerts less influence over the network due to fewer interconnections. Therefore, isolated terminals (terminals far

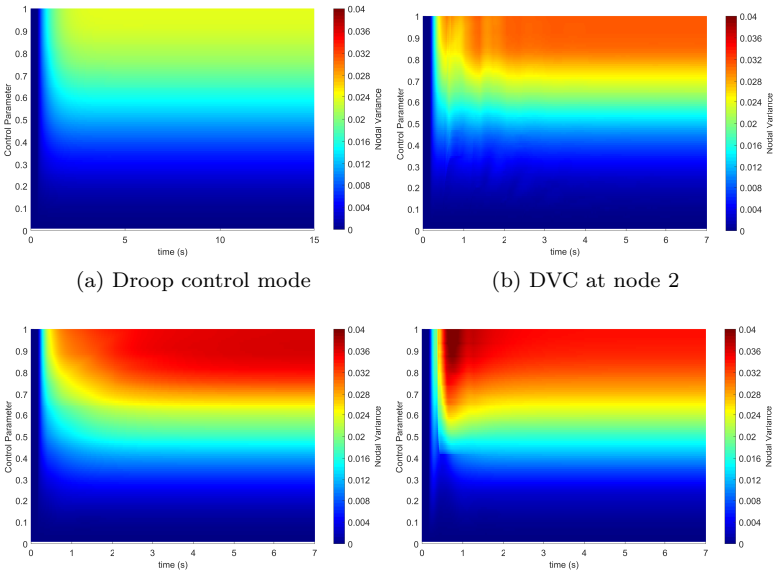

(a) Droop control mode

(b) DVC at node 2

(c) DVC at node 6

(d) DVC at node 12

Figure 6.18: Top view of phase transition plot of nodal variance for different voltage control strategies

away from the centroid of the system) with expected high power demands should not control the direct-voltage or should have higher capacitance to compensate for their isolation or be lightly loaded.

6.6.4 Comparison with Droop Control Strategy

For the case of droop strategy, all nodes in the HVDC grid except nodes 1, 3, 4, 7, 8 collectively control the direct-voltages. Although droop control effectively acts as a balancing mechanism (secondary control), Fig. 6.18 shows the phase transition plot comparison after initialization for both master-slave strategy at different locations and droop. The difference between droop strategy and master-slave strategies at different locations is immediately clear. The droop strategy shows a stronger coherency of nodal voltages, significantly lower maximum variance, and slower transition even for high control parameter compared to master-slave strategy. This is the result of consensus behaviour of droop strategy, where nodal voltages collectively agree on a new operating point and simply adhere to this point. Thus, nodal voltage variance reduces over time (steady-state) irrespective of disturbance; hence coherent. However, it must be noted that the new operating point agreed on by the nodes in droop strategy

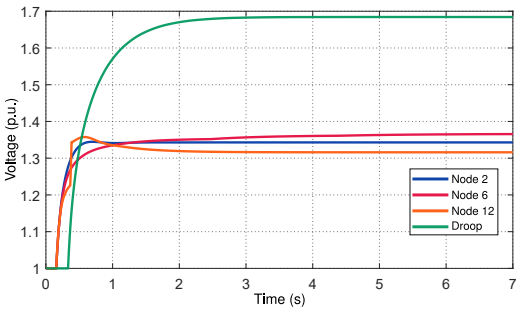

Figure 6.19: Maximum nodal voltages for each case of grid voltage control

may easily breach established voltage limits even for small disturbances such as small changes in active power (depending on the initial operating point). Fig. 6.19 shows the maximum nodal voltages for each of the strategies as implemented in Fig. 6.18. It shows that the droop control strategy has the highest voltage deviation that may well be higher than allowed, thus breaching material limits. Whereas for the master-slave strategies, the voltages are maintained closer to allowed limits with a control parameter of 1. Therefore, in a real HVDC grid, a compromise is required on how many nodes should contribute to droop action at a cost of some acceptable dynamics rather than numerous nodes contributing to droop action despite the inherent benefit.

6.6.5 Coherency under Disturbances

In a more realistic system, constant disturbances such as changes in active power injected or extracted from the DC grid, faults, etc. are constantly expected. For such disturbances, the behaviour of the DC grid will depend on whether the disturbance results in increase or decrease in the direct voltage, the initial operating points of voltage controlling terminals, and their location relative to the network. In the following cases, the disconnection of a node consuming or supplying active power at 1s is performed after the system is already initialized at an operating point. The initial active power flow is as detailed in Table 6.2.

Fig. 6.20 shows the phase transition plots for a complete loss of 599MW at node 4 with different locations of DVC including droop mode. For DVC implemented in nodes 2 and 6 as shown in Figs. 6.20a and 6.20b, there is no significant difference considering that the controller at node 2 simply has to reduce its consumption to compensate for the loss of generation; whereas the node 6 changes from consumption to generation to compensate. Thus, both terminals remain within their capability. However, the system is incoherent above the control parameter of 0.5 and this sets the

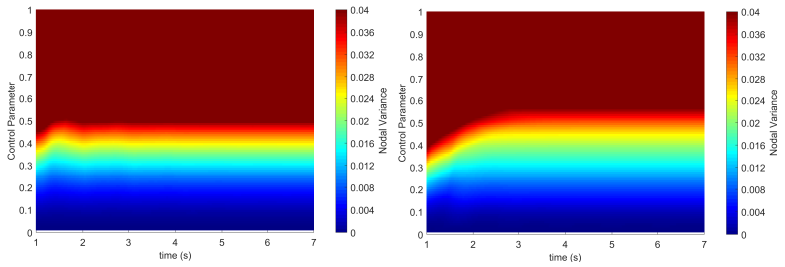

(a) Direct-voltage control in master-slave at node 2

(b) Direct-voltage control in master-slave at node 6

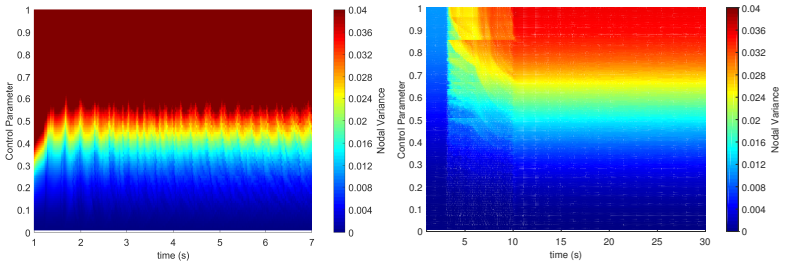

(c) Direct-voltage control in master-slave at node 12

(d) Direct-voltage control in droop mode

Figure 6.20: Phase transition plot of nodal variance for complete loss of generation at node 4 and voltage control at different nodes

limit of safe operation. For a DVC implemented at node 12 as shown in Fig. 6.20c, again, oscillations are apparent. This is a consequence of the initial operating point at node 12 (1106MW) for which a loss of generation (599MW) requires an increase in the power generated, which then results in repeated saturation of the control system. Additionally, the equivalent capacitance at node 12 is lower due to fewer interconnections and an increase in nodal capacitance at node 12 may improve the behaviour. In the case of droop mode as shown in Fig. 6.20d, it is observed that droop, in general, has a significantly lower nodal variance, slower transition to incoherent phase, and thus an indication of improved coherency over master-slave strategies. For an increased nodal capacitance at node 12 from 150μF to 600μF, Fig. 6.21 shows a comparison between both cases. Although the phase transition remains similar, the higher nodal capacitance reduces the severity of the oscillations.

Fig. 6.22 shows the phase transition plots for a complete loss of -318MW at node 6 with different locations of DVC. For a DVC implemented at node 2 as shown in Fig. 6.22a oscillations can be seen for the same reason as

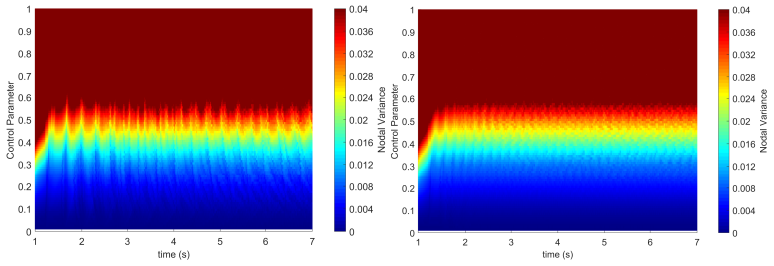

(a) 150μF (b) 600μF

Figure 6.21: Phase transition plots of nodal variance for complete loss of node 4 and voltage control at node 12 with different nodal capacitances

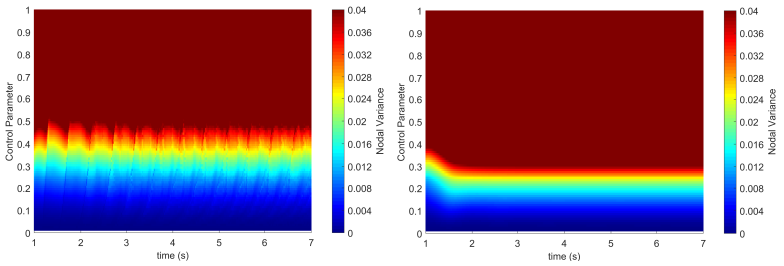

(a) Direct-voltage control in master-slave at node 2 (b) Direct-voltage control in master-slave at node 12

Figure 6.22: Phase transition plot of nodal variance for complete loss of load at node 6 and voltage control at different nodes

previously explained. A loss of a node consuming active power requires the DVC at node 2 to increase its consumption for which it is already at its limit (-1500MW). Therefore, a saturation of the controller results in repeated oscillations. For a DVC implemented at node 12 as shown in Fig. 6.22b, it can be observed that despite the reduction in active power required for this case, the phase transition to the incoherent region is faster than for DVC implemented in node 2. Once again, this is the result of the location of node 12 relative to the disconnected terminal as shown in the connection graph of Fig. 6.6.

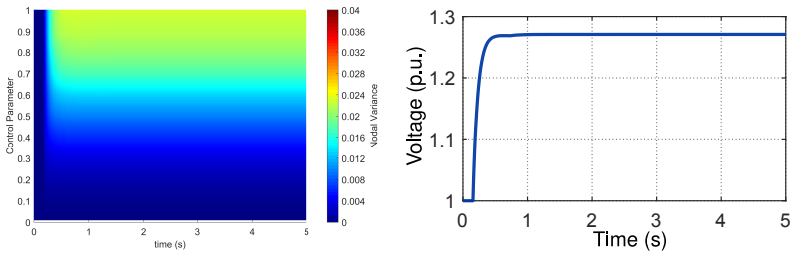

(a) Phase transition plot (b) Maximum nodal voltage

Figure 6.23: Phase transition plot of nodal variance without network control

6.6.6 Coherency in Uncontrolled HVDC Grids

In a more hypothetical case, Fig. 6.23 depicts the phase transition plot for an uncontrolled HVDC grid. Here, a balanced power flow (sum of all power equal to zero) is imposed on the DC grid. It is shown in Fig. 6.23a that the variance is significantly low, the transition to incoherent phase is characteristically low, and the maximum voltages for the maximum control parameter shown in Fig. 6.23b is below 1.3p.u.. This indicates better coherency behaviour. This is the consequence of allowing the system to determine its voltages as a free parameter. However, such an unconstrained system can simply not respond to any disturbance whatsoever. Also, since the system is allowed to freely determine its optimum voltage, this voltage may breach material limits. Nevertheless, it provides may provide a benchmark for assessing the impact of control. Observe that the variance is similar to that obtained by a droop controlled system, and the maximum voltage over time is similar to that obtained by master-slave strategies.

6.7 Characterization of Steady-state Coherency in HVDC Grids

In steady-state, the influence of time factor of dynamics is neglected and the network resistances, thus admittances dictate the responses. In which case, the left-hand side of (6.11) decays to zero. Thus, the terminal voltage responses are obtained by solving the power flow equation. The power flow is solved by assuming the voltage at a specific node to be known — controlled node.

The steady-state coherency provides the underlying nature of the HVDC grids when time is not of the essence. This includes coherency to structural perturbations such as impacts of changes in the topology of a given

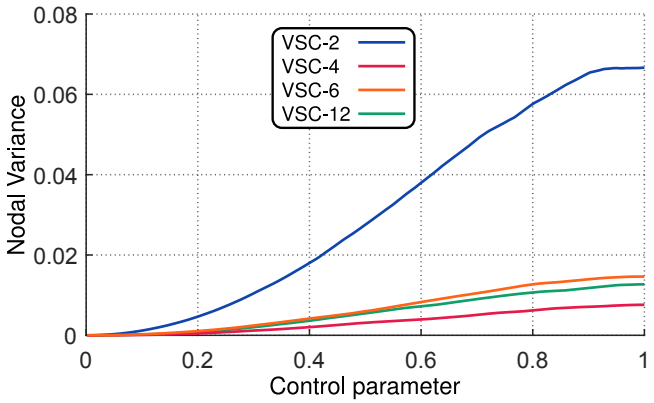

Figure 6.24: Steady-state phase transition plot for different locations of the control node

network. The steady-state coherency based on the power flow of Fig. 6.5 for different locations of the DVC in the master-slave mode is shown in Fig. 6.24. It can be seen that node 2 with the highest nodal variance and the shortest tail is the most vulnerable to structural changes. This is contrary to previous conclusions that node 2 is the best for dynamic balancing and voltage control. This is the result of node 2 being the centroid of the system. Hence, it is vulnerable to topological changes, but also the most responsive to dynamic changes. In contrast, node 4 is the least vulnerable. Additionally, control at nodes 4, 6, and 12 maintain coherency up to a control parameter of ≈ 0.3. Whereas control at node 2 begins to lose coherency at a control parameter of ≈ 0.1. It is important to remark that this assessment depends on the current power flow and a more realistic assessment would include probabilistic power flows.

6.8 Chapter Conclusions

This chapter explored the characterization of random behaviour to describe the macroscopic dynamics of an HVDC network as a single entity. The nodal voltages were adopted as the parameter of choice to describe the change of order of an HVDC grid from coherent to incoherent under statistical and deterministic disturbances. Then, the variance between the nodal voltages was applied as a measure of coherency (or lack thereof) in the system. Then, it was shown that it is possible to obtain an intuitive view of the coherency in large-scale HVDC grids with valuable information for operation and control design.

The HVDC grid was shown to have two important states — coherent

state, and less coherent states, and the transition region between, where both states are supposed to coexist. The threshold of coherency may be assumed to be below this region, and above it, the system is less coherent. It was also shown that, although a droop controlled HVDC grid has a considerably better coherency over a master-slave controlled system, the former requires a significantly overrated and over-designed system to withstand the high voltages. This is despite its advantages in terms of coherency compared to the master-slave approach in which the coherency is poor despite voltages remaining within usual limits. A trade-off in a real system by combining the characteristics of both. We conclude that this approach followed in this chapter, with at most two-state description of each node, turns out to be vigorous when studying large-scale dynamics from a statistical perspective.

7

Conclusions and Future Research

This thesis has investigated increasingly important challenges that are beginning to emerge in power electronic interfaced hybrid AC/DC transmission grids. Specifically, this thesis has tackled the analysis of dynamics, interactions, input-output stability, and large-scale dynamics through wide-ranging systematic approaches. Contrary to previous research efforts where analyses are often specific and assume the availability of detailed information, the methodology employed in this work allows drawing generalized conclusions irrespective of the grid structure, technology of components, and without availability explicit information. As a direct consequence of this, systematic approaches were proposed and demonstrated to control the entire network at large in a manner that incorporates flexibility and coordination.

First, the entire system was decomposed from the network-level to the subnetwork-level, from which several subsystems were identified. Then, subsystems were further broken down into active and passive components. The impacts of these components on the subsystem level, subnetwork-level, and network-level behaviour were thoroughly investigated. Through this approach, the control requirements of each of the subnetworks — AC and DC, and the conflicts in these requirements were highlighted. This directly keys into methodologies to improve the overall hybrid AC/DC grid if they are to be in constant connection with guaranteed minimum performance and stability. Subsequently, the information obtained was leveraged to design, re-design, and modify controllers, to ensure stable condition despite the complexity of the system.

At a subnetwork-level on the DC side, a methodology that exploits the

stability formulations of the grid for mitigating detrimental interactions was proposed. Different ways of exploiting this formulation were demonstrated through the coordinated design of network controllers, thereby mitigating these interactions. Even more importantly, it was demonstrated that controllers can be designed with little to no information about any specific controllable device. Simply, the solutions relied on subnetwork-level information instead. Compared to existing research efforts, this is a significant step towards control of the DC subnetwork where explicit information about controllable devices is often not provided. The flexibility of this approach was demonstrated through analysis and recommendations were provided on the adoption of this methodology. Further, an approach for understanding the macro-scale properties of a large-scale HVDC system was introduced from the perspective of an ordered or disordered system. It was shown that despite the simplicity of this approach, truly large-scale dynamics can be characterized and generalized. However, questions remain if the choice of physical parameter of the DC grid is solely adequate to describe the order (or lack thereof) of the system.

Correspondingly, for the AC subnetwork, unlike previous results, the complexity of the behaviour of the VSC as the interfacing device was presented and thoroughly analysed. This was to better understand the behaviour of this device as seen from the AC subnetwork, under varying conditions. Then, the behaviour of the device when under severe grid conditions was investigated. Contrary to expectations, the control requirement at the subsystem level contradicts with that required when connected to a grid with poor conditions. Although previous research effort has tried to solve this challenge, the solutions often proposed are complex and difficult to adopt. A fundamental approach to better understand the true challenge was followed, and demonstrated, with a significantly simpler solution proposed. The solution was tested through several scenarios to demonstrate its efficacy.

Finally, having solved the most significant challenges at the subnetwork-level, the analysis of how each interconnected network may interact subject to grid conditions of each was detailed through sensitivity analysis. This includes consideration of other non-power electronic devices that may be present in any subnetwork. Then, solutions incorporating the knowledge obtained from each subnetwork analysis, and the potential interaction between all subnetworks were proposed and demonstrated.

7.1 Future Research and Recommendations

Converter interfaced hybrid AC/DC transmission grids are increasingly becoming the focus of current research outlooks. As of today, although systems are still relatively small scale, especially on the DC side, the com-

plexities involving power electronic devices are demanding a different approach to solving challenges. From a simple abstraction of the problem, the work developed in this thesis as related to hybrid AC/DC grids has highlighted numerous research directions. These directions are described chapter-wise:

1. **Chapter 3**
   - In this thesis, a decentralized approach was considered. While such approaches are key, the added cost may be a burden to an already costly system. Hence, coordinated centralized approaches may be sought, and the final signal sent to one or more controllable devices as desired. Therefore, the impacts of communication and corresponding latency, system controllability and observability indices must be investigated.
   - Another perspective that can be adopted is through a top-down approach employing online system identification of equivalents, online analysis, etc. Then, online adaptive, robust, and optimal control of the system. This is different from the analytical approach adopted in this thesis.
   - Incorporation of 'true' system uncertainty representations while taking into consideration more constraints and inherent limitations that may present.
2. **Chapters 4 and 5**
   - Real systems are often discrete in nature. Hence, the impacts of measurement noise, sampling, etc. can be investigated in detail.
   - Perform studies of the impacts of multi-converter interactions on the AC side controlling different physical variables, in a more realistic system set up.
3. **Chapter 6**
   - A truly large-scale system may include hundreds of buses over a network of thousands of cables. Though this may be premature for the DC grid, the approach as described in this thesis through time-domain simulations may be unrealistic. Time-domain simulations are widely known to be computationally expensive even when they are feasible. Instead, spectral graph theory in the frequency domain can be exploited.
   - Analyse impact of structural perturbations such as the impact of different network topologies, and changes to topologies of a specific system.
   - Partitioning behaviour of a system during transitions between coherent and incoherent states.
   - Perform analysis on voltage drops across lines rather than nodal voltages.

Bibliography

[1] K. Meah and S. Ula, "Comparative evaluation of HVDC and HVAC transmission systems," in *2007 IEEE Power Engineering Society General Meeting*, June 2007, pp. 1–5. XIII, 3

[2] W. Krewitt, T. Heck, A. Trukenmller, and R. Friedrich, "Environmental damage costs from fossil electricity generation in germany and europe," *Energy Policy*, vol. 27, no. 3, pp. 173 – 183, 1999. 1

[3] *EU Energy Policy to 2050: Achieving 80-95% Emissions Reductions.* [Online]. Available: http://www.ewea.org 1

[4] F. Kern and A. Smith, "Restructuring energy systems for sustainability? energy transition policy in the netherlands," *Energy Policy*, vol. 36, no. 11, pp. 4093 – 4103, 2008, transition towards Sustainable Energy Systems. 1

[5] "Developing transition pathways for a low carbon electricity system in the uk," *Technological Forecasting and Social Change*, vol. 77, no. 8, pp. 1203 – 1213, 2010, issue includes a Special Section on. 1

[6] E. M. Lightner and S. E. Widergren, "An orderly transition to a transformed electricity system," *IEEE Transactions on Smart Grid*, vol. 1, no. 1, pp. 3–10, June 2010. 1

[7] T. M. Rusche, "The european climate change program: An evaluation of stakeholder involvement and policy achievements," *Energy Policy*, vol. 38, no. 10, pp. 6349 – 6359, 2010, the socio-economic transition towards a hydrogen economy - findings from European research, with regular papers. 1

[8] N. Panwar, S. Kaushik, and S. Kothari, "Role of renewable energy sources in environmental protection: A review," *Renewable and Sustainable Energy Reviews*, vol. 15, no. 3, pp. 1513 – 1524, 2011. 1

[9] E. Tzimas and A. Georgakaki, "A long-term view of fossil-fuelled power generation in europe," *Energy Policy*, vol. 38, no. 8, pp. 4252 – 4264, 2010. 1

[10] GEIDCO, "Global energy interconnection development and cooperation organization," 2016. [Online]. Available: https://en.geidco.org/ 1

[11] N. M. Kirby, Lie Xu, M. Luckett, and W. Siepmann, "HVDC transmission for large offshore wind farms," *Power Engineering Journal*, vol. 16, no. 3, pp. 135–141, June 2002. 2

[12] T. J. Hammons, D. Woodford, J. Loughtan, M. Chamia, J. Donahoe, D. Povh, B. Bisewski, and W. Long, "Role of HVDC transmission in future energy development," *IEEE Power Engineering Review*, vol. 20, no. 2, pp. 10–25, Feb 2000. 2

[13] T. M. Haileselassie and K. Uhlen, "Power system security in a meshed north sea HVDC grid," *Proceedings of the IEEE*, vol. 101, no. 4, pp. 978–990, April 2013. 2

[14] M. Bahrman, "Overview of HVDC transmission," in *Power Systems Conference and Exposition, 2006. PSCE '06. 2006 IEEE PES*, Oct 2006, pp. 18–23. 2, 3

[15] G. Asplund, C. Barker, U. Baur, J. Beerten, P. Christensen, S. Cole, D. Van Hertem, W. Jialiang, D. Jovcic, P. Labra, K. Lindn, A. Marzin, N. Pahalawaththa, M. Rashwan, J. Rittiger, K. Sgaard, D. Westermann, E.-D. Wilkening, and C. Yue, *CIGRE TB 533 - Working Group B4.52 - HVDC Grid Feasibility Study.* CIGR, 2013. 2

[16] B. Andersen, "HVDC transmission-opportunities and challenges," 2006. 2, 6

[17] P. Wang, L. Goel, X. Liu, and F. H. Choo, "Harmonizing AC and DC: A hybrid AC/DC future grid solution," *IEEE Power and Energy Magazine*, vol. 11, no. 3, pp. 76–83, May 2013. 2

[18] A. Lotfjou, Y. Fu, and M. Shahidehpour, "Hybrid AC/DC transmission expansion planning," *IEEE Transactions on Power Delivery*, vol. 27, no. 3, pp. 1620–1628, July 2012. 2

[19] Y. Shao and Y. Tang, "Research survey on multi-infeed AC/DC hybrid power systems," *Power System Technology*, vol. 17, pp. 24–30, 2009. 2

[20] F. Blaabjerg, Z. Chen, and S. B. Kjaer, "Power electronics as efficient interface in dispersed power generation systems," *IEEE Transactions on Power Electronics*, vol. 19, no. 5, pp. 1184–1194, Sept 2004. 2, 17

[21] J. M. Carrasco, L. G. Franquelo, J. T. Bialasiewicz, E. Galvan, R. C. PortilloGuisado, M. A. M. Prats, J. I. Leon, and N. Moreno-Alfonso, "Power-electronic systems for the grid integration of renewable energy sources: A survey," *IEEE Transactions on Industrial Electronics*, vol. 53, no. 4, pp. 1002–1016, June 2006. 2

[22] D. Boroyevich, I. Cvetkovi, D. Dong, R. Burgos, F. Wang, and F. Lee, "Future electronic power distribution systems a contemplative view," in *2010 12th International Conference on Optimization of Electrical and Electronic Equipment*, May 2010, pp. 1369–1380. 2

[23] X. Liang, "Emerging power quality challenges due to integration of renewable energy sources," *IEEE Transactions on Industry Applications*, vol. 53, no. 2, pp. 855–866, March 2017. 2

[24] S. Munir and Y. W. Li, "Residential distribution system harmonic compensation using PV interfacing inverter," *IEEE Transactions on Smart Grid*, vol. 4, no. 2, pp. 816–827, June 2013. 2

[25] H. R. Chamorro, M. Ghandhari, and R. Eriksson, "Wind power impact on power system frequency response," in *2013 North American Power Symposium (NAPS)*, Sep. 2013, pp. 1–6. 2

[26] T. Ackermann, T. Prevost, V. Vittal, A. J. Roscoe, J. Matevosyan, and N. Miller, "Paving the way: A future without inertia is closer than you think," *IEEE Power and Energy Magazine*, vol. 15, no. 6, pp. 61–69, Nov 2017. 2

[27] M. Yu, A. J. Roscoe, A. Dyko, C. D. Booth, R. Ierna, J. Zhu, and H. Urdal, "Instantaneous penetration level limits of non-synchronous devices in the british power system," *IET Renewable Power Generation*, vol. 11, no. 8, pp. 1211–1217, 2017. 2

[28] J. P. Lopes, N. Hatziargyriou, J. Mutale, P. Djapic, and N. Jenkins, "Integrating distributed generation into electric power systems: A review of drivers, challenges and opportunities," *Electric Power Systems Research*, vol. 77, no. 9, pp. 1189 – 1203, 2007, distributed Generation. 2

[29] J. D. McCalley and V. Krishnan, "A survey of transmission technologies for planning long distance bulk transmission overlay in US," *International Journal of Electrical Power & Energy Systems*, vol. 54, pp. 559 – 568, 2014. 3

[30] B. Van Eeckhout, D. Van Hertem, M. Reza, K. Srivastava, and R. Belmans, "Economic comparison of VSC HVDC and HVAC as transmission system for a 300MW offshore wind farm," *European Transactions on Electrical Power*, vol. 20, no. 5, pp. 661–671, 2010. 3

[31] P. Buijs, D. Bekaert, D. Van Hertem, and R. Belmans, "Needed investments in the power system to bring wind energy to shore in belgium," in *PowerTech, 2009 IEEE Bucharest*. IEEE, 2009, pp. 1–6. 3

[32] D. V. Hertem and M. Ghandhari, "Multi-terminal VSC HVDC for the European supergrid: Obstacles," *Renewable and Sustainable Energy Reviews*, vol. 14, no. 9, pp. 3156 – 3163, 2010. 3, 4

[33] N. Flourentzou, V. Agelidis, and G. Demetriades, "VSC based HVDC power transmission systems: An overview," *IEEE Transactions on Power Electronics*, vol. 24, no. 3, pp. 592–602, March 2009. 3

[34] M. Bucher, R. Wiget, G. Andersson, and C. Franck, "Multiterminal

HVDC networks—what is the preferred topology?" *IEEE Transactions on Power Delivery*, vol. 29, no. 1, pp. 406–413, Feb 2014. 4

[35] R. Rudervall, J. Charpentier, and R. Sharma, "High voltage direct current (HVDC) transmission systems technology review paper," *Energy week*, vol. 2000, p. 2, 2000. 4

[36] J. Arrillaga, Y. H. Liu, and N. R. Watson, *Flexible power transmission: the HVDC options*. John Wiley & Sons, 2007. 4

[37] N. G. Hingorani, "Facts-flexible ac transmission system," in *International Conference on AC and DC Power Transmission*, Sep. 1991, pp. 1–7. 4

[38] W. F. Pickard, "The limits of HVDC transmission," *Energy Policy*, vol. 61, pp. 292 – 300, 2013. 4

[39] P. L. Francos, S. S. Verdugo, H. F. lvarez, S. Guyomarch, and J. Loncle, "Inelfe: Europe's first integrated onshore HVDC interconnection," in *2012 IEEE Power and Energy Society General Meeting*, July 2012, pp. 1–8. 4

[40] M. P. Bahrman and B. K. Johnson, "The ABCs of HVDC transmission technologies," *IEEE Power and Energy Magazine*, vol. 5, no. 2, pp. 32–44, March 2007. 4

[41] R. Sellick and M. Akerberg, "Comparison of HVDC light (VSC) and HVDC classic (LCC) site aspects, for a 500mw 400kv HVDC transmission scheme," in *10th IET International Conference on AC and DC Power Transmission (ACDC 2012)*, Dec 2012, pp. 1–6. 5

[42] D. Huang, Y. Shu, J. Ruan, and Y. Hu, "Ultra high voltage transmission in china: Developments, current status and future prospects," *Proceedings of the IEEE*, vol. 97, no. 3, pp. 555–583, March 2009. 5

[43] J. Cao and J. Y. Cai, "HVDC in china," in *Proceedings of the 2013 EPRI HVDC & FACTS Conference, USA*, 2013. [Online]. Available: http://dsius.com/cet/HVDCinChina_EPRI2013_HVDC.pdf 5

[44] W. Lu and B. Ooi, "Multi-terminal HVDC as enabling technology of premium quality power park," in *IEEE Power Engineering Society Winter Meeting, 2002.*, vol. 2, 2002, pp. 719–724 vol.2. 6

[45] T. Haileselassie and K. Uhlen, "Precise control of power flow in multiterminal VSC-HVDCs using DC voltage droop control," in *Power and Energy Society General Meeting, 2012 IEEE*, July 2012, pp. 1–9. 6

[46] J. Liang, O. Gomis-Bellmunt, J. Ekanayake, and N. Jenkins, "Control of multi-terminal VSC-HVDC transmission for offshore wind power," in *Power Electronics and Applications, 2009. EPE '09. 13th European Conference on*, Sept 2009, pp. 1–10. 6

[47] T. Haileselassie and K. Uhlen, "Impact of dc line voltage drops on power flow of mtdc using droop control," *IEEE Transactions on*

Power Systems, vol. 27, no. 3, pp. 1441–1449, Aug 2012. 6

[48] W. Lu and B.-T. Ooi, "DC overvoltage control during loss of converter in multiterminal voltage-source converter-based HVDC (M-VSC-HVDC)," *IEEE Transactions on Power Delivery*, vol. 18, no. 3, pp. 915–920, July 2003. 6

[49] F. D. Bianchi, J. L. Domnguez-Garca, and O. Gomis-Bellmunt, "Control of multi-terminal HVDC networks towards wind power integration: A review," *Renewable and Sustainable Energy Reviews*, vol. 55, pp. 1055 – 1068, 2016. 6, 26, 191, 192

[50] N. Flourentzou, V. G. Agelidis, and G. D. Demetriades, "VSC-based HVDC power transmission systems: An overview," *IEEE Transactions on Power Electronics*, vol. 24, no. 3, pp. 592–602, March 2009. 6

[51] G. Ding, G. Tang, Z. He, and M. Ding, "New technologies of voltage source converter (VSC) for HVDC transmission system based on VSC," in *2008 IEEE Power and Energy Society General Meeting - Conversion and Delivery of Electrical Energy in the 21st Century*, July 2008, pp. 1–8. 6

[52] X. Chen, H. Sun, J. Wen, W. Lee, X. Yuan, N. Li, and L. Yao, "Integrating wind farm to the grid using hybrid multiterminal HVDC technology," *IEEE Transactions on Industry Applications*, vol. 47, no. 2, pp. 965–972, March 2011. 6

[53] H. Rao, "Architecture of nan'ao multi-terminal VSC-HVDC system and its multi-functional control," *CSEE Journal of Power and Energy Systems*, vol. 1, no. 1, pp. 9–18, March 2015. 6

[54] W. Lu and B.-T. Ooi, "Premium quality power park based on multi-terminal HVDC," *IEEE Transactions on Power Delivery*, vol. 20, no. 2, pp. 978–983, April 2005. 6

[55] S. Taggart, G. James, Z. Dong, and C. Russell, "The future of renewables linked by a transnational asian grid," *Proceedings of the IEEE*, vol. 100, no. 2, pp. 348–359, Feb 2012. 6

[56] A. L. P. de Oliveira, C. E. Tibrcio, M. N. Lemes, and D. Retzmann, "Prospects of voltage-sourced converters (VSC) applications in DC transmission systems," in *2010 IEEE/PES Transmission and Distribution Conference and Exposition: Latin America (T D-LA)*, Nov 2010, pp. 491–495. 6

[57] J. Beerten, O. Gomis-Bellmunt, X. Guillaud, J. Rimez, A. van der Meer, and D. Van Hertem, "Modeling and control of HVDC grids: A key challenge for the future power system," in *2014 Power Systems Computation Conference*, Aug 2014, pp. 1–21. 6, 201

[58] K. Sharifabadi, L. Harnefors, H.-P. Nee, S. Norrga, and R. Teodorescu, *Design, control, and application of modular multilevel converters for HVDC transmission systems.* John Wiley & Sons, 2016. 6,

8, 97

[59] N. Mohan and T. M. Undeland, *Power electronics: converters, applications, and design*. John wiley & sons, 2007. 6

[60] A. Nami, J. Liang, F. Dijkhuizen, and G. D. Demetriades, "Modular multilevel converters for HVDC applications: Review on converter cells and functionalities," *IEEE Transactions on Power Electronics*, vol. 30, no. 1, pp. 18–36, Jan 2015. 6

[61] B. Chuco and E. H. Watanabe, "A comparative study of dynamic performance of HVDC system based on conventional VSC and MMC-VSC," in *2010 IREP Symposium Bulk Power System Dynamics and Control - VIII (IREP)*, Aug 2010, pp. 1–6. 6

[62] R. Marquardt, "Modular multilevel converter: An universal concept for HVDC-networks and extended dc-bus-applications," in *The 2010 International Power Electronics Conference - ECCE ASIA -*, June 2010, pp. 502–507. 6

[63] K. Friedrich, "Modern HVDC plus application of vsc in modular multilevel converter topology," in *2010 IEEE International Symposium on Industrial Electronics*, July 2010, pp. 3807–3810. 6

[64] B. Gemmell, J. Dorn, D. Retzmann, and D. Soerangr, "Prospects of multilevel VSC technologies for power transmission," in *2008 IEEE/PES Transmission and Distribution Conference and Exposition*, April 2008, pp. 1–16. 6

[65] S. Debnath, J. Qin, B. Bahrani, M. Saeedifard, and P. Barbosa, "Operation, control, and applications of the modular multilevel converter: A review," *IEEE Transactions on Power Electronics*, vol. 30, no. 1, pp. 37–53, Jan 2015. 6

[66] C. Oates, "Modular multilevel converter design for VSC HVDC applications," *IEEE Journal of Emerging and Selected Topics in Power Electronics*, vol. 3, no. 2, pp. 505–515, June 2015. 6

[67] S. Allebrod, R. Hamerski, and R. Marquardt, "New transformerless, scalable modular multilevel converters for HVDC-transmission," in *2008 IEEE Power Electronics Specialists Conference*, June 2008, pp. 174–179. 6

[68] K. Ji, G. Tang, J. Yang, Y. Li, and D. Liu, "Harmonic stability analysis of MMC-based DC system using DC impedance model," *IEEE Journal of Emerging and Selected Topics in Power Electronics*, pp. 1–1, 2019. 8

[69] J. Beerten, G. B. Diaz, S. D'Arco, and J. A. Suul, "Comparison of small-signal dynamics in mmc and two-level vsc hvdc transmission schemes," in *2016 IEEE International Energy Conference (ENERGYCON)*, April 2016, pp. 1–6. 8

[70] R. D. Middlebrook and S. Cuk, "A general unified approach to modelling switching-converter power stages," in *1976 IEEE Power Elec-*

tronics Specialists Conference, June 1976, pp. 18–34. 18

[71] J. Sun, "Impedance-based stability criterion for grid-connected inverters," *IEEE Transactions on Power Electronics*, vol. 26, no. 11, pp. 3075–3078, Nov 2011. 18, 63, 70

[72] ——, "Small-signal methods for AC distributed power systems–a review," *IEEE Transactions on Power Electronics*, vol. 24, no. 11, pp. 2545–2554, Nov 2009. 18

[73] J. Sun, Z. Bing, and K. J. Karimi, "Input impedance modeling of multipulse rectifiers by harmonic linearization," *IEEE Transactions on Power Electronics*, vol. 24, no. 12, pp. 2812–2820, Dec 2009. 18

[74] X. Wang and F. Blaabjerg, "Harmonic stability in power electronic based power systems: Concept, modeling, and analysis," *IEEE Transactions on Smart Grid*, pp. 1–1, 2018. 18, 67, 121

[75] X. Wang, F. Blaabjerg, M. Liserre, Z. Chen, J. He, and Y. Li, "An active damper for stabilizing power-electronics-based AC systems," *IEEE Transactions on Power Electronics*, vol. 29, no. 7, pp. 3318–3329, July 2014. 18

[76] X. Wang, Y. W. Li, F. Blaabjerg, and P. C. Loh, "Virtual-impedance-based control for voltage-source and current-source converters," *IEEE Transactions on Power Electronics*, vol. 30, no. 12, pp. 7019–7037, Dec 2015. 18

[77] L. Harnefors, L. Zhang, and M. Bongiorno, "Frequency-domain passivity-based current controller design," *IET Power Electronics*, vol. 1, no. 4, pp. 455–465, December 2008. 18, 142

[78] L. Harnefors, A. G. Yepes, A. Vidal, and J. Doval-Gandoy, "Passivity-based controller design of grid-connected VSCs for prevention of electrical resonance instability," *IEEE Transactions on Industrial Electronics*, vol. 62, no. 2, pp. 702–710, Feb 2015. 18, 142

[79] M. Amin, A. Rygg, and M. Molinas, "Impedance-based and eigenvalue based stability assessment compared in VSC-HVDC system," in *2016 IEEE Energy Conversion Congress and Exposition (ECCE)*, Sept 2016, pp. 1–8. 18

[80] M. Amin, M. Molinas, J. Lyu, and X. Cai, "Impact of power flow direction on the stability of VSC-HVDC seen from the impedance nyquist plot," *IEEE Transactions on Power Electronics*, vol. 32, no. 10, pp. 8204–8217, Oct 2017. 18

[81] F. D. Freijedo, S. K. Chaudhary, R. Teodorescu, J. M. Guerrero, C. L. Bak, . H. Kocewiak, and C. F. Jensen, "Harmonic resonances in wind power plants: Modeling, analysis and active mitigation methods," in *2015 IEEE Eindhoven PowerTech*, June 2015, pp. 1–6. 18

[82] M. Amin and M. Molinas, "Understanding the origin of oscillatory phenomena observed between wind farms and HVdc systems," *IEEE Journal of Emerging and Selected Topics in Power Electron-*

ics, vol. 5, no. 1, pp. 378–392, March 2017. 18

[83] L. Jessen and F. W. Fuchs, "Modeling of inverter output impedance for stability analysis in combination with measured grid impedances," in *2015 IEEE 6th International Symposium on Power Electronics for Distributed Generation Systems (PEDG)*, June 2015, pp. 1–7. 18

[84] M. Cespedes and J. Sun, "Modeling and mitigation of harmonic resonance between wind turbines and the grid," in *2011 IEEE Energy Conversion Congress and Exposition*, Sept 2011, pp. 2109–2116. 18

[85] E. Ebrahimzadeh, F. Blaabjerg, X. Wang, and C. L. Bak, "Efficient approach for harmonic resonance identification of large wind power plants," in *2016 IEEE 7th International Symposium on Power Electronics for Distributed Generation Systems (PEDG)*, June 2016, pp. 1–7. 18

[86] E. Ebrahimzadeh, F. Blaabjerg, X. Wang, and C. L. Bak, "Harmonic stability and resonance analysis in large PMSG-based wind power plants," *IEEE Transactions on Sustainable Energy*, vol. 9, no. 1, pp. 12–23, Jan 2018. 18

[87] M. Cheah-Mane, L. Sainz, J. Liang, N. Jenkins, and C. E. U. Loo, "Criterion for the electrical resonance stability of offshore wind power plants connected through HVDC links," *IEEE Transactions on Power Systems*, vol. PP, no. 99, pp. 1–1, 2017. 18

[88] L. Harnefors, M. Bongiorno, and S. Lundberg, "Input-admittance calculation and shaping for controlled voltage-source converters," *IEEE Transactions on Industrial Electronics*, vol. 54, no. 6, pp. 3323–3334, Dec 2007. 18, 122

[89] M. Cespedes and J. Sun, "Impedance modeling and analysis of grid-connected voltage-source converters," *IEEE Transactions on Power Electronics*, vol. 29, no. 3, pp. 1254–1261, March 2014. 18

[90] L. Harnefors, X. Wang, A. G. Yepes, and F. Blaabjerg, "Passivity-based stability assessment of grid-connected VSCsan overview," *IEEE Journal of emerging and selected topics in Power Electronics*, vol. 4, no. 1, pp. 116–125, 2016. 18

[91] X. Wang, F. Blaabjerg, and W. Wu, "Modeling and analysis of harmonic stability in an AC power-electronics-based power system," *IEEE Transactions on Power Electronics*, vol. 29, no. 12, pp. 6421–6432, Dec 2014. 18, 63

[92] Z. Bing, K. J. Karimi, and J. Sun, "Input impedance modeling and analysis of line-commutated rectifiers," *IEEE Transactions on Power Electronics*, vol. 24, no. 10, pp. 2338–2346, Oct 2009. 18

[93] E. Ebrahimzadeh, F. Blaabjerg, X. Wang, and C. L. Bak, "Bus participation factor analysis for harmonic instability in power electronics based power systems," *IEEE Transactions on Power Electronics*,

vol. 33, no. 12, pp. 10 341–10 351, Dec 2018. 18

[94] C. Yoon, H. Bai, R. N. Beres, X. Wang, C. L. Bak, and F. Blaabjerg, "Harmonic stability assessment for multiparalleled, grid-connected inverters," *IEEE Transactions on Sustainable Energy*, vol. 7, no. 4, pp. 1388–1397, Oct 2016. 18

[95] J. Khazaei, M. Beza, and M. Bongiorno, "Impedance analysis of modular multi-level converters connected to weak AC grids," *IEEE Transactions on Power Systems*, vol. 33, no. 4, pp. 4015–4025, July 2018. 18, 70

[96] B. Wen, D. Dong, D. Boroyevich, R. Burgos, P. Mattavelli, and Z. Shen, "Impedance-based analysis of grid-synchronization stability for three-phase paralleled converters," *IEEE Transactions on Power Electronics*, vol. 31, no. 1, pp. 26–38, Jan 2016. 18

[97] M. Beza, M. Bongiorno, and G. Stamatiou, "Analytical derivation of the AC-side input admittance of a modular multilevel converter with open- and closed-loop control strategies," *IEEE Transactions on Power Delivery*, vol. 33, no. 1, pp. 248–256, Feb 2018. 18

[98] B. Wen, D. Boroyevich, R. Burgos, P. Mattavelli, and Z. Shen, "Inverse nyquist stability criterion for grid-tied inverters," *IEEE Transactions on Power Electronics*, vol. 32, no. 2, pp. 1548–1556, 2017. 18

[99] A. J. Agbemuko, J. L. Domnguez-Garca, and O. Gomis-Bellmunt, "An integrated approach to understanding the impact of network resonances and control on dynamic responses in VSC-HVdc networks," *IFAC-PapersOnLine*, vol. 51, no. 28, pp. 344 – 349, 2018, 10th IFAC Symposium on Control of Power and Energy Systems CPES 2018. 18

[100] L. Xu, L. Fan, and Z. Miao, "DC impedance-model-based resonance analysis of a VSC-HVDC system," *IEEE Transactions on Power Delivery*, vol. 30, no. 3, pp. 1221–1230, June 2015. 18, 70

[101] D. Lu, X. Wang, and F. Blaabjerg, "Impedance-based analysis of DC-link voltage dynamics in voltage-source converters," *IEEE Transactions on Power Electronics*, pp. 1–1, 2018. 18

[102] L. Xu and L. Fan, "Impedance-based resonance analysis in a VSC-HVDC system," *IEEE Transactions on Power Delivery*, vol. 28, no. 4, pp. 2209–2216, Oct 2013. 18, 70

[103] A. J. Agbemuko, J. L. Domnguez-Garca, E. Prieto-Araujo, and O. Gomis-Bellmunt, "Impedance modelling and parametric sensitivity of a VSC-HVDC system: New insights on resonances and interactions," *Energies*, vol. 11, no. 4, 2018. 18

[104] G. Stamatiou, M. Beza, M. Bongiorno, and L. Harnefors, "Analytical derivation of the DC-side input admittance of the direct-voltage controlled modular multilevel converter," *IET Generation, Trans-*

mission Distribution, vol. 11, no. 16, pp. 4018–4030, 2017. 18, 70

[105] A. J. Agbemuko, J. L. Domnguez-Garca, E. Prieto-Araujo, and O. Gomis-Bellmunt, "Dynamic modelling and interaction analysis of multi-terminal vsc-hvdc grids through an impedance-based approach," *International Journal of Electrical Power & Energy Systems*, vol. 113, pp. 874 – 887, 2019. 18

[106] A. Rygg, M. Molinas, C. Zhang, and X. Cai, "A modified sequence-domain impedance definition and its equivalence to the dq-domain impedance definition for the stability analysis of ac power electronic systems," *IEEE Journal of Emerging and Selected Topics in Power Electronics*, vol. 4, no. 4, pp. 1383–1396, Dec 2016. 18, 19

[107] ——, "On the equivalence and impact on stability of impedance modeling of power electronic converters in different domains," *IEEE Journal of Emerging and Selected Topics in Power Electronics*, vol. 5, no. 4, pp. 1444–1454, Dec 2017. 18

[108] G. Amico, A. Egea-Alvarez, P. Brogan, and S. Zang, "Small-signal converter admittance in the pn-frame: systematic derivation and analysis of the cross-coupling terms," *IEEE Transactions on Energy Conversion*, pp. 1–1, 2019. 19

[109] X. Wang, L. Harnefors, and F. Blaabjerg, "Unified impedance model of grid-connected voltage-source converters," *IEEE Transactions on Power Electronics*, vol. 33, no. 2, pp. 1775–1787, 2018. 19

[110] A. Yazdani and R. Iravani, *Voltage-sourced converters in power systems: modeling, control, and applications*. John Wiley & Sons, 2010. 20

[111] P. Krause, O. Wasynczuk, S. D. Sudhoff, and S. Pekarek, *Analysis of electric machinery and drive systems*. John Wiley & Sons, 2013, vol. 75. 48

[112] P. Kundur, N. J. Balu, and M. G. Lauby, *Power system stability and control*. McGraw-hill New York, 1994, vol. 7. 49

[113] J. Beerten, S. D'Arco, and J. A. Suul, "Cable model order reduction for HVDC systems interoperability analysis," in *AC and DC Power Transmission, 11th IET International Conference on*, Feb 2015, pp. 1–10. 50, 69

[114] J. J. Grainger and W. D. Stevenson Jr., *Power system analysis*. McGraw-Hill International Editions, 1994. 55

[115] S. Skogestad and I. Postlethwaite, *Multivariable feedback control: analysis and design*. Wiley New York, 2007, vol. 2. 59, 86, 87

[116] L. Harnefors, "Modeling of three-phase dynamic systems using complex transfer functions and transfer matrices," *IEEE Transactions on Industrial Electronics*, vol. 54, no. 4, pp. 2239–2248, Aug 2007. 59

[117] E. Bristol, "On a new measure of interaction for multivariable pro-

cess control," *IEEE Transactions on Automatic Control*, vol. 11, no. 1, pp. 133–134, January 1966. 61

[118] P. Grosdidier and M. Morari, "Interaction measures for systems under decentralized control," *Automatica*, vol. 22, no. 3, pp. 309 – 319, 1986. 61

[119] A. G. MacFarlane and I. Postlethwaite, "The generalized nyquist stability criterion and multivariable root loci," *International Journal of Control*, vol. 25, no. 1, pp. 81–127, 1977. 63

[120] B. Wen, D. Boroyevich, R. Burgos, P. Mattavelli, and Z. Shen, "Small-signal stability analysis of three-phase AC systems in the presence of constant power loads based on measured d-q frame impedances," *IEEE Transactions on Power Electronics*, vol. 30, no. 10, pp. 5952–5963, Oct 2015. 63

[121] M. Belkhayat, "Stability criteria for ac power systems with regulated loads," Ph.D. dissertation, Purdue University, 1997. 63

[122] X. Wang, L. Harnefors, and F. Blaabjerg, "Unified impedance model of grid-connected voltage-source converters," *IEEE Transactions on Power Electronics*, vol. 33, no. 2, pp. 1775–1787, Feb 2018. 63, 122

[123] Z.-P. Jiang and T. Liu, "Small-gain theory for stability and control of dynamical networks: A survey," *Annual Reviews in Control*, vol. 46, pp. 58 – 79, 2018. 63

[124] G. O. Kalcon, G. P. Adam, O. Anaya-Lara, S. Lo, and K. Uhlen, "Small-signal stability analysis of multi-terminal VSC-based DC transmission systems," *IEEE Transactions on Power Systems*, vol. 27, no. 4, pp. 1818–1830, Nov 2012. 69

[125] G. Pinares and M. Bongiorno, "Modeling and analysis of vsc-based hvdc systems for dc network stability studies," *IEEE Transactions on Power Delivery*, vol. 31, no. 2, pp. 848–856, April 2016. 69

[126] J. Beerten, S. D'Arco, and J. A. Suul, "Identification and small-signal analysis of interaction modes in VSC MTDC systems," *IEEE Transactions on Power Delivery*, vol. 31, no. 2, pp. 888–897, April 2016. 69

[127] S. Cole, J. Beerten, and R. Belmans, "Generalized dynamic VSC MTDC model for power system stability studies," *IEEE Transactions on Power Systems*, vol. 25, no. 3, pp. 1655–1662, Aug 2010. 69

[128] E. Prieto-Araujo, A. Egea-Alvarez, S. Fekriasl, and O. Gomis-Bellmunt, "DC voltage droop control design for multiterminal HVDC systems considering AC and DC grid dynamics," *IEEE Transactions on Power Delivery*, vol. 31, no. 2, pp. 575–585, April 2016. 69, 100

[129] E. Prieto-Araujo, F. D. Bianchi, A. Junyent-Ferre, and O. Gomis-Bellmunt, "Methodology for droop control dynamic analysis of mul-

titerminal VSC-HVDC grids for offshore wind farms," *IEEE Transactions on Power Delivery*, vol. 26, no. 4, pp. 2476–2485, Oct 2011. 69

[130] J. Beerten, S. Cole, and R. Belmans, "Modeling of multi-terminal VSC HVDC systems with distributed DC voltage control," *IEEE Transactions on Power Systems*, vol. 29, no. 1, pp. 34–42, Jan 2014. 69

[131] C. Dierckxsens, K. Srivastava, M. Reza, S. Cole, J. Beerten, and R. Belmans, "A distributed DC voltage control method for VSC-MTDC systems," *Electric Power Systems Research*, vol. 82, no. 1, pp. 54 – 58, 2012. 69

[132] S. Shah and L. Parsa, "Impedance modeling of three-phase voltage source converters in dq, sequence, and phasor domains," *IEEE Transactions on Energy Conversion*, vol. 32, no. 3, pp. 1139–1150, Sep. 2017. 70

[133] T. M. Haileselassie and K. Uhlen, "Impact of DC line voltage drops on power flow of MTDC using droop control," *IEEE Transactions on Power Systems*, vol. 27, no. 3, pp. 1441–1449, Aug 2012. 78

[134] P. Rault, "Implementation of a dedicated control to limit adverse interaction in multi-vendor hvdc systems," *IET Conference Proceedings*, pp. 7 (6 pp.)–7 (6 pp.)(1), January 2019. 81

[135] B. Tourgoutian and A. Alefragkis, "Design considerations for the cobracable hvdc interconnector," in *IET International Conference on Resilience of Transmission and Distribution Networks (RTDN 2017)*, Sep. 2017, pp. 1–7. 81

[136] V. Staudt, A. Steimel, M. Kohlmann, M. K. Jger, C. Heising, D. Meyer, K. Vennemann, E. Grebe, and K. Kleinekorte, "Control concept including validation strategy for an ac/dc hybrid link (ultranet)," in *2014 IEEE Energy Conversion Congress and Exposition (ECCE)*, Sep. 2014, pp. 750–757. 81

[137] T. K. Vrana, R. E. Torres-Olguin, B. Liu, and T. M. Haileselassie, "The north sea super grid - a technical perspective," in *9th IET International Conference on AC and DC Power Transmission (ACDC 2010)*, Oct 2010, pp. 1–5. 81

[138] P. Gahinet and P. Apkarian, "Decentralized and fixed-structure $\mathcal{H}_\infty$ control in matlab," in *2011 50th IEEE Conference on Decision and Control and European Control Conference*, Dec 2011, pp. 8205–8210. 83

[139] B. P. Project. (2018) Final recommendations for interoperability of multivendor hvdc systems. [Online]. Available: http://www.bestpaths-project.eu/contents/publications/d93--final-demo2-recommendations--vfinal.pdf 97

[140] J. Rocabert, A. Luna, F. Blaabjerg, and P. Rodrguez, "Control of

power converters in AC microgrids," *IEEE Transactions on Power Electronics*, vol. 27, no. 11, pp. 4734–4749, Nov 2012. 122

[141] R. Piwko, N. Miller, J. Sanchez-Gasca, X. Yuan, R. Dai, and J. Lyons, "Integrating large wind farms into weak power grids with long transmission lines," in *2005 IEEE/PES Transmission Distribution Conference Exposition: Asia and Pacific*, Aug 2005, pp. 1–7. 122

[142] L. Zhang, L. Harnefors, and H. Nee, "Power-synchronization control of grid-connected voltage-source converters," *IEEE Transactions on Power Systems*, vol. 25, no. 2, pp. 809–820, May 2010. 122

[143] L. Zhang, "Modeling and control of vsc-hvdc links connected to weak ac systems," Ph.D. dissertation, KTH, 2010. 122

[144] J. Z. Zhou, H. Ding, S. Fan, Y. Zhang, and A. M. Gole, "Impact of short-circuit ratio and phase-locked-loop parameters on the small-signal behavior of a VSC-HVDC converter," *IEEE Transactions on Power Delivery*, vol. 29, no. 5, pp. 2287–2296, Oct 2014. 122

[145] Y. Huang, X. Yuan, J. Hu, and P. Zhou, "Modeling of vsc connected to weak grid for stability analysis of dc-link voltage control," *IEEE Journal of Emerging and Selected Topics in Power Electronics*, vol. 3, no. 4, pp. 1193–1204, Dec 2015. 122

[146] D. Dong, B. Wen, D. Boroyevich, P. Mattavelli, and Y. Xue, "Analysis of phase-locked loop low-frequency stability in three-phase grid-connected power converters considering impedance interactions," *IEEE Transactions on Industrial Electronics*, vol. 62, no. 1, pp. 310–321, Jan 2015. 122

[147] S.-K. Chung, "A phase tracking system for three phase utility interface inverters," *IEEE Transactions on Power Electronics*, vol. 15, no. 3, pp. 431–438, May 2000. 122

[148] P. Rodriguez, J. Pou, J. Bergas, J. I. Candela, R. P. Burgos, and D. Boroyevich, "Decoupled double synchronous reference frame pll for power converters control," *IEEE Transactions on Power Electronics*, vol. 22, no. 2, pp. 584–592, March 2007. 122

[149] K. Lee, J. Lee, D. Shin, D. Yoo, and H. Kim, "A novel grid synchronization pll method based on adaptive low-pass notch filter for grid-connected pcs," *IEEE Transactions on Industrial Electronics*, vol. 61, no. 1, pp. 292–301, Jan 2014. 122

[150] R. Teodorescu, M. Liserre, and P. Rodriguez, *Grid converters for photovoltaic and wind power systems.* John Wiley & Sons, 2011, vol. 29. 122, 124

[151] J. Zhou, "Vsc transmission limitations imposed by ac system strength and ac impedance characteristics," *IET Conference Proceedings*, pp. 06–06(1), January 2012. 122

[152] M. F. M. Arani and Y. A. I. Mohamed, "Analysis and performance

enhancement of vector-controlled vsc in hvdc links connected to very weak grids," *IEEE Transactions on Power Systems*, vol. 32, no. 1, pp. 684–693, Jan 2017. 122

[153] N. P. W. Strachan and D. Jovcic, "Stability of a variable-speed permanent magnet wind generator with weak ac grids," *IEEE Transactions on Power Delivery*, vol. 25, no. 4, pp. 2779–2788, Oct 2010. 122, 145

[154] A. Egea-Alvarez, S. Fekriasl, F. Hassan, and O. Gomis-Bellmunt, "Advanced vector control for voltage source converters connected to weak grids," *IEEE Transactions on Power Systems*, vol. 30, no. 6, pp. 3072–3081, Nov 2015. 122

[155] G. Wu, J. Liang, X. Zhou, Y. Li, A. Egea-Alvarez, G. Li, H. Peng, and X. Zhang, "Analysis and design of vector control for vsc-hvdc connected to weak grids," *CSEE Journal of Power and Energy Systems*, vol. 3, no. 2, pp. 115–124, June 2017. 122

[156] J. A. Suul, S. D'Arco, P. Rodriguez, and M. Molinas, "Extended stability range of weak grids with voltage source converters through impedance-conditioned grid synchronization," in *11th IET International Conference on AC and DC Power Transmission*, Feb 2015, pp. 1–10. 122

[157] L. Harnefors, X. Wang, A. G. Yepes, and F. Blaabjerg, "Passivity-based stability assessment of grid-connected vscsan overview," *IEEE Journal of Emerging and Selected Topics in Power Electronics*, vol. 4, no. 1, pp. 116–125, March 2016. 142

[158] G. Strang, *Linear Algebra and Its Applications*. Thomson, Brooks/Cole, 2006. 143

[159] L. Harnefors, "Analysis of subsynchronous torsional interaction with power electronic converters," *IEEE Transactions on Power Systems*, vol. 22, no. 1, pp. 305–313, Feb 2007. 145

[160] J. Pan, R. Nuqui, K. Srivastava, T. Jonsson, P. Holmberg, and Y. Hafner, "Ac grid with embedded vsc-hvdc for secure and efficient power delivery," in *2008 IEEE Energy 2030 Conference*, Nov 2008, pp. 1–6. 163

[161] E. Unamuno and J. A. Barrena, "Hybrid ac/dc microgridspart i: Review and classification of topologies," *Renewable and Sustainable Energy Reviews*, vol. 52, pp. 1251 – 1259, 2015. 163

[162] ——, "Hybrid AC/DC microgridspart ii: Review and classification of control strategies," *Renewable and Sustainable Energy Reviews*, vol. 52, pp. 1123 – 1134, 2015. 163

[163] F. Nejabatkhah and Y. W. Li, "Overview of power management strategies of hybrid ac/dc microgrid," *IEEE Transactions on Power Electronics*, vol. 30, no. 12, pp. 7072–7089, Dec 2015. 163

[164] X. Liu, P. Wang, and P. C. Loh, "A hybrid ac/dc microgrid and

its coordination control," *IEEE Transactions on Smart Grid*, vol. 2, no. 2, pp. 278–286, June 2011. 163

[165] X. Lu, J. M. Guerrero, K. Sun, J. C. Vasquez, R. Teodorescu, and L. Huang, "Hierarchical control of parallel ac-dc converter interfaces for hybrid microgrids," *IEEE Transactions on Smart Grid*, vol. 5, no. 2, pp. 683–692, March 2014. 163

[166] T. Van Cutsem and C. Vournas, *Voltage stability of electric power systems*. Springer Science & Business Media, 2007. 188

[167] C. W. Taylor, *Power system voltage stability*. McGraw-Hill, 1994. 188

[168] J. A. Acebrón, L. L. Bonilla, C. J. Pérez Vicente, F. Ritort, and R. Spigler, "The kuramoto model: A simple paradigm for synchronization phenomena," *Rev. Mod. Phys.*, vol. 77, pp. 137–185, Apr 2005. 188

[169] F. Dörfler, M. Chertkov, and F. Bullo, "Synchronization in complex oscillator networks and smart grids," *Proceedings of the National Academy of Sciences*, vol. 110, no. 6, pp. 2005–2010, 2013. 188

[170] J. Schiffer, R. Ortega, A. Astolfi, J. Raisch, and T. Sezi, "Conditions for stability of droop-controlled inverter-based microgrids," *Automatica*, vol. 50, no. 10, pp. 2457 – 2469, 2014. 188

[171] F. Dörfler and F. Bullo, "Synchronization in complex networks of phase oscillators: A survey," *Automatica*, vol. 50, no. 6, pp. 1539 – 1564, 2014. 188

[172] X. Li and G. Chen, "Synchronization and desynchronization of complex dynamical networks: an engineering viewpoint," *IEEE Transactions on Circuits and Systems I: Fundamental Theory and Applications*, vol. 50, no. 11, pp. 1381–1390, Nov 2003. 188

[173] F. Dörfler and F. Bullo, "Exploring synchronization in complex oscillator networks," in *2012 IEEE 51st IEEE Conference on Decision and Control (CDC)*, Dec 2012, pp. 7157–7170. 188

[174] J. W. Simpson-Porco, F. Drfler, and F. Bullo, "Synchronization and power sharing for droop-controlled inverters in islanded microgrids," *Automatica*, vol. 49, no. 9, pp. 2603 – 2611, 2013. 188

[175] A. E. Motter, S. A. Myers, M. Anghel, and T. Nishikawa, "Spontaneous synchrony in power-grid networks," *Nature Physics*, vol. 9, no. 3, p. 191, 2013. 188

[176] J. Schiffer, D. Goldin, J. Raisch, and T. Sezi, "Synchronization of droop-controlled microgrids with distributed rotational and electronic generation," in *52nd IEEE Conference on Decision and Control*, Dec 2013, pp. 2334–2339. 188

[177] C. Chu and H. H. Iu, "Complex networks theory for modern smart grid applications: A survey," *IEEE Journal on Emerging and Selected Topics in Circuits and Systems*, vol. 7, no. 2, pp. 177–191,

June 2017. 188

[178] Y. Tang, F. Qian, H. Gao, and J. Kurths, "Synchronization in complex networks and its application a survey of recent advances and challenges," *Annual Reviews in Control*, vol. 38, no. 2, pp. 184 – 198, 2014. 188

[179] A. Dória-Cerezo, J. M. Olm, M. di Bernardo, and E. Nuo, "Modelling and control for bounded synchronization in multi-terminal VSC-HVDC transmission networks," *IEEE Transactions on Circuits and Systems I: Regular Papers*, vol. 63, no. 6, pp. 916–925, June 2016. 188

[180] L. A. B. Tôrres, J. P. Hespanha, and J. Moehlis, "Synchronization of identical oscillators coupled through a symmetric network with dynamics: A constructive approach with applications to parallel operation of inverters," *IEEE Transactions on Automatic Control*, vol. 60, no. 12, pp. 3226–3241, Dec 2015. 188

[181] B. B. Johnson, S. V. Dhople, A. O. Hamadeh, and P. T. Krein, "Synchronization of nonlinear oscillators in an LTI electrical power network," *IEEE Transactions on Circuits and Systems I: Regular Papers*, vol. 61, no. 3, pp. 834–844, March 2014. 188

[182] S. V. Dhople, B. B. Johnson, F. Drfler, and A. O. Hamadeh, "Synchronization of nonlinear circuits in dynamic electrical networks with general topologies," *IEEE Transactions on Circuits and Systems I: Regular Papers*, vol. 61, no. 9, pp. 2677–2690, Sept 2014. 188

[183] Y. Kuramoto, "Cooperative Dynamics of Oscillator Community: A Study Based on Lattice of Rings," *Progress of Theoretical Physics Supplement*, vol. 79, pp. 223–240, 02 1984. [Online]. Available: https://doi.org/10.1143/PTPS.79.223 189, 195

[184] A. Arenas, A. Daz-Guilera, J. Kurths, Y. Moreno, and C. Zhou, "Synchronization in complex networks," *Physics Reports*, vol. 469, no. 3, pp. 93 – 153, 2008. 189

[185] J. Sethna, *Statistical mechanics: entropy, order parameters, and complexity*. Oxford University Press, 2006, vol. 14. 189, 195, 196

[186] S. H. Strogatz, "From kuramoto to crawford: exploring the onset of synchronization in populations of coupled oscillators," *Physica D: Nonlinear Phenomena*, vol. 143, no. 1-4, pp. 1–20, 2000. 189, 195

[187] M. Rohden, A. Sorge, D. Witthaut, and M. Timme, "Impact of network topology on synchrony of oscillatory power grids," *Chaos: An Interdisciplinary Journal of Nonlinear Science*, vol. 24, no. 1, p. 013123, 2014. 189

[188] M. Rohden, A. Sorge, M. Timme, and D. Witthaut, "Self-organized synchronization in decentralized power grids," *Phys. Rev. Lett.*, vol. 109, p. 064101, Aug 2012. 189

[189] M. Kleman and O. D. Lavrentovich, Eds., *The Order Parameter:*

Amplitude and Phase. New York, NY: Springer New York, 2003, pp. 76–104. 195

[190] M. A. Porter and J. P. Gleeson, "Dynamical systems on networks: a tutorial," *arXiv preprint arXiv:1403.7663*, 2014. 195

[191] T. K. Vrana, Y. Yang, D. Jovcic, S. Dennetière, J. Jardini, and H. Saad, "The cigre b4 dc grid test system," *Electra*, vol. 270, no. 1, pp. 10–19, 2013. 197

A

List of Publications

In this chapter, the list of publications both journals and conferences papers, derived from the development of the thesis are presented.

A.1 Journal articles

J1 Agbemuko, A. J., Domnguez-Garca, J. L., Prieto-Araujo, E. and Gomis-Bellmunt, O., "Impedance modelling and parametric sensitivity of a VSC-HVDC system: New insights on resonances and interactions." Energies 11, no. 4 (2018): 845. Related to Chapter 5.

J2 Agbemuko, A.J., Domnguez-Garca, J.L., Prieto-Araujo, E. and Gomis-Bellmunt, O., "Dynamic modelling and interaction analysis of multi-terminal VSC-HVDC grids through an impedance-based approach." International Journal of Electrical Power & Energy Systems, 113, pp.874-887. Related to Chapters 2 and 3.

J3 Agbemuko, A.J., Domnguez-Garca, J.L., Prieto-Araujo, E. and Gomis-Bellmunt, O., "Advanced Impedance-based Control Design for Multi-Vendor Converter HVDC Grids." IEEE Transactions on Power Delivery (*In review*). Related to Chapter 3.

J4 Agbemuko, A.J., Domnguez-Garca, J.L., Gomis-Bellmunt, O., and Harnefors, L., "Passivity-Based Analysis and Performance Enhancement of a VSC Connected to a Weak AC Grid." IEEE Transactions on Power Delivery (*In review*). Related to Chapter 4.

J5 Agbemuko, A.J., Domnguez-Garca, J.L. and Gomis-Bellmunt, O., "Robust Decentralized Approach to Interaction Mitigation in VSC-HVDC Grids Through Impedance Minimization." Journal of Control Engineering Practice (*In review*). Related to Chapter 3.

J6 Agbemuko, A.J., Domnguez-Garca, J.L. and Gomis-Bellmunt, O., "Impedance-Based Modelling of Hybrid AC-DC Grids with Synchronous Generator for Interaction Study and Dynamic Improvement." Electric Power System Research (*In review*). Related to Chapter 5.

A.2 Conference articles

C1 Agbemuko, A.J., Domnguez-Garca, J.L. and Gomis-Bellmunt, O.,"An integrated approach to understanding the impact of network resonances and control on dynamic responses in VSC-HVdc networks" IFAC-PapersOnLine 51, no. 28 (2018): 344-349. Related to Chapter 3.

C2 Agbemuko, A.J., Domnguez-Garca, J.L., Prieto-Araujo, E. and Gomis-Bellmunt, O.,"Harmonic stability and interactions in meshed vsc-hvdc dominated power systems." In Proceedings of the 16th International Wind Integration Workshop, Berlin, Germany, pp. 25-27. 2017. Related to Chapter 3.

C3 Agbemuko, A.J., Domnguez-Garca, J.L. and Gomis-Bellmunt, O., "Impedance-based Modelling of a Hybrid AC/DC Grid with Z-bus Approach." In 2018 IEEE Power & Energy Society General Meeting (PESGM), pp. 1-5. IEEE, 2018. Related to Chapters 2 and 3.

C4 Agbemuko, A.J., Domnguez-Garca, J.L. and Gomis-Bellmunt, O., "Harmonic stability and interaction in hvdc dominated power systems." In 2017 IEEE NEIS Conference, pp. 1-6. 2017. Related to Chapter 3.

C5 Agbemuko, A.J., Domnguez-Garca, J.L. and Gomis-Bellmunt, O.,"An Impedance-based Robust Supplementary Controller Design for Offshore HV-MTDC Grids." In 2019 Cigré Symposium, pp. 1-11. 2019. Related to Chapter 3.

C6 Agbemuko, A.J., Domnguez-Garca, J.L. and Gomis-Bellmunt, O., "Impacts of Operating Point and Active Power Capability Improvement of a VSC Connected to Very Weak Grids." In 2019 Wind Energy Science Conference. Related to Chapter 4.

A.3 Other publications

Within this section other relevant publications not directly related to the thesis but published during it.

O1 Agbemuko, A., van Meurs, J., and van Driel W. D., "Lightning Effects on LED-Based Luminaires." In Solid State Lighting Reliability Part 2, pp. 573-583. Springer, Cham, 2018.

O2 Agbemuko, A.J., Ndreko, M., Popov, M., RuedaTorres, J.L. and van der Meijden, M.A., "Knowledge-Based Primary and Optimization-Based Secondary Control of Multiterminal HVDC Grids". Dynamic Vulnerability Assessment and Intelligent Control: For Sustainable Power Systems, p.233.

B Linearization

B.1 Variable Transformations

The transformations between the converter and grid reference frames given the PLL output angle is derived as

$$i^c_{cd,q} = i_{cd,q} e^{-j\theta_p} = i_{cd,q}\left(\cos\theta_p - j\sin\theta_p\right); \quad i_{cd,q} = i_{cd} + j i_{cq} \tag{B.1a}$$

$$u^c_{fd,q} = u_{fd,q} e^{-j\theta_p} = u_{fd,q}\left(\cos\theta_p - j\sin\theta_p\right); \quad u_{fd,q} = u_{fd} + j u_{fq} \tag{B.1b}$$

$$u_{cd,q} = u^c_{cd,q} e^{j\theta_p} = u^c_{cd,q}\left(\cos\theta_p + j\sin\theta_p\right); \quad u^c_{cd,q} = u^c_{cd} + j u^c_{cq} \tag{B.1c}$$

The transformation above can be linearized at an operating point as

$$\begin{pmatrix}\Delta i^c_{cd}\\ \Delta i^c_{cq}\end{pmatrix} = \underbrace{\begin{pmatrix}\cos\theta^0_p & \sin\theta^0_p & -i^0_{cd}\sin\theta^0_p + i^0_{cq}\cos\theta^0_p\\ -\sin\theta^0_p & \cos\theta^0_p & -i^0_{cd}\cos\theta^0_p - i^0_{cq}\sin\theta^0_p\end{pmatrix}}_{\mathbf{T}^i}\begin{pmatrix}\Delta i_{cd}\\ \Delta i_{cq}\\ \Delta\theta_p\end{pmatrix} \tag{B.2a}$$

$$\begin{pmatrix}\Delta u^c_{fd}\\ \Delta u^c_{fq}\end{pmatrix} = \underbrace{\begin{pmatrix}\cos\theta^0_p & \sin\theta^0_p & -u^0_{fd}\sin\theta^0_p + u^0_{fq}\cos\theta^0_p\\ -\sin\theta^0_p & \cos\theta^0_p & -u^0_{fd}\cos\theta^0_p - u^0_{fq}\sin\theta^0_p\end{pmatrix}}_{\mathbf{T}^v}\begin{pmatrix}\Delta u_{fd}\\ \Delta u_{fq}\\ \Delta\theta_p\end{pmatrix} \tag{B.2b}$$

$$\begin{pmatrix}\Delta u_{cd}\\ \Delta u_{cq}\end{pmatrix} = \underbrace{\begin{pmatrix}\cos\theta^0_p & -\sin\theta^0_p & -u^{c0}_{cd}\sin\theta^0_p - u^{c0}_{cq}\cos\theta^0_p\\ \sin\theta^0_p & \cos\theta^0_p & u^{c0}_{cd}\cos\theta^0_p - u^{c0}_{cq}\sin\theta^0_p\end{pmatrix}}_{\mathbf{T}}\begin{pmatrix}\Delta u^c_{cd}\\ \Delta u^c_{cq}\\ \Delta\theta_p\end{pmatrix} \tag{B.2c}$$

where all variables with superscript '0' are corresponding operating points; $\mathbf{T}$ is a linearized transformation matrix between converter and grid frame

variables, whereas $\mathbf{T}_v$ and $\mathbf{T}_i$ are equivalent inverse transformation matrices between grid and converter frame variables. They can be written compactly as

$$\mathbf{T}^i = \begin{pmatrix} T^i_{11} & T^i_{12} & T^i_{13} \\ T^i_{21} & T^i_{22} & T^i_{23} \end{pmatrix}; \quad \mathbf{T}^v = \begin{pmatrix} T^v_{11} & T^v_{12} & T^v_{13} \\ T^v_{21} & T^v_{22} & T^v_{23} \end{pmatrix}; \quad \mathbf{T} = \begin{pmatrix} T_{11} & T_{12} & T_{13} \\ T_{21} & T_{22} & T_{23} \end{pmatrix}$$

B.2 PLL Transfer Functions

1. The following transfer functions predict the impact of the closed loop PLL device on the system.

$$\begin{aligned} H_{d\theta}(s) &= \frac{K_{pll}(s)\sin\theta^0_p}{s - K_{pll}(s)(u^0_{fd}\cos\theta^0_p + u^0_{fq}\sin\theta^0_p)} \\ H_{q\theta}(s) &= \frac{K_{pll}(s)\cos\theta^0_p}{s - K_{pll}(s)(u^0_{fd}\cos\theta^0_p + u^0_{fq}\sin\theta^0_p)} \end{aligned} \tag{B.3}$$

2. The following describe the elements of the augmented matrix $\mathbf{V}(s)$ as described in (2.14).

$$\begin{aligned} V_{11}(s) &= K_c(s)T^i_{13}H_{d\theta}(s) + F_d(s)\left(T^v_{13}H_{d\theta}(s) + T^v_{11}\right) \\ V_{12}(s) &= K_c(s)T^i_{13}H_{q\theta}(s) + F_q(s)\left(T^v_{13}H_{q\theta}(s) + T^v_{12}\right) \\ V_{21}(s) &= K_c(s)T^i_{23}H_{d\theta}(s) + F_d(s)\left(T^v_{23}H_{d\theta}(s) + T^v_{21}\right) \\ V_{22}(s) &= K_c(s)T^i_{23}H_{q\theta}(s) + F_q(s)\left(T^v_{23}H_{q\theta}(s) + T^v_{22}\right) \end{aligned}. \tag{B.4}$$

B.3 Inner loop Transfer Functions

For the current controlled converter with equivalent PCC voltage feedforward filters such that $F_d(s) = F_q(s) = F(s)$, the components of the admittance matrix can be expanded compactly as

$$\begin{aligned} y_{dd}(s) &= \frac{y_{ac}(s)}{1 + K_c(s)y_{ac}(s)}\left(H_{d\theta}(s)(a_1 + a_3 - K_c(s)i^0_{cq} - F(s)u^0_{fq}) + 1 - F(s)\right) \\ y_{dq}(s) &= \frac{y_{ac}(s)}{1 + K_c(s)y_{ac}(s)}\left(H_{q\theta}(s)(a_1 + a_3 - K_c(s)i^0_{cq} - F(s)u^0_{fq})\right) \\ y_{qd}(s) &= \frac{y_{ac}(s)}{1 + K_c(s)y_{ac}(s)}\left(H_{d\theta}(s)(a_2 - a_4 + K_c(s)i^0_{cd} + F(s)u^0_{fd})\right) \\ y_{qq}(s) &= \frac{y_{ac}(s)}{1 + K_c(s)y_{ac}(s)}\left(H_{q\theta}(s)(a_2 - a_4 + K_c(s)i^0_{cd} + F(s)u^0_{fd}) + 1 - F(s)\right) \end{aligned} \tag{B.5}$$

where

$$a_1 = u^0_{cq}\cos\theta^0_p; \quad a_2 = u^0_{cq}\sin\theta^0_p; \quad a_3 = u^0_{cd}\sin\theta^0_p; \quad a_4 = u^0_{cd}\cos\theta^0_p.$$

B.4 State-space Linearization

The following expressions details the state-space equations of the VSC for input-output derivation of the impedance models

B.4.1 Alternating/Direct-Voltage Controlled VSC

$$\frac{d}{dt}\Delta i_{cd} = -\frac{R}{L}\Delta i_{cd} - \omega\Delta i_{cq} - \frac{\Delta u_{cd}}{L} + \frac{\Delta u_{fd}}{L} \tag{B.6a}$$

$$\frac{d}{dt}\Delta i_{cq} = -\frac{R}{L}\Delta i_{cq} + \omega\Delta i_{cd} - \frac{\Delta u_{cq}}{L} + \frac{\Delta u_{fq}}{L} \tag{B.6b}$$

$$\frac{d}{dt}\Delta V_{dc} = \frac{\Delta I_{dc}}{C_{dc}} + \frac{\Delta I_n}{C_{dc}}. \tag{B.6c}$$

Given the PI gains of the DVC k_{pv} and k_{iv} respectively, the output of the DVC is obtained as

$$\Delta I^*_{dc} = -k_{pv}\Delta V_{dc} + \Delta x_d \tag{B.7}$$

where

$$\frac{d}{dt}\Delta x_d = -k_{iv}\Delta V_{dc} \tag{B.8}$$

and Δx_d is the state of the DVC integrator. The inner-loop reference can be obtained by substituting ΔI^*_{dc} into the linearized $d-$axis current to obtain

$$\Delta i^*_{cd} = -\frac{kk_{pv}V^0_{dc}}{u^0_{fd}}\Delta V_{dc} - \frac{kP^0_{dc}}{(u^0_{fd})^2}\Delta u_f fd + \frac{kV^0_{dc}}{u_{fd}}\Delta x_d. \tag{B.9}$$

In a similar manner, Δi^*_{cq} can be obtained from the AVC output as

$$\Delta i^*_{cq} = -\frac{k_{pu}u^0_{fd}}{U^0_f}\Delta u_{fd} - \frac{k_{pu}u^0_{fq}}{U^0_f}\Delta u_{fq} + \Delta x_q \tag{B.10}$$

where

$$\frac{d}{dt}\Delta x_q = \frac{-k_{iu}u^0_{fd}}{U^0_f}\Delta u_{fd} - \frac{k_{iu}u^0_{fq}}{U^0_f}\Delta u_{fq}. \tag{B.11}$$

and Δx_q is the state of the AVC integrator.

Assuming all-pass feedforward filters, $F_d = F_q = 1$, the converter voltages on own reference frame is obtained as

$$\begin{aligned}\Delta u^c_{cd} &= -K_c(s)(\Delta i^*_{cd} - \Delta i^c_{cd}) - \omega L\Delta i^c_{cq} + \Delta u^c_{fd}\\ \Delta u^c_{cq} &= -K_c(s)(\Delta i^*_{cq} - \Delta i^c_{cq}) + \omega L\Delta i^c_{cd} + \Delta u^c_{fq}\end{aligned} \tag{B.12}$$

where the linearized transformation matrices in (B.2) are applied to corresponding variables in (B.12) to obtain

$$\begin{aligned}\Delta u_{cd} &= K_c(s)\left(-\cos\theta_p^0\Delta i_{cd}^* + \sin\theta_p^0\Delta i_{cq}^* + \Delta i_{cd} + i_{cq}^0\Delta\theta_p\right) - \omega L\Delta i_{cq}^0 + \Delta u_{fd} \\ &\quad + \left(\omega L i_{cd}^0 - u_{cq}^{c0}\cos\theta_p^0 - u_{cd}^{c0}\sin\theta_p^0 + u_{fq}^0\right)\Delta\theta_p \\ \Delta u_{cq} &= K_c(s)\left(-\cos\theta_p^0\Delta i_{cq}^* - \sin\theta_p^0\Delta i_{cd}^* + \Delta i_{cq} - i_{cd}^0\Delta\theta_p\right) + \omega L\Delta i_{cd}^0 + \Delta u_{fq} \\ &\quad + \left(\omega L i_{cq}^0 + u_{cd}^{c0}\cos\theta_p^0 - u_{cq}^{c0}\sin\theta_p^0 - u_{fd}^0\right)\Delta\theta_p\end{aligned} \tag{B.13}$$

given the PI gains of the inner-loop k_{pi} and k_{ii} respectively, (B.13) can be re-written as

$$\begin{aligned}\Delta u_{cd} &= k_{pi}\left(-\cos\theta_p^0\Delta i_{cd}^* + \sin\theta_p^0\Delta i_{cq}^* + \Delta i_{cd} + i_{cq}^0\Delta\theta_p\right) - \omega L\Delta i_c q^0 + \Delta u_{fd} \\ &\quad + \left(\omega L i_{cd}^0 - u_{cq}^{c0}\cos\theta_p^0 - u_{cd}^{c0}\sin\theta_p^0 + u_{fq}^0\right)\Delta\theta_p + \Delta x_{id} \\ \Delta u_{cq} &= k_{pi}\left(-\cos\theta_p^0\Delta i_{cq}^* - \sin\theta_p^0\Delta i_{cd}^* + \Delta i_{cq} - i_{cd}^0\Delta\theta_p\right) + \omega L\Delta i_{cd}^0 + \Delta u_{fq} \\ &\quad + \left(\omega L i_{cq}^0 + u_{cd}^{c0}\cos\theta_p^0 - u_{cq}^{c0}\sin\theta_p^0 - u_{fd}^0\right)\Delta\theta_p + \Delta x_{iq}\end{aligned} \tag{B.14}$$

where

$$\begin{aligned}\frac{d}{dt}\Delta x_{id} &= \left(-\cos\theta_p^0\Delta i_{cd}^* + \sin\theta_p^0\Delta i_{cq}^* + \Delta i_{cd} + i_{cq}^0\Delta\theta_p\right) \\ \frac{d}{dt}\Delta x_{iq} &= \left(-\cos\theta_p^0\Delta i_{cq}^* - \sin\theta_p^0\Delta i_{cd}^* + \Delta i_{cq} - i_{cd}^0\Delta\theta_p\right)\end{aligned} \tag{B.15}$$

and Δx_{id}, Δx_{iq} are the states of the inner-loop integrators. The references to the inner-loop Δi_{cd}^* and Δi_{cq}^* can be eliminated from (B.14) and (B.15) by substituting (B.9) and (B.10) to obtain

$$\begin{aligned}\Delta u_{cd} &= k_{pi}\Delta i_{cd} - \omega L\Delta i_{cq} + \frac{k k_{pi} k_{pv} V_{dc}^0\cos\theta_p^0}{u_f^{d0}}\Delta V_{dc} \\ &\quad + \left(\omega L i_{cd}^0 - u_{cq}^{c0}\cos\theta_p^0 - u_{cd}^{c0}\sin\theta_p^0 + k_{pi} i_{cq}^0 + u_{fq}^0\right)\Delta\theta_p \\ &\quad + \left(\frac{k k_{pi} P_{dc}^0\cos\theta_p^0}{(u_{fd}^0)^2} - \frac{k_{pi} k_{pu} u_{fd}^0\sin\theta_p^0}{U_f^0} + 1\right)\Delta u_{fd} - \frac{k_{pi} k_{pu} u_{fq}^0\sin\theta_p^0}{U_f^0}\Delta u_f^q \\ &\quad - \frac{k k_{pi} V_{dc}^0\cos\theta_p^0}{u_{fd}^0}\Delta x_d + k_{pi}\sin\theta_p^0\Delta x_q + \Delta x_{id}\end{aligned} \tag{B.16a}$$

$$\begin{aligned}\Delta u_{cq} = {} & \omega L \Delta i_{cd} + k_{pi} \Delta i_{cq} + \frac{k k_{pi} k_{pv} V_{dc}^0 \sin\theta_p^0}{u_f^{d0}} \Delta V_{dc} \\ & + \left(\omega L i_{cq}^0 + u_{cd}^{c0} \cos\theta_p^0 - u_{cq}^{c0} \sin\theta_p^0 + k_{pi} i_{cd}^0 - u_{fd}^0\right) \Delta\theta_p \\ & + \left(\frac{k_{pi} k_{pu} u_{fd}^0 \cos\theta_p^0}{U_f^0} + \frac{k k_{pi} P_{dc}^0 \sin\theta_p^0}{(u_{fd}^0)^2}\right) \Delta u_{fd} + \left(\frac{k_{pi} k_{pu} u_{fq}^0 \cos\theta_p^0}{U_f^0} + 1\right) \Delta u_f^q \\ & - \frac{k k_{pi} V_{dc}^0 \sin\theta_p^0}{u_{fd}^0} \Delta x_d - k_{pi} \cos\theta_p^0 \Delta x_q + \Delta x_{id}\end{aligned} \tag{B.16b}$$

where

$$\begin{aligned}\frac{d}{dt}\Delta x_{id} = {} & \Delta i_{cd} + \left(\frac{k k_{pv} V_{dc}^0 \cos\theta_p^0}{u_{fd}^0} + \frac{k k_{iv} V_{dc}^0 \cos\theta_p^0}{u_{fd}^0}\right) \Delta V_{dc} + i_{cq}^0 \Delta\theta_p \\ & + \left(\frac{k P_{dc}^0 \cos\theta_p^0}{(u_{fd}^0)^2} - \frac{k_{pu} u_{fd}^0 \sin\theta_p^0}{U_f^0} - \frac{k_{iu} u_{fd}^0 \sin\theta_p^0}{U_f^0}\right) \Delta u_{fd} \\ & - \left(\frac{k_{pu} u_{fq}^0 \sin\theta_p^0}{U_f^0} + \frac{k_{iu} u_{fq}^0 \sin\theta_p^0}{U_f^0}\right) \Delta u_{fq}\end{aligned} \tag{B.17a}$$

$$\begin{aligned}\frac{d}{dt}\Delta x_{iq} = {} & \Delta i_{cq} + \left(\frac{k k_{pv} V_{dc}^0 \sin\theta_p^0}{u_{fd}^0} + \frac{k k_{iv} V_{dc}^0 \sin\theta_p^0}{u_{fd}^0}\right) \Delta V_{dc} - i_{cd}^0 \Delta\theta_p \\ & + \left(\frac{k P_{dc}^0 \sin\theta_p^0}{(u_{fd}^0)^2} + \frac{k_{pu} u_{fd}^0 \cos\theta_p^0}{U_f^0} + \frac{k_{iu} u_{fd}^0 \cos\theta_p^0}{U_f^0}\right) \Delta u_{fd} \quad . \\ & + \left(\frac{k_{pu} u_{fq}^0 \cos\theta_p^0}{U_f^0} + \frac{k_{iu} u_{fq}^0 \cos\theta_p^0}{U_f^0}\right) \Delta u_{fq}\end{aligned} \tag{B.17b}$$

Subsequently, (B.16) is substituted into the physical equations in (B.6a) and (B.6b) to obtain

$$\begin{aligned}\frac{d}{dt}\Delta i_{cd} = {} & -\left(\frac{R + k_{pi}}{L}\right) \Delta i_{cd} - \frac{k k_{pi} k_{pv} V_{dc}^0 \cos\theta_p^0}{L u_{fd}^0} \Delta V_{dc} \\ & - \left(\frac{k_{pi} i_{cq}^0 - u_{cq}^{c0} \cos\theta_p^0 - u_{cd}^{c0} \sin\theta_p^0 + u_{fq}^0}{L} + \omega i_{cd}^0\right) \Delta\theta_p \\ & + \left(-\frac{k k_{pi} P_{dc}^0 \cos\theta_p^0}{L (u_{fd}^0)^2} + \frac{k_{pi} k_{pu} u_{fd}^0 \sin\theta_p^0}{L U_f^0}\right) \Delta u_{fd} + \frac{k_{pi} k_{pu} u_{fq}^0 \sin\theta_p^0}{L U_f^0} \Delta u_{fq} \\ & + \frac{k k_{pi} V_{dc}^0 \cos\theta_p^0}{L u_{fd}^0} \Delta x_d - \frac{k_{pi} \sin\theta_p^0}{L} \Delta x_q - \frac{1}{L} \Delta x_{id}\end{aligned} \tag{B.18a}$$

$$\begin{aligned}\frac{d}{dt}\Delta i_{cq} = &-\left(\frac{R+k_{pi}}{L}\right)\Delta i_{cq} - \frac{kk_{pi}k_{pv}V_{dc}^0\sin\theta_p^0}{Lu_f^{d0}}\Delta V_{dc}\\ &+\left(\frac{k_{pi}i_{cd}^0 - u_{cd}^{c0}\cos\theta_p^0 + u_{cq}^{c0}\sin\theta_p^0 + u_{fd}^0 - \omega i_{cq}^0}{L}\right)\Delta\theta_p\\ &+\left(-\frac{kk_{pi}P_{dc}^0\sin\theta_p^0}{L(u_{fd}^0)^2} - \frac{k_{pi}k_{pu}u_{fd}^0\cos\theta_p^0}{LU_f^0}\right)\Delta u_{fd} - \frac{k_{pi}k_{pu}u_{fq}^0\cos\theta_p^0}{LU_f^0}\Delta u_{fq}\\ &+\frac{kk_{pi}V_{dc}^0\sin\theta_p^0}{Lu_{fd}^0}\Delta x_d + \frac{k_{pi}\cos\theta_p^0}{L}\Delta x_q - \frac{1}{L}\Delta x_{iq}.\end{aligned} \tag{B.18b}$$

To include the states of the PLL, (2.9) is linearized and re-written as

$$\begin{aligned}\frac{d}{dt}\Delta\theta_p &= -K_{pll}\Delta u_{fq}^c\\ &= -k_{ppll}\Delta u_{fq}^c - x_{pll}\Delta u_{fq}^c\end{aligned} \tag{B.19}$$

where

$$\frac{d}{dt}\Delta x_{pll} = k_{ipll}\Delta u_{fq}^c$$

and Δx_{pll} is the state of the PLL integrator, and Δu_{fq}^c can be eliminated by substituting from the transformation matrix in (B.2b) to obtain the final state equations as

$$\begin{aligned}\frac{d}{dt}\Delta\theta_p = &\left(k_{ppll}u_{fd}^0\cos\theta_p^0 + k_{ppll}u_{fq}^0\sin\theta_p^0\right)\Delta\theta_p + k_{ppll}\sin\theta_p^0\Delta u_{fd}\\ &- k_{ppll}\cos\theta_p^0\Delta u_{fq} - \Delta x_{pll}\end{aligned} \tag{B.20a}$$

$$\begin{aligned}\frac{d}{dt}\Delta x_{pll} = &-\left(k_{ipll}u_{fd}^0\cos\theta_p^0 + k_{ipll}u_{fq}^0\sin\theta_p^0\right)\Delta\theta_p - k_{ipll}\sin\theta_p^0\Delta u_{fd}\\ &+ k_{ipll}\cos\theta_p^0\Delta u_{fq}\end{aligned} \tag{B.20b}$$

Finally, for the physical DC side equation in (B.6c), ΔI_{dc} can be eliminated by applying the power balance expression to obtain

$$\begin{aligned}\frac{d}{dt}\Delta V_{dc} = &\frac{u_{fd}^0}{kV_{dc}^0C_{dc}}\Delta i_{cd} + \frac{u_{fq}^0}{kV_{dc}^0C_{dc}}\Delta i_{cq} + \frac{i_{cd}^0}{kV_{dc}^0C_{dc}}\Delta u_f^d + \frac{i_{cq}^0}{kV_{dc}^0C_{dc}}\Delta u_{fq}\\ &- \frac{I_{dc}^0}{V_{dc}^0C_{dc}}\Delta V_{dc} + \frac{1}{C_{dc}}\Delta I_n\end{aligned}. \tag{B.21}$$

Equations (B.8), (B.11), (B.17), (B.18), (B.20), (B.21) fully define the state-space equations of the alternating/direct-voltage controlled VSC and are sorted according to the formal state-space notation, given in (B.4.1), and (B.23).

$$
\mathbf{A} = \begin{pmatrix}
-\frac{R+k_{pi}}{L} & 0 & -\frac{kk_{pi}k_{pv}V_{dc}^0\cos\theta_p^0}{Lu_{fd}^0} & \frac{-k_{pi}i_{cq}^0 - i_{cd}^0\omega_1 L + u_{cq}^{c0}\cos\theta_p^0 + u_{cd}^{c0}\sin\theta_p^0 - u_{fq}^0}{L} & \frac{kk_{pi}V_{dc}^0\cos\theta_p^0}{Lu_{fd}^0} & -\frac{k_{pi}\sin\theta_p^0}{L} \\
0 & -\frac{R+k_{pi}}{L} & -\frac{kk_{pi}k_{pv}V_{dc}^0\sin\theta_p^0}{Lu_{fd}^0} & \frac{k_{pi}i_{cd}^0 - i_{cq}^0\omega_1 L + u_{cq}^{c0}\sin\theta_p^0 - u_{cd}^{c0}\cos\theta_p^0 - u_{fd}^0}{L} & \frac{kk_{pi}V_{dc}^0\sin\theta_p^0}{Lu_{fd}^0} & \frac{k_{pi}\cos\theta_p^0}{Lu_{fd}^0} \\
\frac{u_{fd}^0}{kC_{dc}V_{dc}^0} & \frac{u_{fq}^0}{kC_{dc}V_{dc}^0} & -\frac{I_{dc}^0}{C_{dc}V_{dc}^0} & 0 & 0 & 0 \\
0 & 0 & 0 & k_{ppll}u_{fd}^0\cos\theta_p^0 + k_{ppll}u_{fq}^0\sin\theta_p^0 & 0 & 0 \\
0 & 0 & -k_{iv} & 0 & 0 & 0 \\
0 & 0 & 0 & 0 & 0 & 0 \\
1 & 0 & \cos\theta_p^0\left(\frac{k(k_{pv}+k_{iv}V_{dc}^0)}{u_{fd}^0}\right) & i_{cq}^0 & 0 & 0 \\
0 & 1 & \sin\theta_p^0\left(\frac{k(k_{pv}+k_{iv}V_{dc}^0)}{u_{fd}^0}\right) & -i_{cd} & 0 & 0 \\
0 & 0 & 0 & -k_{ipll}u_{fd}^0\cos\theta_p^0 - k_{ipll}u_{fq}^0\sin\theta_p^0 & 0 & 0
\end{pmatrix}
$$

$$
\begin{pmatrix}
-\frac{1}{L} & 0 & 0 \\
0 & -\frac{1}{L} & 0 \\
0 & 0 & 0 \\
0 & 0 & -1 \\
0 & 0 & 0 \\
0 & 0 & 0 \\
0 & 0 & 0 \\
0 & 0 & 0 \\
0 & 0 & 0
\end{pmatrix} \tag{B.22}
$$

$$
\mathbf{B} = \begin{pmatrix}
-\frac{kk_{pi}P^0\cos\theta_p^0}{L(u_{fd}^0)^2} + \frac{k_{pi}k_{pu}u_{fq}^0\sin\theta_p^0}{LU_f^0} & \frac{k_{pi}k_{pu}u_{fq}^0\sin\theta_p^0}{LU_f^0} & 0 \\
-\frac{kk_{pi}P^0\sin\theta_p^0}{L(u_{fd}^0)^2} - \frac{k_{pi}k_{pu}u_{fd}^0\cos\theta_p^0}{LU_f^0} & -\frac{k_{pi}k_{pu}u_{fq}^0\cos\theta_p^0}{LU_f^0} & 0 \\
\frac{i_{cd}^0}{kC_{dc}V_{dc}^0} & \frac{i_{cq}^0}{kC_{dc}V_{dc}^0} & \frac{1}{C_{dc}} \\
k_{ppll}\sin\theta_p^0 & -k_{ppll}\cos\theta_p^0 & 0 \\
0 & 0 & 0 \\
-\frac{k_{iu}u_{fd}^0}{U_f^0} & -\frac{k_{iu}u_{fq}^0}{U_f^0} & 0 \\
\frac{kP^0\cos\theta_p^0}{(u_{fd}^0)^2} - \sin\theta_p^0\left(\frac{k_{pu}u_{fd}^0+k_{iu}u_{fd}^0}{U_f^0}\right) & -\sin\theta_p^0\left(\frac{k_{pu}u_{fq}^0+k_{iu}u_{fq}^0}{U_f^0}\right) & 0 \\
\frac{kP^0\sin\theta_p^0}{(u_{fd}^0)^2} + \cos\theta_p^0\left(\frac{k_{pu}u_{fd}^0+k_{iu}u_{fd}^0}{U_f^0}\right) & 0 & \\
-k_{ipll}\sin\theta_p^0 & k_{ipll}\cos\theta_p^0 & 0
\end{pmatrix} \tag{B.23}
$$

B.4.2 Alternating/Droop/Active Power Controlled VSC

Given the structure of the droop/active power controller, the linearized active current reference to the inner-loop is rewritten as

$$\Delta i_{cd}^{*} = -K_p(s)\left(R_{dc}\Delta V_{dc} + \Delta P\right). \tag{B.24}$$

Given the PI gains of the active power controller k_{pp} and k_{ip} respectively,

$$\Delta i_{cd}^{*} = -k_{pp}(\Delta P + R_{dc}\Delta V_{dc}) - \underbrace{\frac{k_{ip}}{s}(\Delta P + R_{dc}\Delta V_{dc})}_{\Delta x_{pd}} \tag{B.25}$$

and

$$\frac{d}{dt}\Delta x_{pd} = k_{ip}(\Delta P + R_{dc}\Delta V_{dc}) \tag{B.26}$$

where Δx_{pd} is the state of the active power control integrator and ΔP can be eliminated from the above equations by substituting the linearized AC power to obtain

$$\Delta i_{cd}^{*} = -k_{pp}\left(R_{dc}\Delta V_{dc} + \frac{u_{fd}^{0}\Delta i_{cd} + u_{fq}^{0}\Delta i_{cq} + i_{cd}^{0}\Delta u_{fd} + i_{cq}^{0}\Delta u_{fq}}{k}\right) - \Delta x_{pd} \tag{B.27}$$

$$\frac{d}{dt}\Delta x_{pd} = k_{ip}R_{dc}\Delta V_{dc} + \frac{k_{ip}u_{fd}^{0}}{k}\Delta i_{cd} + \frac{k_{ip}u_{fq}^{0}}{k}\Delta i_{cq} + \frac{k_{ip}i_{cd}^{0}}{k}\Delta u_{fd} + \frac{k_{ip}i_{cq}^{0}}{k}\Delta u_{fq} \tag{B.28}$$

For the reactive current reference to the inner-loop, equations (B.10) and (B.11) apply. The state expressions of the inner-loop remain the same as those from equations (B.12) – (B.15). The inner-loop references are then eliminated by substituting (B.27) and (B.10) to obtain

$$\begin{aligned}
\Delta u_{cd} = {} & k_{pi}\left(\frac{k_{pp}u_{fd}^{0}\cos\theta_p^{0}}{k} + 1\right)\Delta i_{cd} + \left(\frac{k_{pi}k_{pp}u_{fq}^{0}\cos\theta_p^{0}}{k} - \omega L\right)\Delta i_{cq} \\
& + k_{pi}k_{pp}R_{dc}\cos\theta_p^{0}\Delta V_{dc} + \left(\omega L i_{cd}^{0} - u_{cq}^{c0}\cos\theta_p^{0} - u_{cd}^{c0}\sin\theta_p^{0} + k_{pi}i_{cq}^{0} + u_{fq}^{0}\right)\Delta\theta_p \\
& + \left(\frac{k_{pi}k_{pp}i_{cd}^{0}\cos\theta_p^{0}}{k} - \frac{k_{pi}k_{pu}u_{fd}^{0}\sin\theta_p^{0}}{U_f^{0}} + 1\right)\Delta u_{fd} \\
& + \left(\frac{k_{pi}k_{pp}i_{cq}^{0}\cos\theta_p^{0}}{k} - \frac{k_{pi}k_{pu}u_{fq}^{0}\sin\theta_p^{0}}{U_f^{0}}\right)\Delta u_{fq} + k_{pi}\cos\theta_p^{0}\Delta x_{pd} \\
& + k_{pi}\sin\theta_p^{0}\Delta x_{pq} + \Delta x_{id}
\end{aligned} \tag{B.29a}$$

$$\begin{aligned}\Delta u_{cq} = &\left(\frac{k_{pi}k_{pp}u_{fd}^0\sin\theta_p^0}{k}+\omega L\right)\Delta i_{cd}+\left(\frac{k_{pi}k_{pp}u_{fq}^0\sin\theta_p^0}{k}+1\right)\Delta i_{cq}\\ &+k_{pi}k_{pp}R_{dc}\sin\theta_p^0\Delta V_{dc}\\ &+\left(\omega L i_{cq}^0+u_{cd}^{c0}\cos\theta_p^0-u_{cq}^{c0}\sin\theta_p^0-k_{pi}i_{cd}^0-u_{fd}^0\right)\Delta\theta_p\\ &+\left(\frac{k_{pi}k_{pu}u_{fd}^0\cos\theta_p^0}{U_f^0}+\frac{k_{pi}k_{pu}i_{cd}^0\sin\theta_p^0}{k}\right)\Delta u_{fd}\\ &+\left(\frac{k_{pi}k_{pu}u_{fq}^0\cos\theta_p^0}{U_f^0}+\frac{k_{pi}k_{pp}i_{cq}^0\sin\theta_p^0}{k}+1\right)\Delta u_{fq}+k_{pi}\sin\theta_p^0\Delta x_{pd}\\ &-k_{pi}\cos\theta_p^0\Delta x_{pq}+\Delta x_{iq}\end{aligned} \tag{B.29b}$$

where

$$\begin{aligned}\frac{d}{dt}\Delta x_{id} = &\left(\frac{k_{pp}u_{fd}^0\cos\theta_p^0}{k}+\frac{k_{ip}u_{fd}^0\cos\theta_p^0}{k}+1\right)\Delta i_{cd}\\ &+\left(\frac{k_{pp}u_{fq}^0\cos\theta_p^0+k_{ip}u_{fq}^0\cos\theta_p^0}{k}\right)\Delta i_{cq}\\ &+R_{dc}(k_{ip}+k_{pp})\cos\theta_p^0\Delta V_{dc}+i_{cq}^0\Delta\theta_p\\ &+\left(\frac{k_{pp}i_{cd}^0\cos\theta_p^0+k_{ip}i_{cd}^0\cos\theta_p^0}{k}-\frac{k_{pu}u_{fd}^0\sin\theta_p^0}{U_f^0}-\frac{k_{iu}u_{fd}^0\sin\theta_p^0}{U_f^0}\right)\Delta u_{fd}\\ &+\left(\frac{k_{pp}i_{cq}^0\cos\theta_p^0+k_{ip}i_{cq}^0\cos\theta_p^0}{k}-\frac{k_{pu}u_{fq}^0\sin\theta_p^0}{U_f^0}-\frac{k_{iu}u_{fq}^0\sin\theta_p^0}{U_f^0}\right)\Delta u_{fq}\end{aligned} \tag{B.30a}$$

$$\begin{aligned}\frac{d}{dt}\Delta x_{iq} = &\left(\frac{k_{pp}u_{fd}^0\sin\theta_p^0}{k}+\frac{k_{ip}u_{fd}^0\sin\theta_p^0}{k}\right)\Delta i_{cd}+\Delta i_{cq}\\ &+R_{dc}(k_{ip}+k_{pp})\sin\theta_p^0\Delta V_{dc}-i_{cd}^0\Delta\theta_p\\ &+\left(\frac{k_{pu}u_{fd}^0\cos\theta_p^0+k_{iu}u_{fd}^0\cos\theta_p^0}{U_f^0}+\frac{k_{pp}i_{cd}^0\sin\theta_p^0}{k}-\frac{k_{ip}i_{cd}^0\sin\theta_p^0}{k}\right)\Delta u_{fd}\\ &+\left(\frac{k_{pp}i_{cq}^0\sin\theta_p^0+k_{ip}i_{cq}^0\sin\theta_p^0}{k}-\frac{k_{pu}u_{fq}^0\cos\theta_p^0}{U_f^0}+\frac{k_{iu}u_{fq}^0\cos\theta_p^0}{U_f^0}\right)\Delta u_{fq}\end{aligned}. \tag{B.30b}$$

Subsequently, (B.29) is substituted into the physical equations to obtain

$$\begin{aligned}\frac{d}{dt}\Delta i_{cd} = &\left(-\frac{R}{L} - \frac{k_{pi}k_{pp}u_{fd}^0\cos\theta_p^0}{kL} - \frac{k_{pi}}{L}\right)\Delta i_{cd} - \frac{k_{pi}k_{pp}u_{fq}^0\cos\theta_p^0}{kL}\Delta i_{cq}\\ &- \frac{k_{pi}k_{pp}R_{dc}\cos\theta_p^0}{L}\Delta V_{dc}\\ &+ \left(-\frac{k_{pi}i_{cq}^0}{L} - i_{cd}^0\omega + \frac{u_{cq}^{c0}\cos\theta_p^0 + u_{cd}^{c0}\sin\theta_p^0 - u_{fq}^0}{L}\right)\Delta\theta_p\\ &+ \left(-\frac{k_{pi}k_{pp}i_{cd}^0\cos\theta_p^0}{kL} + \frac{k_{pi}k_{pu}u_{fd}^0\sin\theta_p^0}{LU_f^0}\right)\Delta u_{fd}\\ &+ \left(-\frac{k_{pi}k_{pp}i_{cq}^0\cos\theta_p^0}{kL} + \frac{k_{pi}k_{pu}u_{fq}^0\sin\theta_p^0}{LU_f^0}\right)\Delta u_{fq} - \frac{k_{pi}\cos\theta_p^0}{L}\Delta x_{pd}\\ &- \frac{k_{pi}\sin\theta_p^0}{L}\Delta x_{pq} - \frac{1}{L}\Delta x_{id}\end{aligned} \tag{B.31a}$$

$$\begin{aligned}\frac{d}{dt}\Delta i_{cq} = &-\frac{k_{pi}k_{pp}u_{fd}^0\sin\theta_p^0}{kL}\Delta i_{cd} + \left(-\frac{R}{L} - \frac{k_{pi}k_{pp}u_{fq}^0\sin\theta_p^0}{kL} - \frac{k_{pi}}{L}\right)\Delta i_{cq}\\ &- \frac{k_{pi}k_{pp}R_{dc}\sin\theta_p^0}{L}\Delta V_{dc}\\ &+ \left(\frac{k_{pi}i_{cd}^0}{L} - i_{cq}^0\omega + \frac{u_{cq}^{c0}\sin\theta_p^0 - u_{cd}^{c0}\cos\theta_p^0 + u_{fd}^0}{L}\right)\Delta\theta_p\\ &+ \left(-\frac{k_{pi}k_{pu}u_{fd}^0\cos\theta_p^0}{LU_f^0} - \frac{k_{pi}k_{pp}i_{cd}^0\sin\theta_p^0}{kL}\right)\Delta u_{fd}\\ &+ \left(-\frac{k_{pi}k_{pp}i_c^{q0}\sin\theta_p^0}{kL} - \frac{k_{pi}k_{pu}u_{fq}^0\cos\theta_p^0}{LU_f^0}\right)\Delta u_{fq} - \frac{k_{pi}\sin\theta_p^0}{L}\Delta x_{pd}\\ &+ \frac{k_{pi}\cos\theta_p^0}{L}\Delta x_{pq} - \frac{1}{L}\Delta x_{iq}\end{aligned} \tag{B.31b}$$

The states of the PLL remain as those of (B.20), whereas the physical DC side state equation remains the same as (B.21). Therefore, in addition to these, equations (B.11), (B.28), (B.30), and (B.31) constitute the complete state-space equations of the droop/active power controlled converter with matrices given in (B.4.2) and (B.33).

$$
\mathbf{A} = \begin{pmatrix}
-\frac{R+k_{pi}}{L} & -\frac{k_{pi}k_{pp}u^0_{fd}\cos\theta^0_p}{kL} & -\frac{k_{pi}k_{pp}u^0_{fq}\cos\theta^0_p}{kL} & -\frac{k_{pi}k_{pp}R_{dc}\cos\theta^0_p}{L} \\
-\frac{k_{pi}k_{pp}u^0_{fd}\sin\theta^0_p}{kL} & -\frac{R+k_{pi}}{L} & -\frac{k_{pi}k_{pp}u^0_{fq}\sin\theta^0_p}{kL} & -\frac{k_{pi}k_{pp}R_{dc}\sin\theta^0_p}{L} \\
\frac{u^0_{fd}}{kC_{dc}V^0_{dc}} & \frac{u^0_{fq}}{kC_{dc}V^0_{dc}} & 0 & -\frac{I^0_{dc}}{C_{dc}V^0_{dc}} \\
0 & 0 & 0 & 0 \\
\frac{k_{ip}u^0_{fd}}{k} & \frac{k_{ip}u^0_{fq}}{k} & k_{ip}R_{dc} & \\
0 & 0 & 0 & \\
\cos\theta^0_p\left(\frac{k_{pp}u^0_{fd}+k_{ip}u^0_{fd}}{k}\right)+1 & \cos\theta^0_p\left(\frac{k_{pp}u^0_{fq}+k_{ip}u^0_{fq}}{k}\right) & \cos\theta^0_p\left(k_{ip}R_{dc}+k_{pp}R_{dc}\right) & \\
\sin\theta^0_p\left(\frac{k_{pp}u^0_{fd}+k_{ip}u^0_{fd}}{k}\right) & \sin\theta^0_p\left(\frac{k_{pp}u^0_{fq}+k_{ip}u^0_{fq}}{k}\right)+1 & sin\theta^0_p\left(k_{ip}R_{dc}+k_{pp}R_{dc}\right) & \\
0 & 0 & 0 &
\end{pmatrix}
$$

$$
\begin{pmatrix}
-\frac{k_{pi}i^0_{cq}-i^0_{cd}\omega_1 L-u^0_{fq}+u^{c0}_{cd}\sin\theta^0_p+u^{c0}_{cq}\cos\theta^0_p}{L} & -\frac{k_{pi}\cos\theta^0_p}{L} & -\frac{k_{pi}\sin\theta^0_p}{L} & -\frac{1}{L} & 0 & 0 \\
-\frac{k_{pi}i^0_{cd}-i^0_{cq}\omega_1 L+u^0_{fd}-u^{c0}_{cd}\cos\theta^0_p+u^{c0}_{cq}\sin\theta^0_p}{L} & -\frac{k_{pi}\sin\theta^0_p}{L} & \frac{k_{pi}\cos\theta^0_p}{L} & 0 & -\frac{1}{L} & 0 \\
0 & 0 & 0 & 0 & 0 & 0 \\
k_{pll}u^0_{fd}\cos\theta^0_p+k_{pll}u^0_{fq}\sin\theta^0_p & 0 & 0 & 0 & 0 & -1 \\
0 & 0 & 0 & 0 & 0 & 0 \\
0 & 0 & 0 & 0 & 0 & 0 \\
i^0_{cq} & 0 & 0 & 0 & 0 & 0 \\
-i_{cd} & 0 & 0 & 0 & 0 & 0 \\
-k_{ipll}u^0_{fd}\cos\theta^0_p-k_{ipll}u^0_{fq}\sin\theta^0_p & 0 & 0 & 0 & 0 & 0
\end{pmatrix}
\tag{B.32}
$$

$$
\mathbf{B} = \begin{pmatrix}
-\frac{k_{pi}k_{pp}i_{cd}^0\cos\theta_p^0}{kL} + \frac{k_{pi}k_{pu}u_{fd}^0\sin\theta_p^0}{LU_f^0} & -\frac{k_{pi}k_{pp}i_{cq}^0\cos\theta_p^0}{kL} + \frac{k_{pi}k_{pu}u_{fq}^0\sin\theta_p^0}{LU_f^0} & 0 \\
-\frac{k_{pi}k_{pp}i_{cd}^0\sin\theta_p^0}{kL} - \frac{k_{pi}k_{pu}u_{fd}^0\cos\theta_p^0}{LU_f^0} & -\frac{k_{pi}k_{pp}i_{cq}^0\sin\theta_p^0}{kL} - \frac{k_{pi}k_{pu}u_{fq}^0\cos\theta_p^0}{LU_f^0} & 0 \\
\frac{i_{cd}^0}{KC_{dc}V_{dc}^0} & \frac{i_{cq}^0}{KC_{dc}V_{dc}^0} & \frac{1}{C_{dc}} \\
k_{ppll}\sin\theta_p^0 & -k_{ppll}\cos\theta_p^0 & 0 \\
\frac{k_{ip}i_{cd}^0}{k} & \frac{k_{ip}i_{cq}^0}{k} & 0 \\
-\frac{k_{iu}u_{fd}^0}{U_f^0} & -\frac{k_{iu}u_{fq}^0}{U_f^0} & 0 \\
\cos\theta_p^0\left(\frac{k_{pp}i_{cd}^0+k_{ip}i_{cd}^0}{k}\right) - sin\theta_p^0\left(\frac{k_{pu}u_{fd}^0-k_{iu}u_{fd}^0}{U_f^0}\right) & \cos\theta_p^0\left(\frac{k_{pp}i_{cq}^0+k_{ip}i_{cq}^0}{k}\right) - sin\theta_p^0\left(\frac{k_{pu}u_{fq}^0-k_{iu}u_{fq}^0}{U_f^0}\right) & 0 \\
sin\theta_p^0\left(\frac{k_{pp}i_{cd}^0-k_{ip}i_{cd}^0}{k}\right) + \cos\theta_p^0\left(\frac{k_{pu}u_{fd}^0+k_{iu}u_{fd}^0}{U_f^0}\right) & \sin\theta_p^0\left(\frac{k_{pp}i_{cq}^0+k_{ip}i_{cq}^0}{k}\right) + cos\theta_p^0\left(\frac{k_{pu}u_{fq}^0+k_{iu}u_{fq}^0}{U_f^0}\right) & 0 \\
-k_{ipll}\sin\theta_p^0 & k_{ipll}\cos\theta_p^0 & 0
\end{pmatrix} \tag{B.33}
$$

B.5 Table of Grid Parameters

Table B.1: System Parameters

Parameter	Value
Rated power	800MVA
Rated Direct-voltage	400kV
Rated alternating-voltage	±220kV (p-p)
PCC capacitance	6μF
Filter inductance	19mH
Filter resistance	0.242Ω
Equivalent transformer inductance	23mH
Equivalent DC capacitance	150μF
Cable inductance	2.6mH/km
Cable capacitance	0.1908μF
System base frequency	50Hz